

**Defined interactions are crucial  
for the structure and function  
of the *Synechocystis* IM30 protein**

Von Jennifer Heidrich, geboren am 21.01.1987 in Wiesbaden

**Dissertation zur Erlangung des Grades eines**

**‘Doctor rerum naturalium (Dr. rer. nat.)’**

der Fachbereiche:

- 08 - Physik, Mathematik und Informatik
- 09 - Chemie, Pharmazie und Geowissenschaften,
- 10 - Biologie,
- Universitätsmedizin

der Johannes Gutenberg-Universität

Mainz, den 28.2.2018



D77

Dekan:

1. Gutachter:

2. Gutachter:

Tag der mündlichen Prüfung: 19.04.2018



Für Juno und Steffen

# I Table of contents

<i>I</i>	<i>Table of contents</i> .....	3
<i>II</i>	<i>Summary</i> .....	9
<i>III</i>	<i>Zusammenfassung</i> .....	10
<i>IV</i>	<i>Publications</i> .....	11
<i>V</i>	<i>Collaborations</i> .....	13
<i>1</i>	<i>Introduction</i> .....	14
1.1	<b>Cyanobacteria and chloroplasts</b> .....	14
1.2	<b>The thylakoid membrane</b> .....	15
1.2.1	Structure and lipid composition .....	15
1.2.2	Biogenesis .....	16
1.3	<b>The availability of Mg<sup>2+</sup> in cyanobacteria and chloroplasts</b> .....	18
1.4	<b>The inner membrane associated protein of 30 kDa (IM30)</b> .....	18
1.4.1	Origin and occurrence .....	18
1.4.2	Structure .....	19
1.4.3	Lipid interaction .....	22
1.4.4	Mg <sup>2+</sup> interaction .....	23
1.4.5	Postulated Functions .....	23
1.5	<b>Objectives of this thesis</b> .....	26
<i>2</i>	<i>Materials and methods</i> .....	29
2.1	<b>Chemicals</b> .....	29
2.2	<b>Buffers and solutions</b> .....	30
2.3	<b>Oligonucleotides</b> .....	32
2.4	<b>Plasmids</b> .....	32
2.5	<b>Enzymes and enzyme buffers</b> .....	32
2.6	<b>Antibodies</b> .....	33
2.7	<b><i>E. coli</i> cells</b> .....	33
2.8	<b>Cell culture media</b> .....	33

<b>2.9</b>	<b>Kits.....</b>	<b>34</b>
<b>2.10</b>	<b>DNA &amp; protein ladders.....</b>	<b>34</b>
<b>2.11</b>	<b>Instruments.....</b>	<b>34</b>
<b>2.12</b>	<b>Consumables.....</b>	<b>35</b>
<b>2.13</b>	<b>Software.....</b>	<b>36</b>
<b>2.14</b>	<b>Molecular biological methods.....</b>	<b>36</b>
2.14.1	Polymerase chain reaction (PCR) .....	36
2.14.2	Site-directed mutagenesis .....	37
2.14.2.1	Primer design.....	38
2.14.3	PCR clean-up .....	38
2.14.4	Generation of pRSET IM30-CFP and pRSET IM30-Venus expression plasmids.....	38
2.14.4.1	pRSET IM30-CFP .....	38
2.14.4.2	pRSET IM30-Venus.....	39
2.14.5	Agarose gel electrophoresis .....	40
2.14.6	Agarose gel elution .....	41
2.14.7	DNA sequencing.....	41
<b>2.15</b>	<b>Microbiological methods.....</b>	<b>41</b>
2.15.1	<i>E. coli</i> plasmid transformation via heat shock .....	41
2.15.2	Preparation of plasmid DNA .....	41
2.15.3	Optical density (OD) determination in <i>E. coli</i> .....	41
2.15.4	Protein expression in <i>E. coli</i> .....	42
2.15.5	<i>E. coli</i> cell disruption via sonification .....	42
<b>2.16</b>	<b>Proteinbiochemical methods.....</b>	<b>42</b>
2.16.1	Protein purification and co-purification via affinity chromatography .....	42
2.16.2	Dialysis .....	43
2.16.3	SDS polyacrylamide gel electrophoresis (SDS-PAGE).....	43
2.16.4	Immunoblot detection .....	44
2.16.5	Concentration determination.....	45
2.16.5.1	Bradford assay .....	45
2.16.5.2	BSA standard SDS-PAGE.....	45
2.16.5.3	Absorbance measurement.....	46
2.16.6	Buffer system.....	46
2.16.7	Concentrating protein samples.....	46
2.16.8	Protein crosslinking .....	47
2.16.8.1	Dissociation of IM30 rings .....	47
2.16.9	Protein denaturation and renaturation .....	47
2.16.10	Protein dephosphorylation .....	48
2.16.11	Tryptic digestion.....	49

---

2.16.11.1	Digestion of IM30 in presence of $Mg^{2+}$ .....	49
2.16.11.2	Digestion of IM30 in presence of DOPG and DOPC liposomes .....	50
2.16.12	Size exclusion chromatography (SEC) .....	50
<b>2.17</b>	<b>Lipidbiochemical methods.....</b>	<b>51</b>
2.17.1	In vitro membrane model systems .....	51
2.17.2	Preparation of multilamellar liposomes .....	51
2.17.3	Preparation of unilamellar liposomes via freeze-thaw .....	51
2.17.4	Preparation of uniformly sized liposomes via extrusion.....	52
<b>2.18</b>	<b>Biophysical methods.....</b>	<b>52</b>
2.18.1	Circular dichroism (CD) spectroscopy .....	52
2.18.1.1	Urea denaturation/renaturation experiments .....	53
2.18.2	Fluorescence spectroscopy .....	54
2.18.2.1	ANS fluorescence.....	55
2.18.2.2	Förster resonance energy transfer (FRET) measurements.....	58
2.18.2.3	Laurdan fluorescence .....	62
2.18.2.4	Liposome destabilization assay .....	65
2.18.2.5	Liposome fusion assay .....	67
2.18.2.6	Tryptophan fluorescence measurements .....	69
2.18.3	Laser-induced liquid bead ion desorption mass spectrometry (LILBID-MS) .....	70
2.18.4	Isothermal titration calorimetry (ITC) .....	70
2.18.5	Single particle tracking (SPT) .....	73
2.18.6	Surface plasmon resonance (SPR).....	73
2.18.7	Transmission electron microscopy (TEM) .....	76
<b>3</b>	<b>Results .....</b>	<b>78</b>
<b>3.1</b>	<b>Expression and purification of IM30 and the mutants <math>\Delta</math>CT, C4 and C7.....</b>	<b>78</b>
3.1.1	Introduction of the used IM30 mutants .....	78
3.1.2	Expression and purification of IM30 and the used IM30 mutants .....	79
3.1.3	Phosphorylation of IM30 .....	81
<b>3.2</b>	<b>The basic building block of IM30 rings.....</b>	<b>82</b>
<b>3.3</b>	<b>Interaction of IM30 with <math>Mg^{2+}</math> .....</b>	<b>83</b>
3.3.1	$Mg^{2+}$ binds to IM30.....	84
3.3.2	Introduction of crosslinked IM30 and IM30 dimers .....	87
3.3.2.1	Introduction of crosslinked IM30.....	87
3.3.2.2	Introduction of IM30 dimers .....	88
3.3.3	Structural flexibility and ring formation of IM30 influences $Mg^{2+}$ binding.....	91
<b>3.4</b>	<b>The effect of <math>Mg^{2+}</math> on the IM30 structure and stability .....</b>	<b>92</b>
3.4.1	$Mg^{2+}$ influences the IM30 secondary structure .....	92
3.4.2	$Mg^{2+}$ influences the IM30 tertiary/quaternary structure.....	95

3.4.3	Introduction of an IM30 FRET system .....	100
3.4.3.1	Expression and purification of IM30-CFP and IM30-Venus .....	100
3.4.3.2	Structure of IM30-CFP, IM30-Venus and IM30-CFP/Venus .....	101
3.4.4	Mg <sup>2+</sup> supports IM30 double-ring formation .....	103
<b>3.5</b>	<b>IM30-membrane interactions.....</b>	<b>107</b>
3.5.1	IM30 interacts with negatively charged membranes .....	107
3.5.2	IM30 interacts with membranes via electrostatic forces .....	109
<b>3.6</b>	<b>The IM30 structure affects membrane interaction .....</b>	<b>112</b>
<b>3.7</b>	<b>Mg<sup>2+</sup> affects the interaction of IM30 with negatively charged surfaces .....</b>	<b>115</b>
<b>3.8</b>	<b>Membrane interaction affects the IM30 oligomerization state .....</b>	<b>118</b>
<b>3.9</b>	<b>IM30-mediated membrane fusion.....</b>	<b>124</b>
3.9.1	IM30 mediates membrane fusion .....	124
3.9.2	MGDG supports IM30-mediated membrane fusion.....	125
3.9.3	Structural flexibility of M30 affects IM30-mediated membrane fusion.....	126
3.9.4	IM30-mediated membrane fusion induces membrane destabilization .....	127
<b>4</b>	<b>Discussion.....</b>	<b>129</b>
<b>4.1</b>	<b>The IM30 oligomerization steps.....</b>	<b>129</b>
<b>4.2</b>	<b>The IM30-Mg<sup>2+</sup> interaction.....</b>	<b>130</b>
4.2.1	Direct binding of Mg <sup>2+</sup> to IM30 .....	131
4.2.2	Structural alterations and stabilization of IM30 upon Mg <sup>2+</sup> binding.....	132
4.2.3	Coordination of Mg <sup>2+</sup> by IM30 residues .....	135
<b>4.3</b>	<b>Interaction of IM30 with membranes.....</b>	<b>138</b>
4.3.1	Forces driving IM30 binding to membranes .....	139
4.3.2	Effect of IM30 ring formation on membrane binding .....	141
4.3.3	Effect of Mg <sup>2+</sup> on IM30 membrane binding.....	142
4.3.4	IM30 ring dissociation upon membrane binding in presence and absence of Mg <sup>2+</sup> .....	143
4.3.5	A model for the IM30-membrane interaction .....	145
<b>4.4</b>	<b>IM30-mediated membrane fusion.....</b>	<b>147</b>
4.4.1	What is required for a functional IM30-mediated membrane fusion?.....	147
4.4.2	The mechanism of the IM30-mediated membrane fusion.....	149
4.4.3	A model for the IM30-mediated membrane fusion .....	151
<b>4.5</b>	<b>The <i>in vivo</i> role of IM30 .....</b>	<b>154</b>
<b>4.6</b>	<b>The <i>in vivo</i> regulation of IM30 .....</b>	<b>156</b>
<b>5</b>	<b>Appendix.....</b>	<b>159</b>
<b>5.1</b>	<b>Protein amino acid sequences.....</b>	<b>159</b>

5.1.1	<i>Synechocystis</i> sll0617/IM30 .....	159
5.1.2	His-tagged IM30 wild type .....	159
5.1.3	His-tagged IM30 $\Delta$ CT.....	160
5.1.4	His-tagged IM30 C4 .....	160
5.1.5	His-tagged IM30 C7 .....	160
5.1.6	His-tagged IM30 A227C.....	161
5.1.7	His-tagged IM30-CFP.....	161
5.1.8	His-tagged IM30-Venus.....	162
<b>5.2</b>	<b>Sequence conservations within the PspA/IM30 family .....</b>	<b>163</b>
<b>5.3</b>	<b>Fluorescence spectra of dyes used in the fusion assays.....</b>	<b>164</b>
5.3.1	Green fusion assay .....	164
5.3.2	Red fusion assay .....	165
<b>5.4</b>	<b>Fluorescence spectra of IM30-CFP and IM30-Venus.....</b>	<b>166</b>
<b>5.5</b>	<b>Fluorescence spectra (triplicate) of IM30-CFP/Venus (1/1).....</b>	<b>166</b>
<b>5.6</b>	<b>TEM micrographs of IM30-CFP, IM30-Venus and IM30-CFP/Venus .....</b>	<b>167</b>
<b>5.7</b>	<b>Membrane fusion of IM30-CFP, IM30-Venus and IM30-CFP/Venus.....</b>	<b>170</b>
<b>5.8</b>	<b>Correction factors of IM30-CFP and IM30-Venus.....</b>	<b>171</b>
5.8.1	IM30-CFP and IM30-Venus fluorescence in presence of 100% DOPG liposomes.....	171
5.8.2	IM30-CFP and IM30-Venus fluorescence in presence of 60%/40% MGDG/DOPG liposomes .....	172
5.8.3	IM30-CFP and IM30-Venus fluorescence in presence of $Mg^{2+}$ .....	174
<b>5.9</b>	<b>Supplemental ITC data.....</b>	<b>176</b>
5.9.1	ITC baselines .....	176
5.9.2	ITC raw data .....	177
<b>5.10</b>	<b>Urea denaturation of IM30 in presence of <math>Mg^{2+}</math> .....</b>	<b>177</b>
<b>5.11</b>	<b>Binding curves of the DOPG interaction of IM30 mutants.....</b>	<b>178</b>
5.11.1	Binding curve of the M30-X/DOPG interaction.....	178
5.11.2	Binding curve of the $\Delta$ CT/DOPG interaction.....	178
5.11.3	Binding curve of the C4/DOPG interaction.....	179
<b>5.12</b>	<b>Supplemental SPR data .....</b>	<b>180</b>
5.12.1	Raw data of the SPR kinetic experiments.....	180
5.12.2	SPR control measurements .....	180
5.12.3	IM30 dissociation from the 16-MHDA layer .....	181
<b>5.13</b>	<b>Mathematical appendix .....</b>	<b>181</b>
5.13.1	Fit functions.....	181
5.13.1.1	Binding fit .....	181

---

5.13.1.2	Boltzmann fit.....	181
5.13.1.3	ExpDec1 fit.....	181
5.13.1.4	ExpDec2 fit.....	182
5.13.1.5	Linear fit.....	182
5.13.1.6	Logistic fit.....	182
5.13.1.7	Hyperbolic fit.....	182
5.13.1.8	Parable fit.....	182
5.13.1.9	Scatter fit.....	182
5.13.2	Derivation of the binding fit.....	182
5.13.3	Gaussian error distribution for $f_D$ .....	183
5.13.4	Estimation of the lipid binding areas for IM30/DOPG interaction.....	183
5.13.5	Estimation of the lipid molecules inside the inner IM30 ring diameter.....	183
<b>VI</b>	<b>List of abbreviations.....</b>	<b>185</b>
<b>VII</b>	<b>List of figures.....</b>	<b>190</b>
<b>VIII</b>	<b>List of tables.....</b>	<b>194</b>
<b>IX</b>	<b>References.....</b>	<b>196</b>
<b>X</b>	<b>Danksagung.....</b>	<b>212</b>
<b>XI</b>	<b>Curriculum vitae.....</b>	<b>214</b>
<b>XII</b>	<b>Declaration.....</b>	<b>217</b>

## II Summary

Biogenesis and maintenance of the thylakoid membranes in cyanobacteria and chloroplasts is a vital process. Nevertheless, the mechanism of the biogenesis has stayed a mystery until today. The IM30 protein appears to play an important role in this process, as has been shown via depletion experiments. Recently, the ability of IM30 to bind to negatively charged lipids and to fuse liposomes in presence of  $Mg^{2+}$  has been demonstrated. This discovery indicates a capability of IM30 to fuse the cytoplasmic membrane in cyanobacteria or the inner envelope in chloroplasts with the constructive thylakoid membrane in order to create a transfer point for lipids and/or proteins. Additionally, connections between different thylakoid membranes through IM30 are thinkable.

In the framework of this thesis, interactions of IM30 leading to membrane fusion and the fusion mechanism itself were investigated. Here, the interplay of IM30 and  $Mg^{2+}$  as well as negatively charged membranes were separately examined via *in vitro* approaches and finally combined in order to have a closer look at the IM30-mediated membrane fusion.

It was observed that  $Mg^{2+}$  binds directly to IM30 and induces a structural alteration in the protein, which results in stabilization against different stressors and an increased tendency of IM30 to form double-rings. The IM30-membrane interaction was shown to depend on the electrostatic interaction with anionic lipids and is enhanced in presence of  $Mg^{2+}$ . Furthermore, lower-ordered IM30 oligomerization states seem to have an increased membrane binding affinity. This circumstance potentially causes the dissociation of IM30 ring oligomers on membranes in absence of  $Mg^{2+}$ . Since the presence of the ring structure is probably crucial for the IM30 function, dissociation of rings might be prevented by  $Mg^{2+}$ . Stabilized by  $Mg^{2+}$ , an IM30 double-ring might be able to fuse two membranes. While doing this, the double-ring seems to dissociate and most probably needs to be reactivated prior to another fusion.

The results of this thesis provide hints concerning the *in vivo* function of IM30, which can now be investigated further in a more target-oriented manner.

### III Zusammenfassung

Die Biogenese und Instandhaltung der Thylakoidmembran in Cyanobakterien und Chloroplasten ist ein lebenswichtiger Prozess. Dennoch ist der Mechanismus der Biogenese bis heute ein Rätsel. Das IM30-Protein scheint in diesem Vorgang eine entscheidende Rolle zu spielen, wie Depletionsexperimente an den Tag gelegt haben. Kürzlich konnte gezeigt werden, dass IM30 an negativ geladene Lipide bindet und Liposomen in Gegenwart von  $Mg^{2+}$  miteinander fusionieren kann. Diese Entdeckung deutet die Fähigkeit des Proteins an, die Cytoplasmamembran in Cyanobakterien bzw. die innere Membran in Chloroplasten mit der sich aufbauenden Thylakoidmembran zu verbinden und eine Übertragung von Lipiden und/oder Proteinen zu ermöglichen. Weiterhin könnte IM30 verschiedene Thylakoidmembranen miteinander verbinden.

Im Rahmen dieser Doktorarbeit sollten Interaktionen von IM30, welche zu der Membranfusion führen, und der Fusionsmechanismus selber näher untersucht werden. Hierbei wurden zunächst die Wechselwirkungen von IM30 mit  $Mg^{2+}$  und negativ geladenen Membranen mit Hilfe von biophysikalischen *in vitro* Experimenten jeweils einzeln untersucht und schließlich miteinander kombiniert, um die durch IM30 induzierte Membranfusion näher zu analysieren.

Es konnte beobachtet werden, dass  $Mg^{2+}$  direkt an IM30 bindet und eine Strukturänderung auslöst, die zur Stabilisierung unter verschiedenen Stressbedingungen und einer erhöhten Tendenz zur Doppelringbildung des Proteins führt. Weiterhin wurde festgestellt, dass die Membranbindung von IM30 durch elektrostatische Wechselwirkungen mit anionischen Lipiden bedingt ist und in Anwesenheit von  $Mg^{2+}$  verstärkt wird. Außerdem scheinen niedere Oligomerisierungsstufen von IM30 eine erhöhte Membranaffinität zu besitzen. Dies trägt vermutlich dazu bei, dass IM30-Ringe in Abwesenheit von  $Mg^{2+}$  durch Membraninteraktion dissoziieren. Da das Vorliegen der Ringstruktur jedoch wichtig für die Ausübung der Fusionsfunktion ist, könnte die Dissoziation zunächst durch  $Mg^{2+}$  verhindert werden. Durch das Kation stabilisiert, könnte ein IM30-Doppelring zwei Membranen miteinander fusionieren. Dabei zerfällt der Doppelring und muss wahrscheinlich vor einer weiteren Fusion reaktiviert werden.

Die Ergebnisse dieser Arbeit liefern Hinweise zur *in vivo*-Funktion von IM30, welche nun gezielter durch weitere Versuche untersucht werden kann.

## IV Publications

The following publications were generated during this thesis:

- Heidrich J.\*, Junglas B. \*, Grytsyk N., Hellmann N., Rusitzka K., Gebauer W., Markl J., Hellwig P. and Schneider D. (2018) Mg<sup>2+</sup>-binding triggers rearrangement of the IM30 ring structure, resulting in augmented exposure of hydrophobic surfaces competent for membrane binding, *J Biol Chem*, in revision  
\*Contributed equally
- Saur M., Hennig R., Young P., Rusitzka K., Hellmann N., Heidrich J., Morgner N., Markl J. and Schneider D. (2017) A Janus-faced IM30 ring involved in thylakoid membrane fusion is assembled from IM30 tetramers, *Structure* **25**, 1380-1390
- Heidrich J., Thurotte A. and Schneider D. (2017) How are thylakoid membranes shaped and maintained?, Layman summary (*Atlas of Science*), URL <https://atlasofscience.org/how-are-thylakoid-membranes-shaped-and-maintained/>
- Heidrich J., Thurotte A. and Schneider D. (2017) Specific interaction of IM30/Vipp1 with cyanobacterial and chloroplast membranes results in membrane remodeling and eventually in membrane fusion, *Biochim Biophys Acta* **1859**, 537–549
- Heidrich J., Wulf V., Hennig R., Saur M., Markl J., Sönnichsen C. and Schneider D. (2016) Organization into higher-ordered ring structures counteracts membrane binding of IM30, a protein associated with inner membranes in chloroplasts and cyanobacteria, *J Biol Chem* **291**, 14954-14962
- Hennig R., Heidrich J., Saur M., Schmäser L., Roeters S.J., Hellmann N., Woutersen S., Bonn M., Weidner T., Markl J. and Schneider D. (2015) IM30 triggers membrane fusion in cyanobacteria and chloroplasts, *Nat Commun* **6**, 7018

The following posters and talks were presented on conferences and meetings during this thesis:

- “IM30/Vipp1 supports thylakoid biogenesis via membrane fusion” (talk) at the First Young Investigator Symposium on Cyanobacteria, Rostock (GER), 5<sup>th</sup>-8<sup>th</sup> October 2016
- “Membrane interaction of the cyanobacterial membrane fusion protein IM30” (poster) at the 10<sup>th</sup> Transporter Colloquium, Rauischholzhausen (GER), 13<sup>rd</sup>-15<sup>th</sup> April 2016

- 
- “Membrane interaction of the cyanobacterial IM30 protein mediates membrane fusion” (poster) at the 67. Mosbacher Kolloquium - Protein Design: From First Principles to Biomedical Applications, Mosbach (GER), 31<sup>st</sup> March- 2<sup>nd</sup> April 2016
  - “IM30 triggers membrane fusion in cyanobacteria and chloroplasts” (poster) at the 15<sup>th</sup> International Symposium on Phototrophic Prokaryotes, Tübingen (GER), 2<sup>nd</sup>-6<sup>th</sup> August 2015
  - “IM30 – a protein that mediates membrane fusion in cyanobacteria” (talk) at the EMBO Practical Course: “The application of transient kinetic methods to biological macromolecules”, Kent (GB), 21<sup>st</sup>-27<sup>th</sup> June 2015
  - “The role of IM30 in the thylakoid membrane biogenesis” (poster) at the 9<sup>th</sup> Transport Colloquium, Rauschholzhausen (GER), May 8<sup>th</sup> – 9<sup>th</sup>, 2014

## V Collaborations

The following theses and reports were supervised during this thesis:

- „Master thesis: Einfluss von Tryptophan 71 auf die Struktur und Funktion des IM30-Proteins aus *Synechocystis* sp. PCC 6803“, Carmen Siebenaller (2016)
- „Master thesis: Einfluss von  $Mg^{2+}$  und anderen zweiwertigen Metallkationen auf die Struktur und Stabilität des IM30-Proteins aus *Synechocystis* sp. PCC 6803“, Benedikt Junglas (2016)
- „FII Report: Untersuchung des Oligomerisierungsverhaltens und der Stabilität in Gegenwart von Magnesium-Ionen von IM30 aus *Synechocystis* sp. PCC 6803“, Benedikt Junglas (2015)
- „Bachelor thesis: Darstellung, Reinigung und Charakterisierung von fluoreszenzmarkierten Vipp1-Proteinen aus *Synechocystis* sp. PCC 6803“, Carmen Siebenaller (2014)

This thesis was supported by the following external collaborations:

- Prof. Nadja Hellmann, Institut für Molekulare Biophysik, Johannes Gutenberg-Universität Mainz
- Prof. Tobias Weidner & Bernhard Menges (group Prof. Mischa Bonn), Max Planck-Institut für Polymerforschung, Mainz
- Kristiane Rusitzka (group Prof. Jürgen Markl), Institut für Zoologie, Johannes Gutenberg-Universität Mainz
- Wolfgang Gebauer, Institut für Zoologie, Johannes Gutenberg-Universität Mainz
- Phoebe Young (group Prof. Nina Morgner), Institut für Physikalische und Theoretische Chemie, Goethe-Universität Frankfurt am Main
- Svenja Winzen (group Prof. Katharina Landfester), Max Planck-Institut für Polymerforschung, Mainz

All data used from the above-mentioned theses and collaborations are marked in the text.

# 1 Introduction

## 1.1 Cyanobacteria and chloroplasts

The existence of an oxygen atmosphere is essential for almost all life on earth. Cyanobacteria, which were formerly known as blue-green algae, have existed for ~3.2 billion years and are the oldest photosynthetic producers of oxygen via photosynthesis (Allwood *et al.* 2006; Bosak *et al.* 2009; Govindjee & Shevela 2011). They were responsible for flooding the earth's atmosphere with the vital gas around ~2.3 billion years ago, and thereby, aerobic conditions for further life development were created (Govindjee & Shevela 2011). Inevitably, the evolution of eukaryotic photosynthesis took place upon endosymbiosis of a cyanobacterial ancestor into the precursor cells of early plants and higher algae, leading to the development of today's chloroplasts (Martin & Kowallik 1999). Consequently, cyanobacteria and chloroplasts share many structural similarities, *e.g.* a complex membrane system. Cyanobacteria are surrounded by an outer membrane (OM) and the cytoplasmic membrane (PM), whereas chloroplasts have an outer envelope (OE) and an inner envelope (IE). Furthermore, cyanobacteria and chloroplasts contain an internal membrane network, the so-called thylakoid membranes (TM), which represent the stage for the light reaction of the photosynthesis. In some cyanobacteria, the TM was observed to converge to the PM. These areas are called thylakoid centers. In *Fig. 1.1* the ultrastructure of the cyanobacterium *Synechocystis* sp. PCC 6803 (*Synechocystis*) is exemplarily shown.

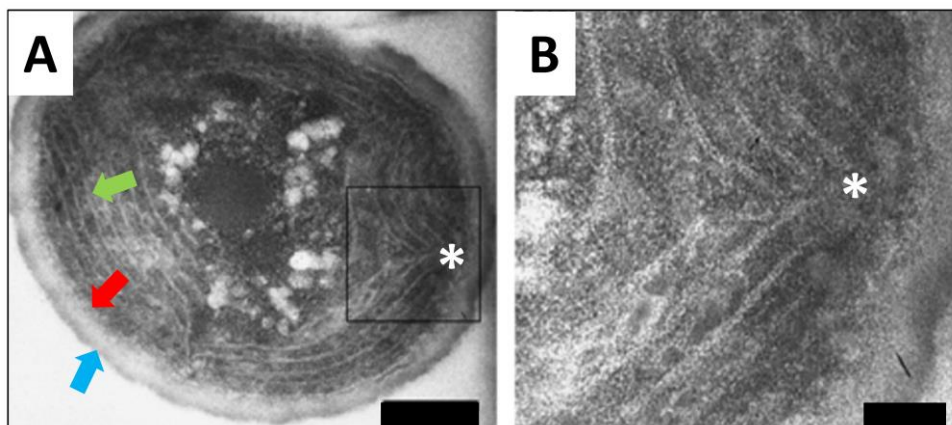


**Fig. 1.1:** *Synechocystis* sp. PCC 6803

An electron micrograph of *Synechocystis* is shown, wherein the OM (blue arrow), the PM (red arrow), a TM (green arrow) and a thylakoid center (\*) are indicated (A). The framed area in (A) is enlarged in (B). Scale bars represent 200 nm (A) and 100 nm (B). Modified from (Nickelsen *et al.* 2011), used with permission from Oxford University Press (license number 4190271041641 via RightsLink).

Due to their common heritage, cyanobacteria are perfectly suitable as a model organism for chloroplasts when it comes to research on photosynthesis and TM biogenesis. The protein of interest in this thesis originates from the cyanobacterium *Synechocystis*.

## 1.2 The thylakoid membrane

Oxygenic photosynthesis requires a special membrane structure which integrates the major complexes of the photosynthetic electron transport chain: the thylakoid membrane. This unique membrane network only exists in organisms performing oxygenic photosynthesis, such as cyanobacteria and chloroplasts (Rasmussen *et al.* 2008).

### 1.2.1 Structure and lipid composition

The TM is an internal bilayer system which encloses another compartment, the thylakoid lumen. The protein complexes photosystem I (PS I), photosystem II (PS II), the cytochrome *b<sub>6</sub>f* complex and the ATP synthase are embedded in the thylakoids and represent ~60% of the total TM mass in pea chloroplasts, including further pigments and cofactors (Chapman *et al.* 1983). The remaining mass is filled by four main classes of lipids: the two galactolipids monogalactosyldiacylglycerol (MGDG) and digalactosyldiacylglycerol (DGDG), the sulfolipid sulfoquinovosyldiacylglycerol (SQDG) and the phosphoglycerolipid phosphatidylglycerol (PG). The galactolipids MGDG and DGDG are uncharged and represent 54% and 18% of the lipid mass in *Synechocystis* and 53% and 27% in spinach leaf chloroplasts, respectively (Wada & Murata 1989; Dorne *et al.* 1990). SQDG and PG, on the other hand, are anionic and make up 15% and 13% of the thylakoid lipids in *Synechocystis* and 7% each in spinach leaf chloroplasts, respectively (Wada & Murata 1989; Dorne *et al.* 1990). The negative charge of SQDG and PG is crucial for a proper TM structure. In cyanobacteria and chloroplasts, the amount of one anionic lipid increases upon a decreased amount of the other one, leading to the conclusion that the negatively charged lipids can replace each other (Benning *et al.* 1993; Sato *et al.* 1995; Guler *et al.* 1996; Essigmann *et al.* 1998; Yu *et al.* 2002; Aoki *et al.* 2004). DGDG, SQDG and PG are quasi-cylindrical and are thus typical bilayer-forming lipids, which prefer formation of a lamellar phase. Due to its small headgroup relative to the broad fatty acid chain, a peculiarity of MGDG is its tendency to form inverse-hexagonal lipid phases. *In vivo*, MGDG can most probably only be maintained in the lamellar phase when protein complexes are present (Simidjiev *et al.* 2000). Advantageously, the unconventional lipid favors curved thylakoid areas, which contain a higher MGDG amount than smooth areas, as was demonstrated for grana and stroma lamella (Gounaris *et al.* 1983).

An overview of the thylakoid lipids' chemical structures as well as their charge, steric structures, and mass ratios is summarized in *Fig. 1.2*.

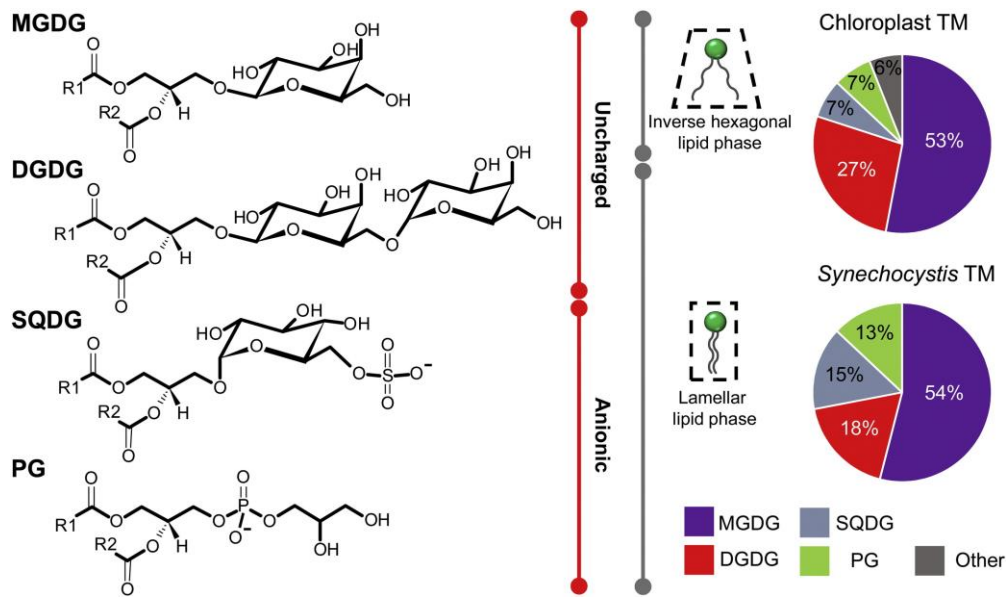


**Fig. 1.2: Thylakoid lipids**

Shown are the chemical structures of the thylakoid lipids MGDG, DGDG, SQDG and PG (left). Furthermore, charge, steric structures, and the thylakoid lipid mass ratios are indicated (right). Taken from (Heidrich *et al.* 2017), used with permission from Elsevier (license number 4190941074655 via RightsLink).

The structure of the TMs in cyanobacteria strongly varies between different organisms. For example, the thylakoids in *Synechocystis* form as parallel sheets, which converge to the PM (*cf.* thylakoid centers in Fig. 1.1) (Kunkel 1982). However, *Synechococcus elongatus* sp. PCC 7942 (*Synechococcus*) has a circular internal TM system but no thylakoid centers (Rexroth *et al.* 2011). The cyanobacterium *Gloeobacter violaceus* (*Gloeobacter*) represents an exception, since it lacks thylakoids and has the electron transfer chain located in the PM (Rippka *et al.* 1974). In chloroplasts, the TMs are built as lamellar stacks, in which there are the commonly-known grana and stroma lamella. However, in both cyanobacteria and chloroplasts, the TM is strongly interconnected (Liberton *et al.* 2006; Nevo *et al.* 2007).

### 1.2.2 Biogenesis

In cyanobacteria, the TMs develop as curved parallel stacks close to the PM in presence of light (Barthel *et al.* 2013), whereas in chloroplasts, the thylakoids begin to form upon light exposure during the maturation of undifferentiated proplastids (Adam *et al.* 2011; Rast *et al.* 2015). However, also in already differentiated plastids, the TM represents a dynamic network, which adjusts to environmental light conditions (Nevo *et al.* 2012). Despite its striking vital importance, the biogenesis and maintenance of the TM in differentiated cyanobacteria and chloroplasts has stayed a secret until today.

TM biogenesis requires a strictly coordinated synthesis and transportation of lipids, proteins, pigments and cofactors, and there has been an ongoing debate on whether the TM is assembled *de novo* or if components as lipids and proteins, which are synthesized at the IE of chloroplasts or the PM of cyanobacteria, respectively, are transported to a constructive TM later. The *de*

*novo* assembly of TMs in cyanobacteria has never been observed, which might be ascribed to the impossibility to remove the TM, as has been shown for dark-grown *Synechocystis* (Barthel *et al.* 2013). A hypothetical transport of lipids/or proteins might be fulfilled by (i) a direct connection of the TM with the PM/IE or (ii) a vesicle transporting system (Nickelsen *et al.* 2011).

The thylakoid centers in *Synechocystis* (*cf. Fig. 1.1*), which are convergency sites of the TM to the PM, were recently assumed to represent a link between the TM and the PM/IE and were thought to be TM biogenesis centers (Nickelsen *et al.* 2011). Noteworthy, the thylakoid centers were also suggested to be an artefact from cell division (Liberton *et al.* 2006). Additionally, contact areas called translation zones (T-zones) were found in green algae (Schottkowski *et al.* 2012; Rast *et al.* 2015) but never in the chloroplasts of plant cells. In addition to thylakoid centers and T-zones, other hypothetical direct connections between the TM and the PM/IE were discussed as exchange bridges (Shimoni *et al.* 2005; van de Meene *et al.* 2006). External fluorescence staining of cyanobacterial cells, on the other hand, implied the absence of any connections, since the dye did not migrate into the TM (Schneider *et al.* 2007). Instead, fluorescent bodies appeared, which might represent vesicles (Schneider *et al.* 2007). Indeed, a vesicle transporting system has been suggested as an alternative to a hypothetical direct connection between the different membranes. Vesicles were detected in chloroplast located at the IE (Lindquist *et al.* 2016) and in the stroma (Hooper *et al.* 1991; Westphal *et al.* 2001b) under certain conditions. Strikingly, some proteins with homologies to components of the secretory pathway were predicted to be present in chloroplasts and cyanobacteria (Andersson & Sandelius 2004; Khan *et al.* 2013). On the other hand, no vesicles have been unambiguously detected in cyanobacteria so far (Rast *et al.* 2015).

The dominating lipid of the TM, the inverse-hexagonal phase forming MGDG, has recently been discussed to play a major role in TM biogenesis due to its ability to break bilayers (Kobayashi *et al.* 2007; Bastien *et al.* 2016). Interestingly, MGDG is one of the major component in prolamellar bodies (PLB), which are semi-crystalline aggregates forming in etioplasts prior to differentiation (Adam *et al.* 2011). Furthermore, several proteins were suggested to play a role in TM biogenesis as, among many others, the inner membrane associated protein of 30 kDa (IM30) (Li *et al.* 1994), the curvature thylakoid 1 protein (CURT1) (Armbruster *et al.* 2013; Heinz *et al.* 2016), the processing associated TPR protein (PratA) (Kunkel 1982; Stengel *et al.* 2012), the DnaK protein (Nimura *et al.* 1996; Rupprecht *et al.* 2010) and the Tlg2-compartment vesicle protein of 38 kDa (Tvp38) (Keller & Schneider 2013).

### 1.3 The availability of Mg<sup>2+</sup> in cyanobacteria and chloroplasts

Mg<sup>2+</sup> ions are the most abundant metal ions in the TM lumen and the cytosol/stroma in cyanobacteria and chloroplasts (Shaul 2002). The concentration of free Mg<sup>2+</sup> ions in cyanobacteria is not known so far, but for chloroplasts it ranges from 0.4 to 120 mM for different plant compartments (reviewed in (Shaul 2002)). Mg<sup>2+</sup> ions seem to have a variety of functions in chloroplasts: They act as cofactors in the oxygenic photosynthetic electron transfer apparatus (*e.g.* as central atom of the chlorophyll molecule) as well as in the Calvin cycle. Furthermore, Mg<sup>2+</sup> ions help in the generation of an electrochemical pH gradient across the TM (Krause 1977).

Most importantly, the availability of Mg<sup>2+</sup> in the chloroplast stroma is strictly regulated in dependence on the outer light conditions. Upon illumination, the ions are released from the thylakoid lumen into the stroma in order to balance the pH gradient across the TM and thereby regulate enzymes as fructose-1,6-bisphosphatase, the ribulose-1,5-bisphosphate carboxylase/oxygenase (RuBisCO) and the RuBisCO activase, which are involved in the CO<sub>2</sub> assimilation in photosynthesis (Lin & Novel 1971; Portis & Heldt 1976; Krause 1977; Portis 1981; Ashton 1998; Ishijima *et al.* 2003; Hazra *et al.* 2015). A light-induced increase of Mg<sup>2+</sup> was found to vary between 1 and 5 mM (Shaul 2002). Since thylakoids develop upon light exposure (Adam *et al.* 2011; Barthel *et al.* 2013; Rast *et al.* 2015; Frain *et al.* 2016), it seems convenient to speculate about an involvement of the ion in TM biogenesis.

### 1.4 The inner membrane associated protein of 30 kDa (IM30)

The IM30 protein was discovered in 1994 in *Pisum sativum*, located at the TMs and the IE, and named after its mass and localization (Li *et al.* 1994). Based on its membrane association, IM30 was early assumed to play an important part in TM biogenesis (Li *et al.* 1994). Noteworthy, due to the observation that vesicular structures which were visible at cold stress in *Arabidopsis thaliana* (*Arabidopsis*) disappeared in a mutant strain lacking IM30, the protein is also known as vesicle-inducing protein in plastids 1 (Vipp1) (Kroll *et al.* 2001).

#### 1.4.1 Origin and occurrence

Phylogenetic studies indicated that the *im30* gene is exclusively found in cyanobacteria and chloroplasts (Li *et al.* 1994; Kroll *et al.* 2001; Westphal *et al.* 2001a; Fuhrmann *et al.* 2009b) and therefore evolved at the same time as TMs and oxygenic photosynthesis in general. It was first studied in detail in *Arabidopsis* and *Synechocystis* (Kroll *et al.* 2001; Westphal *et al.* 2001a).

Most probably, IM30 has evolved from the prokaryotic phage shock protein A (PspA) via gene duplication in an early cyanobacterial ancestor (Westphal *et al.* 2001a; Vothknecht *et al.* 2012).

PspA was first discovered in *Escherichia coli* (*E. coli*) in 1990 as a member of the phage shock proteins system (Psp system), which is involved in bacterial stress response (Darwin 2005) at different membrane stress situations (Brissette *et al.* 1990; Brissette *et al.* 1991; Kobayashi *et al.* 2007). Unlike the *im30* gene, the *pspA* gene was not passed to plant cells during the endosymbiotic event and, thus, cannot be found in plants (Kroll *et al.* 2001). Despite that, the two proteins share several similarities concerning their structure and function. Significantly, IM30 was reported to be able to take over the function of PspA in an *E. coli pspA* deletion strain (DeLisa *et al.* 2004).

#### 1.4.2 Structure

IM30 and PspA share ~30% identity and 50% similarity of the amino acid sequence in *Synechocystis* (Bultema *et al.* 2010). Each member of the IM30/PspA family has a similar N-terminal structure, the so-called PspA domain, which has a size of ~220 amino acids (Westphal *et al.* 2001a). For this domain, computational predictions suggested an almost exclusively  $\alpha$ -helical structure with some amino acids interrupting four or six helices in PspA and IM30, respectively (Hankamer *et al.* 2004; Fuhrmann *et al.* 2009a; Bultema *et al.* 2010; Otters *et al.* 2013; Saur *et al.* 2017). Importantly, in some publications, the IM30 helix 5 and 6 are also assumed as one helix (Saur *et al.* 2017). A recently published crystal structure of an N-terminal PspA fragment (amino acids 1-144) confirmed the predicted structures (Osadnik *et al.* 2015). However, the main difference between IM30 and PspA is the C-terminal extension of IM30: an additional ~16-20 amino acid long  $\alpha$ -helix connected via a short linker region of variable length in different organisms (Westphal *et al.* 2001a; Vothknecht *et al.* 2012; Otters *et al.* 2013), which was often assumed to be responsible for an additional function of IM30 compared to PspA. Despite the fact that most amino acids in the C-terminus are not conserved, it seems to exhibit a pronounced hydrophobicity, which is conserved in cyanobacteria, algae and plants (Vothknecht *et al.* 2012). Secondary structure predictions of IM30 and PspA (Otters *et al.* 2013) and the hypothetical functions of the single  $\alpha$ -helices are illustrated in *Fig. 1.3*.

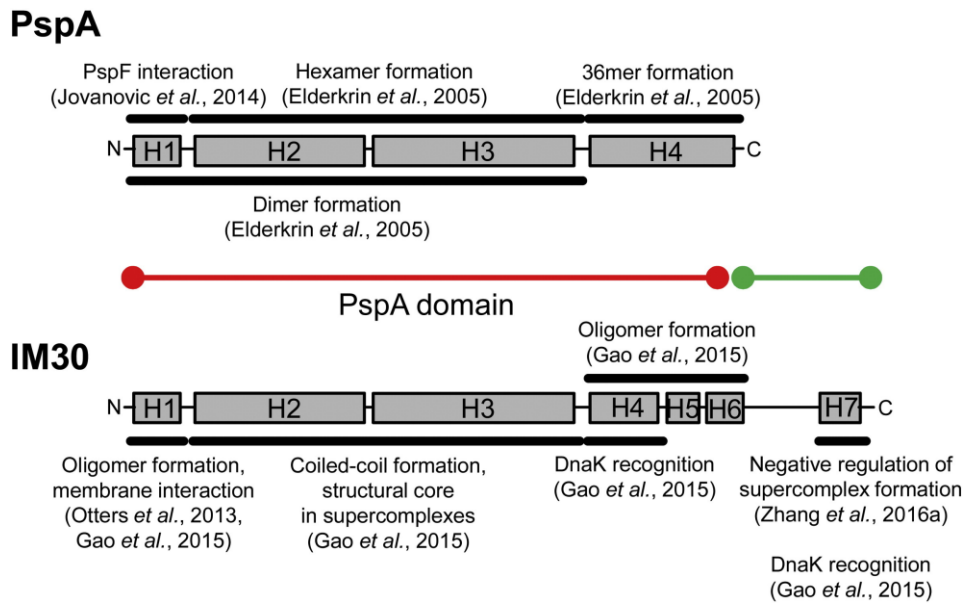


**Fig. 1.3: IM30/PspA secondary structure and hypothetical functions of predicted  $\alpha$ -helices**

Shown are the predicted IM30 and PspA secondary structures from (Otters *et al.* 2013), in which  $\alpha$ -helices (boxes) and random coil domains (lines) are emphasized. Furthermore, the N-terminal PspA domain (red line) and the C-terminus, which is connected to the PspA domain via a linker region (green line), are indicated. The hypothetical functions of the predicted  $\alpha$ -helices are added. Taken from (Heidrich *et al.* 2017), used with permission from Elsevier (license number 4190941074655 via RightsLink).

The  $\alpha$ -helical regions of the PspA domain in both IM30 and PspA are predicted to form coiled-coil structures (Fuhrmann *et al.* 2009a; Bultema *et al.* 2010; Saur *et al.* 2017), which has been partly confirmed by the crystal structure of an N-terminal PspA fragment (Osadnik *et al.* 2015). These coiled-coil domains of IM30 were suggested to play a role in membrane interaction (Otters *et al.* 2013) and quaternary structure formation (Aseeva *et al.* 2004; Elderkin *et al.* 2005; Bultema *et al.* 2010; Otters *et al.* 2013; Gao *et al.* 2015). However, no crystal structure of the full-length protein exists so far. Despite that, a predicted tertiary structure based on the PspA fragment crystal structure (Osadnik *et al.* 2015) has recently been published (Saur *et al.* 2017) and is shown in Fig. 1.4.

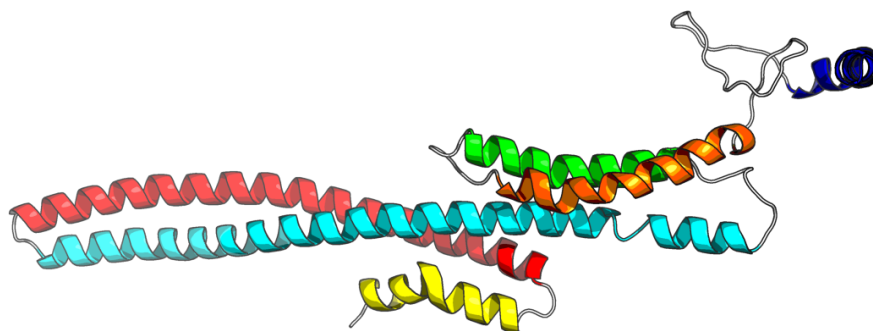


**Fig. 1.4: Predicted tertiary structure of IM30**

The predicted tertiary IM30 structure based on the PspA fragment crystal structure from (Osadnik *et al.* 2015) (PDB: 4WHE) has been introduced in (Saur *et al.* 2017). For this thesis, the figure was generated with PyMOL. Indicated are individual  $\alpha$ -helices: H1 (yellow), H2 (red), H3 (light blue), H4 (green), H5/6 (orange) and H7 (dark blue). The helices are interrupted by loop regions, which consist of random coil areas.

On the quaternary structure level, IM30 forms pronounced homo-oligomeric rings with a mass  $>2$  MDa (Aseeva *et al.* 2004; Hankamer *et al.* 2004; Fuhrmann *et al.* 2009a). Noteworthy, the C-terminal tail is most probably located outside the oligomeric ring structures (Aseeva *et al.* 2004; Zhang *et al.* 2016a; Saur *et al.* 2017). The IM30 rings vary in their rotational symmetries from at least 10-18 (Saur *et al.* 2017) and the smallest building blocks were assumed to be dimers (Hankamer *et al.* 2004) (based on PspA studies) or tetramers (Fuhrmann *et al.* 2009a), but further proof was lacking. Regarding the size, *Synechocystis* IM30 rings possess a diameter of 24-33 nm (Fuhrmann *et al.* 2009a; Saur *et al.* 2017) and a standard height of  $\sim 15$  nm (Saur *et al.* 2017). Importantly, the IM30 oligomers are Janus-faced, which most probably affects membrane binding (Saur *et al.* 2017). Modeling the tertiary structure prediction of IM30 into 3D ring reconstructions recently suggested that the N-terminal PspA domains are located at one site (ring bottom) and the C-termini at the other (ring top) (Saur *et al.* 2017), which is illustrated in Fig. 1.5.

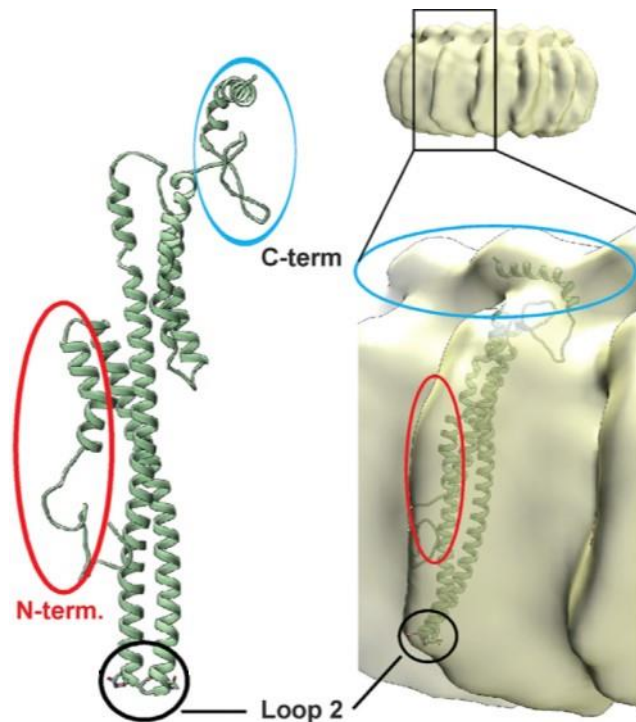


**Fig. 1.5: Predicted IM30 monomer structure inside the ring**

Modeling the tertiary structure prediction of IM30 into 3D ring reconstructions suggested the N-terminal PspA domain located at one site (ring bottom) and the C-terminus at the other (ring top). Indicated are the N-terminus (red circle), the loop 2 region (black circle) and the C-terminus (blue circle). Modified from (Saur *et al.* 2017), used with permission from Elsevier (license number 4204211443929 via RightsLink).

On an even higher oligomerization level, IM30 rings can further assemble into double-rings, as shown for *Arabidopsis* and *Synechocystis* IM30 (Aseeva *et al.* 2004; Fuhrmann *et al.* 2009a). The double-rings are able to stack, forming so-called rods, whereas it is unknown in which way the top- and bottom ring sites are stacked in this higher-ordered structures. It must be added that it is still not clear whether the rod structures are just inactive storage forms for the protein and,

thus, *in vitro* artefacts or if they play an important role in the physiological function of IM30. In fact, they were not observed *in vivo* until now. However, the rods were assumed to be part of a microtubule-like system (Liu *et al.* 2007).

The subsequent *in vitro* assembly of IM30 is schematically illustrated in Fig. 1.6 and electron micrographs of the protein can be found in the results section (*cf.* 3.1).

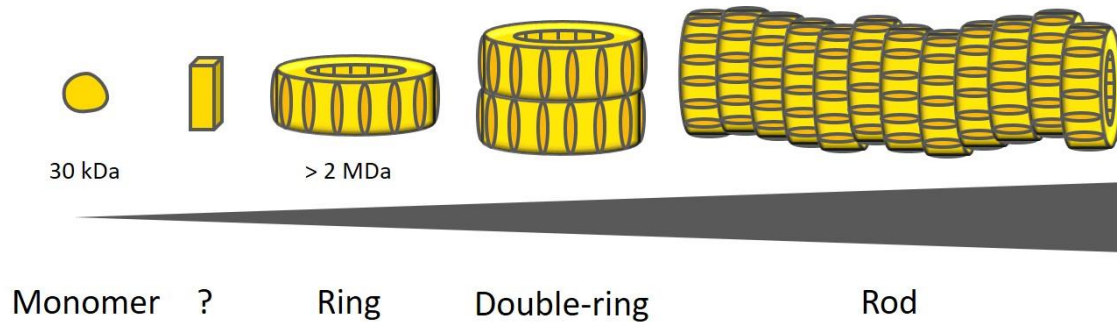


**Fig. 1.6: *In vitro* oligomerization of IM30**

IM30 monomers were suggested to form at least tetramers as basic building blocks of higher-ordered oligomerization forms. IM30 Janus-faced rings consist of 10-18 subunits and can further assemble into double-rings and rod-like structures. The grey triangle indicates the increasing number of oligomerized IM30 molecules.

### 1.4.3 Lipid interaction

IM30 was connected to membranes early, since it was discovered in association with the IE as well as the TM in *Pisum sativum* chloroplasts (Li *et al.* 1994). Due to the fact that the protein does not contain transmembrane domains, it was predicted and later experimentally verified via electron microscopy, to be a peripherally membrane-associated protein (Li *et al.* 1994; Kroll *et al.* 2001; Hennig *et al.* 2015).

Recently, it could be demonstrated that IM30 interacts with the negatively charged thylakoid lipids SQDG (Suppes 2013; Hennig *et al.* 2015) and PG (Suppes 2013; Hennig *et al.* 2015; McDonald *et al.* 2015), but not with the neutral lipids MGDG and DGDG (Suppes 2013; Hennig *et al.* 2015). Whether the IM30-membrane interaction is driven by electrostatic forces has not been investigated so far. However, due to the observation that IM30 interacts with both dioleoylphosphatidylglycerol (DOPG) and dimyristoylphosphatidylglycerol (DMPG) (Suppes 2013; Hennig *et al.* 2015; Heidrich *et al.* 2016), it can be concluded that the lipid acyl length is not important for membrane interaction.

Recent *in vitro* studies demonstrated an effect of IM30 on the membrane polarity. The protein seemed to increase the membrane rigidity of PG liposomes in the bilayer head group as well as the core region (Suppes 2013; Heidrich *et al.* 2016). A subsequent effect is a shift of the liposome phase transition temperature to higher values in presence of IM30 (Suppes 2013; Heidrich *et al.* 2016). The capability of increasing lipid packing seems to be a conserved feature for IM30

and PspA, since the latter was reported to reduce membrane proton leakage in *E. coli* (Kleerebezem *et al.* 1996; Kobayashi *et al.* 2007).

#### 1.4.4 Mg<sup>2+</sup> interaction

Several *in vitro* experiments indicated an interaction of IM30 with Mg<sup>2+</sup> (Suppes 2013; Hennig *et al.* 2015). In a liposome aggregation assay, the lipid vesicles aggregated at a lower cation concentration in presence of IM30 (Hennig *et al.* 2015). Furthermore, a membrane fusion assay revealed the ability of IM30 to mediate liposome fusion (Suppes 2013; Hennig *et al.* 2015), which is described further in 1.4.5. Interestingly, fusion was only possible in presence of Mg<sup>2+</sup> (Suppes 2013; Hennig *et al.* 2015). Since fusion did not take place in absence of IM30, an activating effect of the ion on IM30 was strongly suggested (Suppes 2013; Hennig *et al.* 2015). Until this point, it remained elusive whether the interaction between IM30 and Mg<sup>2+</sup> is based on a direct binding of the ion to the protein or if a structural alteration of IM30 is indirectly induced by Mg<sup>2+</sup>. In fact, it was suggested that the ion might act as a glue between negatively charged membranes and anionic areas on the IM30 surface (Heidrich *et al.* 2017). Furthermore, sum frequency generation (SFG) experiments indicated an increased membrane binding affinity of IM30 in presence of Mg<sup>2+</sup> (Hennig *et al.* 2015).

As already described in 1.2.2 and 1.3, TM biogenesis in cyanobacteria and chloroplasts as well as Mg<sup>2+</sup> release from the thylakoid lumen into the stroma is activated upon light exposure (Lin & Novel 1971; Portis & Heldt 1976; Krause 1977; Portis 1981; Ashton 1998; Ishijima *et al.* 2003; Adam *et al.* 2011; Barthel *et al.* 2013; Hazra *et al.* 2015; Rast *et al.* 2015; Frain *et al.* 2016). IM30 might connect these two phenomena by interacting with Mg<sup>2+</sup> and subsequently mediating processes involved in TM biogenesis. Thus, a threshold Mg<sup>2+</sup> concentration *in vivo* was discussed for IM30 activation (Heidrich *et al.* 2017).

#### 1.4.5 Postulated Functions

As already mentioned above, IM30 was early thought to play a key role in TM biogenesis. This theory was mainly based on an observation made in the *Arabidopsis* mutant line *hcf155*, in which the IM30 expression was decreased (Kroll *et al.* 2001). The mutant chloroplasts had a completely disturbed TM structure, a strongly reduced number of thylakoids, and subsequently a reduced photosynthesis output (Kroll *et al.* 2001). Similar observations were made in IM30 depleted mutants of *Synechocystis* (Westphal *et al.* 2001a). Interestingly, the expression of IM30 in different *Zea mays* leaves varied in dependence of the TM amount (Majeran *et al.* 2005). Bundle sheath types, which contained a very pronounced number of thylakoids, express ten times more IM30 compared to mesophyll types (Majeran *et al.* 2005). Furthermore, the cyanobacterium *Gloeobacter*, which does not contain typical TMs and performs parts of the photosynthesis in the PM (Rippka *et al.* 1974), does not express IM30 (Nakamura *et al.* 2003). All these observations indicate a conserved function of IM30 in relation to TM formation.

For the last two decades, the precise role of IM30 in TM biogenesis has been part of a highly controversial discussion. Several functions were suggested and are summarized in *Fig. 1.7*.

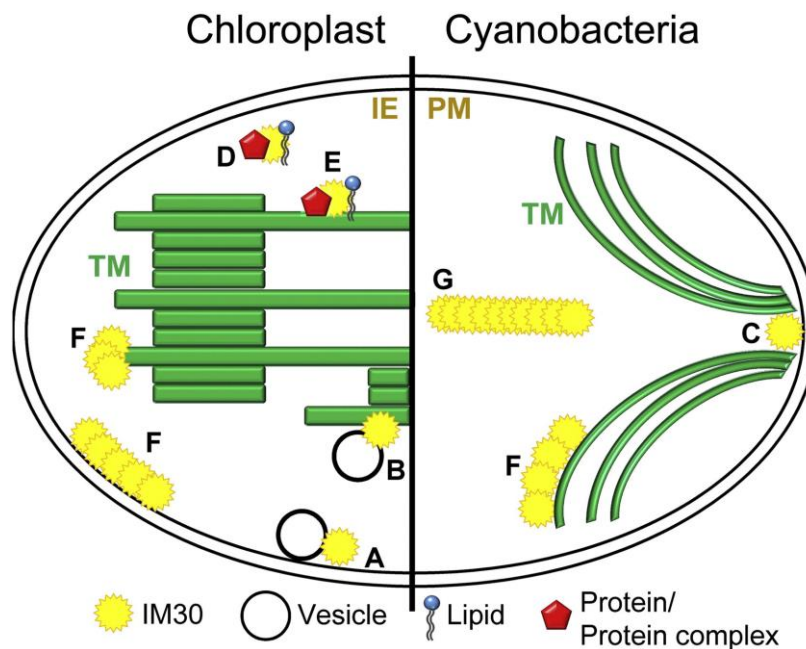


**Fig. 1.7: Postulated IM30 functions in chloroplasts and cyanobacteria**

Postulated IM30 functions in chloroplasts and cyanobacteria are illustrated: Vesicle formation (A), vesicle fusion (B), thylakoid center organization (C), protein/lipid transport (D), protein/lipid insertion (E), membrane stress protection (F) and formation of cyto-skeleton-like elements (G). Taken from (Heidrich *et al.* 2017), used with permission from Elsevier (license number 4190941074655 via RightsLink).

Several components of the TM as proteins, the thylakoid lipid MGDG and other lipids are synthesized within the IE or PM, respectively (Douce 1974; Joyard & Stumpf 1981; Zak *et al.* 2001; Keren *et al.* 2005; Kobayashi *et al.* 2007). Thus, there is an urgent need for a transportation mechanism of those molecules to the constructive TM. In the past, the IM30 function was often discussed in this context.

A lipid transport function of IM30 would be one possibility, as it has been suggested early (Li *et al.* 1994; Benning *et al.* 2006). Indeed, infrared spectroscopy has demonstrated that a recombinant IM30 expressed in *E. coli* has different structures before and after lipase treatment and a significant reduction of lipid group absorption bands (Otters *et al.* 2013). Analogously to lipid transport, IM30 was discussed to be involved in protein transport and subsequent insertion in the TM. For example, the interaction of IM30 with Albino3.2 was observed, a protein involved in the insertion of integral TM membrane proteins (Gohre *et al.* 2006; Walter *et al.* 2015). IM30 and PspA were also linked to the twin arginine transport (Tat)-mediated protein translocation in chloroplasts and cyanobacteria (DeLisa *et al.* 2004; Lo & Theg 2012). Furthermore, binding of IM30 to lots of other proteins involved in photosynthesis and stress response has been suggested (Liu *et al.* 2005; Heide *et al.* 2009; Bryan *et al.* 2014; Feng *et al.* 2014).

Since IM30 can form rod-like structures *in vitro* at higher concentrations and unknown microtubule-like structures have been discovered in chloroplasts and cyanobacteria (Anderson *et al.* 1973; van de Meene *et al.* 2006), it has been debated whether IM30 might form cytoskeleton-like structures, which could be used as rails for proteins and lipids from the IE or PM to the TM (Vothknecht *et al.* 2012). However, experimental proof of the involvement of IM30 in such structures is missing.

Another suggested function of IM30 was the organization of cyanobacterial thylakoid centers, which are under suspicion for being TM biogenesis centers since they represent areas where the TM converges to the PM in *Synechocystis* (Nickelsen *et al.* 2011). IM30 was recently assumed to form a structural component within the thylakoid centers (Rutgers & Schroda 2013), and GFP-labeled IM30 was localized accumulated at the cell periphery (Bryan *et al.* 2014). On the other hand, thylakoid convergence sites are not conserved in all cyanobacteria (*cf.* 1.2.1), indicating that they cannot be responsible for the TM biogenesis in every cyanobacterium. As already mentioned in 1.2.2, T-zones and other hypothetical direct connections between the TM and the PM/IE were found in cyanobacteria, green algae and chloroplasts and discussed as exchange bridges instead (Shimoni *et al.* 2005; van de Meene *et al.* 2006; Charuvi *et al.* 2012; Engel *et al.* 2015).

A vesicle transporting system for those eukaryotic plastids was suggested when vesicle-like objects in *Arabidopsis* and *Pisum sativum* chloroplasts were observed via electron microscopy under special experimental conditions, which prevented membrane fusion of those vesicles (Morre *et al.* 1991; Kroll *et al.* 2001; Westphal *et al.* 2001b). Strikingly, the vesicles were not visible anymore in an *Arabidopsis im30* depletion strain (Kroll *et al.* 2001). Consequently, IM30 was suggested to be involved in the formation of the vesicles, which would provide a possibility for exchange of proteins and/or lipids between IE and TM via a vesicle traffic system. It must be mentioned that further evidence for this hypothetical IM30 function is missing (Vothknecht *et al.* 2012).

All previously observed effects upon IM30 deletion in cyanobacteria and chloroplasts were recently explained by a new hypothetical function of the protein. A membrane fusion assay as well as electron microscopy demonstrated the *in vitro* ability of IM30 to mediate membrane fusion in presence of  $Mg^{2+}$  (Suppes 2013; Hennig *et al.* 2015). Furthermore, for TM biogenesis in chloroplasts, the formation of an MGDG inverse-hexagonal platform was suggested as an exchange point for material between the IE and a constructive TM (Bastien *et al.* 2016). In this model, IM30 was thought to act as a bridge in order to transfer proteins and/or lipids (Bastien *et al.* 2016; Selao *et al.* 2016). Since TM biogenesis probably includes a direct membrane connection between TM and PM/IE or a vesicle traffic system, a fusion-mediating protein seems advantageous. In both cases, IM30 could connect two membranes with each other to enable a ma-

terial exchange. Importantly, a fusion function of IM30 would not contradict the idea of IM30 being a vesicle inducing protein *per se*, but rather suggest the mediation of the opposing event depending on the regulation, *e.g.* the cytosolic  $Mg^{2+}$  content.

Aside from a lipid/protein transportation via membrane fusion, IM30 was also discussed in the context of membrane protection independent from  $Mg^{2+}$ . The membrane integrity as well as the upkeep of electric potential and the proton motive force of thylakoids are crucial for cell viability. PspA has been reported to be involved in membrane stress protection, as in the situation of proton leakage by forming large complexes at the PM (Kleerebezem *et al.* 1996; Kobayashi *et al.* 2007; Standar *et al.* 2008; Yamaguchi *et al.* 2013). Due to its connection to PspA, IM30 was also assumed to play a role in membrane stress protection, *e.g.* during a hypothetical vesicle budding or fission. Indeed, *Arabidopsis* chloroplasts lacking IM30 were found sensitive to hypotonic membrane stress (Zhang *et al.* 2012) and in *Synechocystis*, IM30 was upregulated in presence of the membrane stressor hexane (Liu *et al.* 2012). Furthermore, IM30 could fulfill the PspA protection function in *E. coli* (DeLisa *et al.* 2004; Zhang *et al.* 2012). When IM30 was ectopically expressed in *Arabidopsis*, the tolerance to heat and oxidative stress was increased (Zhang *et al.* 2016a; Zhang *et al.* 2016b), which was ascribed to the C-terminal  $\alpha$ -helix of IM30 (Zhang *et al.* 2016a). Additionally, GFP-labeled IM30 rings in *Arabidopsis* were found to dynamically react in form of dissociation on membranes upon hypotonic treatment via fluorescence live-imaging (Bryan *et al.* 2014; Zhang *et al.* 2016a). As mentioned above (*cf.* 1.4.3), the ability of IM30 to increase the membrane polarity has been shown, and this effect was suggested to play a role in membrane protection (Suppes 2013).

## 1.5 Objectives of this thesis

TM biogenesis is a vital process for all life on earth. Despite its outstanding importance, it is not fully understood yet. Only recently, a huge step was taken into the direction of determining the role of IM30 in this process. Thus, the starting point of this thesis were discoveries made in (Suppes 2013) and (Hennig *et al.* 2015). Here, IM30 was shown to have a dual function in presence and absence of  $Mg^{2+}$ : membrane fusion and protection, the latter seeming to be a heritage from the proteins' bacterial ancestor PspA. Due to the presence of a certain  $Mg^{2+}$  threshold concentration, the ability to connect membranes with each other, on the other hand, seems to be directly related to TM biogenesis. Hence, the main goal of this thesis was to further identify and to illuminate upstream interactions, steps and conditions for the IM30-mediated membrane fusion and to develop a model which describes the IM30 interactions and the fusion process on the macromolecular level. This includes the interaction of IM30 with  $Mg^{2+}$ , with membranes, with other IM30 molecules during oligomerization and deoligomerization, and the interdependency of all components in different equilibria.

A schematic overview of equilibria and events of interest is illustrated in *Fig. 1.8*.

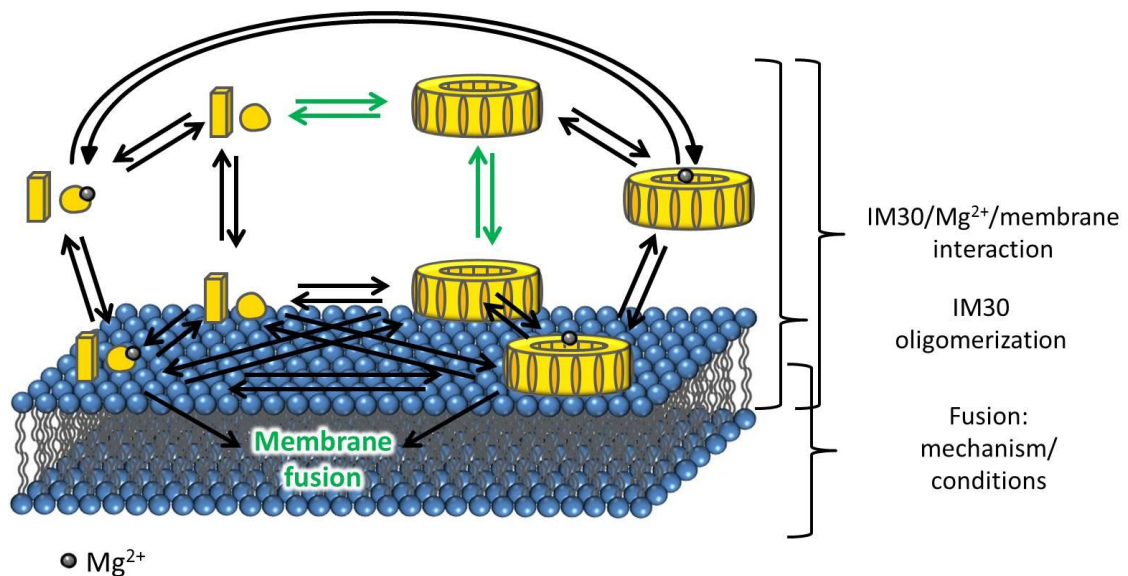


**Fig. 1.8: IM30 interactions of interest**

Interactions of IM30 involve oligomerization and deoligomerization, Mg<sup>2+</sup> and membrane binding at different structural levels. The interactions of the protein eventually end up in membrane fusion. Indicated are formerly confirmed equilibria (green arrows) and equilibria which are supposed to be confirmed or excluded and are investigated further in this thesis (black arrows).

As indicated in *Fig. 1.8*, a main issue of this thesis was to confirm or exclude a direct binding of Mg<sup>2+</sup> to IM30, which has not been unambiguously proven so far and was only indicated in former experiments (Suppes 2013; Hennig *et al.* 2015). In this context, it was also interesting to see which requirements need to be fulfilled for a hypothetical interaction, especially the oligomerization state as well as the structural flexibility of IM30.

Another issue investigated in this thesis was the IM30-membrane interaction. In the past, IM30 has been demonstrated to interact with membranes containing negatively charged lipids (Suppes 2013; Hennig *et al.* 2015). However, the nature of these interactions, which was suggested to base on electrostatic forces, remained elusive and was investigated further. Additionally, binding conditions as the IM30 oligomerization state and the effects of the presence/absence of Mg<sup>2+</sup> were important for an improved understanding of the IM30-membrane interaction.

Furthermore, the oligomerization behavior of IM30 on membranes was not investigated at this point. It has been shown that IM30 mainly exists in higher-ordered oligomerization states in solution (Heidrich *et al.* 2016). The oligomerization state on membranes, on the other hand, was not further described. In the framework of this thesis, a hypothetical IM30 ring dissociation into smaller subunits in presence and absence of Mg<sup>2+</sup> and in dependence of different membrane compositions was examined. To do so, a pair of labeled IM30 mutants, containing the FRET pair forming dyes CFP and Venus was generated for this thesis.

Not only the interactions leading to the final fusion mediation, but also the membrane fusion itself was a main objective in this thesis. Whether IM30 acts as an active fusion protein or an indirect fusion mediator has not been investigated so far. Additionally, fusion conditions, such as the IM30 structural flexibility and the membrane composition, were analyzed.

Importantly, all experiments in this thesis were performed *in vitro* using liposomes as thylakoid model membranes. This approach has already been shown as advantageous in former work (Fuhrmann 2010; Suppes 2013; Hennig 2014; Hennig *et al.* 2015). Since *in vivo*, all interactions and events are directly connected to each other, they are impossible to separate, and secondary effects might be misinterpreted. Thus, the *in vitro* approach has an advantage concerning the isolation of a specific feature in the IM30 interaction cascade by minimizing the components in the samples. By combining the results from individual *in vitro* studies, a putative sequence of events in the IM30 fusion performance can be proposed. Subsequently, a further confirmation of the suggested IM30 membrane fusion *in vivo* can be more target-oriented.

## 2 Materials and methods

### 2.1 Chemicals

Table 2.1: Chemicals

Chemical	Origin
Acetic acid	VWR (Darmstadt, GER)
Acrylamide/bis-acrylamide, 40% solution	AppliChem (Darmstadt, GER)
8-Anilino-1-naphthalenesulfonic acid (ammonium salt) (ANS)	Sigma-Aldrich (München, GER)
Agar-agar	Roth (Karlsruhe, GER)
Agarose GTQ	Roth (Karlsruhe, GER)
Ammonium persulfate (APS)	Merck (Darmstadt, GER)
Ampicillin sodium salt	Roth (Karlsruhe, GER)
<i>N</i> <sub>α</sub> -Benzoyl- <i>L</i> -arginine ethylester (BAEE)	Thermo Scientific (Darmstadt, GER)
Bovine serum albumin (BSA)	Thermo Scientific (Darmstadt, GER)
Bromphenol blue sodium salt	Sigma-Aldrich (München, GER)
Chloroform	VWR (Darmstadt, GER)
Chromium (Cr)	Umicore (Hanau, GER)
Coomassie Brilliant Blue G-250	AppliChem (Darmstadt, GER)
Deoxynucleotidetriphosphate solution set (dNTPs)	BioLabs (Ipswich, MA, US)
Digalactosyldiacylglycerol (DGDG)	Avanti Polar Lipids (Alabaster, AL, US)
Dimethyl sulfoxide (DMSO)	BioLabs (Ipswich, MA, US)
1,2-Dioleoyl- <i>sn</i> -glycero-3-phosphocholine (sodium salt) (DOPC)	Avanti Polar Lipids (Alabaster, AL, US)
1,2-Dioleoyl- <i>sn</i> -glycero-3-phosphoethanolamine labeled with Atto633 (Atto633-PE)	Sigma-Aldrich (München, GER)
1,2-Dioleoyl- <i>sn</i> -glycero-3-phosphoethanolamine- <i>N</i> -(lissaminerhodamine B sulfonyl) (ammonium salt) (LissRhod-PE)	Avanti Polar Lipids (Alabaster, AL, US)
1,2-Dioleoyl- <i>sn</i> -glycero-3-phosphoethanolamine- <i>N</i> -(7-nitro-2-1,3-benzoxadiazol-4-yl) (ammonium salt) (NBD-PE)	Avanti Polar Lipids (Alabaster, AL, US)
1,2-Dioleoyl- <i>sn</i> -glycero-3-phosphoglycerol (sodium salt) (DOPG)	Avanti Polar Lipids (Alabaster, AL, US)
1,2-Dioleoyl- <i>sn</i> -glycero-3-phospho- <i>L</i> -serine (sodium salt) (DOPS)	Avanti Polar Lipids (Alabaster, AL, US)
Disodium phosphate dihydrate (Na <sub>2</sub> HPO <sub>4</sub> *2H <sub>2</sub> O)	Roth (Karlsruhe, GER)
Ethanol (abs.)	Sigma-Aldrich (München, GER)
Ethidium bromide	AppliChem (Darmstadt, GER)
Formic acid	Roth (Karlsruhe, GER)
Glutaraldehyde	Sigma-Aldrich (München, GER)
Glycerol	Sigma-Aldrich (München, GER)
Glycine	AppliChem (Darmstadt, GER)
Gold (Au)	ESG (Rheinstetten, GER)
Hellmanex II solution	Hellma (Jena, GER)
Hydrochloric acid (HCl)	Roth (Karlsruhe, GER)
4-(2-Hydroxyethyl)-1-piperazineethanesulfonic acid (HEPES)	Thermo Scientific (Darmstadt, GER)
Imidazole	AppliChem (Darmstadt, GER)

<b>Chemical</b>	<b>Origin</b>
Isopropyl alcohol	VWR (Darmstadt, GER)
Isopropyl- $\beta$ -D-thiogalactopyranoside (IPTG)	Thermo Scientific (Darmstadt, GER)
Laurdan	Fluka (Taufkirchen, GER)
Magnesium chloride hexahydrate (MgCl <sub>2</sub> *6H <sub>2</sub> O)	AppliChem (Darmstadt, GER)
16-Mercaptohexadecanoic acid (16-MHDA)	ProChimia (Sopot, PL)
Methanol	Sigma-Aldrich (München, GER)
Monogalactosyldiacylglycerol (MGDG)	Avanti Polar Lipids (Alabaster, AL, US)
Monosodium phosphate monohydrate (NaH <sub>2</sub> PO <sub>4</sub> *H <sub>2</sub> O)	Roth (Karlsruhe, GER)
Nickel nitrilotriacetic acid agarose (Ni-NTA-agarose)	Marcherey-Nagel (Düren, GER)
Protease Inhibitor Cocktail P8849	Sigma-Aldrich (München, GER)
Roti-Quant 5x	Roth (Karlsruhe, GER)
Sodium dithionite (Na <sub>2</sub> S <sub>2</sub> O <sub>4</sub> )	Sigma-Aldrich (München, GER)
Sodium chloride (NaCl)	Roth (Karlsruhe, GER)
Sodium dodecyl sulfate (SDS)	Roth (Karlsruhe, GER)
Spectra/Gel Absorbent	Spectrum Labs (Los Angeles, CA, US)
Sulfoquinovosyldiacylglycerol (sodium salt) (SQDG)	Larodan Fine Chemicals (Solna, SWE)
N,N,N',N'-Tetramethylethylenediamine (TEMED)	AppliChem (Darmstadt, GER)
Tris(hydroxymethyl)aminomethane (Tris)	Roth (Karlsruhe, GER)
Triton X-100	Sigma-Aldrich (München, GER)
Tryptone	Roth (Karlsruhe, GER)
Tween20	Sigma-Aldrich (München, GER)
Uranyl acetate	Fluka (Taufkirchen, GER)
Urea	Thermo Scientific (Darmstadt, GER)
Yeast extract	Roth (Karlsruhe, GER)

## 2.2 Buffers and solutions

Table 2.2: Buffers and solutions

<b>Notation</b>	<b>Composition</b>
<u>For agarose gel electrophoresis:</u>	
50x TAE buffer	242 g Tris 57.1 ml Acetic acid 100 ml 0.5 M EDTA, pH 8.0 Add. 1 l ddH <sub>2</sub> O
6x DNA sample buffer	10 mM Tris, pH 7.6 0.03% Bromphenol blue (w/v) 60% Glycerol (v/v) 60 mM EDTA
<u>For SDS-PAGE:</u>	
Loading gel buffer	1.5 M Tris, pH 6.8 0.4% SDS (w/v)
Resolving gel buffer	0.5 M Tris, pH 8.8 0.4% SDS (w/v)

<b>Notation</b>	<b>Composition</b>
10x SDS running buffer	0.25 M Tris 2 M Glycine 1% SDS (w/v)
5x SDS sample buffer	250 mM Tris, pH 6.8 10% SDS (w/v) 0.2% Bromphenol blue (w/v) 50% Glycerol (v/v) 500 mM DTT
Coomassie staining solution	0.125% Coomassie Brilliant Blue G-250 (w/v) 40% Ethanol (v/v) 5% Acetic acid (v/v)
Coomassie destaining solution	10% Acetic acid (v/v) 30% Ethanol (v/v)
<u>For immunoblot detection</u>	
TBS buffer	25 mM Tris 1.25 M Glycine 20% Ethanol (v/v)
TBS-T buffer	TBS buffer 0.05% Tween20 (v/v)
<u>For protein purification:</u>	
NaPh buffer	50 mM NaPh, pH 7.6 300 mM NaCl
<i>Washing buffers</i>	
W20	NaPh buffer 20 mM Imidazole
W50	NaPh buffer 50 mM Imidazole
W100	NaPh buffer 100 mM Imidazole
Elution buffer	NaPh buffer 500 mM Imidazole
<u>For protein storage:</u>	
HEPES buffer	20 mM HEPES, pH 7.6
NaPh buffer	10 mM NaPh, pH 7.6

All buffers used for protein purification and protein storage were filtered and stored at 4 °C.

## 2.3 Oligonucleotides

Table 2.3: Oligonucleotides

Notation	Sequence (5' → 3')	Target Plasmid	Mutation
A227C fw	CCG GGA ACC TCT TGC GCT ACG CCC CAA C	pRSET IM30	A227C
A227C rev	GTT GGG GCG TAG CGC AAG AGG TTC CCG G	pRSET IM30	A227C
IM30 -stop fw	CGG TTA AAT AAT CTG GGA TCC GTG AGC AA	pRSET IM30-CFP	-Stop
IM30 -stop rev	TTG CTC ACG GAT CCC AGA TTA TTT AAC CG	pRSET IM30-CFP	-Stop
Venus fw	TAA GCA GGA TCC GTG AGC AAG GGC GAG GAC	pVenus-GlpF	+ <i>Bam</i> HI at 5' + <i>Eco</i> RI at 3'
Venus rev	TGC TTA GAA TTC TTA CTT GTA CAG CTC GTC CAT GCC	pVenus-GlpF	+ <i>Bam</i> HI at 5' + <i>Eco</i> RI at 3'

All oligonucleotides were obtained from Eurofins MWG Genomic (Martinsried, GER).

## 2.4 Plasmids

Table 2.4: Plasmids

Notation	Mutation	Resistance	Origin
pRSET GpA-CFP	+CFP with the modifications R27K and H232L	Ampicillin	Schneider group
pRSET IM30	-	Ampicillin	Schneider group
pRSET IM30 ΔCT	Δ223-267	Ampicillin	Schneider group
pRSET IM30 A227C	A227C	Ampicillin	This work
pRSET IM30 C4	A75S, A78S, L79A	Ampicillin	Schneider group
pRSET IM30 C7	F168A, E169A, R170A, M171A	Ampicillin	Schneider group
pRSET IM30-CFP	+CFP with the modifications R27K and H232L	Ampicillin	This work
pRSET IM30-Venus	+Venus	Ampicillin	This work
PVenus-GlpF	+Venus	Ampicillin	Schneider group

## 2.5 Enzymes and enzyme buffers

Table 2.5: Enzymes and buffers

Notation	Origin
<i>Bam</i> HI	BioLabs (Ipswich, MA, US)
CIP	BioLabs (Ipswich, MA, US)
CutSmart buffer 10x	BioLabs (Ipswich, MA, US)
<i>Dpn</i> I	BioLabs (Ipswich, MA, US)
<i>Eco</i> RI	BioLabs (Ipswich, MA, US)
NEB 10x buffer 2.1	BioLabs (Ipswich, MA, US)
NEB 10x buffer 3.1	BioLabs (Ipswich, MA, US)
Phusion 5x GC buffer	Thermo Scientific (Darmstadt, GER)
Phusion 5x HF buffer	Thermo Scientific (Darmstadt, GER)

Phusion polymerase	Thermo Scientific (Darmstadt, GER)
T4 ligase	BioLabs (Ipswich, MA, US)
T4 ligase 10x reaction buffer	BioLabs (Ipswich, MA, US)
TLL	Sigma-Aldrich (München, GER)
Trypsin	Roth (Karlsruhe, GER)
<i>Xba</i> I	BioLabs (Ipswich, MA, US)

## 2.6 Antibodies

The antibody  $\alpha$ Vipp420 against IM30 was from (Fuhrmann 2010). The secondary antibody  $\alpha$ rabbit was from Sigma Aldrich (München, GER).

## 2.7 *E. coli* cells

Table 2.6: *E. coli* cells

Notation	Genotype	Origin
<i>E. coli</i> BL21(DE3)	F <sup>-</sup> <i>ompT hsdS</i> (r <sub>B</sub> <sup>-</sup> m <sub>B</sub> <sup>-</sup> ) <i>gal dcm</i> $\lambda$ (DE3)	Novagen (Madison, WI, US)
<i>E. coli</i> XL-1 Blue	<i>recA1 endA1 gyrA96 thi-1 hsdR17 supE44 relA1 lac</i>	Novagen (Madison, WI, US)

## 2.8 Cell culture media

Table 2.7: Cell culture media

Notation	Composition
2YT liquid medium	10 g Yeast extract 5 g NaCl 16 g Tryptone Add. 1 l ddH <sub>2</sub> O, autoclaved
LB agar	15 g Agar 10 g Tryptone 5 g Yeast extract 10 g NaCl Add. 1 l ddH <sub>2</sub> O, autoclaved
LB liquid medium	10 g Tryptone 5 g Yeast extract 10 g NaCl Add. 1 l ddH <sub>2</sub> O, autoclaved

## 2.9 Kits

Table 2.8: Kits

Kit	Notation	Origin
Agarose gel extraction	Gel Extraction Kit	Geneaid Biotech (Taipei, TW)
Immunostaining	Amersham ECL Prime Western Blotting Detection Reagent	GE Healthcare (München, GER)
PCR clean-up	PCR Cleanup Kit	Geneaid Biotech (Taipei, TW)
Plasmid preparation	High-Speed Plasmid Mini Kit	Geneaid Biotech (Taipei, TW)
SEC marker	Molecular Weight Maker Kit	Sigma Aldrich (München, GER)

## 2.10 DNA & protein ladders

Table 2.9: DNA & protein ladders

Notation	Origin
GeneRuler 1kb DNA Ladder	Thermo Scientific (Darmstadt, GER)
PageRuler Prestained Protein Ladder	Thermo Scientific (Darmstadt, GER)
PageRuler Unstained Protein Ladder	Thermo Scientific (Darmstadt, GER)
Pierce Unstained Protein MW Marker	Thermo Scientific (Darmstadt, GER)

## 2.11 Instruments

Table 2.10: Instruments

Instrument	Notation	Origin
CD spectrometer	J-815 Spectropolarimeter	Jasco (Gross-Umstadt, GER)
Centrifuge	Allegra X-15R Centrifuge	Beckman Coulter (Krefeld, GER)
	Avanti J-26XP	Beckman Coulter (Krefeld, GER)
	Centrifuge 5415 R	Eppendorf (Hamburg, GER)
	Centrifuge 5424	Eppendorf (Hamburg, GER)
Electron microscope	Concentrator 5301	Eppendorf (Hamburg, GER)
	FEI Tecnai 12	FEI, Thermo Scientific (Darmstadt, GER)
Electrophoresis adapter	peqPOWER300	PeqLab (Erlangen, GER)
	PowerPac Basic	BioRad (Hercules, CA, US)
Electrophoresis chamber	Mini-Protean 3 Cell	BioRad (Hercules, CA, US)
	Min-Protean Tetra Cell	BioRad (Hercules, CA, US)
	PerfectBlue Gelsystem S, M, L	PeqLab (Erlangen, GER)
Extruder	Mini-Extruder	Avanti Polar Lipids (Alabaster, AL, US)
Fluorimeter	FluoroMax-4	Horiba Scientific (Bensheim, GER)
Gel scanner	Quantum-ST4 1100/26M	PeqLab (Erlangen, GER)
	ViewPix 700	Biostep (Burkhardtsdorf, GER)
Heating bath	Thermomix 1420	Braun (Melsungen, GER)
Heating block	HBT-1 Heiz-Block-Thermostat	HLC BioTech (Pforzheim, GER)
Heating plate/magnetic stirrer	MR Hei-Standard	Heidolph (Schwabach, GER)
Horizontal shaker	Duomax 1030	Heidolph (Schwabach, GER)

<b>Instrument</b>	<b>Notation</b>	<b>Origin</b>
Immunoblot documentation system	STELLA	Raytest (Straubenhardt, GER)
Incubator	Binder Inkubator Serie BF	Binder (Tuttlingen, GER)
ITC instrument	MicroCal VP-ITC Microcalorimeter	Malvern Instruments (Malvern, UK)
Mass spectrometer	Mass spectrometer	Prof. Nina Morgner (Frankfurt, GER)*
Overhead shaker	Rollenmischer CMV-ROM	Fröbel (Lindau, GER)
pH meter	pH 211 Microprocessor	Hanna Instruments (Vöhringen, GER)
Photometer	Lambda 35	PerkinElmer (Rodgau, GER)
	NanoDrop	Thermo Scientific (Darmstadt, GER)
	Novaspec Plus	Amersham Biosciences (Little Chalfont, UK)
	U-5100 Spectrophotometer	Hitachi (Tokio, JPN)
SEC system	ÄKTApurifier 10	GE Healthcare (München, GER)
Shaking incubator	Multitron	Infors HT (Bottmingen, CH)
SPR instrument	SPR instrument	MPI-P (Mainz, GER)*
SPT instrument	NanoSight LM10	Malvern Instruments (Malvern, UK)
Sterile bank	Biological Safety Cabinet	Microflow (Kaufbeuren, GER)
Tank blot equipment	Trans-Blot wet electroblotting system	BioRad (Hercules, CA, US)
Thermo cycler	Thermocycler Primus 25	PeqLab (Erlangen, GER)
Thermo mixer	Thermomixer comfort	Eppendorf (Hamburg, GER)
Ultrasound device	Branson Sonifier 250	Heinemann Labortechnik (Duderstadt, GER)
	Ultrasonic Cleaner	VWR (Radnor, PA, US)
Vacuum coater	Vacuum Coater Auto 306	Edwards (Crawley, UK)
Vacuum pump	High Vacuum Pump	Edwards (Crawley, UK)
Vortex mixer	Vortex Mixer	VWR (Radnor, PA, US)

\*These instruments were in-house built.

## 2.12 Consumables

*Table 2.11: Consumables*

<b>Consumable</b>	<b>Notation</b>	<b>Origin</b>
Blotting paper	Thick Blot Paper	BioRad (Hercules, CA, US)
Copper grids	CF400-Cu, carbon film on 400 mesh copper grids	Electron Microscopy Sciences (Hatfield, UK)
Cuvettes	Acryl cuvettes	Sarstedt (Nümbrecht, GER)
	1.5 ml PMMA cuvettes	Brand (Wertheim, GER)
	Quartz crystal suprasil cuvettes, 3 mm	Hellma (Jena, GER)
	Quartz crystal suprasil cuvettes, 10 mm	Hellma (Jena, GER)
Dialysis tube	Spectra/Por Dialysis Membrane, MWCO: 6-8.000	Spectrum Labs (Rancho Dominguez, CA, US)
	Spectra/Por Dialysis Membrane, MWCO: 3.500	Spectrum Labs (Rancho Dominguez, CA, US)
Disposable column	Disposable 5-ml polypropylene	Thermo Scientific (Darmstadt,

Consumable	Notation	Origin
Extruder membrane	columns Polycarbonate membranes 0.1 $\mu\text{m}$	GER) Avanti Polar Lipids (Alabaster, AL, US)
Immunoblot membrane	Roti-PVDF	Roth (Karlsruhe, GER)
LaSFN9 glass plates	LaSFN9 glass plates	Hellma (Jena, GER)
LaSFN9 prism	LaSFN9 prism	Hellma (Jena, GER)
Rotors	JA-2550	Beckman Coulter (Krefeld, GER)
	JLA-8100	Beckman Coulter (Krefeld, GER)
SEC column	Superdex-200-16/600	GE Healthcare (München, GER)

## 2.13 Software

Table 2.12: Software

Application	Software
Chemical structures	ACD/ChemSketch 12.01 PyMOL
Literature management	EndNote X5
Mathematical analysis	Microsoft Excel 2010 Origin 7G Origin 7.5 OriginPro 8
Picture editing	Adobe Photoshop CS4 Extended CorelDRAW X7 ImageJ 1.47t Microsoft PowerPoint 2010
Sequencing analysis	ClustalX2 Genamics Expression 1.3.2
Spectra analysis	aje UV-Vis-IR Spectral Analysis 2.2
SPR analysis	Winspall 2.20
Text editing	Microsoft Word 2010

The instrument software used in this thesis belonged to the respective instrument (see 2.11).

## 2.14 Molecular biological methods

### 2.14.1 Polymerase chain reaction (PCR)

With the polymerase chain reaction (PCR), the possibility of exponential DNA duplication is given (Mullis & Faloona 1987). In principle, two oligonucleotide primers attach to two complementary DNA regions in the opposite direction. The DNA region is then amplified by a DNA polymerase (here: Phusion polymerase). The process can be divided into three main steps: Denaturing of the original DNA, annealing of the primers to the DNA, and DNA synthesis. Each step is repeated 15-50 times.

In this thesis, PCR was used to amplify regions of interest (the *im30* coding sequence and the *venus* coding sequence) as well as to introduce targeted changes in the DNA sequence called point mutagenesis (see 2.14.2).

The samples were pipetted as shown in *Table 2.13*.

**Table 2.13: Protocol for the PCR**

Component	Concentration	Volume ( $\mu\text{l}$ )
Plasmid	17 ng/ $\mu\text{l}$	4.0
fw primer	10 pmol/ $\mu\text{l}$	2.5
rev primer	10 pmol/ $\mu\text{l}$	2.5
dNTPs	2 mM	5.0
Phusion polymerase	0.5 units	0.5
Phusion HF buffer	5x	10.0
ddH <sub>2</sub> O		25.5

The PCR running program was conducted as listed in *Table 2.14*.

**Table 2.14: Protocol for the PCR running program**

Step	$T$ ( $^{\circ}\text{C}$ )	$t$ (s)	Number of cycles
First denaturation	98	30	1
Denaturation	98	10	} 35
Primer annealing	50	30	
Duplication	72	240	
Last duplication	72	600	1
Storage	4	$\infty$	1

Afterwards, 1  $\mu\text{l}$  of *DpnI* was added in order to cleave the methylated original vector DNA. The mixture was incubated at 37  $^{\circ}\text{C}$  for 30 min.

### 2.14.2 Site-directed mutagenesis

The site-directed mutagenesis is a special case of the PCR (see 2.14.1), in which a specific point mutation is introduced to a plasmid. The protocol was used from a QuickChange Site-Directed Mutagenesis Kit from Agilent Technologies (Santa Clara, CA, US) (Kirsch & Joly 1998). The samples were pipetted as shown in *Table 2.15*.

**Table 2.15: Protocol for the site-directed mutagenesis**

Component	Concentration	Volume ( $\mu\text{l}$ )
Plasmid	100 ng/ $\mu\text{l}$	1
fw primer	10 pmol/ $\mu\text{l}$	1
rev primer	10 pmol/ $\mu\text{l}$	1
dNTPs	2 mM	5
Phusion polymerase	0.5 units	1
Phusion GC buffer	5x	10
MgCl <sub>2</sub>	50 mM	1
DMSO	100%	3
ddH <sub>2</sub> O		27

Here,  $\text{MgCl}_2$  is used to increase the polymerase speed and DMSO helps denaturing the template. The running program was conducted as listed in *Table 2.16*.

**Table 2.16: Protocol for the site-directed mutagenesis running program**

Step	$T$ (°C)	$t$ (s)	Number of cycles
First denaturation	98	30	1
Denaturation	98	20	} 16
Primer annealing	57	30	
Duplication	72	180	
Last duplication	72	600	1
Storage	4	$\infty$	1

Afterwards, 1  $\mu\text{l}$  of *DpnI* was added in order to digest the original vector DNA. The mixture was incubated at 37 °C for 1 h.

#### 2.14.2.1 Primer design

For site-directed mutagenesis, primers were designed in order to introduce a specific point mutation to the pRSET IM30 plasmid. The primer length  $N$  was between 25 and 45 bases. If possible, the primers ended with the bases guanine or cytosine. Furthermore, the melting temperature  $T_m$  stayed below 80 °C and did not exceed 78 °C.

$T_m$  could be calculated via

$$T_m = \left( 81.5 + 0.41 \cdot (\%GC) - \frac{675}{N} - (\%mismatch) \right) \cdot 1^\circ\text{C} \quad \text{Eq. 2.1}$$

where  $\%GC$  is the amount of guanine and cytosine in relation to  $N$  and  $\%mismatch$  is the number of mutated bases in relation to  $N$ .

#### 2.14.3 PCR clean-up

The PCR clean-up was performed using the “PCR Cleanup Kit” as described in the manual.

#### 2.14.4 Generation of pRSET IM30-CFP and pRSET IM30-Venus expression plasmids

In order to create IM30 variants with a chromophore attached, the sequence coding for CFP or Venus were cloned into a pRSET vector after the C-terminus of the IM30 sequence, respectively.

##### 2.14.4.1 pRSET IM30-CFP

A pRSET GpA-CFP plasmid, which contained the sequence of the cyan fluorescent protein (CFP) as described in (Bisicchia *et al.* 2010), including the two modifications R27K and H232L, was used as a vector, after removing the *gpa* sequence. The *im30* sequence, which was encoded on a pRSET IM30 plasmid, was used as the insert. Both plasmids were digested by *BamHI* and *XbaI*, respectively, using the pipetting scheme listed in *Table 2.17*.

**Table 2.17: Protocol for the pRSET IM30-CFP restriction**

Component	Quantity	Volume ( $\mu$ l)
Plasmid	1 $\mu$ g	x
<i>Bam</i> HI	25 units	1.25
<i>Xba</i> I	25 units	1.25
NEB 10x buffer 3.1		5.00
ddH <sub>2</sub> O		Q.s. 50

The mixtures were incubated at 37 °C for 2 h without shaking. The desired fragments were isolated from a 1% agarose gel (see 2.14.5 and 2.14.6) and ligated using the pipetting scheme in Table 2.18.

**Table 2.18: Protocol for the pRSET IM30-CFP ligation**

Component	Quantity	Volume ( $\mu$ l)
Vector	50 ng	x
Insert	37.5 ng	x
T4 ligase	400 units	1.0
T4 ligase 10x reaction buffer		1.5
ddH <sub>2</sub> O		Q.s. 15

The mixture was incubated at 37 °C for 2 h. The enzymes were deactivated afterwards via heating for 10 min at 65 °C. Subsequently, *E. coli* cells were transformed with the ligation product (see 2.15.1) and the plasmid was extracted from a single colony (see 2.15.2).

In order to remove the stop codon between the *im30*- and *cfp* sequence, a site-directed mutagenesis (see 2.14.2) was performed using the primers IM30 -stop fw and IM30 -stop rev. The sequence was checked via sequencing (see 2.14.7).

#### **2.14.4.2 pRSET IM30-Venus**

The plasmid for expression of the IM30-Venus mutant was generated using the pRSET IM30-CFP expression plasmid as a vector after removing the *cfp* sequence. From a pVenus-GlpF plasmid the *venus* gene (Nagai *et al.* 2002) was amplified via PCR (see 2.14.1), using the primers Venus fw and Venus rev. Via the primers, *Bam*HI- and *Eco*RI restriction sites were introduced at the 5' end and 3' end of the *venus* gene, respectively. This allowed a directed insertion of the Venus sequence into the pRSET IM30 plasmid, which contains both restriction sites after the *im30* gene.

The pRSET IM30-CFP plasmid and the PCR product were digested by *Bam*HI and *Eco*RI, respectively, using the pipetting scheme listed in Table 2.19.

**Table 2.19: Protocol for the pRSET IM30-Venus restriction**

Component	Quantity	Plasmid Volume ( $\mu$ l)	PCR product Volume ( $\mu$ l)
Plasmid	1 $\mu$ g	x	-
PCR product	1 $\mu$ g	-	x
<i>Bam</i> HI	20 units	1	1
<i>Eco</i> RI	20 units	1	1
NEB 10x buffer 2.1		5	5
ddH <sub>2</sub> O		Q.s. 50	Q.s. 50

The mixtures were incubated at 37 °C for 1 h. The desired fragment from the plasmid digestion was isolated from a 1% agarose gel (see 2.14.5 and 2.14.6), and for the PCR product digestion a PCR clean-up (see 2.14.3) was performed. The products were then ligated using the pipetting scheme in *Table 2.20*.

**Table 2.20: Protocol for the pRSET IM30-Venus ligation**

Component	Quantity	Volume ( $\mu$ l)
Vector	50 ng	x
Insert	37.5 ng	x
T4 ligase	80 units	0.2
T4 ligase 10x reaction buffer		2.0
ddH <sub>2</sub> O		Q.s. 20

The mixture was incubated at 37 °C for 2 h. The enzymes were deactivated afterwards via incubation for 10 min at 65 °C. Subsequently, a plasmid transformation (see 2.15.1) and a plasmid preparation (see 2.15.2) were performed. Afterwards, the plasmid was sequenced (see 2.14.7).

### 2.14.5 Agarose gel electrophoresis

With the help of agarose gel electrophoresis, DNA- and RNA-fragments can be separated due to their size. The polysaccharide agarose is part of the gel and serves as a sieve. By introducing a current to the gel, the loaded oligonucleotides migrate to the anode due to their negatively charged phosphate groups. Smaller fragments are more motile and can be found at the bottom of the gel.

In this thesis, agarose gel electrophoresis was used in order to (i) monitor the success of PCRs and site-directed mutagenesis or (ii) elute DNA fragments directly from the gel. Only gels from 1% agarose (w/v) in 1xTAE buffer were used. 0.5 g of agarose was weighed and dissolved in 50 ml 1x TAE buffer by heating gently in the microwave. The still hot solution was immediately filled into an agarose gel chamber. A suitable comb was put in the chamber as well and the agarose polymerized for 30 min.

For the sample preparation, 10  $\mu$ l of the PCR product was mixed with 2  $\mu$ l of 6x DNA sample buffer. From this mixture 10  $\mu$ l was loaded on the agarose gel. Electrophoresis was performed

in 1x TAE buffer at 130 V. In order to visualize the bands, the gel was incubated with ethidium bromide for 30 min and afterwards exposed to UV light at a wavelength of 590 nm.

#### **2.14.6 Agarose gel elution**

Agarose gel elution was performed using the “Gel Extraction Kit” as described in the manual.

#### **2.14.7 DNA sequencing**

Sequencing of plasmid DNA was performed by Eurofins MWG Genomic (Martinsried, GER).

### **2.15 Microbiological methods**

#### **2.15.1 *E. coli* plasmid transformation via heat shock**

With the help of plasmid transformation, it was possible to introduce plasmid DNA to a competent *E. coli* cell.

1-2 µl of plasmid DNA solution was added to 50-150 µl of freshly thawed *E. coli* cells. For pre-cultures, *E. coli* BL21 cells and for preparation of plasmid DNA, *E. coli* XL1-Blue cells were used. The cells were incubated on ice for 1 min, then the heat shock leading to a permeable cell membrane was performed in the thermo mixer at 42 °C and 900 rpm for 1 min. Afterwards, 500 µl of 2YT or LB medium was added, and the sample was incubated in the thermo mixer at 37 °C and 900 rpm for 45-60 min. 300 µl of the sample was then transferred on a dry LB agar plate containing the correct antibiotic and plated. The agar plate was kept in the incubator at 37 °C for ~15 h.

In the case of PCR samples, 25-100 µl of plasmid solution was added to the *E. coli* cells. After heat shock and incubation at 37 °C, the cells were centrifuged at 4000 rpm for 2 min. 300 µl of the supernatant was discarded and the cell pellet resuspended in the remaining medium. This was necessary to increase the cell concentration.

#### **2.15.2 Preparation of plasmid DNA**

From an agar plate, which was prepared during plasmid transformation (see 2.15.1), colonies were picked and transferred in 3 ml of 2YT or LB medium. Additionally, ampicillin was added to a final concentration of 100 µg/ml. The overnight cultures were incubated at 37 °C and 200 rpm for ~15 h. Subsequently, preparation of plasmid DNA was performed with the “High-Speed Plasmid Mini Kit” as described in the manual.

#### **2.15.3 Optical density (OD) determination in *E. coli***

In order to determine the cell concentration in *E. coli* cultures, the optical density (OD) was determined by measuring the absorption at 600 nm in a photometer.

### 2.15.4 Protein expression in *E. coli*

For protein expression, *E. coli* BL21 cells were used. Pre-cultures were usually prepared in 200  $\mu$ l of 2YT or LB medium. The medium was inoculated with a colony picked from the agar plate (see 2.15.1). Additionally, ampicillin was added with a final concentration of 100  $\mu$ g/ml. The pre-cultures were incubated at 37 °C and 200 rpm for ~15 h.

For the main culture, 2 l of 2YT or LB medium (pre-incubated at 37 °C) was inoculated with enough pre-culture to reach an  $OD_{600}$  of 0.2. The added volume  $V_{pre-culture}$  was calculated with the  $OD_{600}$  of the pre-culture via

$$V_{pre-culture} = \frac{V_{main\ culture} \cdot 0.2}{OD_{600} \cdot f} \quad Eq. 2.2$$

where  $V_{main\ culture}$  is the volume of the main culture,  $OD_{600}$  the optical density of the pre-culture and  $f$  the dilution factor for the pre-culture. Also, ampicillin was added to a final concentration of 100  $\mu$ g/ml.

The main culture was incubated at 37 °C and 130 rpm until the  $OD_{600}$  reached a value between 0.8 and 1. Then, IPTG was added to a final concentration of 0.5 mM in order to induce overexpression of the desired protein. The cells were harvested 4 h after IPTG induction via centrifuging at 4 °C and 2500 rpm for 10 min. The cell pellets were resuspended in 50 ml of ddH<sub>2</sub>O and centrifuged at 4 °C and 4600 rpm for 10 min. The supernatant was discarded and the cell pellets were frozen in liquid nitrogen.

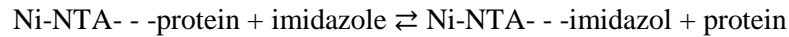
### 2.15.5 *E. coli* cell disruption via sonification

In order to release the desired overexpressed protein from the *E. coli* cells, the cells were disrupted via sonification. The cell pellets were thawed and resuspended in 50 ml of W20 buffer. To protect the proteins from degradation, 35  $\mu$ l of Protease Inhibitor Cocktail P8849 was added. Cell disruption was performed in the ultrasound device for 5 cycles at 2 min with the output signal set at 20%. During the cell disruption, the cells were ice-cooled.

## 2.16 Proteinbiochemical methods

### 2.16.1 Protein purification and co-purification via affinity chromatography

Protein purification was performed via affinity chromatography. The surface of the agarose-NTA carrier material was coordinated with Ni<sup>2+</sup> ions. During the purification, the desired protein, which was always coupled with an N-terminal histidine residue, could coordinate to the Ni<sup>2+</sup> ions in order to form an octahedral complex. Due to this complex formation, the desired protein could be separated from other proteins. Afterwards, a highly concentrated imidazole buffer was added in order to elute the protein in a competing reaction:



2.5 ml of the Ni-NTA matrix, which was previously stored in EtOH, was transferred in ddH<sub>2</sub>O and centrifuged at 500 rpm and 4 °C for 2 min. This step was repeated with another addition of ddH<sub>2</sub>O and subsequent addition of W20 buffer. The washed Ni-NTA matrix was then equilibrated in W20 buffer at RT for 1 h.

In order to load the Ni-NTA with the protein, the previously disrupted *E. coli* cell solution (see 2.15.5) was centrifuged at 10000 rpm and 4 °C for 10 min. 50 ml of the supernatant was then transferred to the washed Ni-NTA matrix, and the mixture was incubated in the overhead shaker at 4 °C for 1.5-2 h. Afterwards, the equilibrated Ni-NTA was washed in order to remove undesired components. To do so, the Ni-NTA was centrifuged at 800 rpm and 4 °C. The supernatant was removed and 50 ml of W20 buffer was added. The step was repeated with W50 and W100 buffer. The washed Ni-NTA was then transferred in W100 buffer into a 5-ml polypropylene column. For protein elution, 1 ml of elution buffer was added five times. The eluates were collected and analyzed via SDS-PAGE (see 2.16.3). The eluates containing the highest IM30 band intensity were dialyzed against HEPES buffer (see 2.16.2).

In order to create oligomeric mixtures of the CFP- and Venus-labeled IM30 versions, *E. coli* pellets containing overexpressed IM30-CFP and IM30-Venus, respectively, were mixed prior to purification. Former unpublished work in our group indicated that the IM30 ring formation takes place after purification. Because of this, it was not necessary to conduct a co-expression, where both, IM30-CFP and IM30-Venus, would have been expressed within the same bacteria culture.

### 2.16.2 Dialysis

In order to change the buffer of a protein solution, dialysis was performed. 1-10 ml of the protein solution was loaded into a semipermeable dialysis tube which had tiny pores (see 2.12) to let smaller molecules pass. The dialysis tube was then placed in ~2 l of the desired buffer at 4 °C for at least 1 h and was stirred thoroughly. The buffer was renewed two times.

### 2.16.3 SDS polyacrylamide gel electrophoresis (SDS-PAGE)

With the help of SDS polyacrylamide gel electrophoresis (SDS-PAGE), proteins can be separated by their size (Laemmli 1970). During sample preparation, the protein solution is exposed to high temperatures of 80-90 °C, the disulfide bridge breaker DTT, and the anionic detergent SDS. Thereby, the proteins are denatured and surrounded by the detergent in a ratio of 1.4 g SDS/g protein (Pitt-Rivers & Impiombato 1968). Due to the common negative charge, the proteins can migrate to the anode and are separated by their mass. The gel contains crosslinked polymers and can detain larger proteins.

In this thesis, gels with different polymerization degrees were used. The respective amounts of components are listed in *Table 2.21*.

**Table 2.21: Protocol for two loading and resolving gels**

Component	Resolving gel				Loading gel
	8%	10%	12%	14%	6%
ddH <sub>2</sub> O (ml)	5.5	5.0	4.5	4.0	3.0
40% Acrylamide/bis-acrylamide (ml)	2.0	2.5	3.0	3.5	0.75
Resolving gel buffer (ml)	2.5	2.5	2.5	2.5	-
Loading gel buffer (ml)	-	-	-	-	1.75
10% APS (μl)	50	50	50	50	25
TEMED (μl)	20	20	20	20	10

For sample preparation, 8 μl of the protein sample was mixed with 2 μl of 5x SDS sample buffer and incubated at 90 °C for 5 min. The pockets in the SDS gel, which was previously placed into the electrophoresis chamber, were (if not otherwise mentioned) loaded with 10 μl of the sample or 3 μl of the marker, respectively. Electrophoresis was performed in 1x SDS running buffer at 200 V for ~45 min.

In order to stain the gel after electrophoresis, it was incubated in a Coomassie staining solution for ~45 min, wherein the dye Coomassie Brilliant Blue G-250 can bind to basic amino acids while stabilizing its anionic form. Afterwards, the gel was destained with a Coomassie destaining solution for ~20 min in order to uncover the protein bands.

#### 2.16.4 Immunoblot detection

Proteins, which were separated on an SDS, gel can be specifically made visible via immunoblot detection.

After SDS-PAGE was performed (*cf.* 2.16.3), the gel was fixed between sponges and blotting papers together with a Roti-PVDF membrane, which was previously activated in methanol, into the tank blot equipment, wherein the PVDF membrane was facing the anode and the gel was facing the cathode. For protein transfer, 100 V was applied for 1 h. The membrane was then washed with TBS-T buffer and blocked with a 5% milk powder solution in TBS-T buffer for 1 h in order to occupy free spots on the membrane. Afterwards, the membrane was washed three times with TBS-T buffer for 5 min, respectively, and then incubated with the primary antibody  $\alpha$ Vipp420 (1/1000 in TBS-T buffer) at 4 °C overnight. Then, the membrane was washed with TBS-T buffer five times for 5 min and was incubated with the secondary antibody  $\alpha$ rabbit (1/10000 in TBS-T buffer) for 1 h and afterwards washed with TBS-T buffer five times for 5 min. The secondary antibody was connected with the enzyme horseradish peroxidase (HRP), which can catalyze the oxidation of luminol in presence of peroxides. This reaction results in a detectable luminescence. Therefore, the membrane was washed with the Amersham ECL Prime

Western Blotting Detection Reagent as described in the manual for 5 min and then developed in the immunoblot documentation system.

## 2.16.5 Concentration determination

### 2.16.5.1 Bradford assay

In a Bradford assay, protein concentrations are determined via photometrical quantification (Bradford 1976). The dye Coomassie Brilliant Blue G-250, which is positively charged in acid environments with an absorbance maximum of 470 nm, switches into the anionic state with an absorbance maximum of 595 nm upon protein binding. With a BSA standard series, a calibration curve can be generated and the protein concentration determined. The samples for the calibration curve, which were pipetted in duplicates, are listed in *Table 2.22*.

*Table 2.22: Protocol for the Bradford assay*

BSA amount ( $\mu\text{g}$ )	0.5 $\mu\text{g}/\mu\text{l}$ BSA ( $\mu\text{l}$ )	ddH <sub>2</sub> O ( $\mu\text{l}$ )
0	0	50
2	4	46
4	8	42
6	12	38
8	16	34
10	20	30

The protein samples were pipetted in triplicates with a volume of 5-50  $\mu\text{l}$  depending on the band intensity in the SDS-PAGE (see 2.16.3). The volume was filled up to 50  $\mu\text{l}$  with ddH<sub>2</sub>O. Afterwards, 50  $\mu\text{l}$  of formic acid was added to all standards and samples and incubated at RT for 10 min. Subsequently, 900  $\mu\text{l}$  Roti-Quant 1x was added and the sample was incubated at RT for 20 min. The absorbance of the standards and samples was measured at 595 nm and the sample concentration was determined via the standard calibration curve, which was evaluated via a linear fit (see 5.13.1.5).

### 2.16.5.2 BSA standard SDS-PAGE

Alternatively to the Bradford assay, BSA standard SDS-PAGEs were used in this thesis. With a BSA standard series, a calibration curve was generated and the protein concentration determined. The samples for the calibration curve are listed in *Table 2.23*.

*Table 2.23: Protocol for the BSA standard SDS-PAGE*

BSA amount ( $\mu\text{g}$ )	0.5 $\mu\text{g}/\mu\text{l}$ BSA ( $\mu\text{l}$ )	SDS sample buffer ( $\mu\text{l}$ )
0.5	1	10 (1x)
1.0	2	10 (1x)
1.5	3	10 (1x)
2.0	4	10 (1x)
2.5	5	2 (5x)
3.0	6	2 (5x)

10  $\mu\text{l}$  of the protein samples was pipetted in triplicates and 2  $\mu\text{l}$  of 5x SDS sample buffer was added. An SDS-PAGE was performed as described in 2.16.3. It was necessary to load the complete sample on the gel. Afterwards, the band intensities were densitometrically evaluated with the program ImageJ 1.47t, which could determine the area below the band intensity peaks. With the BSA standards, a calibration curve was generated and was evaluated via a linear fit (see 5.13.1.5). Based on the standard calibration curve, the sample concentration was determined.

### 2.16.5.3 Absorbance measurement

The dye ratio of mixtures of IM30-CFP and IM30-Venus was determined via estimation of the IM30-Venus concentration due to absorption of the dye. Thus, the protein absorbance was measured from 300 to 800 nm. The scattering in the absorption spectrum due to the protein background was reconstructed with the a|e UV-Vis-IR Spectral Analysis 2.2 software via a scatter fit (*cf.* 5.13.1.9) and subtracted from the raw data. After scattering correction, the absorbance at 515 nm  $A_{515}$ , which was independent of the CFP absorbance, was determined and the concentration of the Venus-labeled protein  $c_{IM30-Venus}$  was calculated via the Lambert-Beer law

$$A_{515} = c_{IM30-Venus} \cdot d \cdot \varepsilon_{515,Venus} \quad \text{Eq. 2.3}$$

where  $d$  is the path length of the cuvette and  $\varepsilon_{515,Venus}$  the extinction coefficient of Venus at 515, which is  $92200 \text{ M}^{-1}\text{cm}^{-1}$  (Nagai *et al.* 2002).

The ratios of Venus and CFP, respectively, were then calculated as

$$\%_{IM30-Venus} = \frac{c_{IM30-Venus}}{c_{IM30-CFP/Venus}} \quad \text{Eq. 2.4}$$

$$\%_{IM30-CFP} = 1 - \%_{IM30-Venus} \quad \text{Eq. 2.5}$$

where  $c_{IM30-CFP/Venus}$  is the concentration of the mixed sample, which was previously determined via BSA standard SDS-PAGE (see 2.16.5.2).

### 2.16.6 Buffer system

If not otherwise mentioned, all following experiments were performed in HEPES buffer.

### 2.16.7 Concentrating protein samples

In some experiments, it was necessary to use a rather high protein concentration, which could not be obtained via the standard protein purification (see 2.16.1). In order to increase the protein concentration, the sample was transferred into a dialysis tube and was overlaid with a thin layer of ‘‘Spectra/Gel Absorbent’’, which was able to absorb some water from the sample. The sample was incubated with the gel at 4  $^{\circ}\text{C}$  for  $\sim 18$  h and the absorbent was exchanged up to three times. After the procedure was finished, the protein was dialyzed as described in 2.16.2 and the concentration was determined via a Bradford assay (see 2.16.5.1).

### 2.16.8 Protein crosslinking

In some experiments, it was necessary to fix the tertiary/quaternary structure of IM30. Glutaraldehyde can connect, among others, amide-, imidazole-, phenol- and thiol groups of proteins (Okuda *et al.* 1991; Migneault *et al.* 2004) and thereby prevent structural changes in the protein, *e.g.* oligomerization and dissociation.

5 vol% of a 2.5% glutaraldehyde solution was added to the protein solution and the mixture was incubated at 37 °C for 5 min. Subsequently, 3.8 vol% of a 2.5 M TrisHCl solution was added in order to stop the crosslinking reaction, since the chemical is able to form complexes with glutaraldehyde. In the case of a protein preparation, the sample was dialyzed afterwards (see 2.16.2) to remove excess glutaraldehyde and TrisHCl.

#### 2.16.8.1 Dissociation of IM30 rings

A hypothetical dissociation of the higher-ordered IM30 structures on liposomes was tested using glutaraldehyde. 3  $\mu\text{M}$  of protein was incubated with increasing lipid concentrations (0-3000  $\mu\text{M}$ ) in presence and absence of 7.5 mM  $\text{MgCl}_2$  for ~2 h at RT. Afterwards, the crosslinker glutaraldehyde was added and an SDS-PAGE was performed. Also, control samples lacking the crosslinker were loaded. Upon IM30 ring dissociation, hypothetically formed monomers could not be crosslinked anymore and would be visible in the SDS gel. The experiment is schematically demonstrated in *Fig. 2.1*.

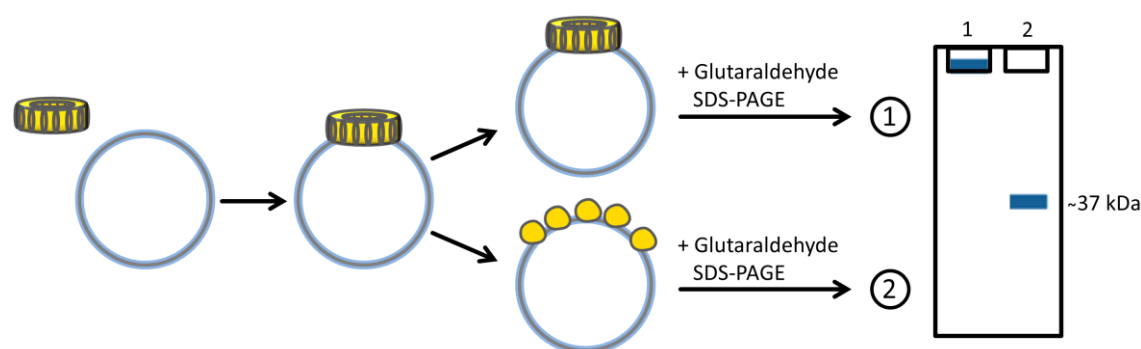


**Fig. 2.1: Dissociation of IM30 rings**

A schematic overview of the IM30 ring dissociation assay is shown. The protein is incubated with liposomes (in presence and absence of  $\text{Mg}^{2+}$ , not shown) and crosslinked prior to an SDS-PAGE analysis. Two scenarios are possible: In the case of a stable unchanged ring oligomerization, all protein monomers would be crosslinked inside the ring and thus, no monomer band in the gel would be visible (1). Upon a ring dissociation, hypothetically formed monomers would migrate away from each other and cannot be crosslinked. Thus, a monomer band in the SDS gel would appear (2).

### 2.16.9 Protein denaturation and renaturation

Urea is a common protein denaturant. It is speculated that the molecule forms hydrogen bonds with peptide groups and thereby replaces water molecules (Lim *et al.* 2009). The urea binding is thermodynamically favored, and a larger surface of proteins in the denatured state is promoted upon urea addition (Auton *et al.* 2007).

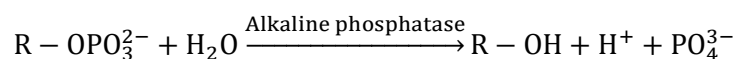
For measuring denaturation curves of IM30 in presence of  $Mg^{2+}$ , urea stocks were prepared containing different urea concentrations between 0 and 6.5 M in NaPh buffer. For sample preparation, 3.16  $\mu M$  of IM30 was incubated with different  $MgCl_2$  concentrations between 0 and 15 mM at RT for 30 min and then mixed with the urea stocks, which already contained the same amount of  $MgCl_2$ . After 45 min of final incubation, the samples were measured as described in 2.18.1.1.

In order to control the reversibility of the denaturation process in presence of  $Mg^{2+}$ , renaturation curves were recorded. 3.16  $\mu M$  of IM30 was incubated with 15 mM  $MgCl_2$  in NaPh buffer at RT for 30 min. After that, the protein was denatured in 7 M of urea solution, which also contained 15 mM  $MgCl_2$ , at RT for 30 min. The urea concentration was then decreased stepwise at a constant  $MgCl_2$  concentration via dialysis with an incubation time of 1.5 h per step. The final step in urea-free NaPh buffer was performed overnight. After each step, samples were taken for the measurement (see 2.18.1.1). For the final sample, another Bradford assay was performed as described in 2.16.5.1 in order to compensate for the protein loss.

The protein denaturation and renaturation experiments were performed in cooperation with Benedikt Junglas.

### 2.16.10 Protein dephosphorylation

Alkaline phosphatases are able to hydrolyze phosphate ester groups and can therefore remove phosphate residues from proteins:



In order to test for a hypothetical phosphorylation, IM30 was incubated with the enzyme Alkaline phosphatase, calf intestinal (CIP). The pipetting scheme is shown in *Table 2.24*.

**Table 2.24: Protocol for the IM30 desphosphorylation**

<b>Component</b>	<b>Control Volume (<math>\mu l</math>)</b>	<b>+CIP Volume (<math>\mu l</math>)</b>
IM30 (10.4 $\mu M$ )	10.0	10.0
CIP	-	0.7
CutSmart buffer 10x	1.5	1.5
ddH <sub>2</sub> O	3.5	2.8

The mixtures were incubated at 37 °C for 1 h. Subsequently, an SDS-PAGE (see 2.16.3) was performed.

Since there is the possibility of single lipid binding to IM30, which would bias the experiment due to a dephosphorylation of the lipids, a control experiment with lipase from *Thermomyces*

*lanuginosus* (TLL), which is able to digest lipids, was performed. The pipetting scheme is shown in Table 2.25.

Table 2.25: Protocol for the IM30 lipolysis

Component	Control Volume ( $\mu\text{l}$ )	+TLL Volume ( $\mu\text{l}$ )
IM30 (10.4 $\mu\text{M}$ )	10	10
TLL	-	1
ddH <sub>2</sub> O	5	4

The mixtures were incubated at 37 °C for 30 min. Subsequently, an SDS-PAGE (see 2.16.3) was performed.

### 2.16.11 Tryptic digestion

In order to investigate the proteolysis resistance of IM30 under different conditions, tryptic digestion was performed. Trypsin is a serine protease which cleaves proteins at the C-terminal side of the alkaline amino acids lysine and arginine (Olsen *et al.* 2004). It is found in digestive systems of vertebrates.

The enzyme was stored at -20 °C in 0.1 mM of HCl. For the experiments, dilutions were prepared using HEPES buffer.

#### 2.16.11.1 Digestion of IM30 in presence of Mg<sup>2+</sup>

2.5  $\mu\text{M}$  of IM30 was mixed with 10 mM MgCl<sub>2</sub>. Afterwards, 0.01 mg/ml trypsin was added, and the samples were incubated at 37 °C. From this stock, samples were taken after different time intervals and mixed with 5x SDS sample buffer in order to stop proteolysis. The same procedure was performed for a control sample lacking MgCl<sub>2</sub>. Subsequently, an SDS-PAGE was performed as described in 2.16.3.

In order to confirm the independence of the trypsin activity in presence of Mg<sup>2+</sup>, a BAEE assay was performed. Here, BAEE is digested by trypsin and the product *N* $\alpha$ -Benzoyl-*L*-arginine can be detected photometrically. The reaction is shown in Fig. 2.2.

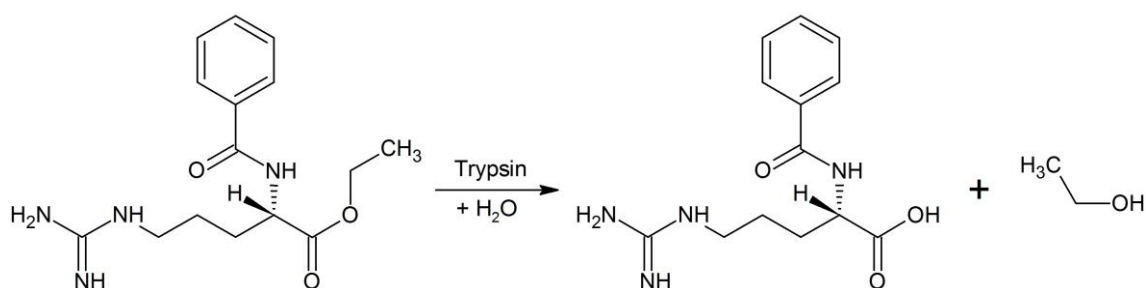
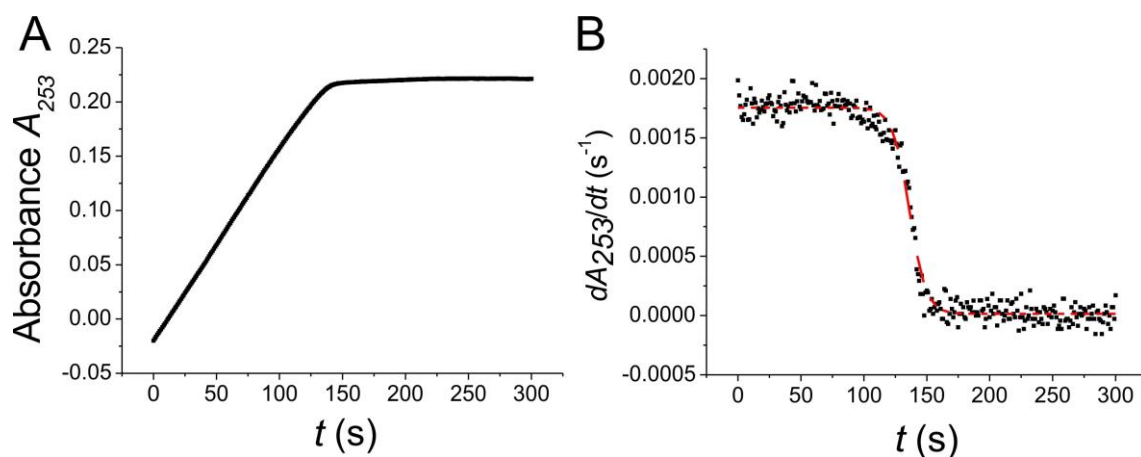


Fig. 2.2: Hydrolysis of BAEE via tryptic digestion

In the BAEE assay, BAEE is hydrolyzed via trypsin. Products are *N* $\alpha$ -Benzoyl-*L*-arginine and ethanol.

0.23 mM of BAEE was mixed with 0.002 mg/ml trypsin and  $\text{MgCl}_2$  in different concentrations. For the blank sample, 0.1 mM of HCl was added instead of trypsin, and no salt was added. After mixing, the absorption at 253 nm was measured for 300 s in order to observe the formation of  $N_\alpha$ -Benzoyl-*L*-arginine. The trypsin activity was then determined as the maximal slope of the absorption curve. In order to do so, the first derivative of this curve was calculated and fitted via a Boltzmann fit (see 5.13.1.2), whereas the variable  $A_t$  was assumed to represent the trypsin activity. An exemplary measurement and evaluation of the BAEE assay is shown in *Fig. 2.3*.



**Fig. 2.3: Exemplary BAEE assay**

An exemplary measurement (A) and evaluation (B) of the BAEE assay is shown for the control sample lacking  $\text{MgCl}_2$ . The absorbance at 253 nm was recorded after mixing BAEE and trypsin (A). The first derivative of this curve (B) was fitted with a Boltzmann fit (red curve,  $R^2=0.989$ ) in order to determine the maximal slope of the absorption curve (A). In cooperation with Benedikt Junglas.

After a triplicate measurement, the obtained slope values were normalized to the value of the sample lacking  $\text{MgCl}_2$ .

The tryptic digestion of IM30 in presence of  $\text{Mg}^{2+}$  and the BAEE assay were performed in cooperation with Benedikt Junglas.

#### **2.16.11.2 Digestion of IM30 in presence of DOPG and DOPC liposomes**

0.3 mM of unilamellar liposomes was prepared as described in 2.17.3 and incubated for at least 30 min with 3.16  $\mu\text{M}$  of IM30. Afterwards, 0.01 mg/ml trypsin was added, and the samples were incubated at 15 °C. From this stock, samples were taken after different time intervals and mixed with 5x SDS sample buffer in order to stop the reaction. Subsequently, an SDS-PAGE was performed as described in 2.16.3. The experiment was performed in cooperation with Carmen Siebenaller.

#### **2.16.12 Size exclusion chromatography (SEC)**

In order to compare the structure of IM30-CFP and IM30-Venus with the IM30 wildtype (WT) structure, size exclusion chromatography (SEC) was performed. 250-350  $\mu\text{g}$  of the protein was loaded onto a Superdex-200-16/600 column at 4 °C using an ÄKTApurifier 10 at a flow rate of

0.55 ml/min. For calibration, the following proteins from the “Molecular Weight Maker Kit” were used: ribonuclease A (13.7 kDa), carbonic anhydrase (29 kDa), BSA (66 kDa),  $\beta$ -amylase (200 kDa), and apoferritin (443 kDa).

## 2.17 Lipidbiochemical methods

### 2.17.1 *In vitro* membrane model systems

In order to investigate protein-membrane interactions, liposomes with different compositions, which have already been established in (Suppes 2013), were created as model membranes for *in vitro* investigations.

The thylakoid membrane composition was already discussed in 1.2.1. Thus, the negatively charged and bilayer-forming lipids SQDG and PG were represented by DOPG. If only membrane interaction was of interest, 100% DOPG liposomes were used to ensure maximal membrane binding of IM30.

In order to investigate the IM30 interaction with specific lipids, liposomes containing 80% of the zwitterionic DOPC as background lipid and 20% of the lipid of interest were created. This mixture was already used in (Suppes 2013), in which the interaction of IM30 with the single thylakoid lipids was investigated. The reason to use DOPC in the mixture is originally based on the issue that 100% MGDG liposomes would not be stable.

For experiments involving membrane fusion, a 60%/40% MGDG/DOPG mixture was normally used as a thylakoid membrane model (Suppes 2013), since it consists of a realistic ratio of negatively charged and neutral lipids. Furthermore, the amount of inverse-hexagonal and lamellar phase forming lipids agrees with the thylakoid *in vivo* situation.

### 2.17.2 Preparation of multilamellar liposomes

For the generation of multilamellar liposomes, the desired lipid amounts (if not otherwise mentioned in w/w), which were usually stored in a 2/1 (v/v) chloroform/methanol solution, were pipetted, and the organic solvent was evaporated under a gentle nitrogen stream. In order to remove the remaining solvent compounds, the lipid film was evacuated in an exsiccator overnight or for at least 5 h. The dried film was resuspended in HEPES buffer, whereby multilamellar liposomes were produced.

### 2.17.3 Preparation of unilamellar liposomes via freeze-thaw

The alternating freezing and thawing (freeze-thaw) of multilamellar liposomes has been demonstrated to result in unilamellar liposomes (Hope *et al.* 1986). Previously produced multilamellar

liposomes (see 2.17.2) were rotationally frozen in liquid nitrogen and thawed in a 37 °C tempered heat bath for five cycles.

#### 2.17.4 Preparation of uniformly sized liposomes via extrusion

Via extrusion, liposomes can be sized to a uniform diameter (Hope *et al.* 1985). A sample of unilamellar liposomes, generated via the freeze-thaw procedure (see 2.17.3), was pressed through an extruder, containing a polycarbonate membrane with the desired pore size of 100 nm. This was repeated 15-25 times.

## 2.18 Biophysical methods

### 2.18.1 Circular dichroism (CD) spectroscopy

Circular dichroism (CD) spectroscopy is based on the observation that optically active substances, such as proteins, feature two different extinction coefficients  $\varepsilon_l$  and  $\varepsilon_r$  for left or right circularly polarized light, respectively. The difference  $\Delta\varepsilon$  is characteristic for each optically active substance, and in the case of proteins, it depends on the secondary structure fractions of the  $\alpha$ -helices,  $\beta$ -sheets,  $\beta$ -turns and random coil areas.

In a typical CD measurement,  $\Delta\varepsilon$  is transferred into the ellipticity  $\Theta$  via

$$\Theta_\lambda = 32.98^\circ \cdot (\varepsilon_{l,\lambda} - \varepsilon_{r,\lambda}) \cdot c \cdot d \quad \text{Eq. 2.6}$$

where  $\Theta_\lambda$  is the wavelength-dependent ellipticity in deg,  $c$  the protein concentration in g/cm<sup>3</sup> and  $d$  the path length of the cuvette in cm. The raw signal from the instrument is given as  $\Theta_\lambda$  in mdeg and can be converted into the molar ellipticity  $[\Theta]_\lambda$  in deg\*cm<sup>2</sup>\*dmol<sup>-1</sup> via

$$[\Theta]_\lambda = \frac{\Theta_\lambda}{100 \cdot c \cdot d} \quad \text{Eq. 2.7}$$

where  $c$  is the protein concentration in mM. Typical CD spectra for the respective secondary structure types are shown in *Fig. 2.4*.

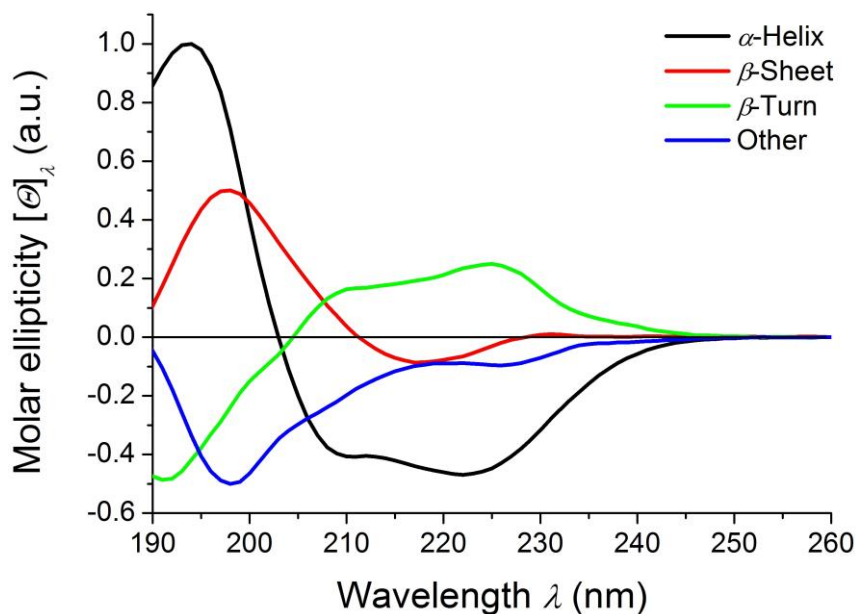


**Fig. 2.4: Typical CD spectra for  $\alpha$ -helices,  $\beta$ -sheets and  $\beta$ -turns**

CD spectra of ideal  $\alpha$ -helices,  $\beta$ -sheets,  $\beta$ -turns and other structures (including random coil) are shown. The amount of the respective secondary structure fractions can usually be calculated from a CD spectrum. The horizontal line indicates a molar ellipticity of 0. The data were obtained from Jasco as part of the J-815 Spectropolarimeter evaluation software.

All CD measurements were performed in 10 mM NaPh buffer.

### 2.18.1.1 Urea denaturation/renaturation experiments

In order to determine the stability of the IM30 secondary structure in presence of different amounts of  $Mg^{2+}$ , urea denaturation and renaturation experiments were performed by incubating the samples with different urea concentrations (see 2.16.9). The measurements were performed in cooperation with Benedikt Junglas.

For the measurement, the following parameters were chosen:

**Table 2.26: Parameters used for the urea denaturation curve CD measurements**

Parameter	Value
Temperature $T$	20 °C
Measured wavelength area $\lambda_{em}$	210-250 nm
Observed wavelength $\lambda_{obs}$	222 nm
Bandwidth	5 nm
Measuring steps	1 nm
Integration time	1 s
Scanning speed	100 nm/min
Repeats	3

In order to compare different denaturation curves with each other, the ratio of denaturated protein  $f_D$  was plotted against increasing urea concentration.  $f_D$  was calculated as described in (Pace 1986) via

$$f_D = \frac{y - y_N}{y_D - y_N} \quad \text{Eq. 2.8}$$

where  $y$  the molar ellipticity at 222 nm and  $y_N$  and  $y_D$  the molar ellipticity at 222 nm in the native and denaturated state, respectively, which implies a two-state mechanism (Pace 1986). The latter two can be obtained by identification of the linear areas of the denaturation curves at low and high urea concentration and calculating the mean value from the data points of these areas. The error for  $f_D$  was determined via Gaussian error distribution of 3 samples (see 5.13.3). Additionally, the inflection points of the denaturation curves  $D_{1/2}$  were calculated via fitting the normalized denaturation curves with a Boltzmann fit (*cf.* 5.13.1.2):

$$f_D = \frac{y_N - y_D}{1 + e^{(x - D_{1/2})/dx}} + y_D \quad \text{Eq. 2.9}$$

where  $x$  is the urea concentration.

### 2.18.2 Fluorescence spectroscopy

Fluorescence spectroscopy is based on the deactivation of excited chromophores upon emitting light, which is red-shifted compared to the excitation light. The reason for this alteration lies in different radiationless relaxation processes prior to deactivation, *e.g.* a steric change or the interaction of the chromophoric molecule with its environment. These processes are called internal conversions. (Winter & Noll 1998)

The fluorescence of a molecule can be manipulated by addition of different solvents or other components and thus, fluorescence spectroscopy is a multifaceted tool in biochemistry or biophysics. In this thesis, several special cases of fluorescence were taken advantage of: (Winter & Noll 1998)

- Dipolar relaxation/Stokes shift: Polar solvent molecules (*e.g.* H<sub>2</sub>O) can decrease and stabilize the energy of an excited fluorophore via antiparallel alignment of their dipole moment compared to the dipole moment of the chromophoric molecules. Subsequently, the lower energy level of the excited fluorophores results in a red-shifted emission spectrum.
- Fluorescence quenching: Some molecules can act as so-called quencher, which can degrade the fluorescence ability of chromophores upon direct interaction. Due to complex formation, irreversible chemical alterations (*e.g.* oxidation) or particle collisions, the quencher destroys the fluorophore or absorbs its energy and releases it as heat instead of light.
- Förster resonance energy transfer (FRET): This effect is a special case of fluorescence quenching and describes an energy transfer between two fluorophores: the donor and the acceptor. The conditions for FRET include the ability of donor and acceptor to form

a dipole-dipole interaction when they are in close proximity. Furthermore, the emission spectrum of the donor must overlap with the excitation spectrum of the acceptor (spectral overlap  $J$ ). An important value is the Förster distance, which describes the distance between two fluorophores with a FRET efficiency of 50%.

### 2.18.2.1 ANS fluorescence

The fluorophore ANS can bind to polar and non-polar protein areas due to its hydrophilic sulfonate group, which undergoes electrostatic interactions with negatively charged amino acids, and its hydrophobic anilino-naphthalene group. The structure of ANS is shown in *Fig. 2.5*.

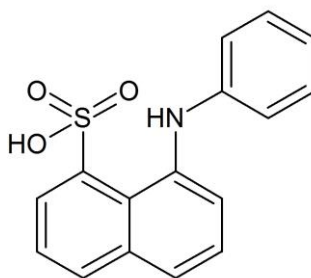


*Fig. 2.5: Structure of ANS*

The amphiphilic fluorophore ANS binds to polar as well as non-polar protein surfaces. Only upon hydrophobic interactions between the fluorophore and a protein, the ANS fluorescence changes significantly.

While interactions of ANS with polar protein surfaces have no significant effect on the ANS fluorescence, binding to hydrophobic protein sites results in a dramatic increase in the ANS fluorescence intensity and a blue shift of the fluorescence emission maximum due to the lack of dipolar relaxation. Thus, the fluorophore is useful when it comes to the detection of a protein conformation change, *e.g.* during binding reactions. (Slavik 1982; Matulis *et al.* 1999)

In this thesis, several experiments based on ANS fluorescence were performed in order to investigate a potential interaction between IM30 and  $Mg^{2+}$ . A typical ANS spectral shift in presence of IM30/ $Mg^{2+}$  is illustrated in *Fig. 2.6*.

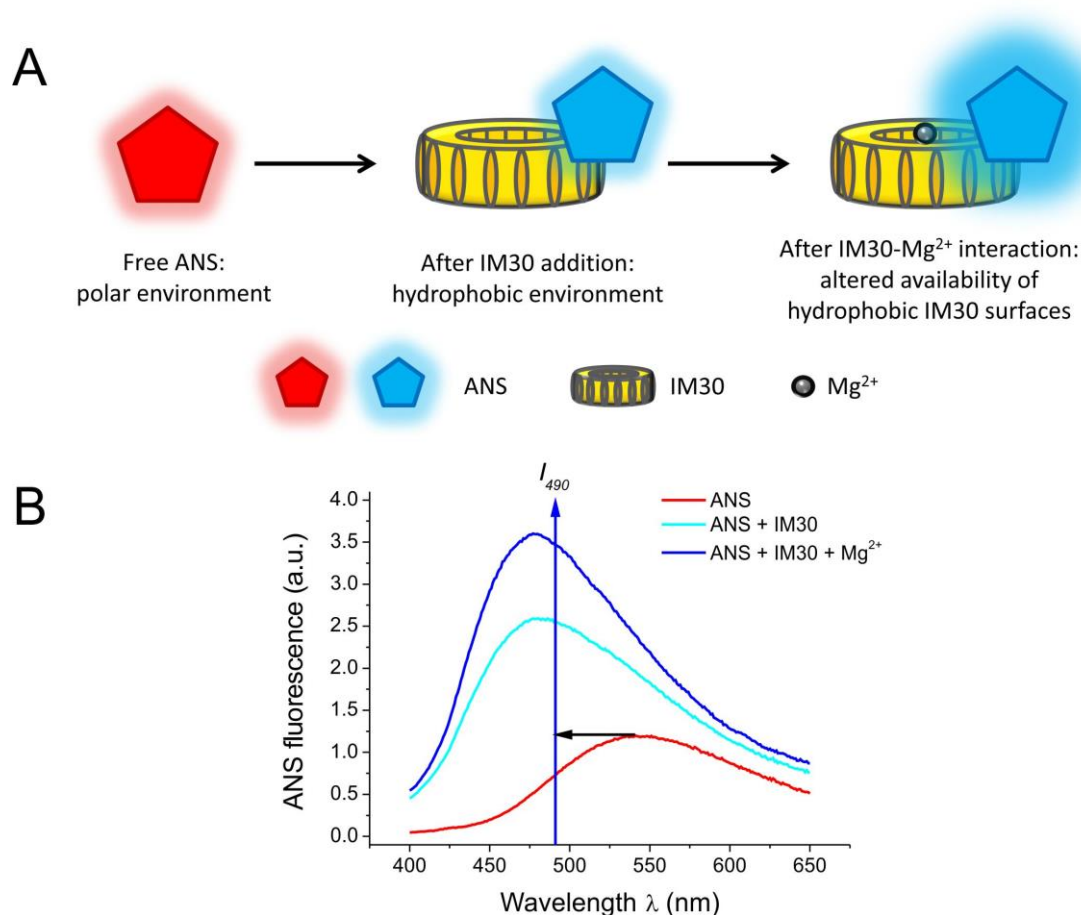


**Fig. 2.6: ANS fluorescence emission spectra blue shift upon IM30 and IM30/Mg<sup>2+</sup>-binding**

Binding of ANS to IM30 results in a decrease in the polarity of the ANS environment, which is further decreased upon Mg<sup>2+</sup> addition (A). This change can be monitored via a blue shift of the maximum in the ANS fluorescence emission spectrum from ~550 nm (red curve) to 490 nm (blue curve) and an increase of the total fluorescence intensity, which is indicated by the black and blue arrows, respectively (B).

### ANS spectra recording

For simple ANS spectra recording, 1  $\mu\text{M}$  protein was incubated with 7.5  $\mu\text{M}$  ANS and different MgCl<sub>2</sub> concentrations between 0 and 10 mM. Additionally, control samples were prepared, lacking IM30, in order to evaluate the influence of Mg<sup>2+</sup> on the ANS fluorescence. The samples were incubated for ~3 h and then measured using the parameters given in Table 2.27.

**Table 2.27: Parameters used for the ANS spectra recording**

Parameter	Value
Temperature $T$	25 °C
Excitation wavelength $\lambda_{ex}$	370 nm
Measured wavelength area $\lambda_{em}$	400-650 nm
Slit width	5 nm
Measuring steps	1 nm
Integration time	0.1 s

All spectra were corrected for buffer background. In order to compare measurements from different days with each other, all spectra for samples containing pure ANS, which were repeated in every new approach, were normalized to the sample containing pure ANS from the initial measurement in which IM30 WT was tested. The obtained correction factors were used to adjust all other spectra.

### **ANS titration curves**

For ANS titration curves, the titrator equipment of the fluorimeter was used. 2500  $\mu\text{l}$  of differently concentrated (0-2  $\mu\text{M}$ ) IM30 solutions, which were incubated with the 7.5-fold amount of ANS, was pre-filled in 10 mm cuvettes. In 5  $\mu\text{l}$ -steps, a total volume of 500  $\mu\text{l}$   $\text{MgCl}_2$  solutions of different concentrations (0.01-0.1 mM) was added, and the change in the ANS fluorescence was measured, respectively. During the experiment, the mixture was stirred thoroughly. The measurement parameters are listed in *Table 2.28*.

**Table 2.28: Parameters used for the ANS titration curves**

<b>Parameter</b>	<b>Value</b>
Temperature $T$	25 °C
Equilibration time $t_{eq}$	1 min
Excitation wavelength $\lambda_{ex}$	370 nm
Measured wavelength area $\lambda_{em}$	400-650 nm
Observed wavelength $\lambda_{obs}$	490 nm
Slit width	Different $c_{\text{Mg}^{2+}}$ : 6 nm Different $c_{\text{IM30}}$ : 5 nm
Measuring steps	1 nm
Integration time	0.1 s

For each dilution step, the raw ANS fluorescence intensities at 490 nm  $I_{490,raw}$  were corrected using

$$I_{490,corr.} = I_{490,raw} \cdot \frac{V_0 + V_{added}}{V_0} \quad \text{Eq. 2.10}$$

with  $V_0$  being the start volume and  $V_{added}$  the added volume. The curves were normalized to the same starting point. For the experiment using different  $\text{MgCl}_2$  concentrations, the obtained binding curves for the IM30- $\text{Mg}^{2+}$  interaction were fitted with a binding fit (*cf.* 2.18.2.3 and 5.13.1.1), respectively, from which the dissociation constants  $K_D$  were calculated.

### **ANS thermofluor assay**

In a thermofluor assay, the protein stability upon ligand binding can be evaluated via a dye-binding thermal shift screen (Lavinder *et al.* 2009).

1.5  $\mu\text{M}$  IM30 was incubated with a 7.5-fold excess of ANS in presence and absence of 10 mM  $\text{MgCl}_2$  for at least 30 min. Control samples lacking IM30 were also prepared. For all samples, a

denaturation curve was recorded. For the samples containing IM30, an additional renaturation curve was recorded. The ANS fluorescence of the samples was measured using the parameters listed in *Table 2.29*.

**Table 2.29: Parameters used for the ANS thermofluor assays**

Parameter	Value
Temperature $T$	fw: 0-80 °C, rev: 80-0 °C
Temperature steps	fw: 1 °C, rev: 5 °C
Equilibration time $t_{eq}$	fw: 1 min, rev: 3 min
Excitation wavelength $\lambda_{ex}$	370 nm
Measured wavelength area $\lambda_{em}$	400-650 nm
Observed wavelength $\lambda_{obs}$	490 nm
Slit width	3 nm
Measuring steps	1 nm
Integration time	0.1 s

For the denaturation process, the fluorescence intensity at 490 nm was then normalized to a relative scale where the intensity at 0 °C is defined as 1 and that at 80 °C is defined as 0:

$$I_{490,rel.,T=x\text{ °C}} = \frac{I_{490,T=x\text{ °C}} - I_{490,T=80\text{ °C}}}{I_{490,T=0\text{ °C}} - I_{490,T=80\text{ °C}}} \quad \text{Eq. 2.11}$$

with  $I_{490,rel.,T=x\text{ °C}}$ ,  $I_{490,rel.,T=0\text{ °C}}$  and  $I_{490,rel.,T=80\text{ °C}}$  being the ANS fluorescence intensity at 490 nm for x, 0 and 80 °C, respectively. From the resulting curves, the difference of the relative fluorescence intensities between sample and control lacking  $Mg^{2+}$  was calculated.

### 2.18.2.2 Förster resonance energy transfer (FRET) measurements

In order to investigate association and dissociation of IM30 rings under different conditions, an IM30 associated FRET pair was used. Thus, two labeled versions of IM30, which are able to act as a FRET pair (Broussard *et al.* 2013), were generated: IM30-CFP and IM30-Venus. The fluorescence excitation and emission spectra of those dyes are illustrated in *Fig. 5.6*. Since FRET is only possible when donor and acceptor fluorophores are in close proximity to each other (*e.g.* as part of the same IM30 ring), a mixture of both mutants was required. Thus, co-purification was performed as described in 2.15.4. In the following, a mixture of IM30-CFP and IM30-Venus is termed as IM30-CFP/Venus.

In all experiments, the ratiometric FRET efficiency  $E_{rat}$  was calculated as described below.  $E_{rat}$  is suitable to compare the relative ratios between donor and acceptor peak in a qualitative manner.

### ***Dissociation experiments of IM30-CFP/Venus on liposomes***

In order to investigate the potential IM30 ring dissociation on membranes in presence and absence of  $Mg^{2+}$ , IM30-CFP/Venus ( $\pm Mg^{2+}$ ) was mixed with liposomes of different compositions. Upon ring dissociation, a decrease in  $E_{rat}$  was expected due to the spatial separation of the dyes.

The liposomes preparation was performed as described in 2.17.2 and 2.17.3. IM30-CFP and IM30-Venus were co-purified (see 2.16.1) with a ratio of 27% CFP and 63% Venus. 0.2  $\mu M$  of the labeled IM30 mixture was incubated with an increasing amount of 100% DOPG or 60% MGDG/40% DOPG lipids (0-1000  $\mu M$ ) for  $\sim 2$  h in the presence or absence of 7.5 mM  $MgCl_2$ . For background correction, identical samples, containing IM30 WT instead of the mutant mixtures, were prepared. Furthermore, in order to determine correction factors, control samples were prepared containing 0.2  $\mu M$  of the single-labeled IM30-CFP or IM30-Venus, respectively, in presence of the liposomes or  $MgCl_2$ . For each sample, two spectra were recorded for CFP- or Venus excitation, respectively, using the parameter listed in *Table 2.30*.

**Table 2.30: Parameters used for the dissociation experiments of co-purified IM30 on liposomes**

<b>Parameter</b>	<b>Value for CFP excitation</b>	<b>Value for Venus excitation</b>
Temperature $T$	25 °C	25 °C
Excitation wavelength $\lambda_{ex}$	420 nm	510 nm
Measured wavelength area $\lambda_{em}$	440-700 nm	517-700 nm
Observed wavelength $\lambda_{obs}$	475 nm, 528 nm	528 nm
Slit width	3 nm	2 nm
Measuring steps	1 nm	1 nm
Integration time	0.1 s	0.1 s

For the evaluation, all spectra were corrected for HEPES buffer. The background spectra recorded at CFP excitation, which were obtained from the samples containing IM30 WT, were normalized to the fluorescence intensity at 440 nm of the CFP excited spectra from the samples containing IM30-CFP/Venus. The same factors were then used to normalize the background spectra with Venus excitation, which were recorded from the samples containing IM30 WT, to the fluorescence intensity of 517 nm. After normalizing, all background spectra were subtracted from the sample spectra originating from the IM30-CFP/Venus mixture.

Correction factors were determined from triplicate measurements of IM30-CFP and IM30-Venus, respectively. After background correction, the mean values, including standard deviation as error bars, of the fluorescence intensities at 475 nm and 528 nm for both excitation conditions, were plotted against increasing lipid or  $MgCl_2$  concentrations, respectively. In case of an apparent trend which was also visible in all single measurements, the curve was fitted with a suitable fit function (*cf.* 5.8). From the fit functions, the respective correction factors were calculated.

All sample spectra recorded at Venus excitation were corrected, if necessary, and then normalized to the sample lacking liposomes in order to counterbalance pipetting errors. The same factors were then used to correct the sample spectra recorded at CFP excitation. The resulting spectra were the final FRET spectra.

In order to calculate  $E_{rat}$ , it was necessary to determine the ratio of the CFP emission in the FRET spectra. Therefore, a pure IM30-CFP spectrum was normalized to the fluorescence intensity of 475 nm of the FRET spectra. This step is demonstrated in *Fig. 2.7*.

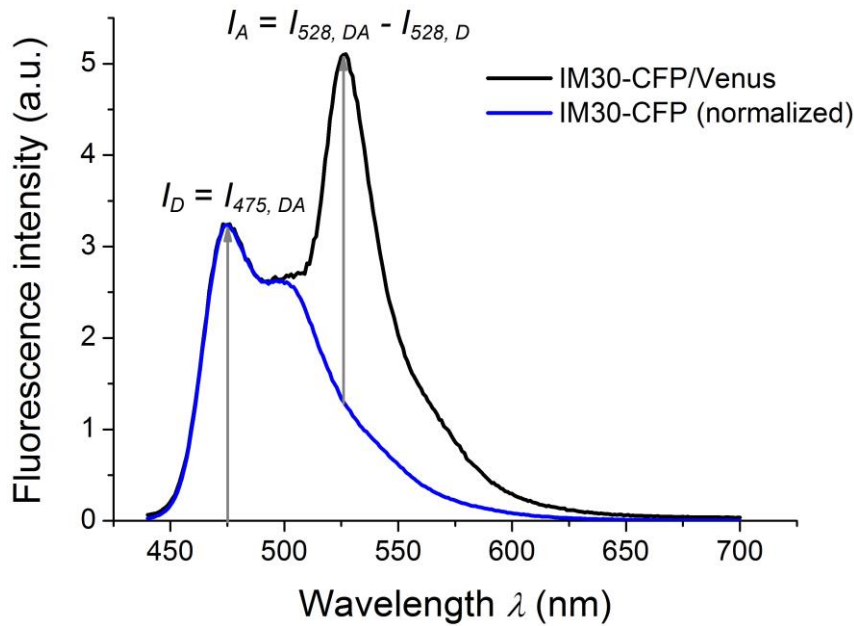


**Fig. 2.7: Evaluation of the final FRET spectra**

Exemplary evaluation of a final FRET spectrum (black curve) is demonstrated. A pure IM30-CFP spectrum (blue curve) is normalized to the fluorescence intensity at 475 nm of the FRET spectrum. The donor intensity  $I_D$  and the acceptor intensity  $I_A$  were calculated as described.

The donor intensity  $I_D$  and the acceptor intensity  $I_A$  from the FRET spectra were then calculated via

$$I_D = I_{475, DA} \tag{Eq. 2.12}$$

and

$$I_A = I_{528, DA} - I_{528, D} \tag{Eq. 2.13}$$

where  $I_{475, DA}$ ,  $I_{528, DA}$  and  $I_{528, D}$  are the respective fluorescence intensities of the FRET spectra (DA) and the normalized donor (D) spectra.  $E_{rat}$  was then calculated as

$$E_{rat} = \frac{1}{1 + \left( \frac{\frac{I_D}{CF_{ex420/em475}}}{\frac{I_A}{CF_{ex420/em528}}} \right)} \quad \text{Eq. 2.14}$$

where  $CF_{ex420/em475}$  and  $CF_{ex420/em528}$  are the correction factors for the donor and the acceptor peaks, respectively (cf. 5.8).

### **Mg<sup>2+</sup> interaction of IM30-CFP and IM30-Venus**

In order to investigate the effect of Mg<sup>2+</sup> on a potential IM30 ring monomer exchange or double-ring formation, IM30-CFP and IM30-Venus were mixed in presence and absence of Mg<sup>2+</sup>. The change of  $E_{rat}$  was observed in equilibrium as well as kinetically.

For equilibrium measurements, samples were prepared containing 1 μM of each labeled protein and 0-25 mM MgCl<sub>2</sub> and were incubated for ~2h. For each sample, two spectra were recorded for CFP- or Venus excitation, respectively, using the parameter listed in *Table 2.31*.

**Table 2.31: Parameters used for the Mg<sup>2+</sup> interaction experiments of separately purified labeled IM30 (equilibrium)**

Parameter	Value for CFP excitation	Value for Venus excitation
Temperature $T$	25 °C	25 °C
Excitation wavelength $\lambda_{ex}$	420 nm	510 nm
Measured wavelength area $\lambda_{em}$	440-700 nm	517-700 nm
Observed wavelength $\lambda_{obs}$	475 nm, 528 nm	528 nm
Slit width	2 nm	1 nm
Measuring steps	1 nm	1 nm
Integration time	0.1 s	0.1 s

The evaluation was performed as described above. Due to the lack of liposomes, no background correction was necessary.

In order to observe the change of  $E_{rat}$  in a time-dependent matter, 1 μM of each labeled protein was mixed in presence or absence of 7.5 mM MgCl<sub>2</sub>. Spectra were recorded after donor excitation in different temporal intervals overnight using the parameters listed in *Table 2.32*.

**Table 2.32: Parameters used for the Mg<sup>2+</sup> interaction experiments of separately purified labeled IM30 (kinetics)**

Parameter	Value
Temperature $T$	25 °C
Excitation wavelength $\lambda_{ex}$	420 nm
Measured wavelength area $\lambda_{em}$	440-700 nm
Observed wavelength $\lambda_{obs}$	475 nm 528 nm
Slit width	2 nm
Measuring steps	1 nm
Integration time	0.1 s

The evaluation was performed as described above, except that, due to the lack of liposomes, no background correction was necessary. Furthermore, for experimental reasons, no spectra for Venus excitation could be recorded. But since the same sample was measured for each time step, normalization in order to correct pipetting errors was not necessary.

To compare the results with an upper limit for  $E_{rat}$ , which would be obtained from a complete protein monomer mixing between differently labeled IM30 rings, a 1  $\mu$ M co-purified IM30-CFP/Venus mixture with a ratio of ~50% CFP and ~50% Venus, simulating a perfect mixture, was measured using the donor excitation wavelength.  $E_{rat}$  was calculated as described above.

### ***Mg<sup>2+</sup> interaction of IM30-CFP/Venus***

In order to further investigate the IM30-Mg<sup>2+</sup> interaction, an IM30-CFP/Venus mixture was prepared (see 2.16.1) with a ratio of 27% CFP and 63% Venus and was measured in presence of different MgCl<sub>2</sub> concentrations.

Samples were prepared containing 0.2  $\mu$ M of IM30-CFP/Venus and 0-15 mM MgCl<sub>2</sub> and were incubated for ~2h. For each sample, two spectra were recorded at CFP- or Venus excitation, respectively, using the parameters listed in *Table 2.33*.

**Table 2.33: Parameters used for the Mg<sup>2+</sup> interaction experiments of co-purified labeled IM30**

<b>Parameter</b>	<b>Value for CFP excitation</b>	<b>Value for Venus excitation</b>
Temperature $T$	25 °C	25 °C
Excitation wavelength $\lambda_{ex}$	420 nm	510 nm
Measured wavelength area $\lambda_{em}$	440-700 nm	517-700 nm
Observed wavelength $\lambda_{obs}$	475 nm, 528 nm	528 nm
Slit width	3 nm	2 nm
Measuring steps	1 nm	1 nm
Integration time	0.1 s	0.1 s

The evaluation was performed as described above. Due to the lack of liposomes, no background correction was necessary.

#### **2.18.2.3 Laurdan fluorescence**

Laurdan fluorescence is often used for the detection of alterations in membrane phases. The fluorophore consists of a hydrophobic tail as well as a polar head group, which has a dipole moment due to a partial charge separation between the 6-carbonyl and the 2-dimethylamino residues. (Sanchez *et al.* 2012)

The Laurdan structure is shown in *Fig. 2.8*.

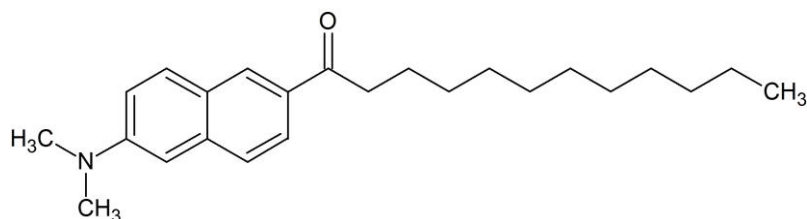


**Fig. 2.8: Structure of Laurdan**

The fluorophore Laurdan consists of a hydrophobic alkyl chain as well as a polar head group, which has a dipole moment due to a charge separation between the 6-carbonyl and the 2-dimethylamino residues.

Laurdan incorporates into the unpolar membrane region of liposomes via its hydrophobic alkyl chain. Due to its chromophoric head group, which is located towards the polar lipid headgroups, it can detect changes in the polarity of the membrane environment via shifting the maximum in the fluorescence emission spectrum from 490 nm to 440 nm (blue shift) or from 440 nm to 490 nm (red shift). This phenomenon can be described by the effect of dipolar relaxation, which is pronounced in polar environments and decreased in unpolar environments. (Winter & Noll 1998; Sanchez *et al.* 2012)

It has already been demonstrated that IM30 binding to liposomes containing negatively charged lipids results in a decreased membrane polarity, which is connected with a loss of water molecules inside the membrane, and can be detected via Laurdan spectroscopy (Suppes 2013). This correlation, which marks Laurdan as a suitable IM30-membrane binding marker, is illustrated in Fig. 2.9.

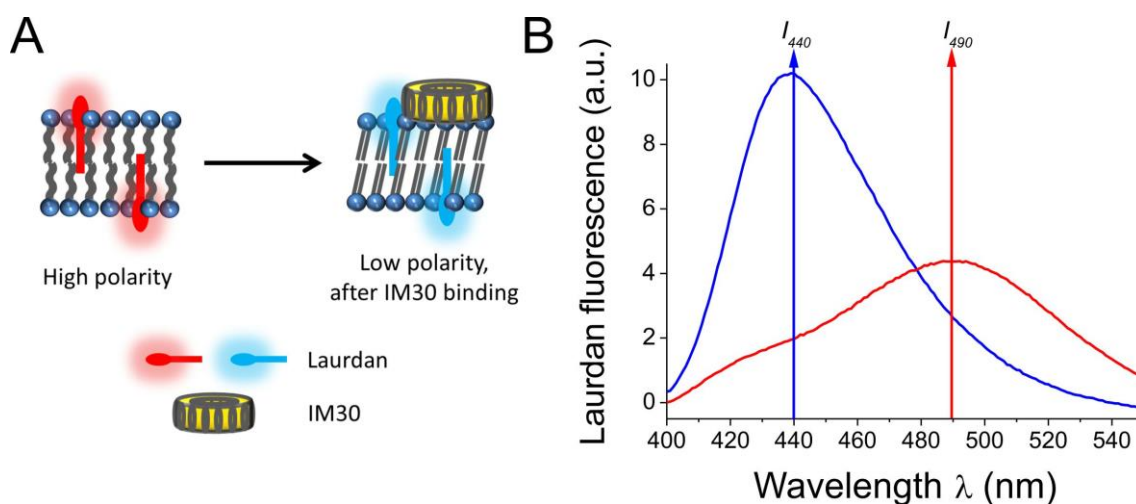


**Fig. 2.9: Blue shift of the Laurdan fluorescence emission spectra upon IM30 membrane binding**

Binding of IM30 to membranes containing negatively charged lipids results in a decrease in the membrane polarity (A). This change can be monitored via a blue shift of the maximum in the Laurdan fluorescence emission spectrum from 490 nm (red curve) to 440 nm (blue curve) (B). The data were obtained from (Suppes 2013).

Shifts in the membrane polarity are quantified via the so-called generalized polarization (GP), which is calculated as

$$\text{Laurdan GP} = \frac{I_{440} - I_{490}}{I_{440} + I_{490}} \quad \text{Eq. 2.15}$$

where  $I_{440}$  and  $I_{490}$  are the fluorescence intensities at 440 and 490 nm, respectively. A GP value between -1 and 0 indicates a high amount of polar membrane areas (liquid-crystalline phases) and a GP value between 0 and 1 is connected to a domination of unpolar membrane areas (gel phases).

### **Laurdan spectra recording**

Laurdan spectra recording has already been established in (Suppes 2013). In general, unilamellar liposomes were prepared as described in 2.17.2 and 2.17.3., except that Laurdan was added in a molar ratio of 1:500 to the lipid mixture prior to solvent evaporation. The desired amount of IM30 was added to the liposomes and the mixture was incubated for ~2 h.

Spectra were recorded using the parameter listed in *Table 2.34*.

**Table 2.34: Parameters used for the Laurdan spectra recording**

<b>Parameter</b>	<b>Value</b>
Temperature $T$	25 °C
Excitation wavelength $\lambda_{ex}$	350 nm
Measured wavelength area $\lambda_{em}$	400-550 nm
Observed wavelength $\lambda_{obs}$	440 nm 490 nm
Slit width	Lipid headgroup interaction: 3 nm $K_D$ determination: 3 nm or 4 nm
Measuring steps	1 nm
Integration time	0.1 s

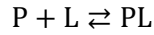
### **IM30 interaction with different lipids, containing negatively charged head groups**

In order to investigate the interaction of IM30 with different lipids, containing negatively charged head groups, liposomes were prepared, containing 80% DOPC and 20% of another lipid of interest, including SQGD, PG and the non-thylakoid lipid DOPS. This composition was chosen to be comparable with similar experiments performed in (Suppes 2013).

0.1 mM of the respective lipid mixture was incubated with 2.5  $\mu$ M IM30 and measured using the parameter listed in *Table 2.34*. The averaged GP values were calculated and normalized to control samples lacking IM30.

### **Membrane binding affinity of IM30 WT and IM30 mutants**

To determine quantitative information concerning the membrane interaction of IM30 and several mutants, a binding assay was developed. This assay is based on the simplified concept that the protein (P) binds to a specific lipid area (L) upon forming a binding complex PL:



The qualitative information of the binding strength is given via the dissociation constant  $K_D$ :

$$K_D = \frac{P \cdot L}{PL} \quad \text{Eq. 2.16}$$

where  $P$ ,  $L$  and  $PL$  are the equilibrium concentrations of the respective components.

An essential condition of this binding assay is the excess of one component (*cf.* 5.13.2). This must be fulfilled during sample preparation. Therefore, 75  $\mu\text{M}$  100% DOPG lipids were incubated with different IM30 WT or IM30 mutant concentrations (0.4-7.0  $\mu\text{M}$ ), in which the protein was assumed to be in excess compared to the available lipid binding area for the following reasons:

- ~50% of the lipids are part of the inner leaflet of the liposomes and therefore not available for binding.
- Not the whole but instead less than ~50% of the outer leaflet membrane area might be suitable for protein binding due to non-perfect packing of multiple proteins. This has been estimated for tightest sphere packing of globular proteins on cylindrical gold nanorods (Pannwitt 2015).
- Several lipids are necessary to form a binding area for the respective protein (*cf.* 5.13.4).

The samples were measured using the parameters listed in *Table 2.34*. The averaged GP values were calculated and plotted against the initial protein concentration  $P_0$ , using the standard deviation as error bars. The resulting binding curve was then fitted via

$$GP = GP_0 + \frac{\Delta GP}{\frac{K_D}{P_0} + 1} \quad \text{Eq. 2.17}$$

where  $GP_0$  is the GP value for 0  $\mu\text{M}$  protein and  $\Delta GP$  is the difference between the initial GP value and the GP value which is reached in the saturation plateau of the binding curve. From the binding fit, the  $K_D$  value was identified. The derivation of the binding fit is described in 5.13.2.

#### **2.18.2.4 Liposome destabilization assay**

The IM30/Mg<sup>2+</sup> mediated membrane fusion mechanism was investigated via a liposome destabilization assay (McIntyre & Sleight 1991; Matsuzaki *et al.* 2000). In principle, liposomes are labeled with the lipid-fluorophore NBD-PE, which is limited in its ability to perform a transverse diffusion inside the membrane. Upon addition of the quencher Na<sub>2</sub>S<sub>2</sub>O<sub>4</sub>, the fluorophores located at the outer liposome leaflets are quenched and the NBD fluorescence decreases to ~50% of the initial fluorescence. A further addition of a potential destabilization component (here: IM30/Mg<sup>2+</sup>) could result in a further decrease of the NBD fluorescence, since also the

fluorophores located at the inner liposome leaflets are quenched due to the induced permeability of the liposomes. If this were not the case, the NBD fluorescence would keep its previous level. The experimental design was developed together with Prof. Nadja Hellmann, the measurements were performed by myself. The experiment is schematically illustrated in *Fig. 2.10*.

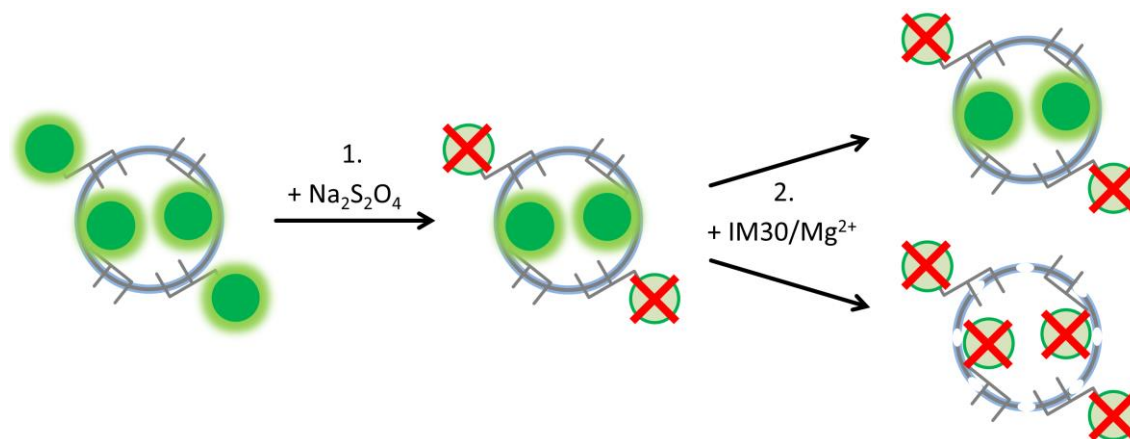


**Fig. 2.10: Liposome destabilization**

For assaying the liposome destabilization, liposomes were labeled with the lipid-fluorophore NBD-PE (green). Upon addition of the quencher  $\text{Na}_2\text{S}_2\text{O}_4$  (1.) the fluorescence decreases to  $\sim 50\%$  since the fluorophore at the outer liposome leaflets are quenched. Further addition of  $\text{IM30}/\text{Mg}^{2+}$  (2.) might result in a membrane destabilization, which would be visible via a further decrease of the NBD fluorescence.

60%/40% MGDG/DOPG unilamellar liposomes, containing NBD-PE in a 1:500 molar ratio, were prepared as described in 2.17.2 and 2.17.3 and sized to 100 nm as described in 2.17.4. The samples always contained 0.15 mM of lipid. A positive control containing 1% (v/v) Triton X-100 was also prepared. Triton X-100 is a detergent which is supposed to disrupt liposomal structures. In order to determine dilution factors, a sample containing only HEPES buffer was prepared. The samples were incubated at 10 °C for 5 min prior to the measurement. Then, the NBD fluorescence was observed, using the parameters listed in *Table 2.35*.

**Table 2.35: Parameters used for the liposome destabilization assay**

Parameter	Value
Temperature $T$	10 °C
Excitation wavelength $\lambda_{ex}$	460 nm
Measured wavelength $\lambda_{em}$	535 nm
Slit width	4 nm
Total measuring time $t_M$	840 s
Time before $\text{Na}_2\text{S}_2\text{O}_4$ addition	120 s
Time before component addition	490 s
Time between points $\Delta t$	1 s

During each measurement, 0.11 M of  $\text{Na}_2\text{S}_2\text{O}_4$  was added after 120 s. Different amounts of IM30 and/or 11 mM  $\text{MgCl}_2$  were added after 490 s. Exceptions were the negative control and the dilution control, in which only HEPES buffer was added. The duration of the addition steps was estimated to be 20 s.

For the evaluation, all curves were corrected for dilution using the NBD fluorescence intensities from the dilution sample before and after the respective addition steps. For normalization, the initial NBD fluorescence of each sample was set as 100%.

### 2.18.2.5 Liposome fusion assay

In order to investigate the membrane fusion ability of IM30 WT and IM30 mutants under different conditions, two different types of liposome fusion assays were performed. In both cases, liposomes were created containing two species of lipid-fluorophores, which were able to form a FRET pair, respectively. Upon fusing with plane liposomes, the lipid-fluorophores are separated due to the enlarged surface, and the FRET efficiency decreases. Two different combinations of donor and acceptor fluorophores were used:

- Green fusion assay: The combination NBD-PE as donor and LissRhod-PE as acceptor was described in (Struck *et al.* 1981) and has already been used in IM30 research (Suppes 2013; Hennig *et al.* 2015).
- Red fusion assay: The combination LissRhod-PE as donor and Atto633-PE as acceptor was specifically developed for fusion assays of IM30-CFP, IM30-Venus and IM30-CFP/Venus.

The respective fluorescence excitation and emission spectra, including the spectral overlap  $J$ , are shown in 5.3.1 and 5.3.2. Illustrations of the two fusion assays are shown in *Fig. 2.11*.

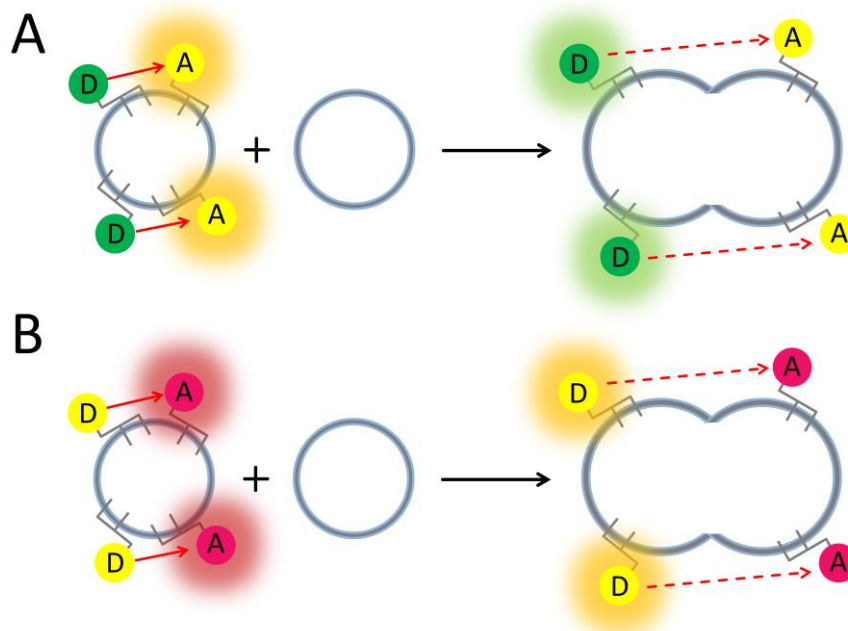


**Fig. 2.11: Liposome fusion assays**

The green fusion assay utilizes NBD-PE and LissRhod-PE as donor and acceptor fluorophores (A), whereas in the red fusion assay LissRhod-PE acts as donor and Atto633-PE as acceptor (B). In both cases, the lipid-fluorophores are part of the same labeled liposomes and can form a FRET pair. Upon fusion with plane liposomes, the lipid-fluorophores are separated from each other due to the enlarged liposome surface, and the FRET efficiency decreases.

The protocol for the fusion assay was developed in (Suppes 2013) and is based on (EncapsulaNanoSciencesLLC 2012). For sample preparation, 3 different liposome types were prepared:

- Labeled liposomes: Liposomes containing a molar fraction of 0.8% of the lipid-fluorophores
- Plane liposomes: Unlabeled liposomes
- Mock-fused liposomes: Liposomes containing a molar fraction of 0.08% of the lipid-fluorophores in order to simulate fused liposomes

If not otherwise mentioned, 60%/40% MGDG/DOPG unilamellar liposomes, containing the respective amount of lipid-fluorophores, were prepared as described in 2.17.2 and 2.17.3 and sized to 100 nm as described in 2.17.4. For sample preparation, labeled and plane liposomes were mixed in a ratio of 1:9 and a total lipid concentration of 0.1 mM. The desired amounts of MgCl<sub>2</sub> and IM30 WT or IM30 mutants were added. Additionally, a negative control containing the same lipid composition but lacking Mg<sup>2+</sup> and protein, as well as a positive control containing the mock-fused liposomes in the same total lipid concentration were prepared (*cf.* 5.3.1 and 5.3.2).

After mixing, the samples were measured immediately by observing the donor fluorescence, using the parameter listed in *Table 2.36*.

**Table 2.36: Parameters used for the liposome fusion assay**

Parameter	Value for green fusion assay	Value for red fusion assay
Temperature $T$	25 °C	25 °C
Excitation wavelength $\lambda_{ex}$	460 nm	560 nm
Measured wavelength $\lambda_{em}$	535 nm	583 nm
Slit width	5 nm	3 nm
Death time $t_D$	12 ± 1 s	12 ± 1 s
Total measuring time $t_M$	1500-2000 s	1500 s
Time between points $\Delta t$	5 s	5 s

If not otherwise mentioned, the recorded curves were evaluated as described in (Suppes 2013). In order to quantify the fusion activity and to eliminate bleaching effects, all samples were normalized setting the negative control as 0% and the positive control as 100% via

$$\text{Fusion} = \frac{I_t - I_{t,0\%}}{I_{t,0\%} - I_{t,100\%}} \quad \text{Eq. 2.18}$$

where  $I_t$  is the donor fluorescence intensity of the samples at time  $t$ ,  $I_{t,0\%}$  is the donor fluorescence intensity of the negative control at time  $t$  and  $I_{t,100\%}$  is the donor fluorescence intensity of the positive control at time  $t$ .

Furthermore, the death time  $t_D$  was estimated to be  $(12 \pm 1)$  s, and this value was added to all time points. For the curves, in which no fusion could be observed, the value at 12 s was used for 0 s as well. All other curves were fitted via an ExpDec2 fit (see 5.13.1.4), and the fusion activity for 0 s was calculated.

In order to reconstruct a starting point, the averaged value from the fusion activities at 0 s  $\overline{I_{t=0}}$  was calculated, and the standard deviation was assumed as the error for the fusion activity. All curves were then normalized to this starting point via

$$I_t = I_{t,raw} - (I_{t=0,raw} - \overline{I_{t=0}}) \quad \text{Eq. 2.19}$$

whereas  $I_{t,raw}$  is the donor fluorescence intensity of the raw data at time  $t$ .

### 2.18.2.6 Tryptophan fluorescence measurements

The intrinsic tryptophan fluorescence of proteins is often used in biophysical assays. In this thesis, the tryptophan fluorescence of IM30, which possesses a single tryptophan (W71) (*cf.* 5.1.1), was used to investigate the hypothetical electrostatic nature of the IM30-membrane interaction. In principle, the protein was pre-incubated with 100% DOPG liposomes, and a titration with increasing NaCl concentration was performed to see whether  $\text{Na}^+$  can remove IM30 from the membrane surface through electrostatic shielding. IM30 dissociation from the membrane might result in changed environment of W71. Since the tryptophan fluorescence depends on the polarity of the surrounding periphery, a shifted tryptophan fluorescence might be observable. The assay was not possible using Laurdan fluorescence (see 2.18.2.3) since  $\text{Na}^+$  ions also influence the membrane polarity.

0.1 mM of the 100% DOPG lipids was incubated with 2.5  $\mu\text{M}$  of IM30 and different NaCl concentrations (0-200 mM). Control samples lacking liposomes were also prepared. The samples were incubated for at least  $\sim 2$  h and then measured using the parameters listed in *Table 2.37*.

**Table 2.37: Parameters used for the replacement assay**

<b>Parameter</b>	<b>Value</b>
Temperature $T$	25 °C
Excitation wavelength $\lambda_{ex}$	300 nm
Measured wavelength area $\lambda_{em}$	310-380 nm
Observed wavelength $\lambda_{obs}$	333 nm
Slit width	4 nm
Measuring steps	1 nm
Integration time	0.1 s

For evaluation, the averaged tryptophan fluorescence at 333 nm was plotted against the increasing  $\text{Na}^+$  concentration. Subsequently, the difference between the values of samples containing

liposomes and samples lacking liposomes was calculated. The error was determined via Gaussian error distribution.

### **2.18.3 Laser-induced liquid bead ion desorption mass spectrometry (LILBID-MS)**

Laser-induced liquid bead ion desorption mass spectrometry (LILBID-MS) is a native mass spectrometry method. Here, micro-droplets are irradiated by IR-laser pulses in a vacuum. The droplets can then emit charged biomolecules that can be analyzed via MS. The advantage of this soft method compared to other MS settings is the suitability for investigations of noncovalently bonded biomolecule complexes (Morgner *et al.* 2006).

Samples used in the experiments contained 18  $\mu\text{M}$  of IM30 and 5% glycerol. Sample preparation was done by myself. The LILBID-MS measurements were performed by Phoebe Young. Design and setting were used as described in (Morgner *et al.* 2006) in an in-house built instrument. Evaluation was performed by Phoebe Young as described in (Morgner & Robinson 2012).

### **2.18.4 Isothermal titration calorimetry (ITC)**

Isothermal titration calorimetry (ITC) is used to describe thermodynamic parameters in molecular interaction (*e.g.* protein-ligand) reactions. Two identical cells (the sample- and the reference cell) in a heat bath are surrounded by an adiabatic mantle. When the heat in the sample cell changes due to addition of a component, the heat rate  $\Delta P$  necessary to counterbalance the temperature difference between the two cells is measured.

Here, ITC was performed to study the IM30- $\text{Mg}^{2+}$  interactions. In a standard ITC measurement, the ligand is titrated into the protein solution, which was investigated in cooperation with Svenja Winzen in pre-experiments (not shown in this thesis). The other way around is called reverse ITC (Grossoehme *et al.* 2010) and was used in the measurement due to the huge dilution heat of  $\text{Mg}^{2+}$  in aqueous solutions. The main reverse ITC experiment using IM30 WT was mainly performed and evaluated by Prof. Nadja Hellmann and Benedikt Junglas, whereas I was advising and supervising Benedikt in the framework of his master thesis.

The experimental set-up is schematically shown in *Fig. 2.12*.

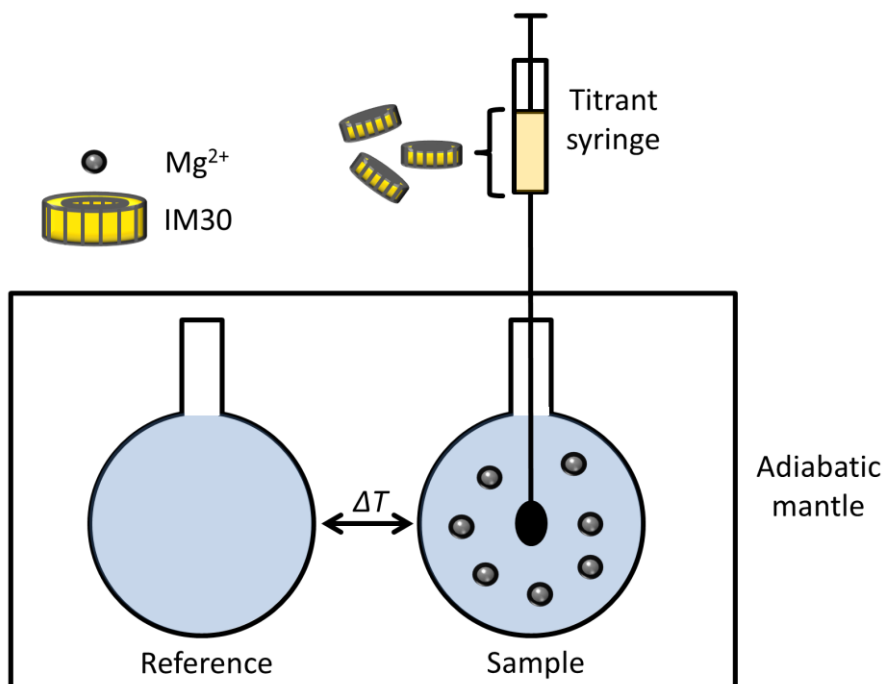


**Fig. 2.12: Reverse ITC**

In a reverse ITC, the ligand (here: Mg<sup>2+</sup>) is provided in the sample cell and the protein is the titrant. Upon an intermolecular interaction, the heat in the sample cell changes and is readjusted to the reference cell. The heat rate  $\Delta P$  is measured and converted into the enthalpy change  $\Delta H$ .

Differently concentrated MgCl<sub>2</sub> solutions (0-100 mM) were filled into the sample cell, respectively, and a 20  $\mu$ M IM30 solution was in the titrant syringe. The reference cell was filled with buffer. All solutions were degassed for 5 min and precooled to 19.7 °C. Prior to each injection, 2  $\mu$ l test volume was added to remove potential air bubbles and diluted protein in the syringe tip. Then, 30  $\mu$ l was injected three times and  $\Delta P$  was measured. For the measurement, the following parameters were chosen:

**Table 2.38: Parameters used for the ITC measurement**

Parameter	Value
Temperature $T$	20 °C
Stirring speed	199 rpm
Reference heat rate $P$	20 $\mu$ cal/s
Equilibration	Automatic and fast
Feedback	high
Measuring time $t_M$	40 s
Time between measurements	210-260 s

With the help of the MicroCal VP-ITC Microcalorimeter instrument software, a baseline was created, and the area below the  $\Delta P$  peaks was determined as enthalpy change  $\Delta H$  and then normalized to the molar ratio  $N$  between protein and ligand  $n_{Protein}/n_{Ligand}$ . From the three data points, the averaged value could be calculated due to the insignificant protein dilution. The procedure was repeated at different Mg<sup>2+</sup> concentrations in the sample cell in order to obtain a

binding curve for the IM30-Mg<sup>2+</sup> interaction. An exemplary measurement for 10 mM MgCl<sub>2</sub> is shown in *Fig. 2.13*.

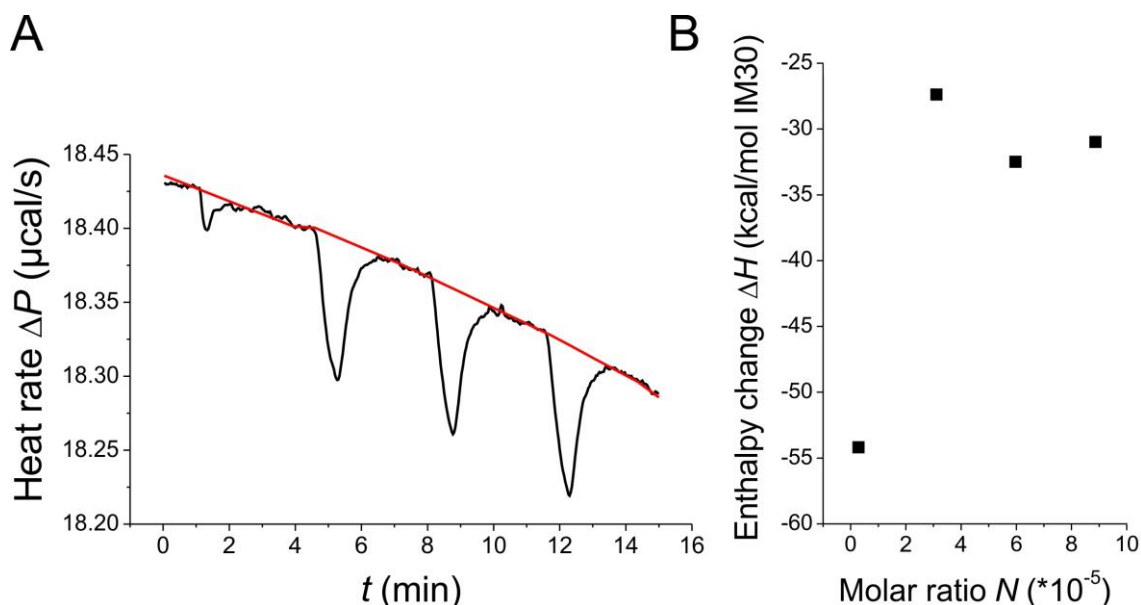


**Fig. 2.13: Exemplary ITC measurement**

A typical ITC measurement is shown for 10 mM MgCl<sub>2</sub> in the sample cell. The heat rate was measured after addition of 2  $\mu$ l and three times 30  $\mu$ l of protein solution, respectively (A). The baseline is shown in red. After integrating the area between heat rate peaks and baseline, the enthalpy change was normalized to the molar ratio  $N$  (B). In cooperation with Prof. Nadja Hellmann and Benedikt Junglas.

Furthermore, it was necessary to consider the dilution enthalpy of the MgCl<sub>2</sub> solution. Thus, correction measurements were performed by injecting only buffer into the MgCl<sub>2</sub> solution. After fitting the data with a Logistic fit (*cf.* 5.13.1.5), the obtained baseline could be subtracted from the main measurements.

Additionally, the enthalpy effect of unspecific cation binding was measured by titrating IM30 to a NaCl solution. Also in this case, the dilution enthalpy needed to be considered. Thus, the data were fitted with a parabolic fit (*cf.* 5.13.1.8) and the obtained baseline subtracted from the correction measurement. The calculated data were then fitted with a hyperbolic fit (*cf.* 5.13.1.7), from which the respective points for the main measurement were calculated and subtracted. The fit functions were chosen based on good empirical matching.

After subtracting the data belonging to the mentioned effects (in due consideration of the cation equivalent concentrations, respectively), the obtained binding curve for the IM30-Mg<sup>2+</sup> interaction was fitted with a binding fit (*cf.* 2.18.2.3 and 5.13.1.1) from which the dissociation constant  $K_D$  was calculated.

Additional corrections to compensate for the dilution enthalpy of IM30 and the buffer protonation enthalpy were recorded by Benedikt Junglas (independent from his supervised master thesis) and found to be insignificant for the  $K_D$  determination (*cf.* (Heidrich *et al.* 2018)).

### 2.18.5 Single particle tracking (SPT)

Single particle tracking (SPT) can be used to observe the movement of individual particles, *e.g.* liposomes. A requirement for using this method is the visibility of such particles, for instance via fluorescence labeling. The fluctuation can then be observed via fluorescence microscopy. Due to the laws of Brownian motion, the observed movement is correlated to the diffusion coefficient and the size of the particles. In this thesis, SPT was performed to find a further confirmation of IM30/Mg<sup>2+</sup>-mediated membrane fusion. Thus, upon addition of IM30/Mg<sup>2+</sup>, the motion of the liposomes was expected to change due to a size increase. The experiment was performed in cooperation with Prof. Nadja Hellmann.

60%/40% MGDG/DOPG unilamellar liposomes containing the lipid-fluorophore LissRhod-PE in a molar ratio of 1:500 were prepared as described in 2.17.2 and 2.17.3 and sized to 100 nm as described in 2.17.4. A reaction sample was prepared by mixing 0.15 mM of lipids with 1.3  $\mu$ M of IM30 and 7.5 mM of MgCl<sub>2</sub>. A control sample lacking IM30 was also prepared. After the respective reaction time, a 10  $\mu$ l sample from the reaction sample was extracted and diluted 1:2000 into HEPES buffer in order to stop the reaction. The particle size distribution was then determined via SPT based on the fluorescence signal using the parameters listed in *Table 2.39*.

*Table 2.39: Parameters used for the SPT measurements*

Parameter	Value
Temperature $T$	23 °C
Excitation wavelength $\lambda_{ex}$	532 nm
Emission filter (long-pass) wavelength $\lambda_{em}$	565 nm
Measuring time $t_M$	30 s
Repeats	10

Subsequently, the average size distribution was calculated by the instrument software. The final evaluation was performed by Prof. Nadja Hellmann by normalizing the particle size distribution to the particle concentration.

### 2.18.6 Surface plasmon resonance (SPR)

In metals, free electrons can be described as an electron liquid of high density, also called plasma. At the metal surface, fluctuations of such a liquid upon interaction with an electric field are called surface plasmon. In other words, a surface plasmon is characterized as a surface charge density wave at a metal surface. If the wave vector of the incoming  $p$ -polarized electric field  $k_0$  equals the wave vector of the surface plasmon  $k_{sp}$ , a total resonance coupling, the surface plasmon resonance (SPR), is induced and the light is completely absorbed (Winter & Noll 1998):

$$k_0 = k_{sp}$$

*Eq. 2.20*

$$\frac{\omega}{c} \sqrt{\frac{\varepsilon_m(\lambda) \varepsilon_s(\lambda)}{\varepsilon_m(\lambda) + \varepsilon_s(\lambda)}} = \frac{\omega}{c} \sqrt{\varepsilon_p} \sin \theta \quad \text{Eq. 2.21}$$

Here,  $\omega$  is the light frequency,  $c$  is the speed of light,  $\varepsilon_m$ ,  $\varepsilon_s$  and  $\varepsilon_p$  are the dielectric constants of the metal, the surrounding media and the prism, respectively, and  $\theta$  is the incident angle of the light.  $k_{sp}$  depends on the refractive index of the metal, which shifts upon binding of material at the metal surface. This shift can indirectly be measured by observing the incident angle of the light  $\theta_{SPR}$  at which a surface plasmon resonance appears. Thus, with SPR measurements it is possible to observe biomolecular interactions at liquid-solid interfaces.

A typical SPR scan measurement is shown in *Fig. 2.14*.

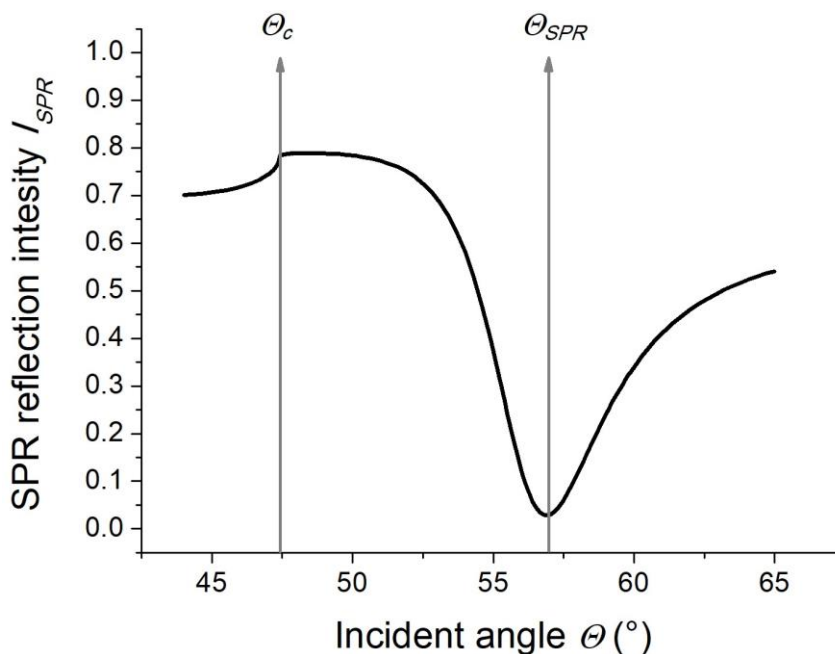


**Fig. 2.14: Typical SPR scan measurement**

A typical SPR spectrum of Cr/Au coated LaSFN9 glass exposed to HEPES buffer is shown. At the critical incident angle  $\theta_c$ , the light is totally reflected, whereas at the incident angle of plasmon resonance  $\theta_{SPR}$ , the light is completely absorbed by the surface electrons. In cooperation with Prof. Tobias Weidner and Bernhard Menges.

In this thesis, SPR measurements were performed to investigate the interaction of IM30 with a negatively charged surface in presence and absence of  $Mg^{2+}$ . As the negatively charged surface, the thiol-coupled fatty acid 16-MHDA was provided. The measurements were performed in cooperation with Prof. Tobias Weidner and Bernhard Menges. The experimental set-up is schematically shown in *Fig. 2.15*.

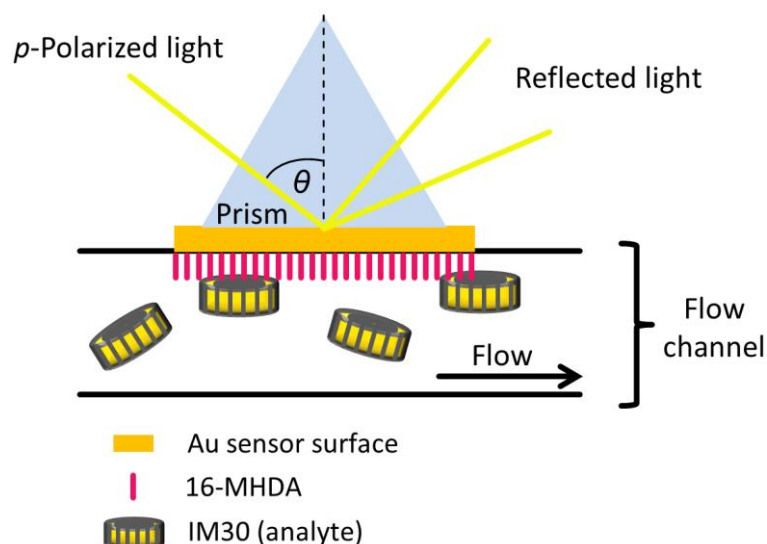


**Fig. 2.15: SPR**

In an SPR measurement, *p*-polarized light impacts on a prism, which is attached to a LaSFN9 sensor chip loaded with layers of Cr and Au. Upon addition of other components (here: 16-MHDA and IM30) through the flow channel, the refractive index of the sensor chip changes, resulting in a shifted  $\theta_{SPR}$ .

For the SPR experiments, LaSFN9 glass plates were used as sensor chips. Prior to usage, they needed to be cleaned and coated with Au/Cr layers. Thus, the plates were purged 5-6 times with ddH<sub>2</sub>O and gently rubbed with dishwashing detergent. Afterwards, the glass plates were again rinsed with ddH<sub>2</sub>O for 10 times, then placed in Hellmanex II solution and sonificated in an ultrasonic cleaner for 25 min. Subsequently, the plates were rinsed with ddH<sub>2</sub>O 10 times and then thoroughly rinsed in isopropyl alcohol. After drying, the clean LaSFN9 plates were placed in a vacuum coater and coated with a Cr layer of ~2 nm and a Au layer of ~50 nm.

The measurement was carried out in an in-house built SPR instrument, equipped with a HeNe-Laser, using the Kretschmann configuration (Kretschmann 1972). The sensor chips were attached to an LaSFN9 prism via index matching immersion oil and fixated on a microfluidic cell. Solutions were pumped into the cell using a peristaltic pump. Gradually, components were added to the sensor chip:

- HEPES buffer
- 350 mM 16-MHDA in a 2/1 (v/v) chloroform/methanol solution
- 3.12  $\mu$ M IM30  $\pm$  10 mM MgCl<sub>2</sub>

The addition of the single components was usually observed kinetically, choosing an incident angle  $\theta$  at ~30% of SPR reflection intensity  $I_{SPR}$ . After addition of each component, a scan measurement was performed, respectively, if not otherwise mentioned. The measurements were carried out using the parameters listed in *Table 2.40*.

**Table 2.40: Parameters used for the SPR measurements**

Parameter	Value
Temperature $T$	RT
Laser wavelength $\lambda$	633 nm
Incident angle $\theta$ area for scan measurements	44-65°
Pump speed for kinetic measurements	40 $\mu$ l/min

In order to estimate the layer thicknesses, the scan measurements were evaluated by using the program Winspall 2.20. With a combination of manual and iterative fitting, the parameters for the fit were adapted to the scan curves. Here, the real and imaginary parts of the respective dielectric constants,  $\epsilon_{real}$  and  $\epsilon_{img}$ , were considered. The values listed in *Table 2.41* were used as initial values.

**Table 2.41: Initial fitting parameters used for SPR scan measurements**

Layer	Thickness (nm)	$\epsilon_{real}$	$\epsilon_{img}$
LaSFN9 prism	0*	3.4036	0
Cr	2	-6.3	18
Au	50	-12.3	1.29
16-MHDA	2	2.1	0
IM30 $\pm$ Mg <sup>2+</sup>	7	2.1	0
HEPES buffer	0*	1.778	0

\*0 nm stands for infinite.

Importantly, the parameters were kept constant after fitting one layer, and only the parameters for the new layer were adjusted. The surface coverage for 16-MHDA and IM30 was then calculated via

$$\text{Surface coverage} = \frac{\text{Thickness layer}}{\text{Thickness molecule}} \quad \text{Eq. 2.22}$$

### 2.18.7 Transmission electron microscopy (TEM)

With transmission electron microscopy (TEM), protein structures can be made visible. Electrons are accelerated and focused via magnetic lenses. Upon interaction with material-rich areas of the fixated sample, some of the electrons are scattered. The remaining electrons can pass the sample and can be displayed on a screen by further focusing. In order to increase the contrast, the sample can be treated with a heavy metal solution, *e.g.* uranyl acetate. The uranyl cations are then supposed to arrange around the proteins. The electrons are scattered more strongly at heavy metals, resulting in a higher contrast due to the brightening of the protein structures, which is called negative staining. (Winter & Noll 1998)

The structure of IM30 WT and several IM30 mutants were examined under different conditions. The sample design and biochemical preparation was done by myself. Some of the experiments were also performed in cooperation with Benedikt Junglas or Carmen Siebenaller. The sample

fixation and negative staining for TEM and measurements were performed by Kristiane Rusitzka or Wolfgang Gebauer.

The concentration of the analyzed protein samples was ~0.1-0.2 mg/ml. 3 mm copper grids, coated with graphene, were hydrophilized/negatively charged via glow discharge and stripped through 5  $\mu$ l droplets of the respective sample. The grids were air-dried, and the step was repeated with ddH<sub>2</sub>O and a heavy metal solution of 2% (v/v) uranyl acetate, pH 2.0, for negative staining. The sample grids were measured with an electron microscope afterwards or stored under vacuum.

## 3 Results

The IM30 protein has been linked to thylakoid membrane biogenesis for more than 20 years (Li *et al.* 1994). Due to *in vivo* experiments in the last fifteen years, several putative functions for IM30 have been suggested (see 1.4.5). Only recently, we could demonstrate via biophysical *in vitro* approaches that the protein mediates membrane fusion in presence of  $Mg^{2+}$  (Suppes 2013; Hennig *et al.* 2015).

The goal of this PhD thesis was the investigation of the IM30 interactions and fusion function and, if possible, developing a model for the events during the IM30-mediated membrane fusion (*cf.* 1.5). To do so, *in vitro* experiments were performed exclusively. Since *in vivo* all processes and events are impossible to separate, the *in vitro* approach has an advantage over *in vivo* experiments: the isolation of interactions of interest. In the following, investigations of the IM30 oligomerization and interactions with  $Mg^{2+}$  and membranes are described.

### 3.1 Expression and purification of IM30 and the mutants $\Delta$ CT, C4 and C7

All proteins used in this thesis were heterologously expressed in *E. coli* as described in 2.15.4.

#### 3.1.1 Introduction of the used IM30 mutants

In addition to the IM30 WT, three further IM30 mutants were used for several experiments:

- IM30  $\Delta$ CT ( $\Delta$ CT):  $\Delta$ CT is a mutant lacking the C-terminal seventh helix and the linker region between helix 6 and helix 7.  $\Delta$ CT has been shown to behave similarly to the WT concerning the membrane fusion activity and structure, except that the double-ring formation is dramatically enhanced (Hennig 2014).
- IM30 C4 (C4): The mutation of C4 is a highly conserved amino acid cluster at the loop 2 region. C4 mainly forms rings and is not able to perform membrane fusion (Hennig 2014).
- IM30 C7 (C7): The mutation of C7 is a highly conserved amino acid cluster in helix 4. This mutant has been demonstrated to form smaller IM30 particles and no rings (Hennig 2014). The smaller particles are assumed to be tetramers (Heidrich *et al.* 2016). Furthermore, the fusion function of C7 is impaired (Hennig 2014).

The respective positions of the cluster mutations of  $\Delta$ CT, C4 and C7 are schematically shown in *Fig. 3.1*.

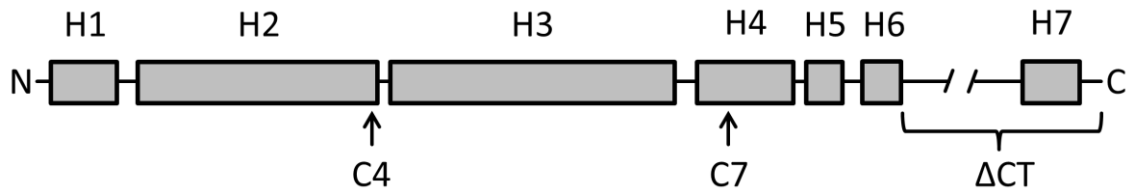


**Fig. 3.1: Positions of cluster mutations in the IM30 secondary structure**

The IM30 mutants used in this thesis are indicated in a schematic representation of the IM30 secondary structure.

The primary structures of the IM30 mutants with indications of the mutated amino acids can be found in 5.1.3, 5.1.4 and 5.1.5, respectively.

### 3.1.2 Expression and purification of IM30 and the used IM30 mutants

Expression and purification of the IM30 WT and the above-mentioned set of IM30 mutants has already been established in previous work (Fuhrmann 2010; Hennig 2014) and is described in detail in 2.15.4, 2.15.5 and 2.16.1. To confirm whether IM30 and the mutants  $\Delta$ CT, C4 and C7 were successfully expressed and purified, SDS-PAGE and immunoblot analysis using the  $\alpha$ Vipp420 antibody were performed as described in 2.16.3 and 2.16.4 and are shown in *Fig. 3.2*.

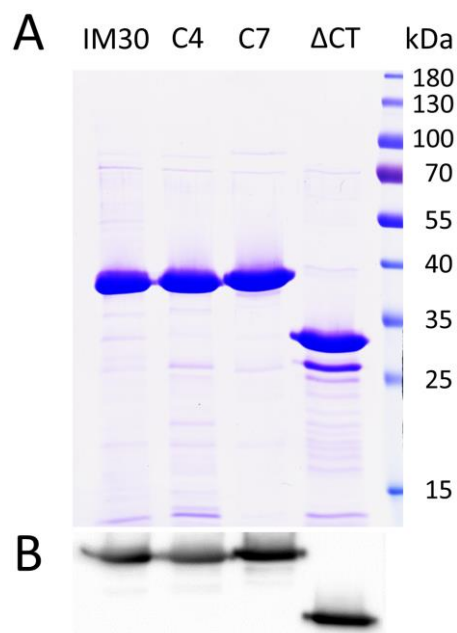


**Fig. 3.2: Purification of IM30, C4, C7 and  $\Delta$ CT**

Expression and successful purification of IM30 WT and IM30 mutants were confirmed on 12% SDS gels (A) and in an immunoblot analysis using the  $\alpha$ Vipp420 antibody (B).

All lanes in *Fig. 3.2* contain one significant band, representing the respective protein. For an unknown reason, IM30 and the IM30 mutants with a similar size (as C4 and C7) ran at a molecular weight at  $\sim$ 37 kDa in SDS gels, instead of the expected molecular weight at  $\sim$ 32 kDa. This

phenomenon might be accredited to structural properties of IM30. Anyway, as can be seen in several other theses and publications, this behavior seems to be usual (Fuhrmann *et al.* 2009a; Otters 2011; Hennig 2014). Since the C-terminal  $\alpha$ -helix and the linker region between helix 6 and helix 7 is lacking, the gel band for  $\Delta$ CT is found at a lower molecular weight at  $\sim$ 30 kDa. The slightly weaker band above 25 kDa found in the lane containing the  $\Delta$ CT sample is an unknown degradation product, which has already been observed in former work (Hennig 2014).

Additionally, in cooperation with Kristiane Rusitzka and Benedikt Junglas, TEM was performed as described in 2.18.7 to check the structure of the IM30 WT (Fig. 3.3).

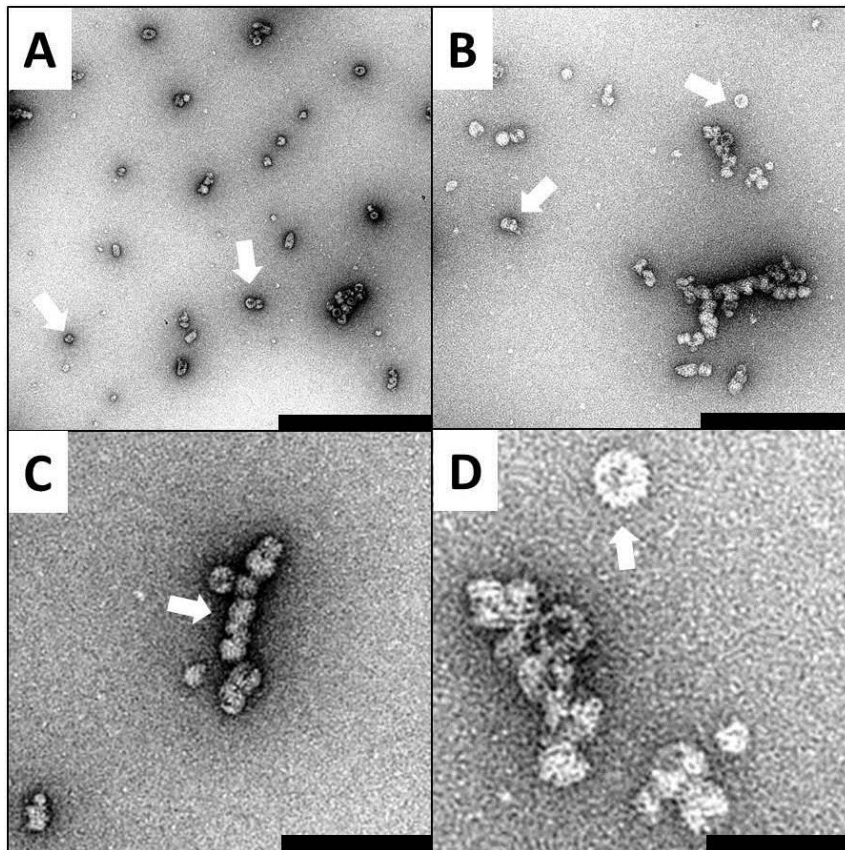


**Fig. 3.3: TEM micrographs of IM30**

Representative TEM micrographs of IM30 samples are shown. Arrows indicate rings. Scale bars represent 500 nm (A, B), 167 nm (C) and 125 nm (D). In cooperation with Kristiane Rusitzka and Benedikt Junglas.

The micrographs revealed an overall significant appearance of oligomeric ring structures, which is in perfect agreement with previous results (Fuhrmann 2010). Further representative micrographs of  $\Delta$ CT, C4 and C7 were already shown in (Hennig 2014).

Altogether, the controls indicated a regular expression and structural arrangement of IM30 WT and the IM30 mutants. Thus, the proteins purified for this thesis were used without any further reservations.

### 3.1.3 Phosphorylation of IM30

Several SDS-PAGEs in which IM30 samples were loaded tended to exhibit a second and less intense band above the main IM30 band (*cf.* Fig. 3.2, Fig. 3.9, Fig. 3.12, Fig. 3.18, Fig. 3.26, Fig. 3.31 and Fig. 3.32). This band was thought to represent a phosphorylated version of IM30, which was included in purified samples as an artefact from the expression in *E. coli*. To confirm a phosphorylation of the protein, dephosphorylation of IM30 was performed using the phosphatase CIP, as described in 2.16.10, to see whether the additional band in the SDS gel disappears when plotting the sample. Furthermore, to exclude the possibility of lipid binding to IM30, which would have biased the experiment due to a dephosphorylation of the lipids, a control experiment, using the lipase TLL, was performed. TLL can digest lipids and thus, the additional band in the SDS-PAGE would have disappeared in case of single lipid binding, which must also be accessible for the lipase. The results are shown in Fig. 3.4.

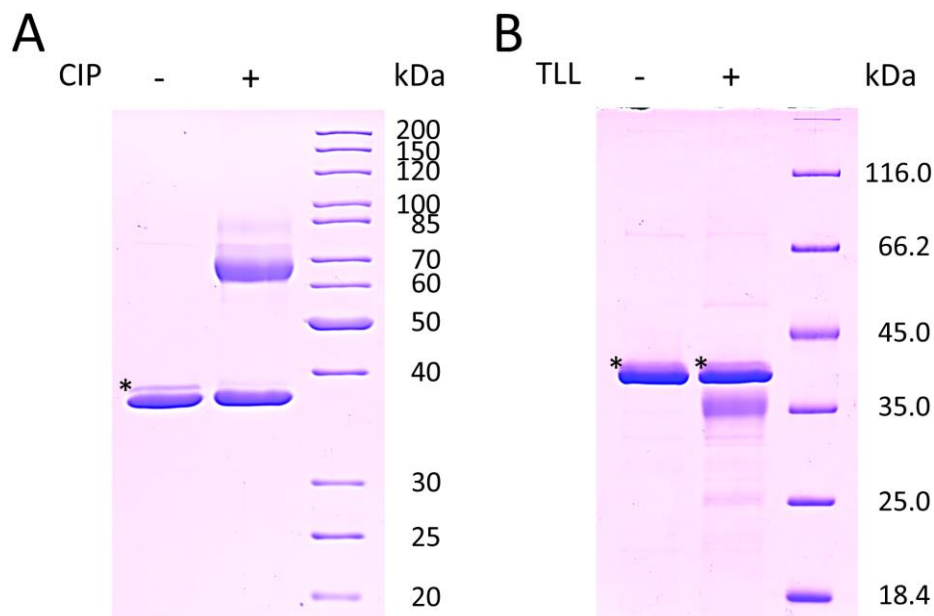


**Fig. 3.4: Dephosphorylation of IM30**

To investigate a phosphorylation of IM30, dephosphorylation was performed using the phosphatase CIP (A). To exclude the possibility of single lipid binding to IM30, which would have biased the experiment due to a dephosphorylation of the lipids, a control experiment using TLL was performed (B). Here, hypothetical lipids could be digested. In both experiments, the samples were separated on 12% SDS gels. The CIP band in (A) can be found below 70 kDa and the TLL band in (B) can be found at ~35 kDa. The bands which might represent the phosphorylated IM30 are indicated (\*).

In the SDS gel shown in Fig. 3.4A, the band for the phosphorylated IM30 is not visible anymore upon CIP addition. This result indicates the existence of phosphorylated IM30 originating from the heterologous protein expression in *E. coli*. Importantly, as can be seen in the experiment shown in Fig. 3.4B, incubating the protein with the lipase TLL, did not seem to influence the band above the IM30 main band. Thus, the additional IM30 band probably did not originate from IM30-bound lipids. However, there is still the possibility that potentially bound lipids were not available for TLL.

### 3.2 The basic building block of IM30 rings

In a recent publication, it has been indicated that the C7 mutant forms tetramers rather than rings (Heidrich *et al.* 2016). The IM30 WT, however, is known for forming huge ring oligomers and rod-like structures. There is little information concerning the complexity of lower-ordered oligomers. Given the observation that the IM30 rings are highly symmetrical, it appears likely that the WT ring assembles from a common building block, which was suggested to be a tetramer or a dimer of dimers in the past (Aseeva *et al.* 2004; Fuhrmann *et al.* 2009a; Bultema *et al.* 2010). In fact, only modelling four monomers, for which the tertiary structure was predicted based on a PspA crystal structure of the first three N-terminal  $\alpha$ -helices (Osadnik *et al.* 2015), as tetramer building blocks into ring spikes resulted in a proper filling of the electron density (Saur *et al.* 2017). Nevertheless, no distinct experimental observation of IM30 WT dimer and/or tetramer formation has been shown so far.

In order to resolve the basic building block of IM30 rings, LILBID-MS was performed for the IM30 WT in cooperation with Phoebe Young as described in 2.18.3. LILBID-MS is a native mass spectrometry method and suitable for investigations of noncovalently bonded biomolecule complexes. The mass spectrum is shown in Fig. 3.5.

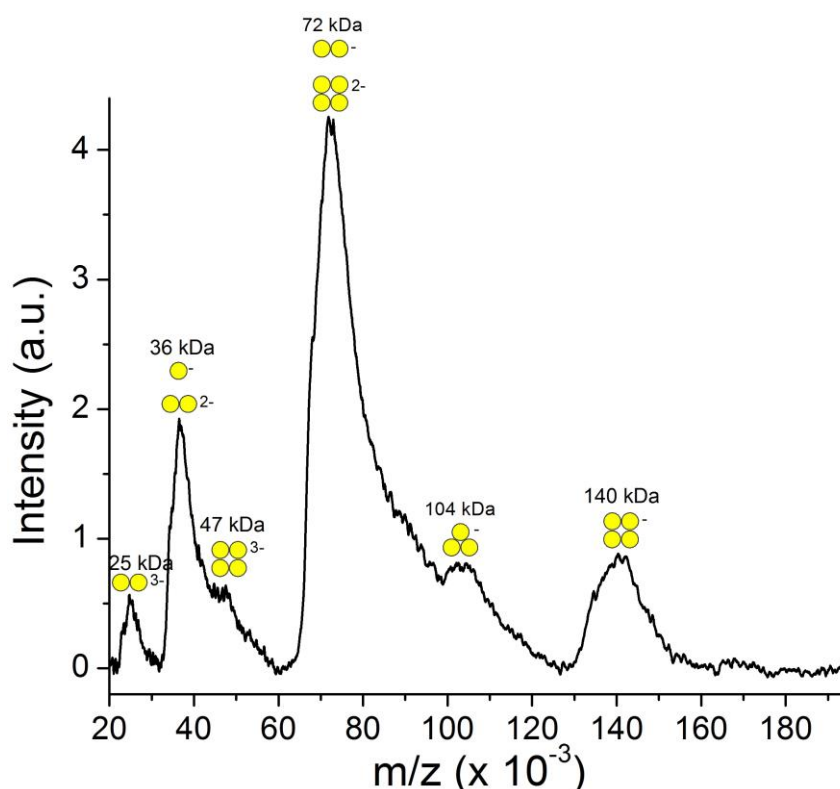


Fig. 3.5: LILBID-MS of IM30

Native mass spectrometry of IM30 low-mass complexes indicated the presence of IM30 monomers, dimers, tetramers and potentially trimers. Oligomerization states including their respective charges are indicated (yellow circles). In the case of a spectral overlap, both species are indicated. In cooperation with Phoebe Young. The results in this figure are published in (Saur *et al.* 2017).

IM30 monomers, dimers, trimers and tetramers could be identified in the mass spectrum, as indicated in *Fig. 3.5*. Compared to the other species, the trimer fraction appeared rather small, which supports the idea of a preference of IM30 for dimer and tetramer formation. Additionally, pentamer oligomerizations of IM30 seemed to be absent, further dismissing the idea of a random association of the monomers. To a greater extent, stable dimer and tetramer oligomers were identified, supporting the model of dimer-dimer formation as the smallest IM30 ring building block.

It must be mentioned that for experimental reasons, the concentration of IM30 in this experiment was not more than 18  $\mu\text{M}$ . The ring concentration in this case would have been only 0.3  $\mu\text{M}$  (for a ring with 15 spikes and  $15 \times 4$  monomers), if nearly all protein was oligomerized as shown in (Fuhrmann *et al.* 2009a; Heidrich *et al.* 2016). Since the detection limit of LILBID-MS is 1  $\mu\text{M}$ , no further structures of higher masses were detected.

Overall, it could be indicated that IM30 monomers prefer to oligomerize into dimers and tetramers instead of trimers, pentamers or other random monomer associations. Thus, the tetramer formation might indeed base on a dimer-dimer complex formation. These findings are important for further structural simulations and investigations on the IM30 oligomerization.

### 3.3 Interaction of IM30 with $\text{Mg}^{2+}$

Recently, the ability of IM30 to perform membrane fusion *in vitro* has been observed in different experiments (Suppes 2013; Hennig *et al.* 2015). Interestingly, IM30 possesses its membrane fusion ability only in presence of  $\text{Mg}^{2+}$ . The ion is important in light-dependent processes involved in photosynthesis (Portis & Heldt 1976; Ishijima *et al.* 2003). In fact, an increasing  $\text{Mg}^{2+}$  concentration in the cyanobacterial cytosol and the plant stroma seems to regulate several proteins (Portis *et al.* 1977; Portis 1981; Portis 1992). Since  $\text{Mg}^{2+}$  is also known to aggregate liposomes (Leventis *et al.* 1986), the question arises how  $\text{Mg}^{2+}$  is involved in the IM30-mediated membrane fusion. A solely  $\text{Mg}^{2+}$ -activated fusion due to aggregation of liposomes was previously excluded via adjusting liposome composition and curvature (Suppes 2013; Hennig *et al.* 2015). Thus, it may be concluded that IM30 interacts with  $\text{Mg}^{2+}$ .

One of the goals of this thesis was to identify a potential IM30- $\text{Mg}^{2+}$  interaction. Furthermore, the effects of this interaction on IM30 concerning structure stability, structure flexibility, double-ring formation and/or monomer exchange between IM30 rings were investigated.

### 3.3.1 $Mg^{2+}$ binds to IM30

In order to investigate a potential binding of  $Mg^{2+}$  to IM30, ANS experiments were performed as described in 2.18.2.1. ANS is able to bind to hydrophobic and polar areas of proteins and changes its fluorescence emission spectrum in unpolar environments due to the lack of dipolar relaxation. Thus, the experiments had a more indirect nature, since ANS only detects changes in the surface structure of the protein, which might result from  $Mg^{2+}$  binding.

IM30 samples were incubated with ANS and different  $MgCl_2$  concentrations between 0 and 10 mM. Control samples lacking IM30 were prepared to evaluate the influence of  $Mg^{2+}$  on the ANS fluorescence. ANS spectra were recorded and are shown in *Fig. 3.6*.

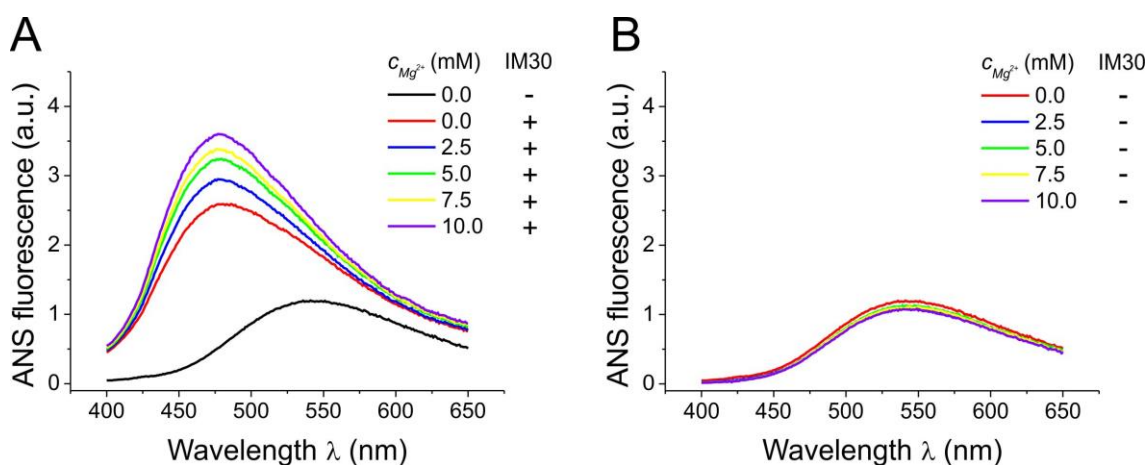


**Fig. 3.6:** ANS spectra of IM30 in presence and absence of  $Mg^{2+}$

Shown are ANS spectra of IM30 samples, incubated with different  $MgCl_2$  concentrations (A) and control spectra from samples lacking IM30 to exclude an influence of  $Mg^{2+}$  on ANS fluorescence (B). The experiment was repeated three times.

In presence of IM30, addition of  $Mg^{2+}$  was coupled with an increased ANS fluorescence (*Fig. 3.6 A*), indicating exposure of hydrophobic surfaces at increased  $Mg^{2+}$  concentrations. This observation strongly supports the idea of  $Mg^{2+}$  binding to IM30, followed by a structural rearrangement, whereat a greater amount of unpolar surfaces is exposed. Essentially, the ANS fluorescence was not affected by  $Mg^{2+}$  (*Fig. 3.6 B*), which indicated that the observed effect (*Fig. 3.6 A*) can be completely ascribed to IM30.

The interaction of IM30 with  $Mg^{2+}$  seemed to directly affect the ANS fluorescence emission. To further quantify the observations from the experiments and to calculate a dissociation constant  $K_D$  for the interaction, titration curves with more measuring points were recorded as described in 2.18.2.1. Differently concentrated IM30 solutions, which were previously incubated with ANS, were titrated with  $MgCl_2$  solutions, and the change in the ANS fluorescence emission at 490 nm was monitored. Different IM30 stocks titrated with the same  $Mg^{2+}$  stock and the same IM30 stock titrated with different  $Mg^{2+}$  stocks were compared. The results are shown in *Fig. 3.7*.

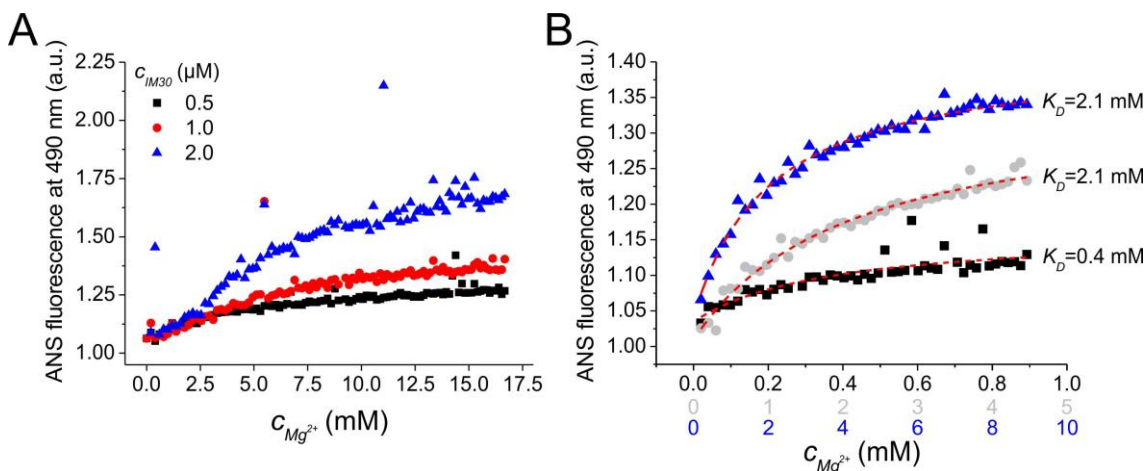


**Fig. 3.7: Titration of IM30 with  $Mg^{2+}$**

Titration curves were recorded using different IM30 concentrations provided in the sample solution and 0.1 M  $Mg^{2+}$  as titrator (A). In a complementary approach, 1  $\mu$ M IM30 was titrated with  $MgCl_2$  stocks of different concentrations (B). For the latter experiment, the titration curves were fitted with a binding fit in order to determine  $K_D$  values.  $R^2=0.731$  (black curve),  $R^2=0.982$  (grey curve),  $R^2=0.975$  (blue curve). Single points identified as extreme outliers were excluded.

Upon  $Mg^{2+}$  addition, an increase in the ANS fluorescence emission at 490 nm was monitored (Fig. 3.7). In the first approach, differently concentrated IM30 samples of 0.5-2.0  $\mu$ M were titrated with a 0.1 M  $MgCl_2$  solution (Fig. 3.7 A). As expected, a plateau was reached at a smaller amount of added  $Mg^{2+}$  for the lower concentrated IM30 samples, probably due to earlier saturation. In a second approach, identically concentrated IM30 samples of 1  $\mu$ M were titrated with different  $MgCl_2$  solutions. The latter experiment was used to determine  $K_D$  values for the IM30- $Mg^{2+}$  interaction by using binding fits (see 5.13.1.1). For each sample, the  $K_D$  values were determined from the fit and the weighted mean value for  $K_D$  was calculated. The results are listed in Table 3.1.

**Table 3.1: Calculated  $K_D$  values from the ANS titration curves**

$c_{Mg^{2+}}$ (mM)	$K_D$ (mM)	Weighted $K_D$ (mM)
0-1	$2.10 \pm 0.29$	$1.33 \pm 0.60$
0-5	$2.05 \pm 0.20$	
0-10	$0.36 \pm 0.19$	

The calculated weighted  $K_D$  of ( $1.33 \pm 0.60$ ) mM is in perfect agreement with the  $K_D$  value ( $(1.1 \pm 0.5)$  mM) determined from the ANS spectra in (Junglas 2016), which were recorded in cooperation with Benedikt Junglas.

As mentioned above, the ANS experiments only provide indirect hints for a binding of  $Mg^{2+}$  to IM30. A more direct experiment, including a  $K_D$  determination, was reverse ITC, in which the reaction heat was determined. Since a standard ITC, in which the ligand  $Mg^{2+}$  was titrated to the protein solution, was not suitable for this investigation due to the high dilution heat of  $Mg^{2+}$  itself (demonstrated in cooperation with Svenja Winzen, not part of this thesis), a reverse ITC

was performed in cooperation with Prof. Nadja Hellmann and Benedikt Junglas as described in 2.18.4. Here, an IM30 stock was titrated to a solution containing  $\text{MgCl}_2$ , and the enthalpy change  $\Delta H$  was determined for different  $\text{Mg}^{2+}$  concentrations. The final titration curve, which illustrates the specific enthalpy change upon IM30 addition to differently concentrated  $\text{Mg}^{2+}$  solutions, is shown in *Fig. 3.8*. All baseline corrections for dilution heat minus unspecific ionic effects (baselines and raw data are illustrated in 5.9, missing data were calculated via fit functions) are included.

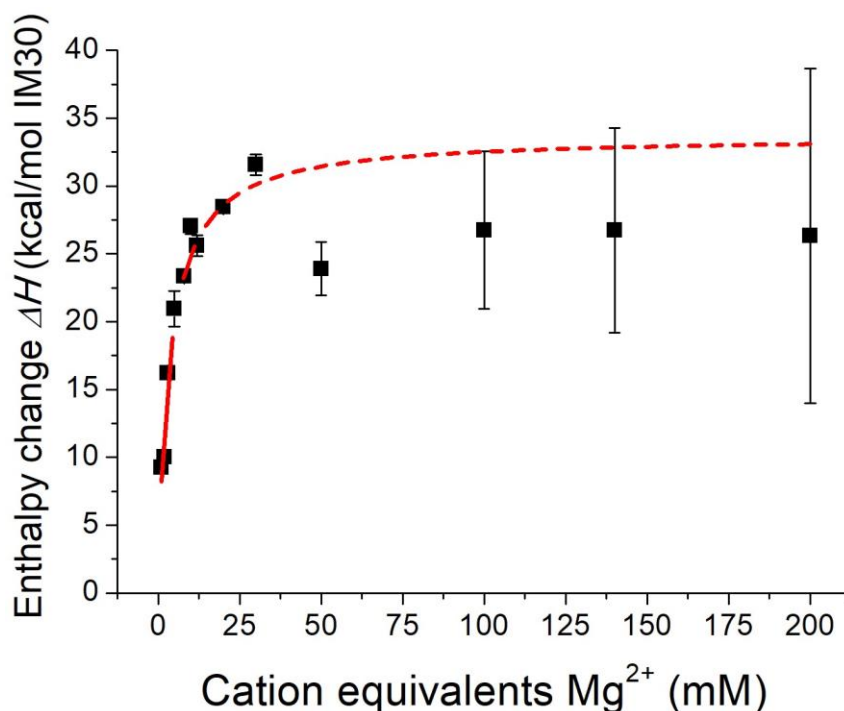


**Fig. 3.8:** Reverse ITC of  $\text{Mg}^{2+}$  titration with IM30

To demonstrate the direct binding of  $\text{Mg}^{2+}$  to IM30, a reverse ITC was performed via titrating IM30 samples to a  $\text{MgCl}_2$  solution and measuring the enthalpy change  $\Delta H$ . The data were fitted with a binding fit.  $R^2=0.976$ , error bars represent standard deviation ( $n=3$ ). The large error bars for high  $\text{Mg}^{2+}$  cation equivalent concentrations result from the strong enthalpy change of the baseline. In cooperation with Prof. Nadja Hellmann and Benedikt Junglas. The results in this figure are published in (Heidrich *et al.* 2018).

The specific enthalpy change of the IM30- $\text{Mg}^{2+}$  interaction, shown in *Fig. 3.8*, describes a saturation curve in good approximation. Since  $\text{Mg}^{2+}$  was in large excess compared to IM30, the curve was fitted with a binding fit (*cf.* 5.13.1.1). At lower  $\text{Mg}^{2+}$  cation equivalent concentrations  $<25$  mM, the curve increased steeply and leveled off at  $\sim 30$  kcal/mol into saturation. Importantly, the development of  $\Delta H$  in *Fig. 3.8* describes an endothermal domination in the IM30- $\text{Mg}^{2+}$  binding, indicating that the reaction was entropically driven. From the binding fit, the  $K_D$  value was calculated to be  $(3.72 \pm 0.36)$  mM for the cation equivalents which was converted to a  $K_D$  of  $(1.86 \pm 0.18)$  mM for the  $\text{Mg}^{2+}$  concentration. In (Junglas 2016), a different one-site binding fit was used, resulting in a similar  $K_D$  value of  $(1.53 \pm 0.11)$  mM. These values resemble the  $K_D$  values determined in the ANS titration curves (see above).

In summary, the interaction between IM30 and  $Mg^{2+}$  was observed indirectly via ANS fluorescence as well as directly via reverse ITC. From the ANS experiments, the observation was made that the structure of IM30 alters upon  $Mg^{2+}$  binding, probably due to hydrophobic surface exposure. The positive enthalpy change for the IM30- $Mg^{2+}$  binding obtained from the ITC measurement revealed an apparent endothermic nature of this interaction. Furthermore, the ANS titration and reverse ITC revealed  $K_D$  values for the IM30- $Mg^{2+}$  interaction in the range of 1-2 mM.

### 3.3.2 Introduction of crosslinked IM30 and IM30 dimers

To identify potential necessary dynamical properties of IM30 rings during  $Mg^{2+}$  binding, the IM30 quaternary structure was influenced via two different approaches: (i) a crosslinked version of IM30 in order to fixate the ring structures due to additional covalent connections and (ii) a forced dimer formation of IM30 via covalent disulfide bridges, partially preventing the formation of IM30 rings.

#### 3.3.2.1 Introduction of crosslinked IM30

In order to create crosslinked IM30 (IM30-X), the crosslink agent glutaraldehyde was used as described in 2.16.8. Glutaraldehyde is able to connect amide, imidazole-, phenol- and thiol compounds of proteins (Okuda *et al.* 1991; Migneault *et al.* 2004), and thereby creates a fixated structure of the protein. TrisHCl was added subsequently in order to stop the crosslinking reaction, since the chemical is able to form complexes with glutaraldehyde.

To confirm successful crosslinking of IM30, an SDS-PAGE analysis was performed. Here, samples containing only IM30, IM30 incubated with TrisHCl, and IM30 first incubated with glutaraldehyde and subsequent addition of TrisCl were loaded. The gel is shown in Fig. 3.9.

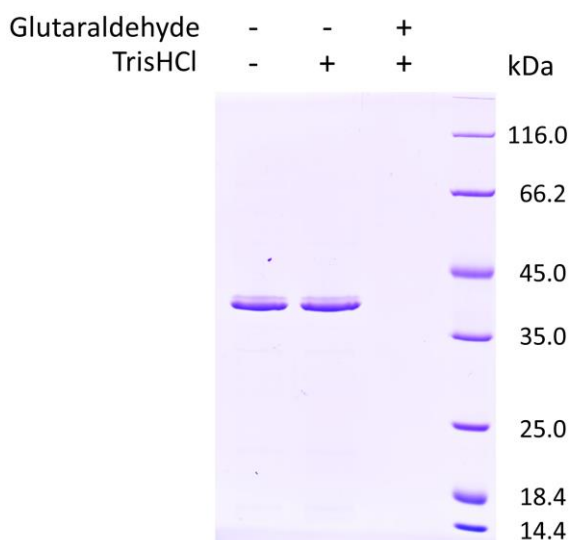


**Fig. 3.9: Confirmation of successful IM30 crosslinking**

In order to confirm successful crosslinking of IM30, samples were loaded on a 12% SDS gel containing only IM30, IM30 incubated with TrisHCl, and IM30 first incubated with glutaraldehyde and subsequent addition of TrisHCl.

Obviously, the IM30 band at  $\sim 37$  kDa in *Fig. 3.9* is only visible in the lanes containing the samples which were not incubated with glutaraldehyde. When adding the crosslinking agent to IM30, the protein seemed to be completely crosslinked and is, thus, not visible in the resolving gel. Importantly, TrisHCl did not seem to have an intrinsic effect on IM30. The findings confirm a successful crosslinking of IM30.

Since the crosslink agent might have influenced the correct formation of IM30 ring oligomers or could have induced excessive aggregate formation, a further structure control via TEM was necessary. The micrographs of IM30-X, recorded in cooperation with Kristiane Rusitzka, are shown in *Fig. 3.10*.

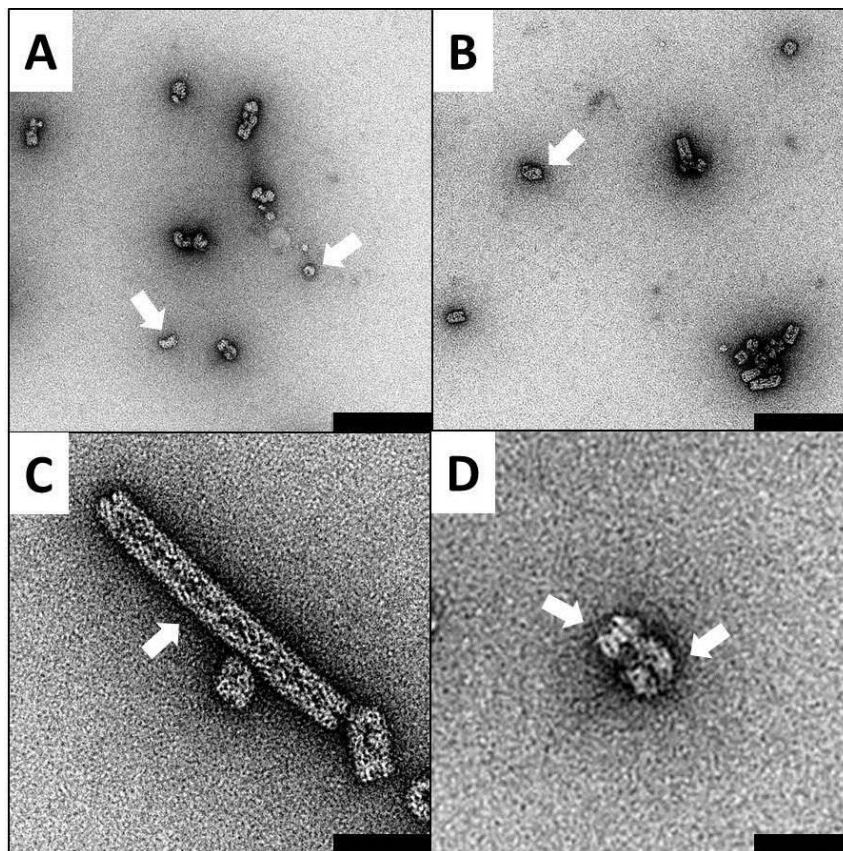


**Fig. 3.10: TEM micrographs of IM30-X**

Representative TEM micrographs of IM30-X samples are shown. Arrows indicate rings (A, B), rods (C) and double-rings (D). Scale bars represent 200 nm (A, B), 67 nm (C) and 50 nm (D). In cooperation with Kristiane Rusitzka.

As displayed in *Fig. 3.10*, crosslinked IM30 was still able to form rings and even rod structures. Similar to the non-crosslinked WT (*cf. Fig. 3.3*), some aggregates are visible (*Fig. 3.10 B*). In conclusion, the TEM micrographs confirm the correct oligomerization of IM30 in presence of glutaraldehyde.

### **3.3.2.2 Introduction of IM30 dimers**

In order to partially prevent higher-ordered oligomerization of IM30, the dimerization of IM30 via covalent disulfide bridges was enabled. Since the IM30 WT does not contain any cysteine

residues, site-directed mutagenesis changing an alanine for a cysteine residue in the linker region between helix 6 and helix 7 was performed (see 2.14.2). This region was assumed not to interfere with ring formation in absence of disulfide bridges (Otters *et al.* 2013). The mutation is schematically shown in *Fig. 3.11*.

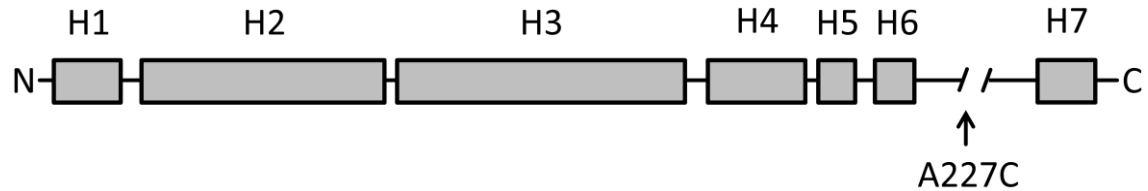


**Fig. 3.11: Position of the point mutation A227C in the IM30 secondary structure**

The IM30 point mutation A227C is indicated in a schematic representation of the IM30 secondary structure.

In order to confirm a successful formation of IM30 dimers, an SDS-PAGE and immunoblot analysis were performed using samples of IM30 A227C (A227C) in presence and absence of the disulfide reducing agent DTT inside the sample buffer (*Fig. 3.12*).

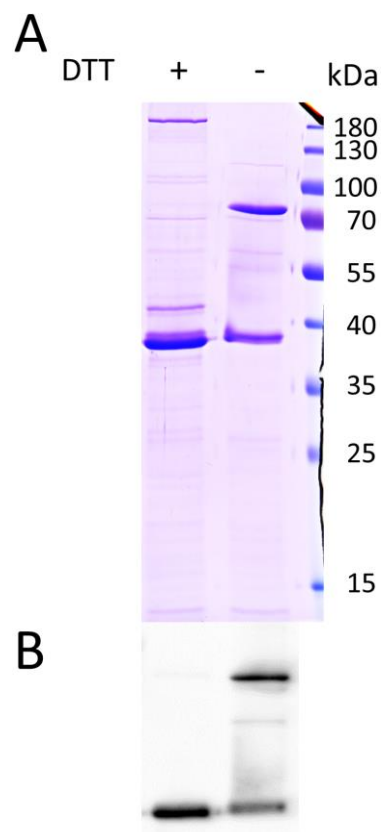


**Fig. 3.12: Purification and dimer formation of A227C in presence and absence of DTT**

Expression and successful purification of A227C was confirmed on 12% SDS gels (A) and in an immunoblot analysis using the  $\alpha$ Vipp420 antibody (B). Furthermore, in the lane containing the sample lacking 10 mM DTT, the IM30 dimers appear above the 70 kDa marker band (A and B).

As displayed in *Fig. 3.12*, the dimer band above the 70 kDa marker band can be found in the gel lane containing the sample lacking DTT. Still, a less intense monomer band is also visible in this lane, indicating incomplete dimer formation.

In order to investigate the structure of A227C further, TEM was performed in cooperation with Wolfgang Gebauer, Kristiane Rusitzka, and Carmen Siebenaller for protein samples containing and lacking 10 mM DTT. The micrographs are shown in *Fig. 3.13*.

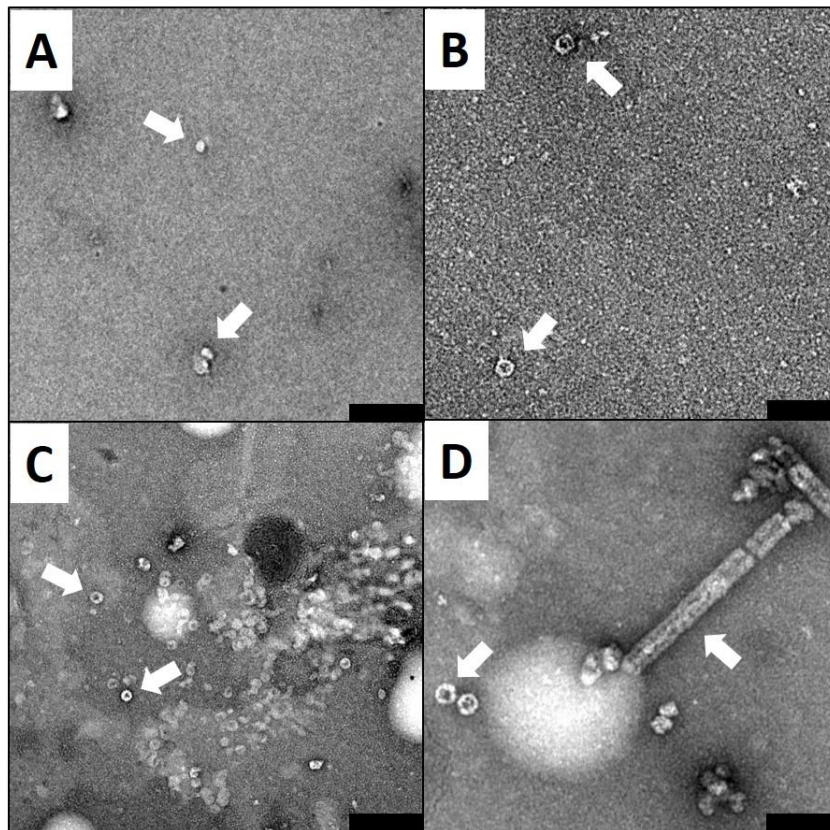


**Fig. 3.13: TEM micrographs of A227C in presence and absence of DTT**

Representative TEM micrographs of A227C in the absence (A, B) and presence (C, D) of 10 mM DTT are shown. Arrows indicate particles or aggregates (A), rings (B, C, D) and rods (D). Scale bars represent 200 nm (A, C) and 100 nm (B, D). In cooperation with Wolfgang Gebauer, Kristiane Rusitzka and Carmen Siebenaller.

Upon lacking of DTT, A227C was obviously impaired in oligomer formation (*Fig. 3.13* A and B), which might be ascribed to the formation of disulfide bridges and the resulting reduced structural flexibility. In contrast, upon addition of DTT, A227C returned to its ability to oligomerize as ring structures and rod-like structures (*Fig. 3.13* C and D).

Overall, the mutant A227C was found to be suitable for experiments requiring IM30 dimers, which are impaired in oligomerization but can be triggered to form rings and rod-like structures upon DTT addition.

### 3.3.3 Structural flexibility and ring formation of IM30 influences $Mg^{2+}$ binding

After indicating the ability of IM30 to directly interact with  $Mg^{2+}$  (see 3.3.1), the question arised whether a dynamic structure and the oligomeric ring formation of the protein is necessary for the binding reaction. To tackle this issue, further ANS experiments were performed using the crosslinked IM30-X (see 3.3.2.1) and the mutant A227C (see 3.3.2.2), which forms dimers and only a strongly decreased amount of higher-ordered structures in absence of DTT. If structural flexibility and ring formation were mandatory for  $Mg^{2+}$  binding, a reduced shift in the ANS spectra for IM30-X and A227C in absence of DTT upon  $Mg^{2+}$  addition could be expected.

Samples of IM30 ( $\pm$  crosslinker) and A227C ( $\pm$  DTT) were incubated with ANS and 10 mM of  $MgCl_2$ , respectively. A control lacking  $Mg^{2+}$  and a control containing only DTT and ANS were also prepared. ANS spectra were recorded and are shown in *Fig. 3.14*.

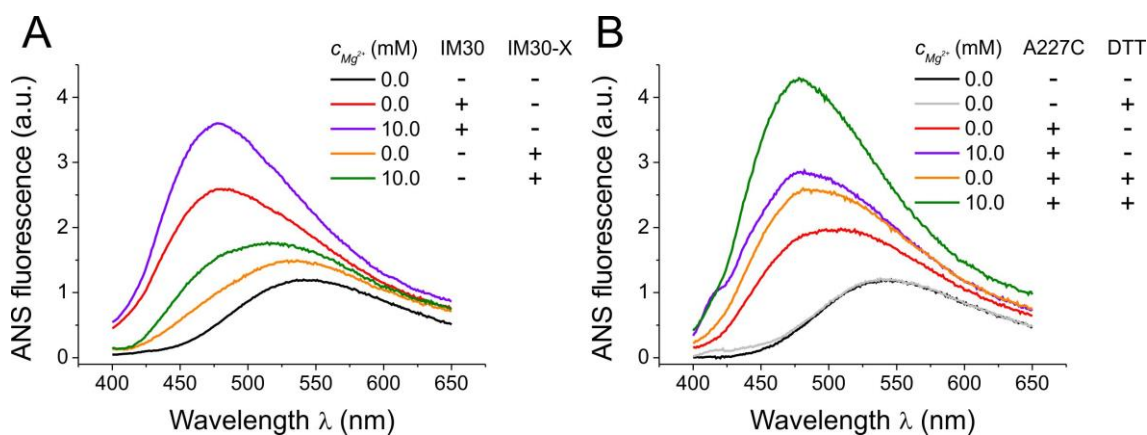


**Fig. 3.14:** ANS spectra of IM30/IM30-X and A227C ( $\pm$  DTT) in presence and absence of  $Mg^{2+}$

To investigate the influence of the IM30 structure flexibility on the  $Mg^{2+}$  interaction, ANS spectra of crosslinked and uncrosslinked IM30 samples in presence and absence of 10 mM  $MgCl_2$  were recorded (A). Complementarily, to examine the influence of ring-formation on the  $Mg^{2+}$  interaction, ANS spectra of A227C samples ( $\pm$  10 mM DTT) in presence and absence of 10 mM  $MgCl_2$  were recorded (B). The experiment was repeated two times.

It has been demonstrated that using the protocol for crosslinking IM30 most probably results in a nearly complete crosslinked protein (*cf. Fig. 3.9*). As shown in *Fig. 3.14A*, the ANS fluorescence emission spectra of samples containing IM30-X were far more red-shifted compared to the ANS spectra of the IM30 WT samples, indicating a reduced affinity of the crosslinked protein for ANS. Upon  $Mg^{2+}$  addition, a blue shift was observed for both, samples containing IM30 or IM30-X. Nevertheless, this shift was dramatically decreased in the case of the crosslinked protein compared to the uncrosslinked IM30 and could have resulted from a small fraction of uncrosslinked IM30 species in the sample, which would still have been able to alter their structure. It must be mentioned that the observations do not exclude  $Mg^{2+}$  binding to IM30-X prior to reduced structural rearrangements *per se*.

As displayed in *Fig. 3.14B*, the ANS spectra for the A227C samples lacking DTT, in which IM30 was partly dimerized and was, thus, not able to oligomerize (*cf. 3.3.2.2*), also showed a

decreased blue shift upon  $\text{Mg}^{2+}$  addition compared to the samples containing DTT. Importantly, in the control sample containing only DTT and ANS, the detergent was found not to influence the fluorescence of the dye. Since addition of DTT has been shown to restore the ring formation of A227C (*cf. Fig. 3.13*) and the ANS fluorescence was dramatically increased in these samples, it seems reasonable to assume that IM30 ring formation is required for  $\text{Mg}^{2+}$  binding. However, the experiment does not exclude the  $\text{Mg}^{2+}$  binding to higher-ordered IM30 structures other than rings.

In summary, the ANS experiments using IM30-X and A227C provided first hints for the conditions of the IM30- $\text{Mg}^{2+}$  interaction: IM30 must most probably exist in the oligomerized ring state, which is furthermore supposed to stay flexible during or after  $\text{Mg}^{2+}$  binding. The latter requirement is in perfect agreement with the observed exposure of hydrophobic surfaces upon  $\text{Mg}^{2+}$  addition, made in ANS experiments for the IM30 WT (*cf. Fig. 3.6* and *Fig. 3.7*). While crosslinked, the protein is supposed to be completely fixated in the oligomerized form (*cf. 3.3.2.1*) and is, thus, no longer able to conduct any structural alteration.

### 3.4 The effect of $\text{Mg}^{2+}$ on the IM30 structure and stability

In 3.3, it has been described that  $\text{Mg}^{2+}$  probably directly binds to IM30 rings and/or other higher-ordered IM30 structures upon an increase of hydrophobic surfaces. The next issue of interest was the effect of this interaction on physical properties such as the thermodynamic stability of the protein. Furthermore, the induced change of the IM30 surface properties upon  $\text{Mg}^{2+}$  binding seems to be predisposed for a more global structural alteration, *e.g.* concerning increased double-ring formation.

#### 3.4.1 $\text{Mg}^{2+}$ influences the IM30 secondary structure

The stability of the IM30 secondary structure upon  $\text{Mg}^{2+}$  addition was investigated via urea denaturation/renaturation and CD spectroscopy as described in 2.16.9 and 2.18.1.1. In general, IM30 samples were incubated with different amounts of  $\text{Mg}^{2+}$ , the samples were exposed to different urea concentrations, and CD spectra were recorded. Subsequently, the ratio of denaturated protein  $f_D$  was plotted against increasing urea concentration. All CD experiments were performed in cooperation with Benedikt Junglas.

IM30 has already been demonstrated to renaturate in absence of  $\text{Mg}^{2+}$  (Debus 2013), but not in presence of the metal ion yet. Thus, this was investigated in a preliminary test by denaturation and renaturation of IM30 in presence of 15 mM  $\text{MgCl}_2$ , which is illustrated in *Fig. 3.15*.

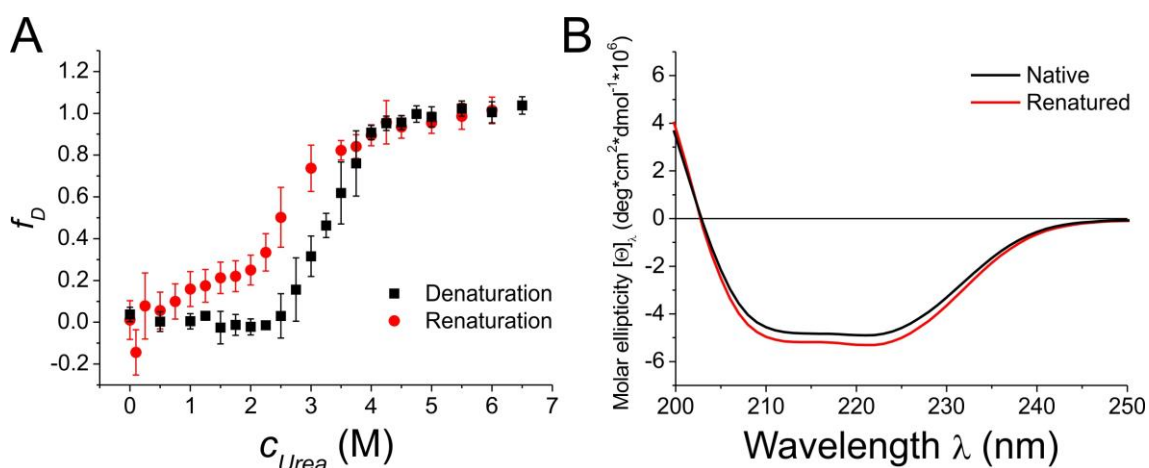


**Fig. 3.15: Urea denaturation and renaturation of IM30 in presence of  $Mg^{2+}$**

The reversibility of the urea denaturation and renaturation of IM30 in presence of 15 mM  $Mg^{2+}$  was investigated via CD spectroscopy. The ratio of denatured protein  $f_D$  was plotted against increasing urea concentration in order to check whether start and ending points as well as the curve form were identical (A). Error bars were calculated via Gaussian error distribution of three samples. Additionally, CD spectra prior to denaturation and after renaturation were recorded and compared (B). In cooperation with Benedikt Junglas. The results in this figure are published in (Heidrich *et al.* 2018).

The denaturation and renaturation curves of IM30 in presence of  $Mg^{2+}$  in Fig. 3.15A strongly differ from each other concerning a shift of the denaturation curve to higher urea concentrations. The two curves resemble a hysteresis loop, indicating an irreversible reaction (Andrews *et al.* 2013). However, as already suggested in (Junglas 2016), the shift could have originated from different folding and unfolding mechanisms. Furthermore, the renaturation curve in Fig. 3.15A resembles the renaturation curve for an IM30 sample lacking  $Mg^{2+}$  (Hennig 2014), which indicates the dissociation of the IM30- $Mg^{2+}$  complex in the denaturation process (Junglas, p.c.). When comparing CD spectra prior denaturation and after renaturation, as illustrated in Fig. 3.15B, the curves slightly differ from each other due to smaller  $[\Theta]_\lambda$  values for the renatured protein. However, both CD spectra clearly indicate a mainly  $\alpha$ -helical structure of IM30 in presence of  $Mg^{2+}$ .

After the reversibility of the IM30 denaturation process was investigated, denaturation curves of the protein for different  $MgCl_2$  concentrations were recorded. For a better overview, only the curves for 0 mM  $Mg^{2+}$ , 15 mM  $Mg^{2+}$  and the cation equivalent 30 mM  $Na^+$  as negative control are shown in Fig. 3.16. The data for the other investigated  $Mg^{2+}$  concentrations including the respective Boltzmann fits can be found in 5.10.

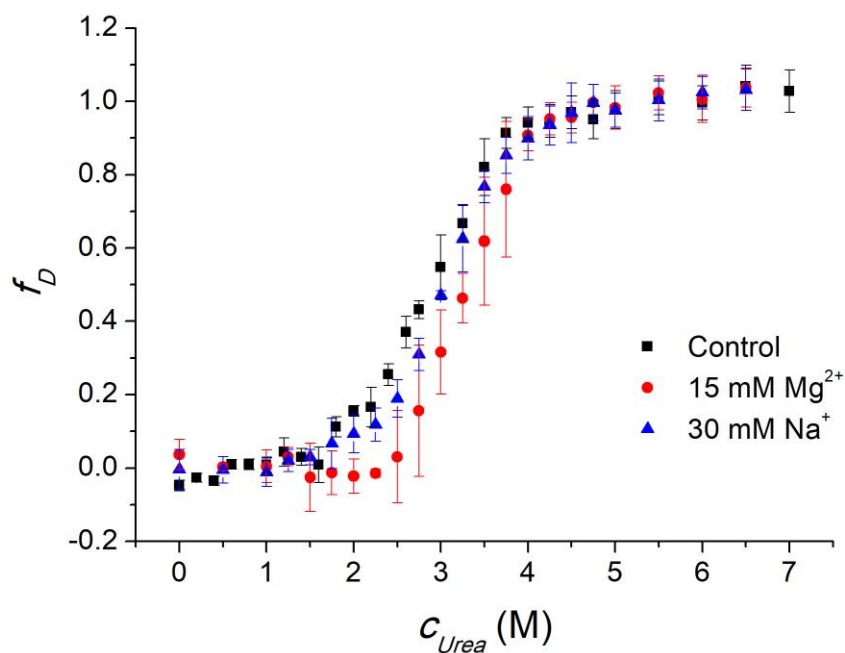


**Fig. 3.16:** Urea denaturation of IM30 in presence and absence of 15 mM  $\text{Mg}^{2+}$  and 30 mM  $\text{Na}^+$

In order to investigate the effect of  $\text{Mg}^{2+}$  on the IM30 secondary structure stability, urea denaturation curves for IM30 in the presence of 0 mM  $\text{Mg}^{2+}$ , 15 mM  $\text{Mg}^{2+}$  and 30 mM  $\text{Na}^+$ , respectively, are shown. Error bars were calculated via Gaussian error distribution of three samples. In cooperation with Benedikt Junglas. Several results in this figure are published in (Heidrich *et al.* 2018).

All recorded denaturation curves, illustrated in Fig. 3.16 and Fig. 5.23, show the expected sigmoidal trend, which is further emphasized by fitting with a Boltzmann fit (*cf.* Fig. 5.23). The plateaus of the curves typically range from 0-2 M urea and 4-7 M urea, respectively. The steep sections of the denaturation curves are shifted to higher urea concentrations with increasing  $\text{MgCl}_2$  concentrations. The negative control containing 30 mM  $\text{Na}^+$ , which is the cation equivalent for 15 mM  $\text{Mg}^{2+}$ , was assumed not to influence the form of the denaturation curve compared to the sample lacking any additional ions. In fact, the impact of  $\text{Na}^+$  on the IM30 denaturation seems to be insignificant since the curve is hardly shifted. Thus, the effect of  $\text{Mg}^{2+}$  on IM30 seems to be specific. Due to the shift to higher urea concentrations in the denaturation curves,  $\text{Mg}^{2+}$  can be assumed to stabilize the IM30 secondary structure. Combined with the observation that  $\text{Mg}^{2+}$  triggers the exposure of hydrophobic surfaces of IM30 (see 3.3), it seems most likely that the stability of IM30 is increased due to a structural rearrangement upon  $\text{Mg}^{2+}$  binding.

In order to quantify the IM30 denaturation curves in presence of  $\text{Mg}^{2+}$ ,  $D_{1/2}$  values for all samples with different  $\text{MgCl}_2$  concentrations were calculated as described in 2.18.1. The results are illustrated in Fig. 3.17.

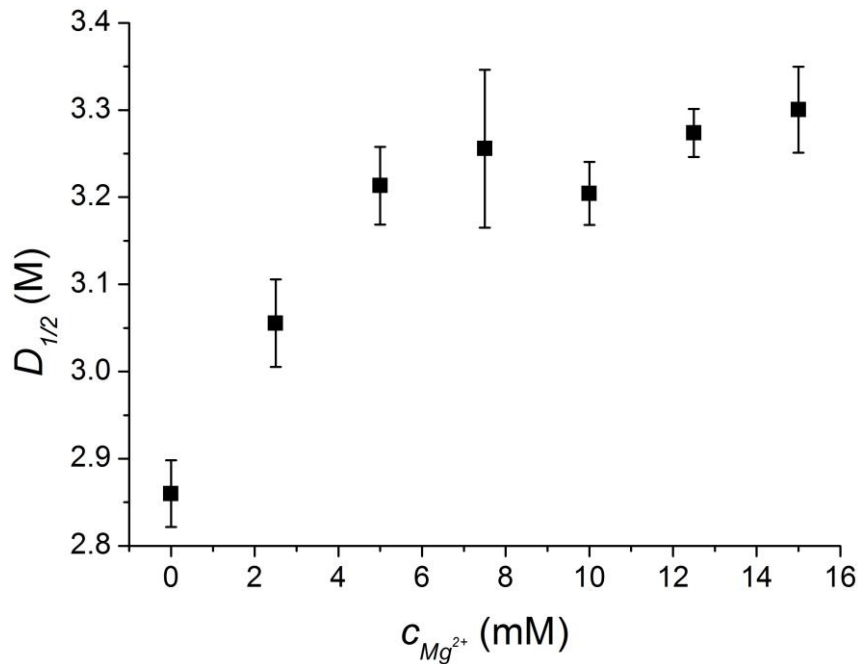


**Fig. 3.17:**  $D_{1/2}$  values of IM30 at different  $Mg^{2+}$  concentrations

The  $D_{1/2}$  values of IM30 at different  $Mg^{2+}$  concentrations were calculated from the urea denaturation curves by fitting with a Boltzmann fit. Error bars were also obtained from the Boltzmann fit. In cooperation with Benedikt Junglas. The results in this figure are published in (Heidrich *et al.* 2018).

As can be seen in Fig. 3.17, the inflection points of the denaturation curves  $D_{1/2}$  increase from ~2.9 M to ~3.3 M. A plateau is reached at ~5 mM  $MgCl_2$ .

Overall, the analysis of the IM30/ $Mg^{2+}$  denaturation curves supports the impression that the ion increases the stability of the IM30 secondary structure. This effect seems to require at least 5 mM of  $Mg^{2+}$  for maximal stabilization.

### 3.4.2 $Mg^{2+}$ influences the IM30 tertiary/quaternary structure

As described in 3.3.1, it has been observed that  $Mg^{2+}$  induces increased exposure of hydrophobic surfaces and, thus, a change of the IM30 tertiary and/or quaternary structure. Another possibility to further illuminate this issue was the determination of the molar ellipticity ratio  $[\Theta]_{222\text{ nm}}/[\Theta]_{208\text{ nm}}$  from the CD spectra. This ratio provides information concerning the coiled-coil amount of the  $\alpha$ -helices inside the protein (Lau *et al.* 1984; Zhou *et al.* 1992), which might be changed upon structural alteration due to an influence of  $Mg^{2+}$ . A calculated value  $\leq 0.86$  normally stands for isolated  $\alpha$ -helices, whereas a value  $> 1.0$  indicates the presence of coiled-coil structures (Lau *et al.* 1984). Here, the  $[\Theta]_{222\text{ nm}}/[\Theta]_{208\text{ nm}}$  ratio was calculated from CD spectra of samples containing IM30 in presence and absence of 15 mM  $Mg^{2+}$ . Furthermore, the ratio was also calculated for a control sample containing IM30 and the cation equivalent 30 mM  $Na^+$ . The experiment was performed in cooperation with Benedikt Junglas. The results are listed in Table 3.2.

**Table 3.2: Ratio  $[\Theta]_{222\text{ nm}}/[\Theta]_{208\text{ nm}}$  of IM30 in presence and absence of 15 mM  $\text{Mg}^{2+}$  and 30 mM  $\text{Na}^+$** 

Sample	Ratio $[\Theta]_{222\text{ nm}}/[\Theta]_{208\text{ nm}}^*$
Control	$1.097 \pm 0.016$
15 mM $\text{Mg}^{2+}$	$1.194 \pm 0.017$
30 mM $\text{Na}^+$	$1.116 \pm 0.009$

In cooperation with Benedikt Junglas. Several results in this table are published in (Heidrich *et al.* 2018). \*Errors represent the standard deviation ( $n=3$ ).

The calculated  $[\Theta]_{222\text{ nm}}/[\Theta]_{208\text{ nm}}$  ratio for the IM30 control sample was  $\sim 1.1$ , indicating a pronounced coiled-coil amount in the proteins' structure. Upon  $\text{Mg}^{2+}$  addition, this value shifted to  $\sim 1.2$ . Thus, stronger clustering of  $\alpha$ -helices and an increased coiled-coil amount could be assumed. Importantly, the control sample containing the cation equivalent of  $\text{Na}^+$  was not significantly altered concerning the  $[\Theta]_{222\text{ nm}}/[\Theta]_{208\text{ nm}}$  ratio compared to the pure IM30 sample, implying a specific effect of  $\text{Mg}^{2+}$  on the coiled-coil portion of IM30. The results are in perfect agreement with findings in (Hennig 2014) and indicate an increased stability of IM30 upon  $\text{Mg}^{2+}$  binding due to a more compact tertiary/quaternary structure. Importantly, the outcome of the experiment does not exclude the formation of coiled-coil structures between several IM30 molecules when part of the same ring oligomer.

In another complementary experiment, the influence of  $\text{Mg}^{2+}$  binding on the IM30 stability against proteolysis was tested, as described in 2.16.11.1. A change in the tertiary/quaternary structure of IM30 upon  $\text{Mg}^{2+}$  binding was expected to result in an altered accessibility for proteases, leading to a different degradation pattern. The serine protease trypsin, which was used in this assay, cleaves proteins at the C-terminal side of the alkaline amino acids lysine and arginine (Olsen *et al.* 2004).

To exclude an effect of  $\text{Mg}^{2+}$  on the trypsin activity, which would have affected the results of the main proteolysis assay, a BAEE assay was performed previously. Here, BAEE was digested by trypsin in presence and absence of different  $\text{Mg}^{2+}$  concentrations, and the product  $N_\alpha$ -Benzoyl-*L*-arginine was detected photometrically. The trypsin activity was determined as the maximal slope of the absorption curve (*cf.* Fig. 2.3) and the obtained values were normalized to the sample lacking  $\text{Mg}^{2+}$ . The experiment was performed in cooperation with Benedikt Junglas. The results are listed in Table 3.3.

**Table 3.3: Trypsin activity in presence of  $\text{Mg}^{2+}$** 

$c_{\text{Mg}^{2+}}$ (mM)	Trypsin activity (%)*
0	$100 \pm 9$
5	$117 \pm 9$
10	$109 \pm 11$

In cooperation with Benedikt Junglas. The results in this table are published in (Heidrich *et al.* 2018). \*Errors represent the standard deviation ( $n=3$ ).

As can be seen in Table 3.3, the trypsin activity was slightly increased in presence of  $\text{Mg}^{2+}$ , but this shift is negligible considering the error. Furthermore, there is no trend upon  $\text{Mg}^{2+}$  addition,

since the trypsin activity for the sample containing 10 mM of  $\text{MgCl}_2$  was decreased compared to the sample containing 5 mM of  $\text{MgCl}_2$ . Thus, an effect of  $\text{Mg}^{2+}$  on the trypsin activity was neglected in the following tryptic digestion.

The tryptic digestion was performed for samples containing IM30 in presence and absence of 10 mM  $\text{MgCl}_2$ . Upon trypsin addition, samples were taken at different time intervals, mixed with 5x SDS sample buffer in order to stop the reaction and loaded on an SDS gel. The experiment was performed in cooperation with Benedikt Junglas. The gels are shown in *Fig. 3.18*.

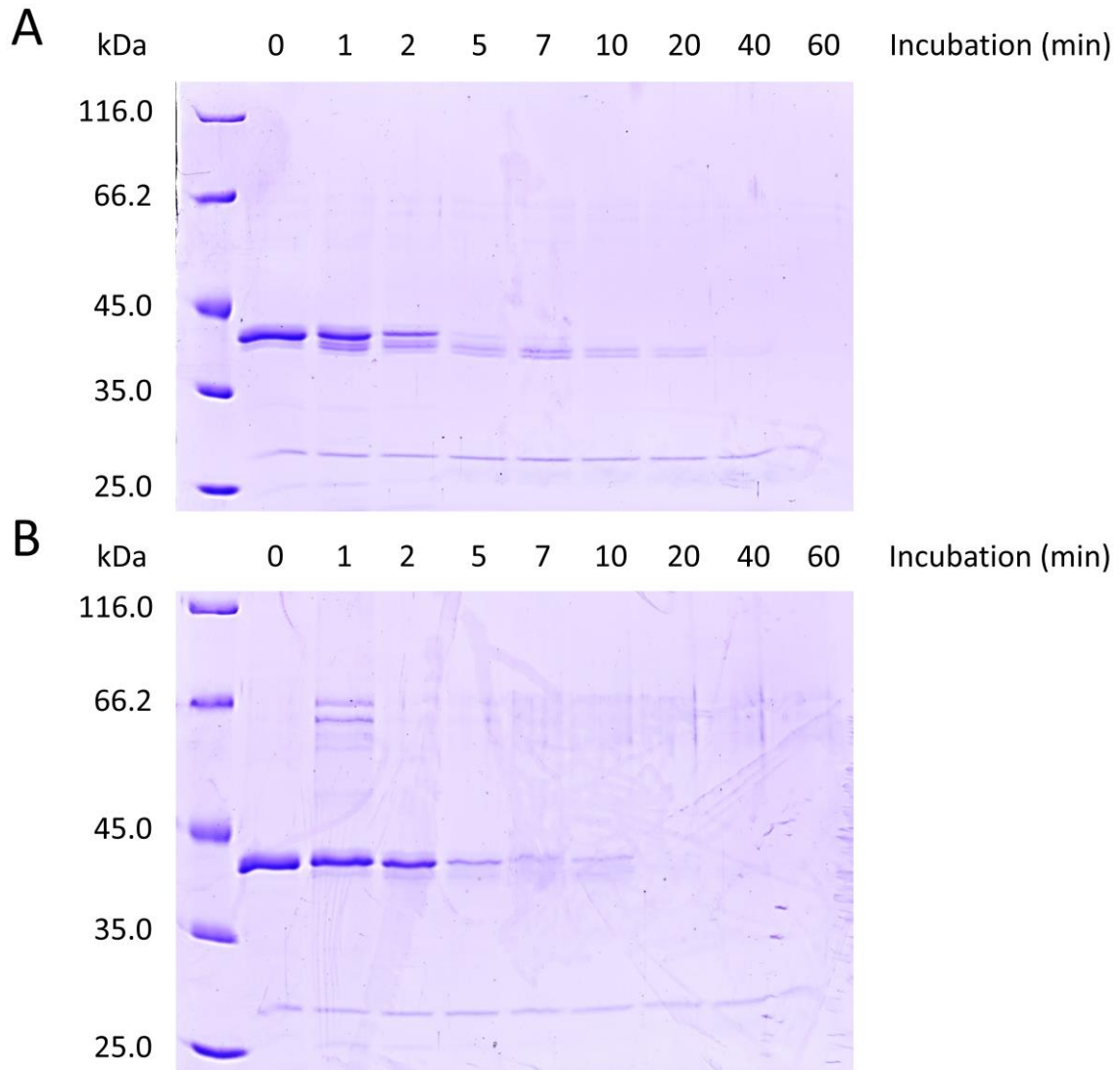


**Fig. 3.18: Tryptic digestion of IM30 in presence and absence of 10 mM  $\text{Mg}^{2+}$**

Tryptic digestion was performed to investigate the proteolytic stability of IM30 upon  $\text{Mg}^{2+}$  binding. Samples from a tryptic digestion of IM30 in absence (A) and presence (B) of 10 mM  $\text{Mg}^{2+}$  were separated on a 10% SDS gel. Indicated are the incubation times of the respective samples with trypsin. The trypsin band can be found in each lane on the SDS gels below 25 kDa. The experiment was repeated two times. In cooperation with Benedikt Junglas. The results in this figure are published in (Heidrich *et al.* 2018).

As expected, the IM30 band is always located above 35 kDa at ~37 kDa (*cf. Fig. 3.2*). In both *Fig. 3.18A* and *Fig. 3.18B*, a second band is visible below the IM30 full-length band upon incu-

bation with trypsin, which is named “degradation band” in the following. Due to recent findings indicating a flexible C-terminus, which was easily cleaved by trypsin and subtilisin, it can be assumed that the degradation band was the N-terminal PspA domain of IM30 (Otters *et al.* 2013; Gao *et al.* 2015). Indeed, determination of hypothetical cleavage sites of IM30 upon tryptic digestion include a cleavage site in the linker region after amino acid R285 with a probability of nearly 100%, resulting in a cleavage product of ~4 kDa (Junglas 2016). Further bands which might form from additional degradations are not visible in the gel.

In the SDS gel containing the sample lacking  $Mg^{2+}$  (*Fig. 3.18A*), the IM30 full-length band already started to vanish after 1 min and disappeared after 7 min. In presence of  $Mg^{2+}$  (*Fig. 3.18B*), on the other hand, the main band seemed to stay stable for 2 min and was still slightly visible after 10 min of incubation with trypsin. In both gels, the disappearance of the full-length band was accompanied by the appearance of the degradation band before the latter was also degraded. Thus, for the control sample in *Fig. 3.18A*, the degradation band appeared rather early at 0 min, whereat the unknown death time needs to be considered. Instead, for the IM30 in presence of 10 mM  $Mg^{2+}$  in *Fig. 3.18B*, the degradation band first appeared after 1 min and only very weak. Overall, the stability of IM30 against tryptic digestion seemed to be increased in presence of  $Mg^{2+}$  since it took more time to (i) form the degradation product, if at all, and (ii) to completely digest the full-length protein. This result can most probably be explained by a change of the tertiary/quaternary structure of IM30 upon  $Mg^{2+}$  binding, which would result in an altered accessibility for trypsin. As argued above, this structural change could include a protection of the IM30 C-terminus due to a change of its structure and/or localization.

To further investigate the stability of the IM30 tertiary/quaternary structure upon  $Mg^{2+}$  binding, ANS thermofluor experiments were performed as described in 2.18.2.1. Here, IM30 was incubated with ANS in presence and absence of 10 mM  $Mg^{2+}$ , and the temperature was increased from 0 to 80°C. Additionally, control samples containing only ANS and ANS incubated with 10 mM of  $Mg^{2+}$  were prepared in order to investigate the effect of an increased temperature on the dye. For each step, the ANS fluorescence at 490 nm was measured. The results are shown in *Fig. 3.19*.

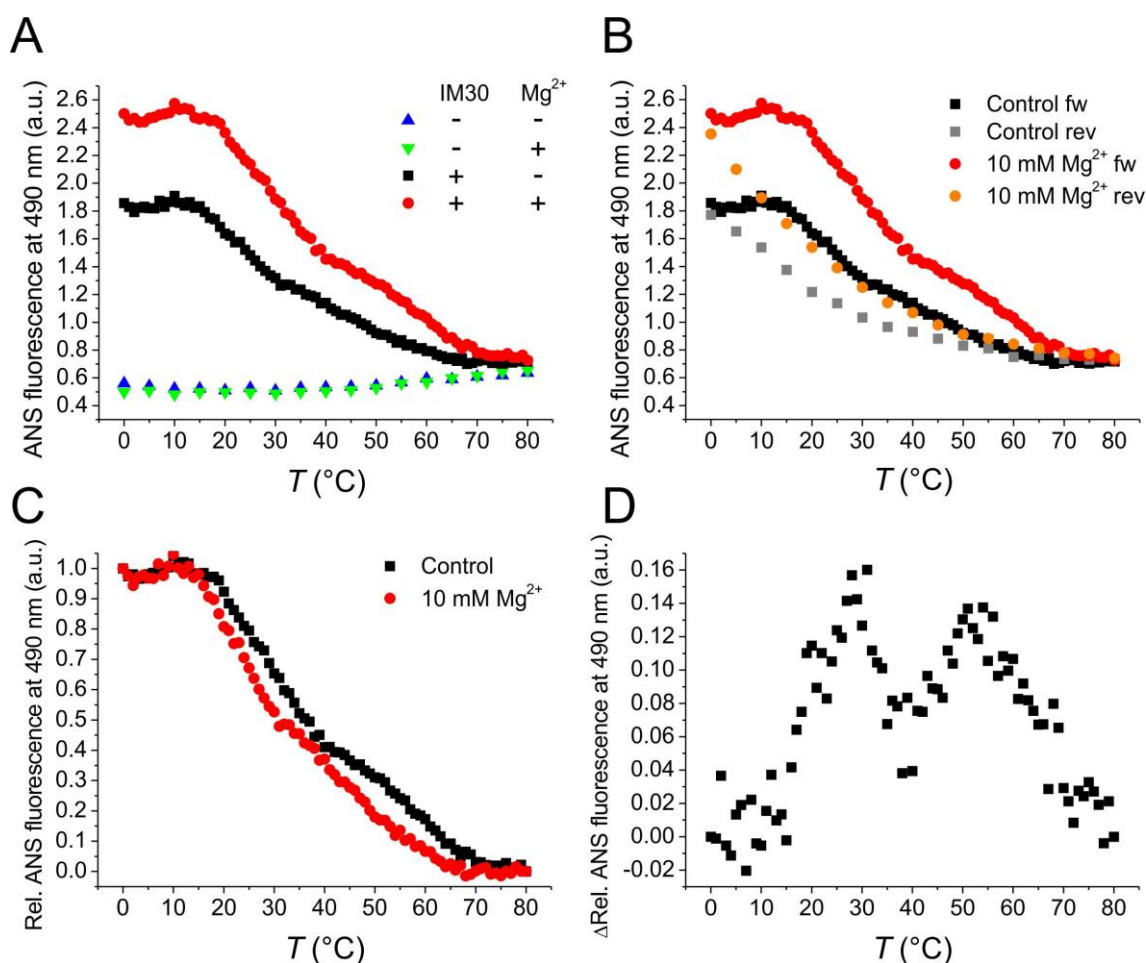


**Fig. 3.19: ANS thermofluor experiment for the IM30/Mg<sup>2+</sup> interaction**

ANS thermofluor measurements were performed to investigate the thermal stability of the IM30 tertiary/quaternary structure in presence of Mg<sup>2+</sup>. Samples containing IM30 were incubated with ANS in presence and absence of 10 mM MgCl<sub>2</sub>. The temperature was increased and the ANS fluorescence was measured at 490 nm. The raw data revealed an increased ANS fluorescence in presence of IM30/Mg<sup>2+</sup> compared to the sample lacking Mg<sup>2+</sup> (A). Nevertheless, the fluorescence decreased with increasing temperature, which was not the case for the control samples lacking IM30. At 80 °C, the curves seemed to converge, indicating a complete dissociation of ANS from IM30. After a temperature increase, the samples were cooled down again, resulting in a recovery of the initial ANS fluorescence (B). The raw data were normalized to 0 and 80 °C degrees as 1 and 0, respectively (C), and the difference between the two curves was calculated (D), indicating two plateaus of increased stability. The experiment was repeated two times.

In Fig. 3.19A, the raw data from the ANS thermofluor measurement are shown. While the ANS fluorescence decreased in presence of IM30 and IM30/Mg<sup>2+</sup> when increasing the temperature, it slightly increased when free in solution. Temperature-induced changes in the hydrophobic IM30 surface area, which is available for ANS binding, probably became visible as a change in the ANS fluorescence. As already shown in Fig. 3.6, Mg<sup>2+</sup> did not influence the ANS fluorescence, as can be seen for the control samples. Importantly, all curves converged at ~80 °C, indicating dissociation of the IM30-ANS complex with increasing temperature. The reversibility of the experiment was demonstrated via cooling the samples after heating (Fig. 3.19B). As already observed in the urea denaturation experiments for denaturation and renaturation curves (cf. Fig. 3.15), the forward- and reverse curves were shifted. However, the findings also excluded a potential thermal bleaching of ANS and supported the theory of an IM30-ANS complex dissocia-

tion (Fig. 3.19A). Nevertheless, when the relative ANS intensities (shown in Fig. 3.19C) and subsequently, the differences between the spectra containing  $Mg^{2+}$  and the control sample without  $Mg^{2+}$  were calculated, two temperature ranges could be identified, where the stability of IM30 was increased due to  $Mg^{2+}$ -binding: (i) between  $\sim 25$ - $35$  °C and (ii) between  $\sim 45$ - $60$  °C (Fig. 3.19D). The stabilizing of IM30 by  $Mg^{2+}$  is in agreement with the results presented above.

Overall, the experiments tackling the influence of  $Mg^{2+}$  on the IM30 tertiary/quaternary structure revealed a structural alteration resulting in a stabilization of the protein at temperature stress and an increased IM30 stability against tryptic digestion. This might result from the protection of the C-terminal domain in presence of  $Mg^{2+}$ .

### 3.4.3 Introduction of an IM30 FRET system

In order to investigate potential monomer exchanges between IM30 oligomers and IM30 double-ring formation in presence and absence of  $Mg^{2+}$ , two C-terminal labeled versions of IM30, which can act as a FRET pair, were created: IM30-CFP and IM30-Venus. Importantly, recent findings showed that a fluorescent protein tag at the IM30 C-terminus does not inhibit the IM30 *in vivo* activity (Bryan *et al.* 2014).

#### 3.4.3.1 Expression and purification of IM30-CFP and IM30-Venus

Cloning of the two labeled IM30 mutants was successfully performed as described in 2.14.4. The amino acid sequences can be found in 5.1.7 and 5.1.8, respectively. In order to confirm the correct expression of IM30-CFP and IM30-Venus, SDS-PAGE and immunoblot analysis were performed (Fig. 3.20).

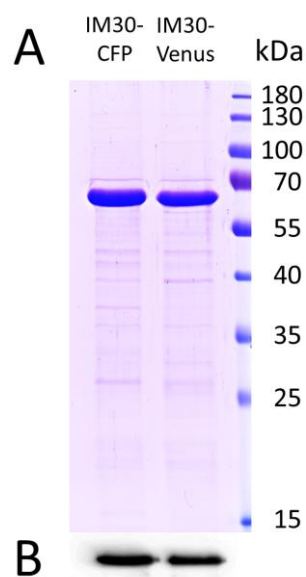


**Fig. 3.20: Purification of IM30-CFP and IM30-Venus**

Expression and successful purification of IM30-CFP and IM30-Venus were confirmed on 12% SDS gels (A) and in an immunoblot analysis using the  $\alpha$ Vipp420 antibody (B).

In the gel shown in *Fig. 3.20 A*, there is one significant strong band in each lane, representing the mutants IM30-CFP and IM30-Venus below the 70 kDa marker band, respectively. This is in agreement with the expected molecular masses of ~59 kDa for IM30-CFP and ~58 kDa for IM30-Venus. The immunoblot shown in *Fig. 3.20 B* further confirms the two mutants.

### 3.4.3.2 Structure of IM30-CFP, IM30-Venus and IM30-CFP/Venus

In order to control the ring formation and to exclude the existence of an increased amount of lower-ordered oligomers, SEC was performed with the labeled mutants as described in 2.16.12. The results are shown in *Fig. 3.21*.

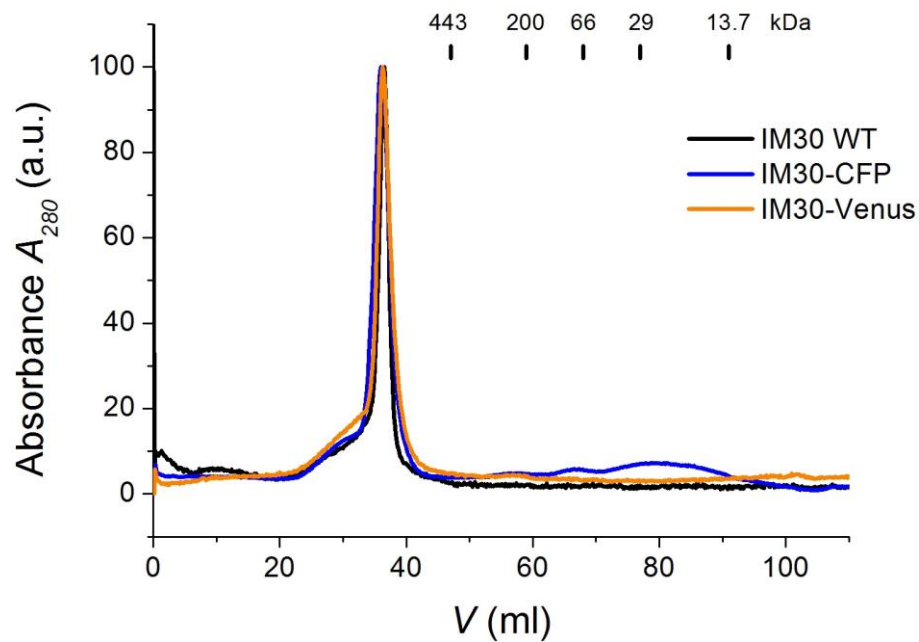


**Fig. 3.21:** SEC of IM30 WT, IM30-CFP and IM30-Venus

A SEC of the labeled IM30 mutants was performed for comparison with the IM30 WT. For calibration, the following proteins from the “Molecular Weight Maker Kit” were used: ribonuclease A (13.7 kDa), carbonic anhydrase (29 kDa), BSA (66 kDa),  $\beta$ -amylase (200 kDa) and apoferritin (443 kDa). The data for the IM30 WT and the marker proteins were from Adrien Thurotte. The results in this figure are published in (Heidrich *et al.* 2018).

The elution profiles of IM30-CFP and IM30-Venus strongly resemble the one from the IM30 WT. Only for IM30-CFP, a smaller fraction (<10%) with a molecular weight below 66 kDa indicated some lower-ordered oligomers. However, most of the protein was found in the void volume, which included structures above 443 kDa. As it was already discussed in (Heidrich *et al.* 2016), SEC cannot distinguish between proper ring structures and other larger aggregates. Thus, the structure of the protein was further investigated via TEM in cooperation with Wolfgang Gebauer. The micrographs of the single-labeled mutant and the mixtures are shown in *Fig. 5.8*, *Fig. 5.9* and *Fig. 5.10*. All micrographs indicated the capability of the labeled IM30 mutants to form ring structures, even though there appeared to be more lower-ordered particles compared to the WT (*Fig. 3.3*). In order to confirm correct folding of the fluorophores CFP and Venus, which would result in proper fluorescence, fluorescence emission and excitation spectra

were recorded using the labeled proteins. The normalized fluorescence spectra are shown in *Fig. 5.6*.

Additionally, it was necessary to demonstrate the ability of the labeled mutants to form a FRET pair when they are part of the same ring. Thus, the CFP fluorescence was supposed to decrease whereas the Venus fluorescence should increase. In order to investigate this, fluorescence emission spectra of IM30-CFP and IM30-Venus, both recorded with donor fluorescence excitation (*cf.* 2.18.2.2), were compared to the spectrum of an IM30-CFP/Venus mixture. In this mixture, the ratio between IM30-CFP and IM30-Venus was coincidentally found to be  $\sim 1/1$ . The fluorescence of the IM30-CFP/Venus sample was normalized to the same amount of protein used for the IM30-CFP and IM30-Venus mutants, respectively. For this experiment, it should be kept in mind that the concentrations of IM30-CFP and IM30-Venus were not determined with the same method as for IM30-CFP/Venus (*cf.* 2.16.5.2 and 2.16.5.3). Therefore, the nature of this comparison was more qualitative. The spectra are shown in *Fig. 3.22*.

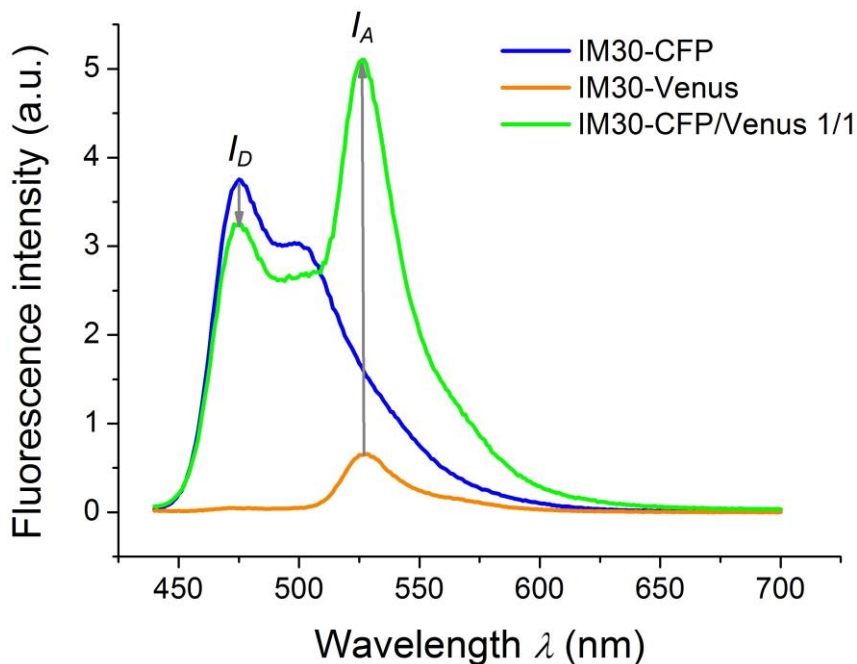


**Fig. 3.22: Fluorescence emission spectra of IM30-CFP, IM30-Venus and IM30-CFP/Venus**

Fluorescence emission spectra of IM30-CFP, IM30-Venus and IM30-CFP/Venus were recorded with an excitation wavelength of 420 nm and compared. The peak intensity alterations of donor and acceptor fluorescence emission are indicated via grey arrows, respectively.

As can be seen in *Fig. 3.22*, the donor fluorescence in the co-purified mixture is decreased compared to the spectrum of the single-labeled IM30-CFP whereas the acceptor fluorescence is increased compared to the single-labeled IM30-Venus. Those observations strongly indicate formation of a FRET pair. As mentioned above, this conclusion is more qualitative. However, it was important to see whether FRET is possible or not. The  $E_{rat}$  for the 1/1 mixture of IM30-

CFP/Venus was calculated to be 0.54 with a negligible error in a triplicate measurement (spectra are shown in *Fig. 5.7*).

### 3.4.4 $Mg^{2+}$ supports IM30 double-ring formation

As described in 1.4.2, IM30 is able to form pronounced ring structures, which can further assemble into double-rings and rod-like structures. Strictly speaking, the latter two might be called “pentamery structures” of IM30. The effect of  $Mg^{2+}$  on these IM30 super-complexes was investigated and is described in the following.

The results presented in 3.4.2 indicate a structural alteration of IM30 in presence of  $Mg^{2+}$ , which might result in an increased protection of the proteins’ C-terminus and/or increased double-ring formation. In fact, masking of the C-terminus inside a ring or a double-ring might explain the observations described above. To further investigate this issue, the C-terminally labeled mutants IM30-CFP and IM30-Venus, which can form a FRET pair when they are in proximity to each other (*cf.* 3.4.3), were mixed in a 1/1 molar ratio and were incubated with different  $MgCl_2$  concentrations (0-25 mM). The samples were measured in equilibrium and the FRET efficiency  $E_{rat}$  was calculated as described in 2.18.2.2. Furthermore, kinetic measurements were conducted after mixing the two labeled mutants in absence and presence of 7.5 mM  $MgCl_2$ . The results are illustrated in *Fig. 3.23*.

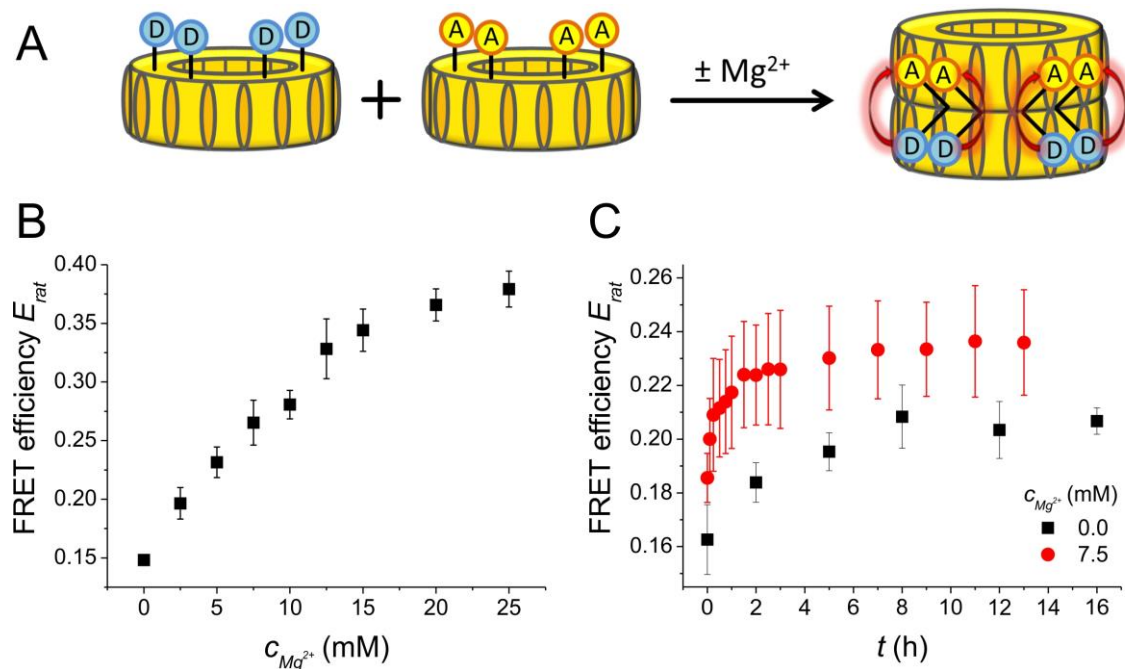


**Fig. 3.23: IM30-CFP and IM30-Venus in presence and absence of different  $Mg^{2+}$  concentrations**

The labeled IM30 mutants IM30-CFP and IM30-Venus were mixed in a 1/1 molar ratio in presence and absence of different  $Mg^{2+}$  concentrations to investigate potential double-ring formation (A). Equilibrium measurements (B) as well as kinetic measurements (C) were performed. Error bars represent the standard deviation ( $n=3$ ). The results in this figure are published in (Heidrich *et al.* 2018).

For the equilibrium measurement, which is shown in *Fig. 3.23B*, a steady increase of  $E_{rat}$  from  $\sim 0.15$  to  $\sim 0.40$  was observed with increasing  $Mg^{2+}$  concentration. A plateau was reached at  $Mg^{2+}$  concentrations  $>20$  mM. The increase indicates a  $Mg^{2+}$ -driven interaction of the two labeled protein species. In a complementary approach, the mixing of IM30-CFP and IM30-Venus in presence and absence of 7.5 mM  $MgCl_2$  was observed kinetically (*Fig. 3.23C*). For the sample lacking  $Mg^{2+}$ ,  $E_{rat}$  increased until after  $\sim 8$  h a plateau was reached at  $\sim 0.20$ . In presence of 7.5 mM  $Mg^{2+}$ , on the other hand,  $E_{rat}$  increased much faster, and a plateau was reached already after  $\sim 2$  h. Importantly, the final  $E_{rat}$  value ( $\sim 0.23$ ) was higher for the sample containing  $Mg^{2+}$ . The origin of this increase could have been a monomer exchange between differently labeled IM30 rings or a dye-dye crosstalk due to double-ring formation, which is illustrated in *Fig. 3.23A*. To tackle this problem, the maximum  $E_{rat}$  for a co-purified 1/1 mixture of IM30-CFP/Venus was calculated to be 0.54 with an insignificant error (spectra are shown in 5.5). Since in *Fig. 3.23B* a lower plateau for  $E_{rat}$  was reached in the absence as well as in presence of  $Mg^{2+}$ , it is reasonable to assume that a monomer exchange, which would have led to a similar  $E_{rat}$  as in the co-purified mixture, did not take place. Thus, an increased double-ring formation of the labeled IM30 variants in presence of  $Mg^{2+}$  seems most likely. Importantly, recent structural simulation of IM30 revealed that its C-terminus is probably located at one of the ring surfaces (Saur *et al.* 2017). Since the Förster radius of the CFP-YFP pair is  $\sim 50$  Å (Patterson *et al.* 2000) and the height of one IM30 is  $\sim 150$  Å (Saur *et al.* 2017) (or  $\sim 300$  Å for double-rings), an increased  $E_{rat}$  was probably only possible upon double-ring formation with the C-termini facing each other (top-to-top orientation).

To confirm the conclusion drawn above, a similar experiment as shown in *Fig. 3.23B* was performed, using IM30-CFP/Venus with a ratio of 27% CFP and 63% Venus. The protein mixture was again incubated with increasing  $MgCl_2$  concentrations and the  $E_{rat}$  values were calculated. The results are shown in *Fig. 3.24*.

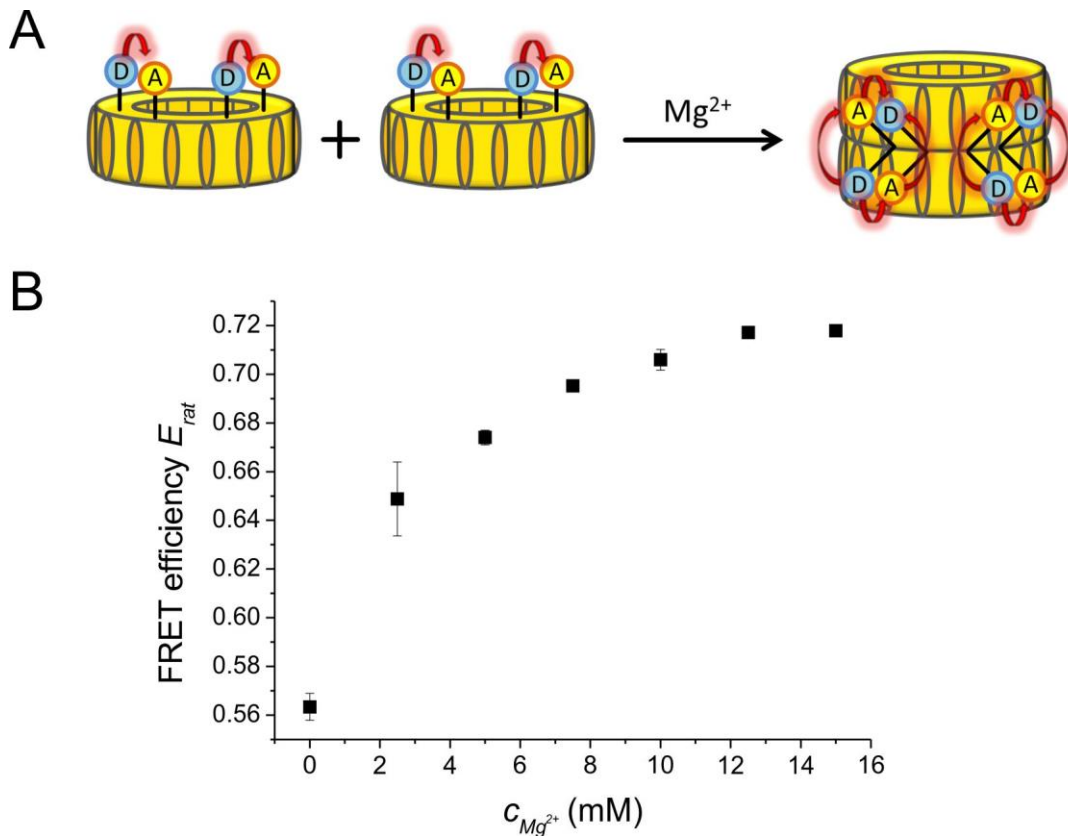


**Fig. 3.24: IM30-CFP/Venus in presence and absence of different  $Mg^{2+}$  concentrations**

IM30-CFP/Venus was exposed to different  $Mg^{2+}$  concentrations to investigate potential double-ring formation (A, B). Error bars represent the standard deviation ( $n=3$ ). Note that this figure is not directly comparable to **Fig. 3.23** since a ratio of 27% CFP and 63% Venus was used here.

As displayed in **Fig. 3.24B**, the  $E_{rat}$  values increased from  $\sim 0.56$  to  $\sim 0.72$  until a plateau was reached at a  $Mg^{2+}$  concentration  $>12$  mM. Importantly, the experiment shown in **Fig. 3.24B** is not directly comparable to the results in **Fig. 3.23B** due to the different ratio of IM30-CFP/IM30-Venus. Nevertheless, the main conclusion is identical for both experiments: The increase in the  $E_{rat}$  values can most likely be explained by increased double-ring formation of IM30 in presence of  $Mg^{2+}$ , illustrated in **Fig. 3.23A** and **Fig. 3.24A**. For the experiment using IM30-CFP/Venus (**Fig. 3.24B**), this could be explained by the consideration that a simple monomer exchange would not have changed the FRET efficiency for statistical reasons. The observation that the  $E_{rat}$  values were dramatically higher compared to those obtained from the single-labeled mixtures (**Fig. 3.23B**), might be explained by the assumption that in the IM30-CFP/Venus mixture the energy transfer took place ring-internally as well as ring-externally, leading to an overall increased FRET.

An increased formation of IM30 double-rings upon  $Mg^{2+}$  addition should be easily observable via electron microscopy. Thus, TEM was performed in cooperation with Kristiane Rusitzka and Benedikt Junglas. The micrographs are presented in **Fig. 3.25**.

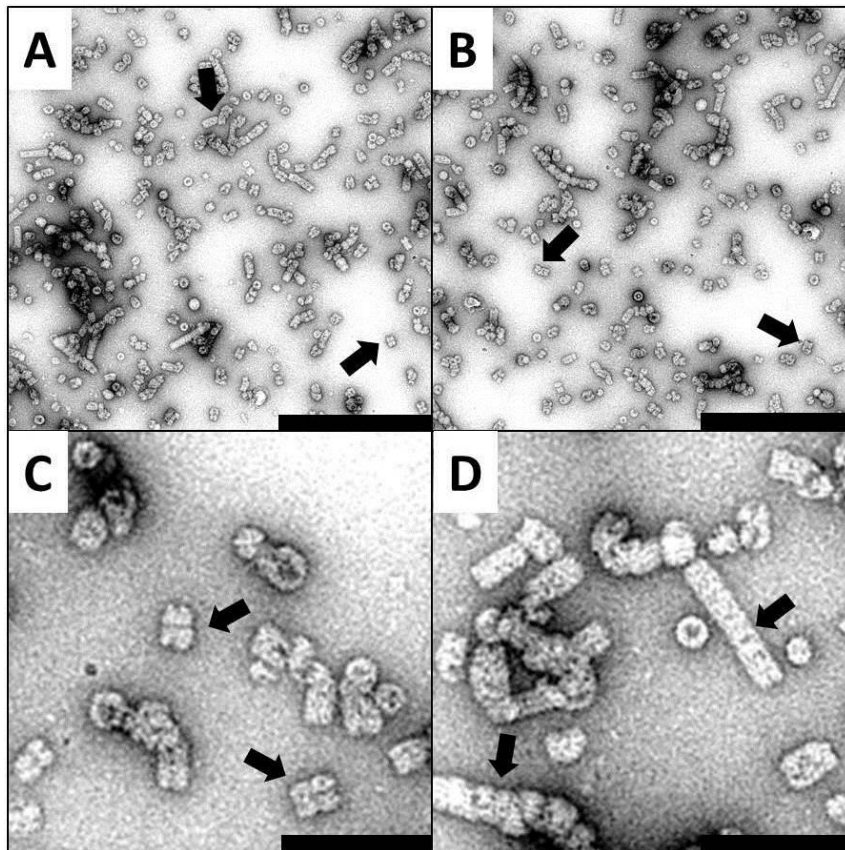


**Fig. 3.25: TEM micrographs of IM30 in presence of  $Mg^{2+}$**

Representative TEM micrographs of IM30 samples in presence of 15 mM  $Mg^{2+}$  are shown. Arrows indicate double-rings (A, B, C) and rods (D). Scale bars represent 500 nm (A, B) and 125 nm (C, D). In cooperation with Kristiane Rusitzka and Benedikt Junglas.

Indeed, TEM of IM30 in presence of  $Mg^{2+}$  revealed an increased formation of IM30 double-rings. Compared to *Fig. 3.3*, these higher-ordered oligomers were also observed in absence of  $Mg^{2+}$ , but not as extensively as shown in *Fig. 3.25*. Those observations support the assumption that ring stacking is the major cause of the increasing  $E_{rat}$  value for IM30 in presence of  $Mg^{2+}$ .

In conclusion, the experiments described in 3.4.2, which indicated structural rearrangements and the protection of the C-terminus of IM30 in presence of  $Mg^{2+}$ , can probably be explained by an increased IM30 double-ring formation and hiding of the C-terminus at the interface between two rings.

### 3.5 IM30-membrane interactions

In former work, it has been demonstrated that IM30 interacts with membranes containing the negatively charged thylakoid lipids PG and SQDG (Otters *et al.* 2013; Suppes 2013; Hennig *et al.* 2015). With the neutral thylakoid lipids MGDG and DGDG on the other hand, no interaction has been observed yet (Suppes 2013; Hennig *et al.* 2015). Consequently, those results suggested an electrostatic nature of the IM30-membrane interaction. This hypothetical ionic binding was investigated and is described in the following.

#### 3.5.1 IM30 interacts with negatively charged membranes

First, it was supportive to have a further proof for the interaction of IM30 with negatively charged membranes. Thus, the influence of membrane binding on the IM30 stability against tryptic digestion was tested similarly as in the previous tryptic digestion using  $Mg^{2+}$  (*cf.* 3.4.2). Membrane binding of IM30 could result in an altered accessibility for proteases and, thus, a different degradation pattern on the SDS-PAGE gel.

Tryptic digestion was performed for samples containing IM30 in presence and absence of 100% DOPG liposomes. Another negative control sample containing 100% DOPC liposomes was also prepared, since it has been indicated that IM30 does not to interact with DOPC (Suppes 2013; Hennig *et al.* 2015). Upon trypsin addition, samples were taken after different time intervals, mixed with 5x SDS sample buffer in order to stop the reaction and loaded on an SDS gel. Additionally, in each gel, a sample of IM30 which was not incubated with trypsin was loaded for comparison. The experiment was performed in cooperation with Carmen Siebenaller as described in 2.16.11.2. The gels are shown in *Fig. 3.26*.

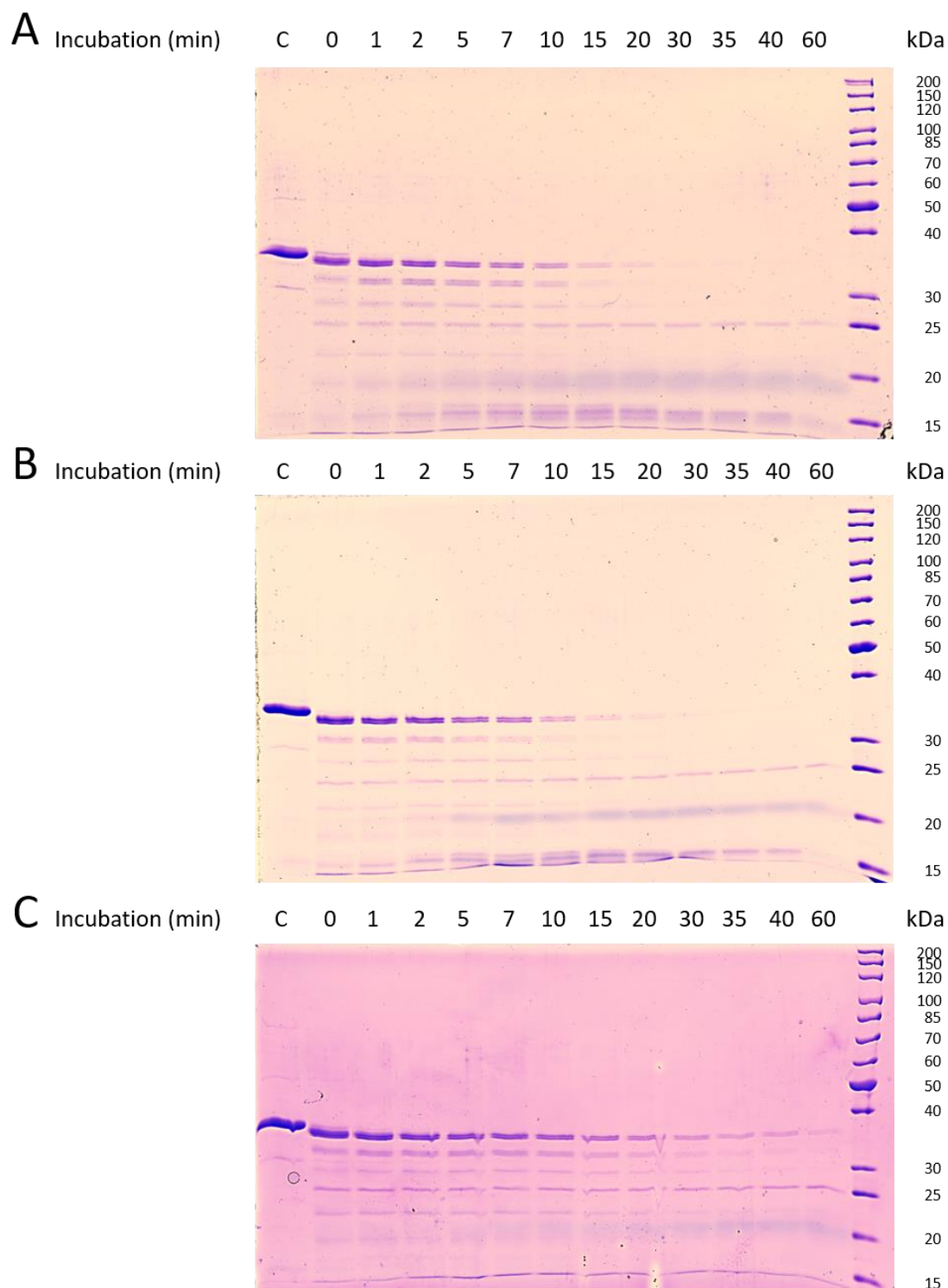


**Fig. 3.26: Tryptic digestion of IM30 in presence and absence of liposomes**

Tryptic digestion was performed to investigate the proteolysis stability of IM30 upon membrane binding. Samples from a tryptic digestion of IM30 in the absence (A) and presence of 0.3 mM 100% DOPC (B) and 100% DOPG (C) liposomes were separated on a 12% SDS gel. Indicated are the incubation times of the respective samples with trypsin. The trypsin band can be found in each lane on the SDS gels below 25 kDa. The experiment was repeated three times. In cooperation with Carmen Siebenaller.

In all gels shown in *Fig. 3.26*, the IM30 full-length band is located at ~37 kDa (*cf. Fig. 3.2*). A degradation band below the full-length band, which was assumed to represent the N-terminal

PspA domain of IM30 lacking the C-terminus (*cf. Fig. 3.18*), is also found in each gel already at 0 min after the death time. Other than in *Fig. 3.18*, further degradation bands were visible in this experiment. It should be mentioned that for experimental reasons, the tryptic digestion of IM30 in presence and absence of  $Mg^{2+}$  was performed at 37 °C whereas in presence and absence of liposomes 15 °C were applied. Furthermore, it was not possible to conduct a control assay to investigate the influence of liposomes on the trypsin activity, probably due to interactions of BAEE with liposomes. However, due to the observation that in the gels shown in *Fig. 3.26* samples containing DOPC and DOPG behave different concerning tryptic digestions of IM30, an influence of lipids on the trypsin activity seems unlikely.

*Fig. 3.26A* shows the tryptic digestion of IM30 in absence of liposomes. The main band as well as the degradation band started to vanish after ~5 min. The IM30 full-length band was almost vanished at ~30 min and the degradation band at ~20 min. Unsurprisingly, the digestion pattern was identical for the negative control sample containing IM30 incubated with 100% DOPC liposomes, shown in *Fig. 3.26B*. Since IM30 was not supposed to interact with the zwitterionic DOPC as demonstrated in (Suppes 2013; Hennig *et al.* 2015), the protein probably stayed in solution and had the same availability for trypsin as in the sample lacking liposomes. For the sample containing 100% DOPG liposomes, on the other hand, the IM30 full-length band and the degradation band were visible until 7 min and both bands were still slightly visible after 60 min. Overall, the stability of IM30 against tryptic digestion seems to be increased in presence of 100% DOPG liposomes since it took more time to completely digest the protein. This result could be explained by a shielding effect of the membrane and/or a structural alteration of IM30 upon membrane binding. Both cases would result in an altered trypsin accessibility.

### 3.5.2 IM30 interacts with membranes via electrostatic forces

To investigate a hypothetical electrostatic interaction of IM30 with negatively charged membranes, a displacement assay was performed. Here, IM30 was pre-incubated with 100% DOPG liposomes and titrated with an increasing NaCl concentration to see whether an excess of  $Na^+$  could electrostatically shield IM30 from the membrane surface (illustrated in *Fig. 3.27A*). This assay only worked in the case of an electrostatic interaction between IM30 and DOPG. Furthermore, in order to distinguish between bound and non-bound IM30, dissociation of the protein from the membrane must result in an altered environment of W71 due to the fact that the tryptophan fluorescence depends on the environment of the fluorophore. The experiment was conducted as described in 2.18.2.6 and the results are shown in *Fig. 3.27*.

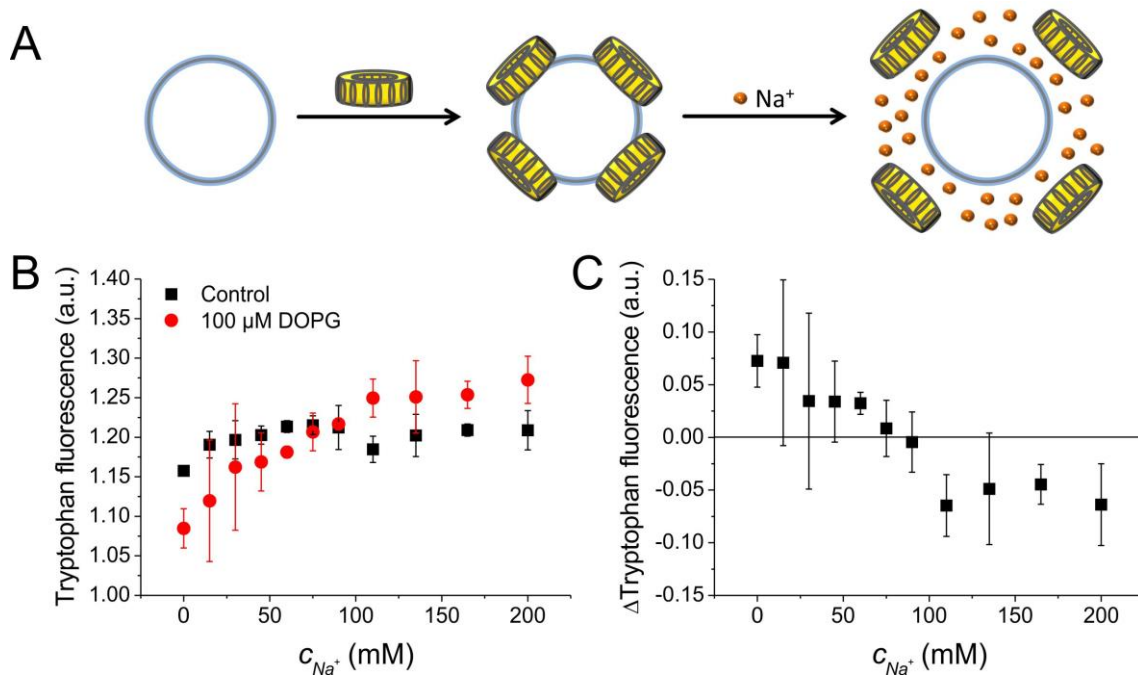


**Fig. 3.27: Electrostatic interaction of IM30 with DOPG membranes**

It was tested whether  $Na^+$  can electrostatically shield IM30 from 100% DOPG liposomes (A). Samples of IM30 in presence and absence of DOPG were titrated with increasing NaCl concentrations (B) and the difference between the two titration curves was calculated (C). The line indicates a difference of 0. Error bars represent the standard deviation ( $n=3$ ).

The titration of 100% DOPG liposomes, which were pre-incubated with IM30, with  $Na^+$  reveals a steady increase of the tryptophan fluorescence (see Fig. 3.27B). A plateau is reached at  $\sim 100$  mM NaCl. This increase is not visible for the control sample lacking liposomes, excluding a direct influence of  $Na^+$  on IM30. Strikingly, the titration curve for the samples containing liposomes exceeds the control curve above  $\sim 100$  mM NaCl to some extent. This observation might be explained by the assumption that the previously bound IM30 was completely released from the liposomes above this point and therefore had a similar tryptophan fluorescence compared to the control sample. When calculating the difference between the two titration curves, the dissociation curve for IM30-DOPG is revealed (see Fig. 3.27C), with a constant difference above  $\sim 100$  mM NaCl, again indicating an electrostatic shielding of the liposomes by  $Na^+$ . Due to the initial shift of the tryptophan fluorescence in the  $Na^+$  titration curve and the difference between the two curves (Fig. 3.27B) resulting in a dissociation curve, the displacement of IM30 by  $Na^+$  from the 100% DOPG liposomes is strongly implied. Thus, it seems reasonable to assume that the IM30-DOPG interaction has an electrostatic nature.

Next, the question was tackled whether the electrostatic interaction of IM30 with negatively charged membranes is specific for the negatively charged thylakoid lipids and, thus, headgroup-dependent. A similar assay was performed as already described in (Suppes 2013). Here, Laurdan-labeled liposomes containing 80% of the zwitterionic lipid DOPC and 20% of another lipid of interest were prepared in presence and absence of IM30. The negatively charged thylakoid

lipids PG and SQDG as well as the anionic non-thylakoid lipid PS were tested. Upon membrane binding of IM30, the Laurdan GP value was assumed to change compared to the respective control sample lacking IM30 (*cf.* 2.18.2.3). Additionally, a sample containing 100% DOPC liposomes was prepared as negative control. The experiment was conducted as described in 2.18.2.3, and the results are shown in *Fig. 3.28*.

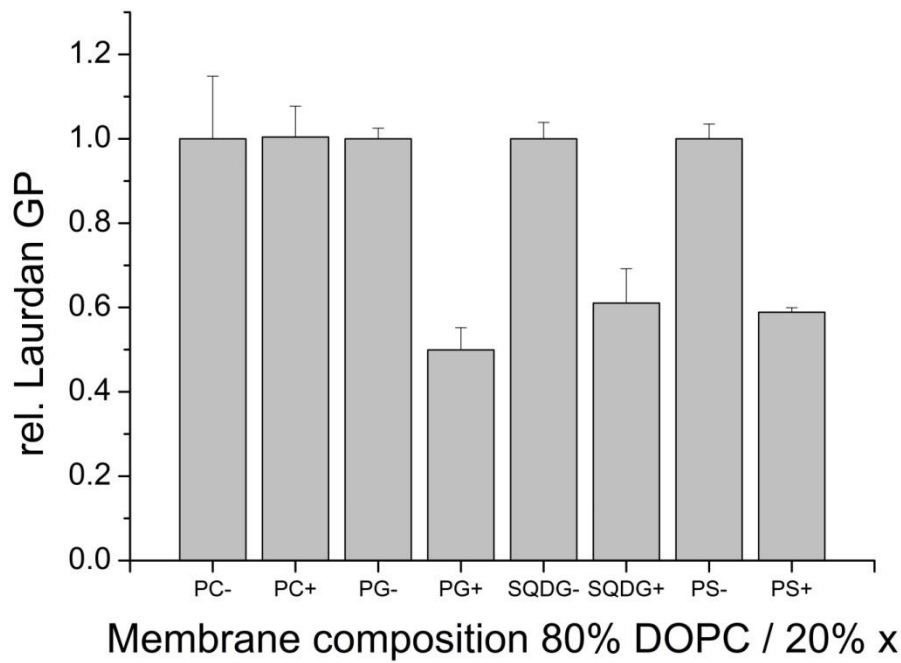


**Fig. 3.28: Negatively charged headgroup binding of IM30**

To check whether the electrostatic interaction of IM30 with negatively charged membranes is specific for anionic thylakoid lipids, lipid binding was investigated by using Laurdan-labeled liposomes containing 80% of the lipid PC and 20% of the thylakoid lipids PG and SQDG or the non-thylakoid lipid PS, respectively. The relative Laurdan GP values are plotted for samples containing IM30 (+) and control samples lacking the protein (-). The control samples are set as 1. Error bars represent the standard deviation ( $n=3$ ).

As can be seen in *Fig. 3.28*, the relative Laurdan GP values decrease to  $\sim 0.5$  for all tested negatively charged lipids in presence of IM30, since the protein probably increased the membrane rigidity (*cf.* 2.18.2.3). Importantly, the control sample containing 100% DOPC liposomes was not influenced by IM30, which supports the eligibility of DOPC as bulk lipid. The observation that also the non-thylakoid lipid PS induced IM30-membrane interaction implies a binding of IM30 to negatively charged lipids, including non-thylakoid lipids. This result is in perfect agreement with observations made in (McDonald *et al.* 2015), where *E. coli* PspA was shown to bind to PS.

In conclusion, the results imply that IM30 binds to negatively charged membranes, independent from the availability of thylakoid lipids, in an electrostatic interaction.

### 3.6 The IM30 structure affects membrane interaction

The physiological relevance of IM30 rings is a widely-discussed topic. Upon deletion of the first  $\alpha$ -helical domain of IM30 from *Arabidopsis*, which was assumed to be involved in IM30 oligomerization, ring formation as well as membrane binding was disturbed (Otters *et al.* 2013). Thus, it has been assumed that the oligomerization of the protein is necessary for membrane interaction (Otters *et al.* 2013). Furthermore, TEM measurements indicated that IM30 rings bind to negatively charged lipid bilayers (Hennig *et al.* 2015). Since smaller IM30 oligomers (*e.g.* tetramers, *cf.* 3.1.3) are not visible in TEM micrographs, it has been an open question whether also lower-ordered IM30 structures can bind to lipids and to which extent. First hints were given in (Hennig 2014), where 100% DOPG membrane binding of C7 was qualitatively shown. In order to further investigate an interaction of lower-ordered IM30 oligomers with membrane and to quantify interaction of IM30 WT and mutants with membranes, a quantitative binding assay for the IM30 wildtype/IM30 mutants-membrane interaction was established. The set of IM30 mutants introduced in 3.1.1 and the crosslinked IM30 WT (*cf.* 3.3.2.1) were used for the experiments in order to benefit from different IM30 structural variants.

To directly compare membrane interaction of higher-ordered ring structures and tetrameric versions of IM30, the determination of the dissociation constants  $K_D$  via a binding assay using 100% DOPG liposomes, labeled with Laurdan as probe, was performed using the WT and the C7 mutant protein. For the WT, a mainly higher-ordered ring structure formation has been suggested recently via SEC, as well as the formation of tetramers for C7 (Heidrich *et al.* 2016). Samples were prepared with a constant DOPG concentration of 75  $\mu\text{M}$  and an increasing protein amount of 0.4-7.0  $\mu\text{M}$ . An essential condition of this binding assay was the excess of the protein compared to the available lipid binding surface (*cf.* 5.13.2). The reasons why this requirement was most probably fulfilled are listed in 2.18.2.3. For each sample, Laurdan spectra were recorded, from which the GP values were calculated and plotted against the protein concentration. The experiment was performed as described in 2.18.2.3, and the results for the IM30 WT and C7 are shown in *Fig. 3.29*.

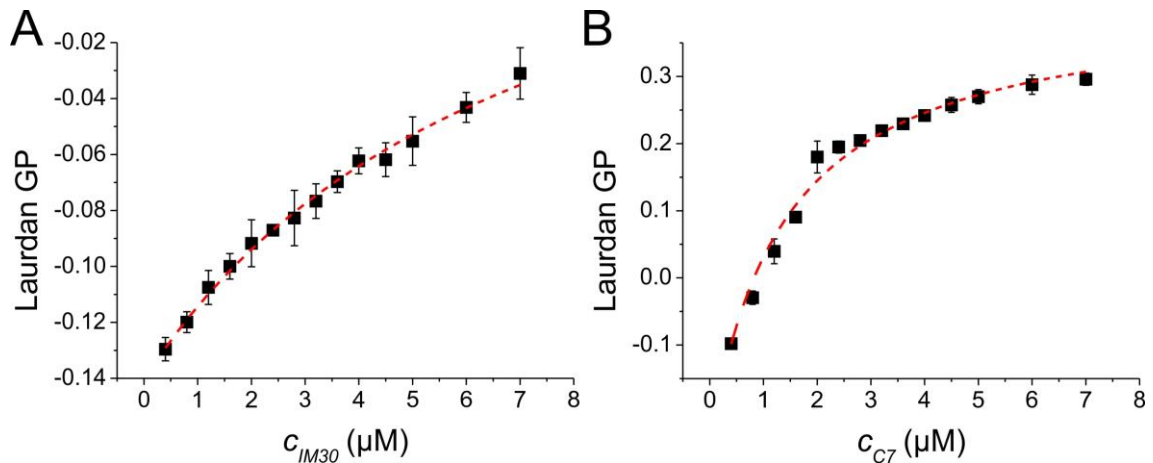


**Fig. 3.29:  $K_D$  determinations of the interaction of IM30 and C7 with DOPG**

To compare the DOPG binding affinity of different IM30 structural variants with each other,  $K_D$  determinations for IM30 (A) and C7 (B) were performed. The data were fitted with a binding fit, from which the dissociation constants  $K_D$  was calculated.  $R^2=0.997$  (A),  $R^2=0.998$  (B), error bars represent the standard deviation ( $n=3$ ). The results in this figure are published in (Heidrich *et al.* 2016).

Aside from the quantitative information, the results shown in Fig. 3.29B clearly indicated the DOPG binding of C7, since an increase of the GP values with increasing protein concentration was monitored. This discovery confirmed the result in (Hennig 2014) and showed that binding of IM30 to negatively charged membranes does not depend on IM30 ring formation.

When comparing the DOPG binding curves of IM30 and C7 (Fig. 3.29), it seems noticeable that the plateau of the C7 binding curve is almost reached at the highest concentration used in this assay, which is not the case for the binding curve of IM30. This observation indicated a higher binding affinity of C7. Strikingly, the GP values obtained for the samples containing the mutant were in general much higher compared to the WT. This difference could originate from the structures of the different protein species on membranes, which might have had different effects on the membrane polarity and, thus, on the Laurdan fluorescence. Since only the concentration at which the plateau of the GP values is reached is important for the evaluation of the binding affinity and, thus, the absolute GP values are neglected at this point.

The curves obtained from the binding assays (Fig. 3.29) were fitted with a binding fit (*cf.* 5.13.1.1), from which the dissociation constants  $K_D$  were calculated. The  $K_D$  values for IM30, all investigated mutants and the crosslinked variant IM30-X are listed in Table 3.4, the remaining binding assay diagrams are presented in 5.11.

**Table 3.4:  $K_D$  determination for the DOPG interaction of IM30 and IM30 mutants**

Mutant	Structure	$K_D$ ( $\mu\text{M}$ )*
IM30	Rings	$7.20 \pm 0.95$
IM30-X	Rings (crosslinked)	$9.35 \pm 7.29$
$\Delta\text{CT}$	Rings	$5.71 \pm 0.76$
C4	Rings	$2.05 \pm 0.39$
C7	Tetramers	$1.39 \pm 0.22$

Several results in this table are published in (Heidrich *et al.* 2016). \*Errors represent the standard deviation ( $n=3$ ).

It must be mentioned that the calculated  $K_D$  values listed in *Table 3.4* were rather apparent than originating from a typical 2<sup>nd</sup> order reaction. Thus, they do not reveal information concerning potential structural alteration during the membrane interaction. However, as they were measured under equilibrium conditions, they allow a comparison of IM30 and the IM30 mutants with one another.

Most interesting is the comparison between the the  $K_D$  values of IM30 and the C7 mutant in order to illuminate differences between the binding of ring structures and tetramers, respectively. With 7.20 vs. 1.39  $\mu\text{M}$ , the  $K_D$  value is significantly increased ( $\sim 5$ -fold) for IM30 compared to C7. Since a higher  $K_D$  stands for a weaker binding, it can consequently be speculated that the formation of higher-ordered oligomers counteracts membrane binding of IM30. Due to the assumption that the measurement was performed in excess of the protein compared to the available lipid binding surface, it seems reasonable to assume that only few potential ring dissociations of IM30 took place. However, the increased membrane binding affinity of lower-ordered structures indeed supports the idea of IM30 ring dissociation.

The observation that IM30-X binds to membranes was important to confirm a functional membrane binding of the protein in presence of the crosslink reagent (*cf.* 3.3.2.1), even though the error for the calculated  $K_D$  value was rather high. Besides that, the dissociation constant seems to lie in the same size range as the values for the other investigated proteins. This is of interest when comparing the fusion activity of IM30-X with the WT (*cf.* 3.9.2). Furthermore, the similar  $K_D$  values of IM30 and IM30-X again indicate the disability of the WT to dissociate when in excess to the available membrane surface.

For the DOPG interaction of the  $\Delta\text{CT}$  and C4 mutants, smaller  $K_D$  values were calculated compared to the IM30 WT. Interestingly, an increased hydrophobic surface of both the  $\Delta\text{CT}$  mutant and IM30 WT incubated with  $\text{Mg}^{2+}$  has already been suggested (Junglas 2016). Indeed, an increased membrane binding affinity of IM30 in presence of  $\text{Mg}^{2+}$  was indicated via SFG measurements (Hennig *et al.* 2015), which would be in agreement with this theory. The effect of  $\text{Mg}^{2+}$  on the IM30 binding to negatively charged surfaces is further described in 3.7. The enhanced binding affinity of the mainly ring-forming C4 mutant, on the other hand, could originate from a decreased hydrophobicity due to the mutation in the loop 2 region, which might be involved in membrane interaction via electrostatic forces (*cf.* 3.5.2).

In conclusion,  $K_D$  values for the interaction of IM30 WT and several IM30 mutants with DOPG were determined. Most importantly, the C7 mutant, which seems to predominantly form tetramers (Heidrich *et al.* 2016), has been observed to bind to negatively charged membranes. A lower  $K_D$  for the interaction with DOPG was determined for C7 and, thus, an increased membrane binding affinity of the mutant compared to the mainly ring forming IM30 WT.

### 3.7 $Mg^{2+}$ affects the interaction of IM30 with negatively charged surfaces

In previous experiments, an effect of  $Mg^{2+}$  on the IM30 structure resulting in stabilization of the double-rings was observed (*cf.* 3.4). Furthermore, it has been demonstrated that the protein binds to negatively charged membranes (*cf.* 3.5). Thus, the effect of  $Mg^{2+}$  on the IM30 interaction with anionic surfaces was investigated. Recently performed SFG measurements already showed an increased binding affinity of IM30 to DOPG monolayers in presence of  $Mg^{2+}$  (Hennig *et al.* 2015). To further investigate this behavior, SPR measurements were performed in cooperation with Prof. Tobias Weidner and Bernhard Menges. The advantage of this method is the exclusion of background fusion effects due to the experimental design by using a fatty acid monolayer. Furthermore, effects of  $Mg^{2+}$  to the binding surface are not as relevant for the signal output as they would have been using other experimental set-ups, *e.g.* Laurdan experiments.

Probably due to repulsive interactions between lipids, all initial attempts to create a negatively charged membrane surface on the Au sensor chips failed. Thus, the thiol-coupled fatty acid 16-MHDA was used as the negatively charged surface. The binding of IM30 and IM30/ $Mg^{2+}$  to 16-MHDA was observed by measuring kinetics. Furthermore, after addition of each component, a scan measurement was conducted to evaluate layer thicknesses. The measurements were performed and evaluated as described in 2.18.6. The results of representative measurements are illustrated in *Fig. 3.30A* and *B*. The raw data of the kinetic measurements are shown in *Fig. 5.27*.

*Fig. 3.30A* shows representative scan measurements. As expected, the incident angle of light  $\Theta_{SPR}$  is shifted after addition of 16-MHDA and IM30, respectively, indicating a successful binding of the components. Importantly, a control measurement demonstrated that IM30 does not bind to the empty Au surface (*cf. Fig. 5.28*). In *Fig. 3.30B*, representative kinetic measurements were chosen to illustrate the difference between the binding of IM30 in absence of  $Mg^{2+}$  and IM30 pre-incubated with 10 mM  $Mg^{2+}$  to the 16-MHDA surface, respectively. Obviously,  $Mg^{2+}$  has a noticeable effect on the interaction. In presence of the ion, the plateau was already reached after ~3000 s, whereas in its absence it took ~6000 s. Furthermore, upon  $Mg^{2+}$  addition, the

maximal reflection intensity  $I_{SPR}$  of the laser signal was dramatically increased, indicating a thicker layer and, thus, an increased binding affinity of the protein in presence of  $Mg^{2+}$ .

Due to experimental conditions, it was not possible to compare different SPR measurements, as shown in *Fig. 3.30B*, in a quantitative manner, since the bound protein apparently could not be completely washed off after binding (*cf. Fig. 5.29*) and, consequentially, the same sensor chip could not be used for multiple measurements. Thus, for each experiment, new sensor chips were used. To confirm a qualitative reproducibility and to allow a comparison concerning layer thicknesses and surface coverages of different sensor chips, a rough evaluation of four measurements (two control experiments and two experiments in presence of  $Mg^{2+}$ ) was conducted via iterative fitting of simulated SPR curves to the scan data as described in 2.18.6. The results are listed in *Table 3.5*.

**Table 3.5: Estimated layer thicknesses of the SPR experiments**

Layer	Thickness (nm) + IM30		Thickness (nm) + IM30/ $Mg^{2+}$		Medium surface coverage (%)	
	#1	#2	#1	#2	+IM30	+IM30/ $Mg^{2+}$
Cr	0.86	1.73	1.80	2.47	100*	100*
Au	47.24	47.39	48.19	46.96	100*	100*
16-MHDA**	1.35	1.44	1.43	1.37	~70	~70
IM30 $\pm$ $Mg^{2+}$	4.92	4.30	6.57	6.72	~31 (ring)	~44/22 (ring/double-ring)

In cooperation with Prof. Tobias Weidner and Bernhard Menges. \*The 100% surface coverage for Cr and Au was assumed due to the preparation of the sensor chips. \*\*The length of a 16-MHDA molecule is 2 nm (Wang *et al.* 2014b). The height of an IM30 ring was assumed to be 15 nm and 30 nm for an IM30 double-ring (Saur *et al.* 2017).

As can be seen in *Table 3.5*, the 16-MHDA layer had a similar thickness and a surface coverage of ~70% in each experiment, indicating the reproducibility of the binding of the thiol-coupled fatty acid. Noteworthy, steric reasons might have prevented a 100% surface coverage. Furthermore, from these measurements, it could not be decided whether 16-MHDA was homogeneously distributed on the Au surface or if it formed raft-like areas. The IM30 and IM30/ $Mg^{2+}$  layer thicknesses also seemed reproducible. Strikingly, the values differed in presence and absence of  $Mg^{2+}$  as already mentioned above. Since the precise structure of IM30 when bound to negatively charged surfaces is not known and might include partial deoligomerization of the IM30 rings, it was hardly possible to estimate a surface coverage. Thus, a quantitative comparison of the protein amount bound to the 16-MHDA layer in presence and absence of  $Mg^{2+}$  was difficult at this point, even though an increased binding affinity of IM30/ $Mg^{2+}$  was already implied in (Hennig *et al.* 2015). However, based on former SFG measurements which suggested an upright monomer orientation on lipid monolayers and, thus, the disability of IM30 rings to dissociate under these conditions (Hennig *et al.* 2015), the existence of IM30 rings on the 16-MHDA layer could be assumed. For IM30 pre-incubated with  $Mg^{2+}$  it seemed reasonable to assume that the ring structure and/or double-ring structure are stabilized. Using the height of an IM30 ring of 15 nm or 30 nm for a double-ring (Saur *et al.* 2017), it could be estimated that the protein covered

~31% of the surface in the absence and ~44% (as rings) or ~22% (as double-rings) in presence of  $Mg^{2+}$ , respectively. These values seemed justified considering the approximation that not the whole but instead less than ~50% of the binding area might have been available for protein binding due to non-perfect packing of multiple proteins, as it has been calculated for the binding of globular proteins on cylindric gold nanorods, which were coupled with lipids (Pannwitt 2015).

The results shown in *Fig. 3.30B* imply an increased association rate constant  $k_{on}$  for the IM30-16-MHDA interaction in presence of  $Mg^{2+}$ . To further support this observation, two kinetic experiments, including the addition of both components sequentially, were performed on the identical sensor chip and are illustrated in *Fig. 3.30C* and *Fig. 3.30D*.

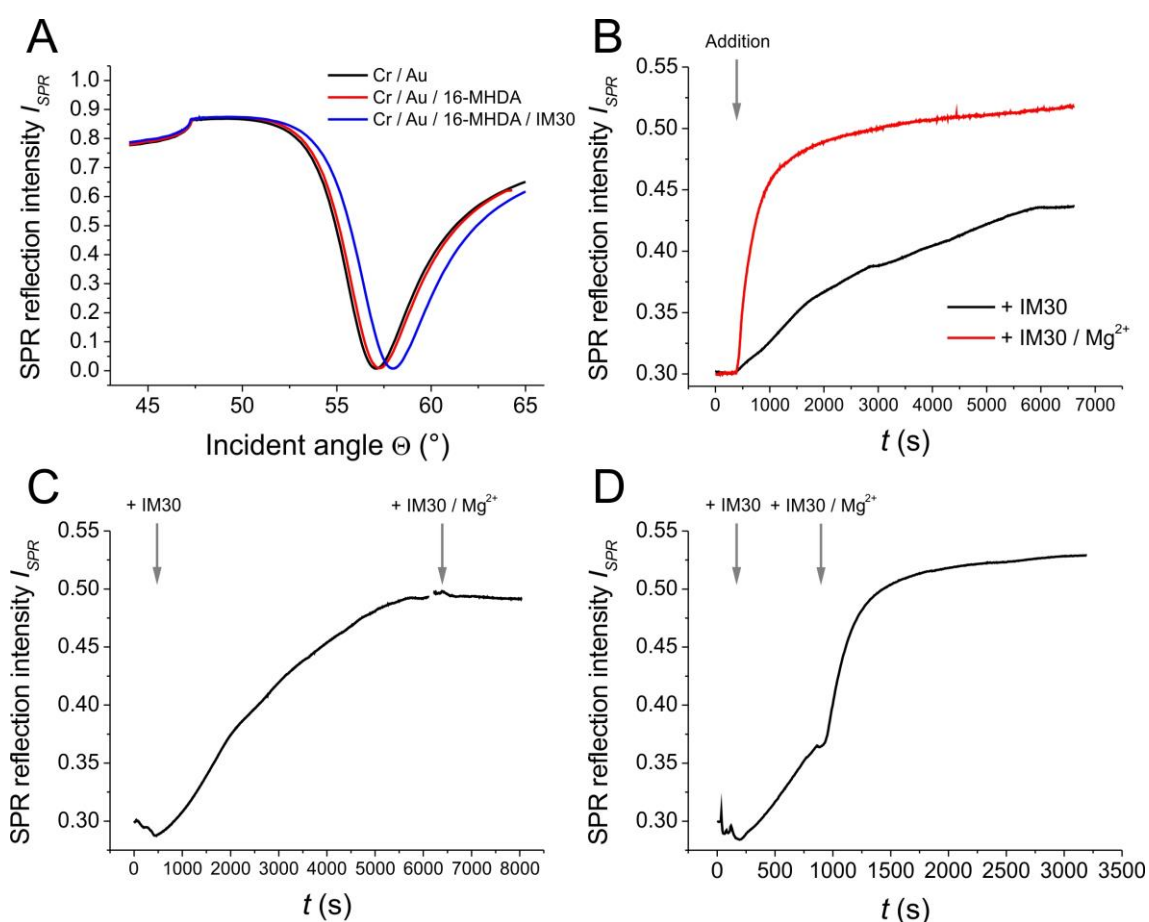


**Fig. 3.30:** SPR measurements of IM30 interacting with 16-MHDA surfaces in presence and absence of  $Mg^{2+}$

To investigate the effect of  $Mg^{2+}$  on the IM30 interaction with anionic surfaces (here: 16-MHDA), SPR measurements were performed. Addition of IM30 and IM30/10 mM  $Mg^{2+}$  to the 16-MHDA surface were observed in scan measurements (A) as well as kinetically (B). Note that new sensor chips were used for each approach. To have a further direct comparison, IM30 and IM30/ $Mg^{2+}$  were added to the identical sensor chip sequentially after different durations (C, D). The experiments were repeated two times, representative data are shown. In cooperation with Prof. Tobias Weidner and Bernhard Menges.

In the experiment shown in *Fig. 3.30C*, an IM30 sample was initially added to the 16-MHDA surface until a plateau for  $I_{SPR}$  was reached. Then, IM30 pre-incubated with  $Mg^{2+}$  was added. As expected, the surface was already completely covered and no further increase of the reflection

intensity was observed. In another approach, shown in *Fig. 3.30D*, the second addition step of IM30/Mg<sup>2+</sup> was performed before the plateau was reached. Here, a second increase was recorded which was significantly stronger than the first increase when IM30 in absence of Mg<sup>2+</sup> was added. In this experiment, the enhancing effect of Mg<sup>2+</sup> on the association kinetics is strongly indicated.

In summary, the SPR measurements revealed an altered association kinetic and binding affinity of IM30 to negatively charged surfaces in presence of Mg<sup>2+</sup>.

### 3.8 Membrane interaction affects the IM30 oligomerization state

In former work and as part of this thesis, the required membrane properties and protein structure for the IM30-membrane interaction were observed: Most likely, the membrane needs to contain negatively charged lipids (*cf.* 3.5.1) (Suppes 2013). Furthermore, it has been indicated that IM30 ring oligomers as well as lower ordered structures can bind to membranes (*cf.* 3.6) (Hennig *et al.* 2015). Nevertheless, the effect of membrane interaction on the IM30 oligomeric structure was not investigated so far. Thus, the questions if and under which conditions the IM30 ring dissociate on membranes were further investigated.

In a preliminary experiment, dissociation of the higher-ordered IM30 ring structures on liposomes was tested. IM30 was incubated with increasing lipid concentrations of 100% DOPG or 60%/40% MGDG/DOPG (0-3000  $\mu$ M), respectively, in presence and absence of 7.5 mM MgCl<sub>2</sub>. Subsequently, the crosslinker glutaraldehyde was added and an SDS-PAGE analysis was performed. Also, control samples lacking the crosslinker were loaded on the same SDS-PAGE. On the SDS gel, the IM30 monomer band was only visible upon oligomer dissociation since the monomers were subsequently distributed on the membrane and could not be cross-linked anymore. On the other hand, if no monomer band was visible, the presence of stable ring structures or lower-ordered oligomers was indicated. The experiment was performed as described in 2.16.8, and the results are shown in *Fig. 3.31* for 100% DOPG liposomes and in *Fig. 3.32* for 60%/40% MGDG/DOPG liposomes.

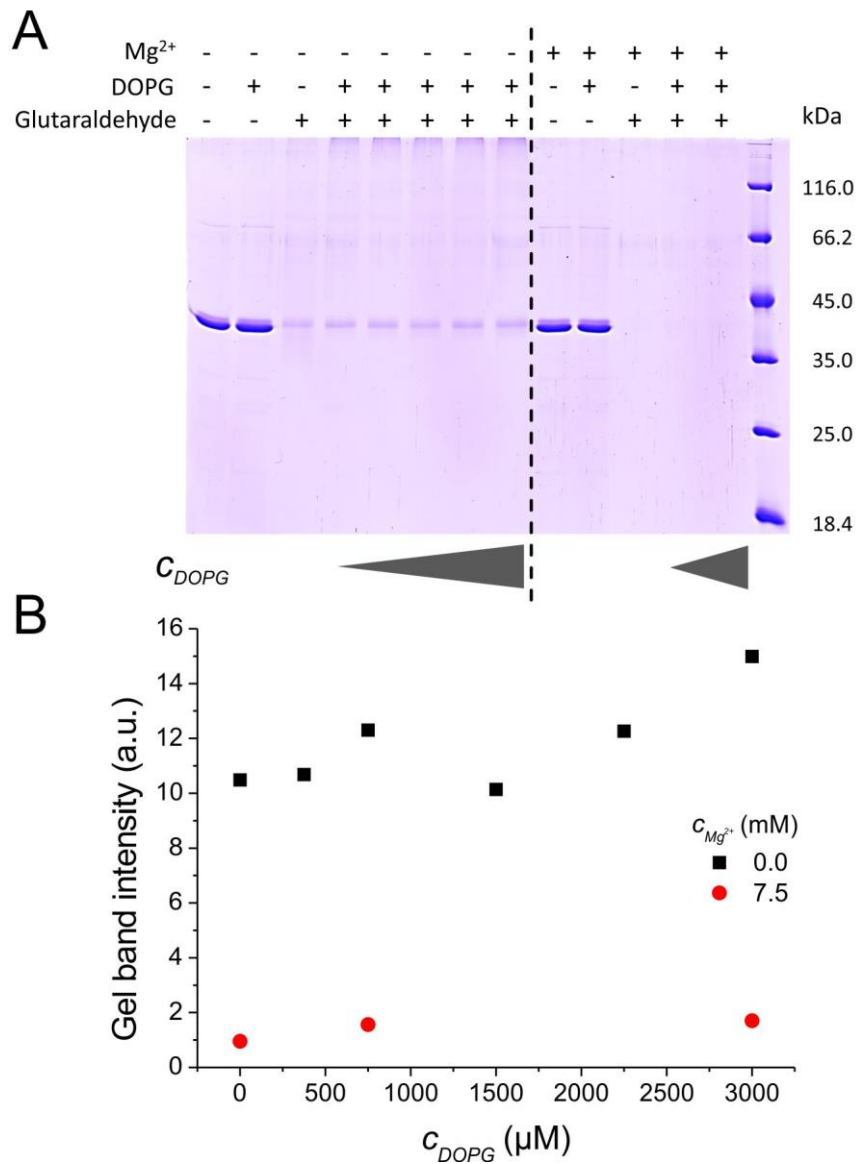


**Fig. 3.31: IM30 ring dissociation in presence of 100% DOPG liposomes**

The IM30 ring dissociation in presence of 100% DOPG was tested in order to investigate structural alteration of the protein upon membrane addition. IM30 was incubated with different lipid concentrations in presence and absence of 7.5 mM  $Mg^{2+}$ , respectively. Afterwards, the crosslinker glutaraldehyde was added, and the samples were loaded on a 12% SDS gel (A). Furthermore, the IM30 gel bands from the samples including lipids were graphically evaluated via ImageJ 1.47t, and the gel band intensities were plotted against the lipid concentration (B). A representative gel is shown in (A). The experiment was repeated three times. Note that it was not possible to compare different gels in a quantitative manner, but the qualitative trend was reproducible.

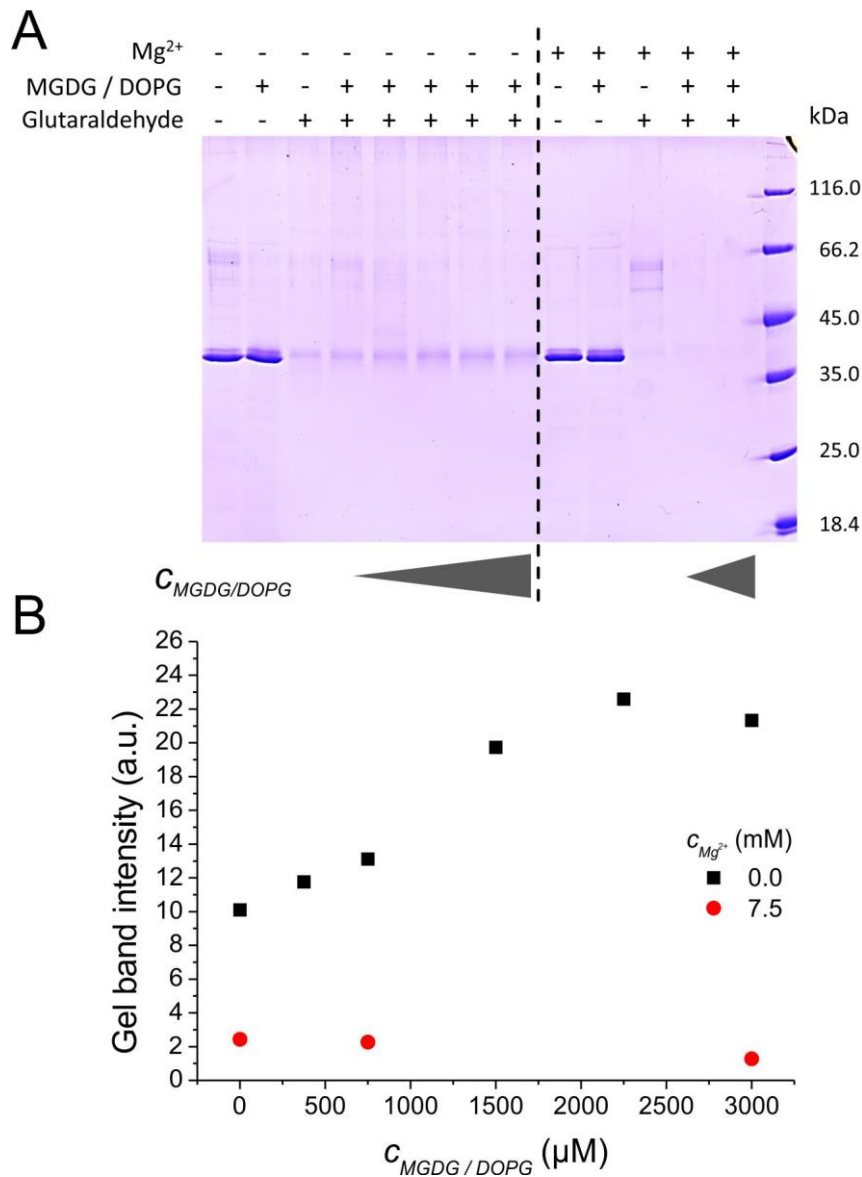


**Fig. 3.32: IM30 ring dissociation in presence 60%/40% MGDG/DOPG liposomes**

The IM30 ring dissociation in presence of 60%/40% MGDG/DOPG was tested in order to investigate structural alteration of the protein upon membrane addition. IM30 was incubated with different lipid concentrations in presence and absence of 7.5 mM Mg<sup>2+</sup>, respectively. Afterwards, the crosslinker glutaraldehyde was added, and the samples were loaded on a 12% SDS gel (A). Furthermore, the IM30 gel bands from the samples including lipids were graphically evaluated via ImageJ 1.47t, and the gel band intensities were plotted against the lipid concentration (B). A representative gel is shown in (A). The experiment was repeated two times. Note that it was not possible to compare different gels in a quantitative manner, but the qualitative trend was reproducible.

The gels from the IM30 oligomer dissociation experiment are shown in Fig. 3.31A and Fig. 3.32A for two different types of liposomes. Since the qualitative information of the two gels are similar, they can be discussed at the same time. In the control lanes containing the IM30 samples lacking DOPG/glutaraldehyde and glutaraldehyde, the IM30 band can be identified at ~37 kDa. This band is less intense upon addition of liposomes in absence of Mg<sup>2+</sup>, whereas in presence of the ion it has completely disappeared.

The protein bands from the samples including lipids were graphically evaluated via the program ImageJ 1.47t, and the gel band intensities were plotted against the lipid concentration, as shown

in *Fig. 3.31B* and *Fig. 3.32B*. For the samples lacking  $Mg^{2+}$ , an increasing IM30 band intensity with increasing lipid amount can be observed. For the gels shown in *Fig. 3.31A* and *Fig. 3.32A*, this trend seems more pronounced for the samples containing 60%/40% MGDG/DOPG. However, the experiment was only qualitatively reproducible and, thus, the degree of IM30 oligomer dissociation cannot be compared between different liposome composition. Anyhow, the observed correlation indicates a liposome-dependent dissociation of the proteins' higher ordered ring structure. The observation that the band intensities for the samples containing liposomes are less intense than those belonging to the control samples in *Fig. 3.31A* and *Fig. 3.32A* could have had different origins: The dissociation might not have been complete due to an incomplete membrane binding of the protein. Indeed, there probably is an equilibrium between membrane-bound and non-bound protein, whereas the latter seems to stay in the ring state. On the other hand, oligomerized IM30 did not necessarily dissociate only into monomers, which were visible in the SDS gel. In 3.1.3, it was indicated that the smallest IM30 ring building block is indeed a tetramer, formed from dimers of dimers. Also, the formation of other lower-ordered structures during the dissociation process could have been possible. As displayed in *Fig. 3.31B* and *Fig. 3.32B*, the samples containing  $Mg^{2+}$  show a constant low IM30 band intensity compared to the sample lacking the ion. This is in agreement with *Fig. 3.31A* and *Fig. 3.32A*, where no IM30 bands are visible upon  $Mg^{2+}$  addition. This observation strongly supported a stabilizing effect of the ion, as it has already been described in 3.4. However, since only monomers were resolved in the gel, an IM30 oligomer dissociation into lower-ordered oligomers despite the presence of  $Mg^{2+}$  cannot be completely excluded.

Since the number of IM30 oligomerization states that are observable on the SDS gel appeared limited, experiments using a mixture of IM30-CFP and IM30-Venus were performed next. Importantly, the mutants were able to mediate membrane fusion (*cf.* 5.7), which indirectly demonstrated the ability of the labeled proteins to interact with membranes. In the case of ring dissociation upon membrane binding, the FRET efficiency  $E_{rat}$  was expected to decrease, since the monomers and/or subunits would move away from each other, resulting in a reduced energy transfer (schematically and simplified shown in *Fig. 3.33A*). Here, the degree of dissociation does not matter, since also a less expanded dissociation would have been detectable. Thus, IM30-CFP/Venus was incubated with increasing lipid concentrations of 100% DOPG or 60%/40% MGDG/DOPG liposomes (0-1000  $\mu$ M), respectively, in presence and absence of 7.5 mM  $MgCl_2$ . The low protein concentration of 0.2  $\mu$ M was supposed to ensure an excess of available protein binding areas. The samples were measured in equilibrium, and the FRET efficiency  $E_{rat}$  was calculated as described in 2.18.2.2. The results are shown in *Fig. 3.33B*.

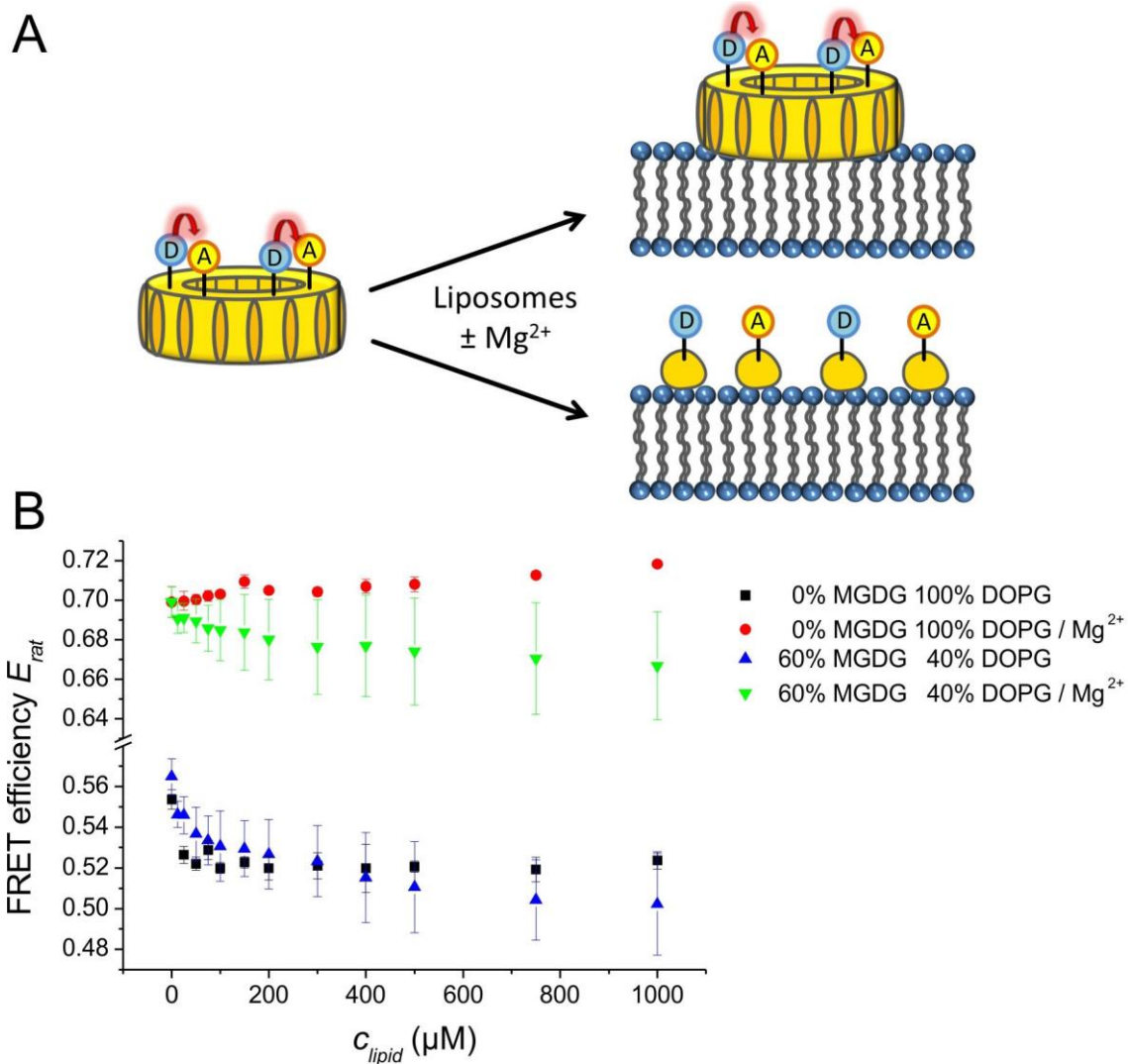


**Fig. 3.33: IM30-CFP/Venus oligomer dissociation in presence of 100% DOPG and 60%/40% MGDG/DOPG liposomes**

A FRET-based assay using an IM30-CFP/Venus mixture was performed to investigate the dissociation of the protein upon membrane addition. The protein was incubated with 100% DOPG and 60%/40% MGDG/DOPG liposomes, respectively, in presence and absence of 7.5 mM  $\text{Mg}^{2+}$ . Upon ring dissociation, a decrease in FRET was expected (A). The FRET efficiencies  $E_{rat}$  were calculated and plotted against the increasing lipid concentration (B). IM30-CFP/Venus ratio: 37% CFP, 63% Venus, error bars represent the standard deviation ( $n=3$ , for 60%/40% MGDG/DOPG liposomes:  $n=4$ , for 60%/40% MGDG/DOPG liposomes in presence of  $\text{Mg}^{2+}$ :  $n=6$ ).

The results shown in Fig. 3.33B provide information regarding the dissociation of IM30 oligomers upon membrane interaction. In absence of  $\text{Mg}^{2+}$ ,  $E_{rat}$  decreased with increasing lipid concentration for both 100% DOPG and 60%/40% MGDG/DOPG mixtures. This indicates dissociation of IM30 rings independent from the lipid MGDG and is in agreement with the dissociation into monomers shown in Fig. 3.31 and Fig. 3.32, even though dissociation into other lower-ordered oligomers might be possible as well. The starting value for  $E_{rat}$  at 0  $\mu\text{M}$  lipid was at  $\sim 0.55$  for 100% DOPG and  $\sim 0.57$  for 60%/40% MGDG/DOPG liposomes, respectively. Those values were in the same size range as the  $E_{rat}$  value calculated for the 1/1 mixture of IM30-CFP/Venus (0.54, cf. Fig. 5.7), even though the ratio used here was 37% CFP/63% Venus. The  $E_{rat}$  values decreased until a plateau was reached at  $\sim 0.52$  and  $\sim 0.49$ , respectively. The observa-

tion that the curves did not decrease further can be ascribed to an incomplete dissociation, which could have originated from (i) an incomplete membrane binding despite the large lipid excess and/or (ii) the retaining of lower-ordered protein oligomers, *e.g.* tetramers (*cf.* 3.1.3), which would still have exhibited a rather high energy transfer. Furthermore, it cannot be excluded that (iii) already dissociated particles still interacted slightly with one another.

In presence of  $Mg^{2+}$ , the situation looked rather different. The starting values for  $E_{rat}$  of the IM30-CFP/Venus mixture were at  $\sim 0.70$  for both, the sample containing 100% DOPG liposomes and the one with 60%/40% MGDG/DOPG liposomes. The influence of  $Mg^{2+}$  on an increased  $E_{rat}$  had already been observed (3.4.3) and was explained by an increased double-ring formation. For the samples containing 100% DOPG liposomes, no increase of the  $E_{rat}$  values was observed upon lipid addition. On the contrary, they even seemed to slightly increase to a value of  $\sim 0.72$  upon DOPG addition for an unknown reason. Hypothetically, membrane interaction slightly affects the IM30 packing inside the ring structure resulting in an enhanced interaction of CFP and Venus. However, IM30-CFP/Venus most probably does not dissociate on 100% DOPG liposomes in presence of  $Mg^{2+}$ . This was in agreement with the results shown in *Fig. 3.31* and could be explained by a stabilization effect of  $Mg^{2+}$ . In contrast, the  $E_{rat}$  values of the IM30-CFP/Venus mixture decreased to  $\sim 0.67$  when adding 60%/40% MGDG/DOPG liposomes in presence of  $Mg^{2+}$ , whereas the small decrease might be explained by the same reasons as listed above. Notably, the latter experiment was conducted under the same conditions used in the standard membrane fusion assays. Thus, this observation indicated an influence of the lipid MGDG on the dissociation of the proteins' higher-ordered structures in presence of  $Mg^{2+}$ . Whether this was connected to the presence of the inverse-hexagonal lipid in the membrane fusion process, as suggested in (Bastien *et al.* 2016), was investigated further and is described in 3.9.2. Furthermore, considering the results shown in *Fig. 3.32*, where no IM30 monomers were observable in presence of 60%/40% MGDG/DOPG and  $Mg^{2+}$ , it can be assumed that the ion stabilizes at least other lower or higher-ordered oligomers of IM30.

In conclusion, it seems that higher-ordered IM30 oligomers dissociates on negatively charged membranes, independent of the lipid MGDG. This dissociation includes formation of at least a few monomers as it can be seen in the SDS-PAGEs.  $Mg^{2+}$  stabilized the IM30 ring structure, on the other hand, and the dissociation on 100% DOPG membranes is not possible anymore. In contrast, when MGDG is present in the liposomes, the protein dissociates despite the presence of  $Mg^{2+}$ . However, the ion probably conserves some lower or higher-ordered oligomeric structures due to the observation that no monomer bands were visible in the SDS-PAGE anymore.

### 3.9 IM30-mediated membrane fusion

In former work, it has been demonstrated that IM30 mediates membrane fusion *in vitro* in presence of  $Mg^{2+}$  (Suppes 2013; Hennig *et al.* 2015). Furthermore, several mutants were identified with increased or decreased fusion activity (Hennig 2014; Hennig *et al.* 2015) and thus, important protein domains for the IM30 fusion activity are probably identified in the future. Nevertheless, the required conditions for the fusion process, *e.g.* protein flexibility and membrane properties, have hardly been investigated so far. Furthermore, membrane destabilization as part of the mechanism of IM30-mediated membrane fusion was of great interest.

#### 3.9.1 IM30 mediates membrane fusion

In previously performed membrane fusion assays and TEM (Suppes 2013; Hennig *et al.* 2015), small liposomes with a mean diameter of 100 nm were fused. In order to further confirm the IM30-mediated membrane fusion and to investigate the extent to which the small liposomes are fused, SPT measurements were performed. Here, the particle size distribution of 60%/40% MGDG/DOPG liposomes, which were sized to 100 nm and labeled with the fluorescence probe LissRhod-PE, were temporally observed in presence of IM30 and 7.5 mM  $Mg^{2+}$ . Upon membrane fusion, the particle size was supposed to increase and a wider size distribution was expected. As a control, samples containing only liposomes and only liposomes/ $Mg^{2+}$  were monitored. The experiment was performed as described in 2.18.5 in cooperation with Prof. Nadja Hellmann. The results are shown in *Fig. 3.34*.

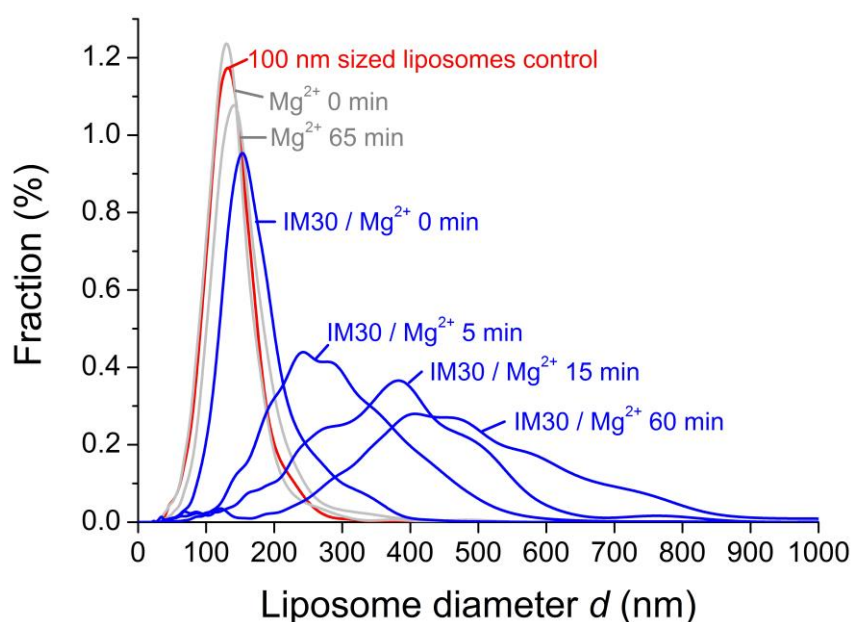


**Fig. 3.34: Liposome size-distribution for IM30-mediated membrane fusion**

SPT was performed to further confirm the IM30-mediated membrane fusion. The particle size distribution of 60%/40% MGDG/DOPG liposomes was temporally monitored upon IM30/ $Mg^{2+}$  addition (blue curves). Additionally, control samples containing only liposomes (red curves) and liposomes in presence of  $Mg^{2+}$  (grey curves) were also prepared. The experiment was repeated two times. In cooperation with Prof. Nadja Hellmann. The results in this figure are published in (Hennig *et al.* 2015).

As can be seen in *Fig. 3.34*, the mean liposome diameter of the  $Mg^{2+}$  control sample is just slightly shifted compared to the initial size to  $\sim 130$  nm after 65 min. In presence of both IM30 and  $Mg^{2+}$ , on the other hand, a distinct temporal liposome size shift is visible, wherein the peak is located at  $\sim 400$  nm after 60 min. The observation that the liposome diameter increases with increasing incubation time supports the necessity of the presence of IM30 and  $Mg^{2+}$  for the membrane fusion. Thus, the result is in line with the observations shown in (Suppes 2013) and (Hennig *et al.* 2015).

### 3.9.2 MGDG supports IM30-mediated membrane fusion

In 3.8, a special role of the lipid MGDG has been described for  $Mg^{2+}$ -dependent IM30 ring dissociation. Recently, the necessity of the inverse-hexagonal phase forming lipid for *in vivo* membrane fusion was suggested (Bastien *et al.* 2016), but so far, experimental evidence was missing. Thus, the role of MGDG in the fusion process was investigated further. To do so, a fusion assay, using liposomes with varying amounts of MGDG and DOPG, was performed as described in 2.18.2.5. No liposomes with a higher MGDG content than 60% were investigated due to former experiments which showed that no lamellar phase forms above this MGDG concentration (Suppes 2013). Importantly, for each composition separately prepared positive and negative controls were used. The results are illustrated in *Fig. 3.35*.

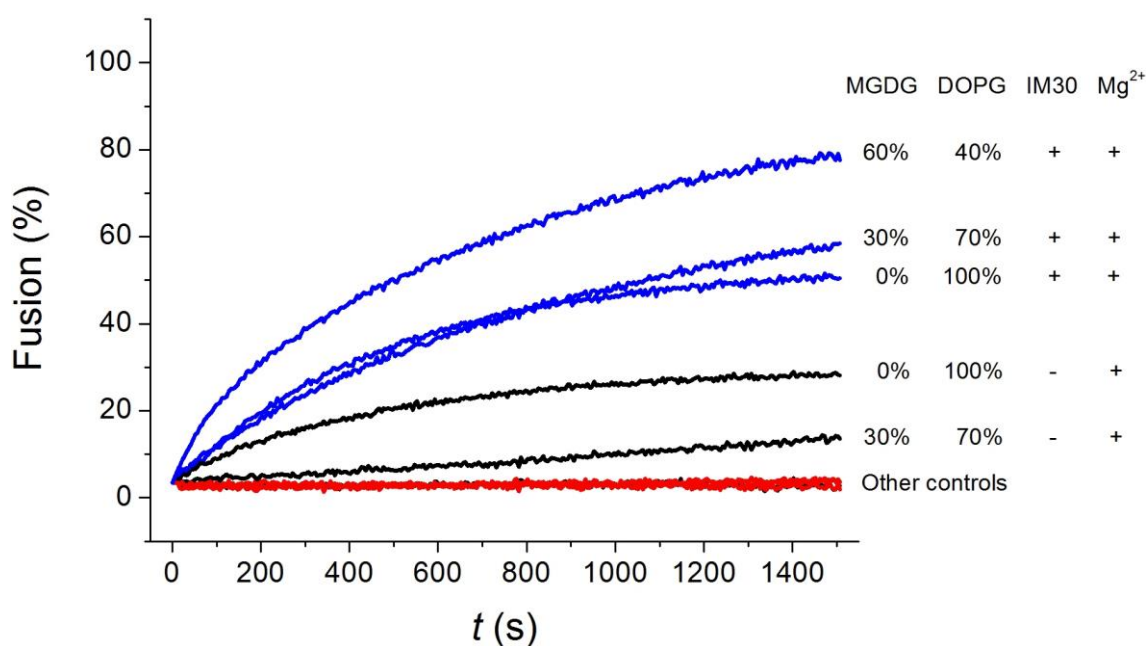


**Fig. 3.35: IM30-mediated fusion of differently composed liposome**

A fusion assay was performed in order to investigate the required liposome composition for IM30-mediated membrane fusion. Thus, the assay was performed with samples containing liposomes with varying amounts of MGDG and DOPG. Control curves were recorded with samples containing only  $2.5 \mu\text{M}$  of IM30 (red curves) or only  $7.5 \text{ mM}$   $Mg^{2+}$  (black curves). Fusion was measured with samples containing  $2.5 \mu\text{M}$  IM30 and  $7.5 \text{ mM}$   $Mg^{2+}$  (blue curves).  $\Delta\text{Fusion} = \pm 4.3\%$ ,  $\Delta t = \pm 1 \text{ s}$ . The experiment was repeated two times.

The results in *Fig. 3.35* indicate a correlation between the membrane composition and fusion induced by IM30: The number of fused liposomes increased with increasing amount of MGDG. Strikingly, when not using the standard lipid composition 60%/40% MGDG/DOPG but an increased DOPG amount up to 100%, the liposomes already fused in sole presence of  $Mg^{2+}$ , as can be seen for the respective controls. This effect seems more pronounced for higher DOPG amounts. For 100% DOPG liposomes, it is hard to distinguish between the effect of  $Mg^{2+}$  and IM30/ $Mg^{2+}$ , since it is not known how they influence each other. Thus, it seems reasonable to assume that despite the enhancing effect of MGDG on the maximal fusion, even the sole presence of MGDG is required for IM30-mediated membrane fusion. This hypothesis might be ascribed to physical properties of the lipid, which is a breaker of lamellar phases (*cf.* 1.2.1).

### 3.9.3 Structural flexibility of M30 affects IM30-mediated membrane fusion

It has previously been observed that C7, which probably forms tetramers (Heidrich *et al.* 2016), is not able to mediate membrane fusion (Hennig 2014). Furthermore, a correlation between the dissociation of the IM30 rings and the presence of  $Mg^{2+}$  and 60%/40% MGDG/DOPG liposomes, was striking (*cf.* 3.8). Thus, it was investigated whether a structural flexibility of IM30 is necessary for membrane fusion. A fusion assay was performed to compare the fusion activity of IM30 and IM30-X. The crosslinked version of the protein was assumed not to dissociate due to the glutaraldehyde crosslink, and the fusion activity was thought to be decreased in case of a required structural flexibility. The results are shown in *Fig. 3.36*.

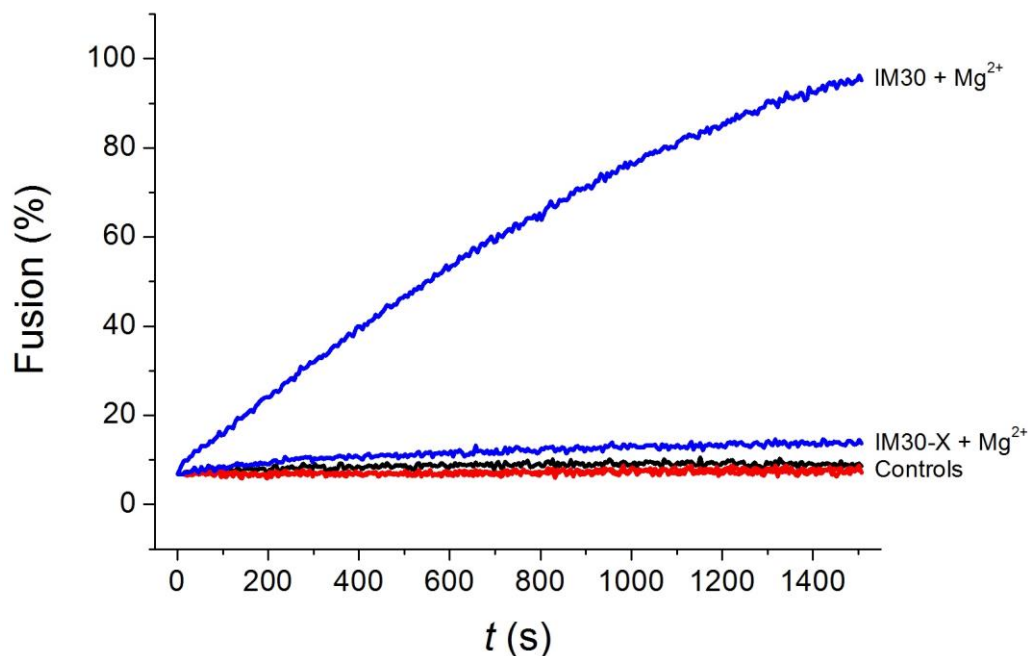


**Fig. 3.36: Fusion assay of IM30-X**

A fusion assay was performed in order to investigate the necessity of structural flexibility of IM30 for the membrane fusion process. Control curves were recorded with samples containing only 2.5  $\mu$ M of the respective protein (red curves) or only 7.5 mM  $Mg^{2+}$  (black curve). Fusion was measured with samples containing 2.5  $\mu$ M of the respective protein and 7.5 mM  $Mg^{2+}$  (blue curves).  $\Delta$ Fusion =  $\pm$  5.7%,  $\Delta$ t =  $\pm$  1 s. The experiment was repeated two times.

As can be seen in *Fig. 3.36*, the fusion activity of IM30-X seems dramatically decreased compared to the uncrosslinked version in presence of  $Mg^{2+}$  (~10% vs. 90% fusion after 1500 s). Importantly, it has previously been shown that a similar dissociation constant for membrane interaction of IM30-X and IM30 WT are obtained (*cf.* 3.6). Thus, it can be excluded that IM30-X did not fuse due to a weaker membrane interaction. Overall, the experiment provided hints for the necessity of structural alterations of IM30 for the proteins' fusion activity. The low fusion activity of IM30-X might have originated from uncrosslinked IM30.

#### **3.9.4 IM30-mediated membrane fusion induces membrane destabilization**

So far, the ability of IM30 to mediate membrane fusion has been demonstrated via fusion assays (Suppes 2013; Hennig *et al.* 2015), TEM (Hennig *et al.* 2015) and SPT (*cf.* 3.9.1). Some electron micrographs showed the formation of large multilamellar 60%/40% MGDG/DOPG liposomes in presence of IM30 and  $Mg^{2+}$ , indicating an uncontrolled, passive fusion (Hennig *et al.* 2015). Nevertheless, none of the mentioned experiments could provide hints concerning the fusion mechanism. The protein might be a direct fusion protein similar to soluble *N*-ethylmaleimide-sensitive-factor attachment receptor (SNARE) proteins (Marsden *et al.* 2011) as well as a passive fusion mediator, which destabilizes membranes followed by a spontaneous, random reorganization of the lipid bilayers. Also, a direct fusion combined with destabilization might be thinkable. To further illuminate this issue, a liposome destabilization assay was performed to investigate membrane destabilization by IM30. Here, NBD-PE labeled 60%/40% MGDG/DOPG liposomes were exposed to the quencher sodium dithionite, which was supposed to initially quench ~50% of the fluorophores located at the outer leaflet of the liposomes. Upon further addition of IM30/ $Mg^{2+}$ , the fluorophores located at the inner leaflet of the liposomes were expected to be quenched in case of membrane destabilization, since  $Na_2S_2O_4$  could pass the membrane barrier in this case. The protein was used in different concentrations. Furthermore, samples containing only IM30 or  $Mg^{2+}$  and a positive control for total quenching, using the detergent Triton X-100, were also prepared. The experiment was performed as described in 2.18.2.4 in cooperation with Prof. Nadja Hellmann. The results are shown in *Fig. 3.37*.

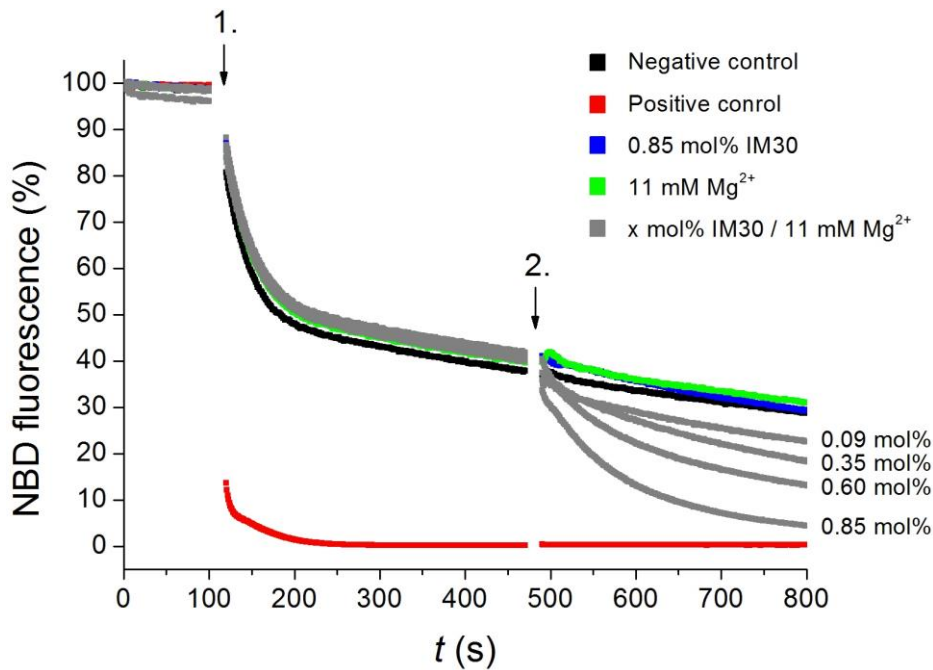


**Fig. 3.37: Liposome destabilization by IM30/Mg<sup>2+</sup>**

In order to investigate a liposome destabilization during the IM30-mediated membrane fusion, a destabilization experiment was performed. 60%/40% MGDG/DOPG liposomes, which were labeled with the fluorescence probe NBD-PE, were exposed to the quencher Na<sub>2</sub>S<sub>2</sub>O<sub>4</sub> (1). After ~60% of the dye, located at the outer liposome leaflet, were quenched, IM30 and/or 11 mM Mg<sup>2+</sup> were added (2). A further intensified decrease at this point indicated membrane destabilization. Furthermore, the detergent Triton X-100 was added to the positive control in (1). The experiment was repeated two times. In cooperation with Prof. Nadja Hellmann. The results in this figure are published in (Hennig *et al.* 2015).

As displayed in Fig. 3.37, the NBD fluorescence is decreased to ~40% after the addition of sodium dithionite. The decrease did not level off, which might be explained by the potential ability of NBD-PE to perform a very slow lipid flip-flop. Thus, the dye which was first at the inner liposome leaflet could flip to the outer liposome leaflet later. Another explanation might be an intrinsic permeability of the liposomes for Na<sub>2</sub>S<sub>2</sub>O<sub>4</sub>. In the following, a steady continuance of the NBD fluorescence decrease after the addition of IM30 and/or Mg<sup>2+</sup> was interpreted as non-destabilization. This was given for the negative control, in which only buffer was added, as well as for the control samples containing only IM30 and Mg<sup>2+</sup>, respectively. This is in agreement with the observation that in the fusion assay both protein and Mg<sup>2+</sup> need to be present for membrane fusion (Suppes 2013; Hennig *et al.* 2015). An enhanced decrease of the NBD fluorescence was indeed observed for samples containing IM30 and Mg<sup>2+</sup>, indicating membrane destabilization. This conclusion is supported by the observation that the decrease correlated with the amount of IM30. Importantly, for the positive control containing the detergent Triton X-100, a prompt decrease to an NBD fluorescence of 0% was monitored since the liposomes were dissolved and all dyes were available for the quencher. This control confirmed the functionality of the experiment. Overall, the results of the experiment support the theory of membrane destabilization as a part of the mechanism for the IM30-mediated membrane fusion.

## 4 Discussion

In this thesis, IM30 interactions which lead to membrane fusion were investigated via *in vitro* methods. This included homo-oligomerization of the protein, interaction with  $Mg^{2+}$ , and membrane binding. In this context, the influence of IM30 structural properties on the respective interactions were analyzed. Also, the effect of the interactions with  $Mg^{2+}$ /membranes on the IM30 structure and oligomerization were of great interest.

In the following chapter, the results described in chapter 3 are discussed. Finally, models for the sequence of the steps leading to membrane fusion and a mechanism for the membrane fusion itself are presented and placed in a biological context. It must be mentioned that the suggested models are based on the experiments made for the heterologously expressed *Synechocystis* IM30. However, due to the strong structural conservation of the protein in different organisms (Bultema *et al.* 2010), the results can likely be transferred to other IM30 variants as well.

### 4.1 The IM30 oligomerization steps

The ability to form higher-ordered oligomeric ring structures is a conserved feature of IM30 and PspA (Aseeva *et al.* 2004; Hankamer *et al.* 2004; Fuhrmann *et al.* 2009a; Bultema *et al.* 2010). The rotational symmetries were recently shown to vary at least between 10-18 and are visible in electron micrographs as so-called spikes (Saur *et al.* 2017). Due to this variability, it has been assumed that the ring oligomers are assembled from a common building block (Bultema *et al.* 2010). The number of IM30 molecules filling a spike has been indicated via SDS titration to be tetrameric (Fuhrmann *et al.* 2009a), but further evidence has been lacking so far.

To further investigate the formation of tetramers, native mass spectrometry method LILBID-MS, which is suitable for investigations of noncovalently bonded biomolecule complexes, was performed. The mass spectrum shown in *Fig. 3.5* revealed a significant number of dimers and tetramers in the used IM30 sample. The trimer fraction, on the other hand, appeared rather small and, thus, insignificant. Therefore, it seems reasonable to assume that the smallest IM30 oligomers are dimers or dimers of dimers and.

After all, the subsequent oligomerization steps of IM30 was probably already correctly predicted in (Vothknecht *et al.* 2012). Probably, IM30 dimers are the smallest oligomer and IM30 tetramers the basic building blocks of IM30 rings. Indeed, recent modeling of predicted IM30 structures into 3D ring reconstructions showed a perfect matching of tetramers inside recurring

ring elements (Saur *et al.* 2017). Furthermore, IM30 rings were shown to oligomerize into double-rings and rod-like structures *in vitro* (Aseeva *et al.* 2004; Fuhrmann *et al.* 2009a). A schematic overview of the suggested *in vitro* oligomerization is illustrated in Fig. 4.1.

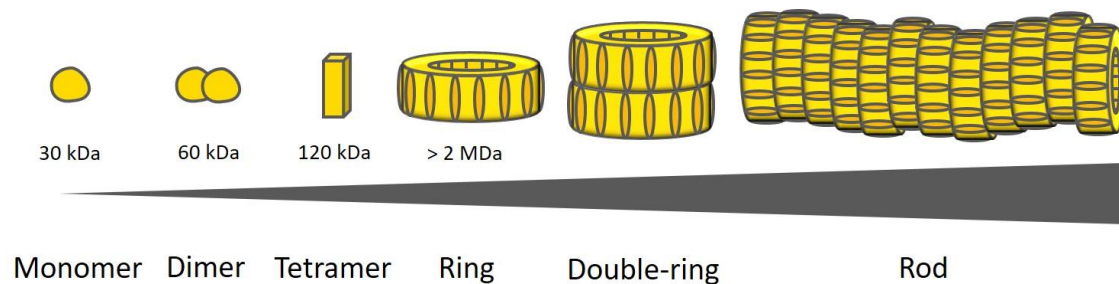


**Fig. 4.1: *In vitro* oligomerization of IM30**

IM30 monomers were observed to form dimers and tetramers as the basic building blocks of higher-ordered oligomers. IM30 rings consist of at least 10-18 subunits and can assemble into double-rings and rod-like structures. The grey triangle indicates the increasing number of oligomerized IM30 molecules.

It needs to be mentioned that there is no evidence for the existence of double-rings and rod structures *in vivo*. Whether they represent *in vitro* artefacts or play an important role for the IM30 activity, as it is suggested for double-rings in the following chapters, needs to be investigated in the future. However, the findings summarized in Fig. 4.1 are important for the following discussion. In different situations (*e.g.* upon membrane binding), IM30 rings dissociate into lower-ordered oligomers, which can now be assumed to be tetramers or at least dimers. Most probably, the C7 mutant, which forms tetramers, is a suitable representative of the IM30 ring building block.

## 4.2 The IM30-Mg<sup>2+</sup> interaction

Mg<sup>2+</sup> is a common binding partner for pro- and eukaryotic proteins (Bellsollell *et al.* 1994; Chinsang & Spence 1996; Ohki *et al.* 1997; Sissi & Palumbo 2009; Piovesan *et al.* 2012). As already described in 1.3, the ion plays a major role in cyanobacteria and chloroplasts. It has a regulatory function and is the central ion of chlorophyll (Krause 1977). Additionally, it seems reasonable to connect Mg<sup>2+</sup> with TM biogenesis since the Mg<sup>2+</sup> concentration in the chloroplast stroma is influenced by outer light conditions as well as the formation of the TM (Lin & Novel 1971; Portis & Heldt 1976; Portis 1981; Ishijima *et al.* 2003). The fusion activity of IM30 has recently been shown to be influenced by Mg<sup>2+</sup> since the protein can only mediate membrane fusion in presence of the ion (Suppes 2013; Hennig *et al.* 2015). However, neither information concerning a direct binding of Mg<sup>2+</sup> to IM30 nor the effect of this interaction on the IM30 structure have been available so far.

#### 4.2.1 Direct binding of $Mg^{2+}$ to IM30

ANS experiments were performed in order to investigate a potential binding of  $Mg^{2+}$  to IM30. The fluorescent dye ANS binds to hydrophobic and polar areas of proteins and changes its fluorescence emission spectrum in hydrophobic environments due to the lack of dipolar relaxation (Slavik 1982; Matulis *et al.* 1999). For IM30, this shift in the fluorescence was observed in dependence of increasing  $Mg^{2+}$  concentrations (*cf.* Fig. 3.6 and Fig. 3.7), which indicated a direct influence of the ion on the protein. A dissociation constant  $K_D$  for the interaction was calculated to be  $(1.3 \pm 0.6)$  mM (*cf.* Fig. 3.7) or  $(1.1 \pm 0.5)$  mM in (Junglas 2016), respectively. Since ANS experiments only indirectly demonstrate binding reactions, but instead structural alterations of proteins coupled to the dye, reverse ITC measurements were additionally performed to control whether titration of IM30 to a  $MgCl_2$  solution resulted in a measurable reaction heat (*cf.* Fig. 3.8). Indeed, the ITC measurements indicated an interaction of  $Mg^{2+}$  with IM30 upon a positive enthalpy change with a  $K_D$  of  $(1.9 \pm 0.2)$  mM, which is in perfect agreement with the results from the ANS experiments. Thus, it can be summarized that IM30 and  $Mg^{2+}$  probably directly interact with each other and that the binding reaction has a  $K_D$  in the range of  $\sim 1$ -2 mM. This is in agreement with other  $K_D$  values for protein- $Mg^{2+}$  interaction ( $10^{-2}$ - $10^{-5}$  M) found in the literature (Black *et al.* 1994). Considering the *in vivo* situation, the obtained  $K_D$  lies in the transition concentration of  $Mg^{2+}$  in the stroma upon light exposure (1-5 mM) (Shaul 2002). Thus, an activation of the IM30 fusion activity by  $Mg^{2+}$  seems likely.

Interactions between proteins and ions usually have an electrostatic nature and are exothermally driven (Yamashita *et al.* 1990). However, the positive enthalpy change  $\Delta H$  of  $\sim 20$  kcal/mol for the IM30- $Mg^{2+}$  interaction, which was obtained from the ITC measurement (*cf.* Fig. 3.8), revealed an apparent overall endothermic nature of this binding reaction. This might be explained by proton release reactions of IM30 on buffer molecules and intramolecularly, which was recently indicated (Heidrich *et al.* 2018). Furthermore, recent fourier transform infrared (FTIR) spectroscopy experiments suggested the deprotonation of glutamic acid or aspartic acid side chain carboxyl groups of IM30 in presence of  $Mg^{2+}$  (Heidrich *et al.* 2018). The proton release could be coupled with an endothermic enthalpy change (Heidrich *et al.* 2018), since such reactions often affect the total enthalpy change (Baker & Murphy 1996). Thus, it might superpose the exothermic enthalpy change for an electrostatic IM30- $Mg^{2+}$  binding. Due to the second law of thermodynamics, the binding reaction must be entropically supported instead of having an overall exergonic reaction. Therefore, it most probably involves additional events, such as structural alterations of IM30. Indeed, since a blue shift of the IM30 attached ANS fluorescence upon increasing  $Mg^{2+}$  concentration was observed (Fig. 3.6), a structural alteration of IM30 is indicated. Due to the observation that ionic interactions of ANS did not significantly influence its fluorescence emission (Slavik 1982; Matulis *et al.* 1999), the observed shift can be ascribed to an increased exposure of hydrophobic IM30 surfaces caused by structural alteration of flexi-

ble domains such as the C-terminus, which is accompanied by a decrease of free water molecules. Upon forming a hydrate shell around the hydrophobic area, the water molecules become more ordered and, thus, the entropy decreases (Winter & Noll 1998). However, since this effect counteracts the binding of  $Mg^{2+}$  to IM30, another reaction must take place in order to have an overall exergonic reaction. Thus, it was speculated that  $Mg^{2+}$  binding and/or the deprotonating reactions of IM30 are accompanied by an additional unknown structural alteration which results in an increased entropy via water molecule release (Junglas, p.c.) (*cf.* 4.2.3).

The ability of IM30 to expose hydrophobic surfaces upon  $Mg^{2+}$  binding and, thus, the necessity of the protein to be flexible during or after the binding reaction, was additionally indicated by repeating the ANS experiment with IM30-X (*cf.* Fig. 3.14A). As expected, the ANS fluorescence of the sample containing the crosslinked protein was dramatically decreased compared to the sample containing IM30 WT due to the fixation of the IM30 ring in the crosslinked version. This indicated the lack of IM30 structural alteration in the case of an unflexible IM30 ring. Importantly, the experiment did not exclude binding of  $Mg^{2+}$  to IM30-X.

Next, the potential requirement of IM30 ring or other higher-ordered oligomer formation for  $Mg^{2+}$  binding were investigated. It has recently been indicated via ANS experiments that the non-ring forming IM30 mutant C7 is not influenced by  $Mg^{2+}$  addition (Hennig 2014). This implies a requirement of higher-ordered IM30 structures for interaction with the metal ion. To further investigate this issue, an ANS experiment was performed using the IM30 mutant A227C in presence and absence of  $Mg^{2+}$ /DTT (*cf.* Fig. 3.14). Importantly, A227C forms disulfide-linked dimers and only a strongly decreased amount of higher-ordered IM30 structures in absence of DTT, whereas upon addition of DTT, it oligomerizes (*cf.* Fig. 3.12 and Fig. 3.13). As can be seen in Fig. 3.14, the  $Mg^{2+}$  related fluorescence intensity is strongly increased in presence of DTT. This observation supported the necessity of IM30 ring formation or other higher-ordered IM30 structures for the  $Mg^{2+}$  binding. Binding of divalent cations to ring-like oligomers is not unusual. For instance, the  $Ca^{2+}$  sensor synaptotagmin-1, which is involved in synchronous neurotransmitter release, oligomerizes into ring structures under calcium-free conditions (Wang *et al.* 2014a). However, unlike the IM30- $Mg^{2+}$  interaction, the synaptotagmin-1 rings dissociate upon  $Ca^{2+}$  binding (Wang *et al.* 2014a).

#### 4.2.2 Structural alterations and stabilization of IM30 upon $Mg^{2+}$ binding

After indicating a direct binding of  $Mg^{2+}$  to IM30, which probably results in alterations of the protein structure, the effect of the ion on the IM30 secondary, tertiary and quaternary structure was investigated further.

As recently shown,  $Mg^{2+}$  probably influences the IM30 secondary structure, since the CD spectrum of IM30 alters in presence of  $Mg^{2+}$  (Hennig 2014; Heidrich *et al.* 2018). The stability of

the IM30 secondary structure, which is mainly  $\alpha$ -helical (Fuhrmann *et al.* 2009a; Bultema *et al.* 2010; Otters *et al.* 2013), was investigated via urea denaturation/renaturation and CD spectroscopy. IM30 was incubated with increasing urea amount in presence of different  $\text{MgCl}_2$  concentrations (*cf.* Fig. 3.16 and Fig. 5.23). The steep areas of the denaturation curves were shifted to higher urea concentrations with increasing  $\text{MgCl}_2$  concentrations. This shift was also quantitatively visible when calculating the transition points  $D_{1/2}$  of the denaturation curves (*cf.* Fig. 3.17), which increased upon  $\text{Mg}^{2+}$  addition. Thus,  $\text{Mg}^{2+}$  can be assumed to have a stabilizing effect on the IM30 secondary structure. This was further confirmed by thermal denaturation of IM30 in presence of different  $\text{Mg}^{2+}$  concentrations (Junglas 2016). The origin of this stabilization might be ascribed to the involvement of several  $\alpha$ -helices in the coordination of  $\text{Mg}^{2+}$ , resulting in tighter packing of IM30.

As already discussed in 4.2.1, ANS titration experiments indicated an altered tertiary/quaternary structure of IM30 in presence of  $\text{Mg}^{2+}$ , including the exposure of hydrophobic surfaces. In order to further investigate the effect of  $\text{Mg}^{2+}$  on the IM30 tertiary/quaternary structure, coiled-coil formation of IM30 upon addition of the ion was studied. Thus, the molar ellipticity ratio  $[\Theta]_{222\text{ nm}}/[\Theta]_{208\text{ nm}}$  was calculated from the CD spectra of IM30 in presence and absence of  $\text{Mg}^{2+}$  (*cf.* Table 3.2). Here, a value  $\leq 0.86$  stands for isolated  $\alpha$ -helices, whereas a value  $> 1.0$  indicates the presence of coiled-coil structures (Lau *et al.* 1984). The  $[\Theta]_{222\text{ nm}}/[\Theta]_{208\text{ nm}}$  ratio for the control sample shifted from  $\sim 1.1$  to  $\sim 1.2$  for the sample including  $\text{Mg}^{2+}$ , indicating an increased amount of coiled-coil structures in presence of the ion. Coiled-coil formation likely result in a tighter packing of IM30 in presence of  $\text{Mg}^{2+}$ . This is supported by acrylamide quenching experiments, which revealed a decreased availability of the amino acid W71 upon  $\text{Mg}^{2+}$  addition (Heidrich *et al.* 2018).

To further investigate the influence of  $\text{Mg}^{2+}$  on the stability of the IM30 tertiary/quaternary, tryptic digestion of the protein in presence and absence of the ion was performed and subsequently investigated in an SDS gel (*cf.* Fig. 3.18). The observed changed degradation pattern of IM30 in presence of  $\text{Mg}^{2+}$  most probably resulted from an altered trypsin accessibility due to a changed IM30 tertiary and/or quaternary structure. Obviously, the stability of IM30 against tryptic digestion seems to be increased in presence of  $\text{Mg}^{2+}$  since it took more time to completely digest the full-length protein. Strikingly, below the main IM30 band, a degradation band appeared during proteolysis, which most probably showed the N-terminal PspA domain of IM30, as demonstrated via immunoblot detection (Heidrich *et al.* 2018) and calculation of hypothetical IM30 cleavage sites (Junglas 2016). A flexible C-terminal  $\alpha$ -helix, which is easily cleaved by trypsin and subtilisin, was already suggested in the past (Otters *et al.* 2013; Gao *et al.* 2015), and recently, modeling of predicted IM30 structures into 3D ring reconstructions confirmed the C-terminus to be outside of the IM30 ring (Saur *et al.* 2017). Since the degradation band in Fig.

3.18 appeared temporally deferred and was only slightly visible in presence of  $Mg^{2+}$ , alteration of the IM30 structure most probably included a protection of the IM30 C-terminus due to a change of its structure and/or localization, *e.g.* via double-ring formation. This idea is in perfect agreement with a tighter packing of IM30 in presence of  $Mg^{2+}$ , as suggested above.

In a complementary ANS thermofluor experiment, the stability of the IM30 tertiary/quaternary structure upon  $Mg^{2+}$  binding was further investigated during thermal denaturation (*cf.* Fig. 3.19). Here, the protein was incubated with ANS in presence and absence of 10 mM  $Mg^{2+}$ , and the temperature was increased from 0 to 80°C. IM30 was found to be stabilized in presence of  $Mg^{2+}$  at two temperature ranges of ~25-35 °C and ~45-60 °C. This stabilizing effect of  $Mg^{2+}$  is in agreement with the results presented above. However, the type of stabilization was not determined in the ANS thermofluor experiment. Considering other observations described in 3.3 and 3.4, the two temperature ranges might represent a retardation of the reorganization of monomers or lower-ordered oligomers inside the IM30 ring (first range), potentially involving a dislocation of the C-terminus, and double-ring/ring/tetramer dissociation with contemporaneous denaturation (second range), which is in agreement with thermal denaturation experiments shown in (Junglas 2016). The hypothetical stabilization steps are schematically illustrated in Fig. 4.2.

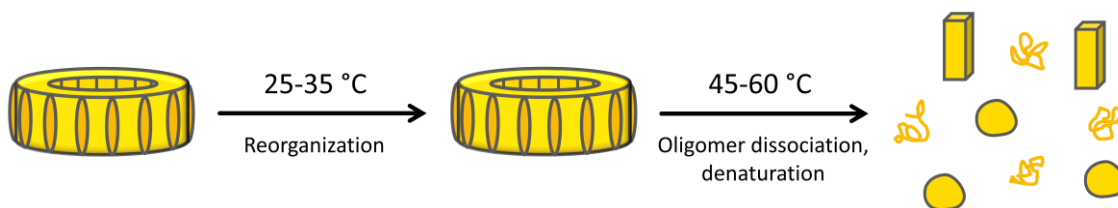


**Fig. 4.2: Suggested stabilizations of IM30 induced by  $Mg^{2+}$  during thermal denaturation**

The ANS thermofluor experiment revealed two temperature ranges with increased IM30 stability upon thermal denaturation in presence of  $Mg^{2+}$  (*cf.* Fig. 3.19). The ion might stabilize a reorganization of IM30 monomers or lower-ordered oligomers inside the ring structure and/or other higher-ordered oligomers (first range) and contemporaneous deoligomerization/denaturation of higher-ordered structures (second range). The IM30 ring in this figure stands for all types of higher-ordered oligomers.

Both tryptic digestion and the ANS thermofluor experiments indicated a stabilization of IM30 structures in presence of  $Mg^{2+}$ . A stabilization triggered by  $Mg^{2+}$  is not unusual and can also be found in other proteins, such as protein kinase C (Lester *et al.* 1990) and  $\alpha$ -tropomyosin (Correa *et al.* 2009). Specifically,  $Mg^{2+}$  is often responsible for protection against thermal denaturation, as shown for the pancreatic elastase (Favre-Bonvin *et al.* 1986) and the creatine kinase (Cao *et al.* 1999).

Based on the results of the proteolysis assay, it seems reasonable to assume an altered structure of the IM30 C-terminus in presence of  $Mg^{2+}$ , resulting in its increased protection. Thus, it does not seem far-fetched to assume the C-termini buried inside the ring or being masked by double-ring formation. Therefore, the C-terminally labeled IM30 mutants IM30-CFP and IM30-Venus,

which can form a FRET pair, were used to investigate a double-ring formation of IM30 triggered by  $Mg^{2+}$ . Importantly, a normal ring formation has been demonstrated for both mutants via SEC and TEM (cf. Fig. 3.21, Fig. 5.8 and Fig. 5.9). The differently labeled IM30 mutants were mixed and the ratiometric FRET efficiency  $E_{rat}$  was measured in equilibrium for different  $Mg^{2+}$  concentrations (cf. Fig. 3.23A) and kinetically monitored in presence and absence of 7.5 mM  $Mg^{2+}$  (cf. Fig. 3.23B). In both experiments, an increase of  $E_{rat}$  was observed upon  $Mg^{2+}$  addition. In the kinetic measurement, a plateau for  $E_{rat}$  was reached faster and on a higher level in presence of  $Mg^{2+}$  compared to the control sample. Since the plateau did not reach the maximum value for  $E_{rat}$  as calculated for a co-purified 1/1 mixture of IM30-CFP/Venus, a monomer exchange between IM30 rings was excluded. Thus, the  $E_{rat}$  increase most probably originated from double-ring formation, which was enhanced in presence of  $Mg^{2+}$ . This is supported by a recently performed simulation showing the IM30 C-terminus located at the ring edges (Saur *et al.* 2017). Upon double-ring formation via head-to-head connection with the C-termini facing each other, the two dyes are in close proximity to each other and able to interact. Indeed, an increased FRET might only be possible upon double-ring formation via head-to-head since the Förster radius of the CFP-YFP pair is  $\sim 50$  Å (Patterson *et al.* 2000) and the height of one IM30 is  $\sim 150$  Å (Saur *et al.* 2017) (or  $\sim 300$  Å for double-rings). The result was further supported by a similar experiment using IM30-CFP/Venus (cf. Fig. 3.24) and TEM (cf. Fig. 3.25). Furthermore, recently performed static light scattering (SLS) measurements, which showed an increased IM30 particle size in presence of  $Mg^{2+}$ , also indicated the  $Mg^{2+}$  induced double-ring formation of the protein (Heidrich *et al.* 2018). Whether the double-rings are an *in vitro* artefact or if they also appear *in vivo* remains elusive at this point. However, it appears tempting to speculate about their potential involvement in membrane fusion.

It can be concluded that  $Mg^{2+}$  binding most probably alters the IM30 structure, including exposure of hydrophobic surfaces. This effect is accompanied by stabilization of the protein from secondary to quaternary structure against stress, such as urea addition, proteolysis and heat. This is most probably caused by a tighter packing of the IM30 ring upon coiled-coil formation and an enhanced generation of IM30 double-rings, which results in an increased protection of the proteins' secondary structure, *e.g.* by a decreased availability for urea. Consequentially, the C-terminal  $\alpha$ -helix is probably protected inside the ring or between two rings upon double-ring formation.

#### 4.2.3 Coordination of $Mg^{2+}$ by IM30 residues

Coordination of  $Mg^{2+}$  in proteins usually involves the formation of octahedral complexes (Black *et al.* 1994). Since the ion is a hard base after the HSAB concept, it prefers hard oxygen ligands, such as carboxylates, hydroxyls, carbonyls and water (Black *et al.* 1994). The most important coordination partners for  $Mg^{2+}$  are glutamic acid or aspartic acid carboxylic side chains, but also

glutamine and asparagine side chains as well as the peptide backbone carbonyl groups are common ligands (Dudev *et al.* 1999). Unoccupied positions in the octahedral sphere are usually filled with water molecules (Dudev & Lim 2007). As already mentioned, a proton release of a carboxyl group has indeed been observed (Heidrich *et al.* 2018). Thus, it seems reasonable to assume that glutamic acid and/or aspartic acid are involved in the  $Mg^{2+}$  coordination. Furthermore,  $Mg^{2+}$  sometimes tends to coordinate at proteins via phosphate bridges (Mbah 2014; Khrustalev *et al.* 2016) and interestingly, the property of IM30 to be phosphorylated has been indicated in this work for heterologous protein expression in *E. coli* (*cf.* 3.1.3).

Since neither a crystal structure of the IM30 full-length protein nor a stoichiometry for the IM30- $Mg^{2+}$  binding reaction is available so far, it is difficult to suggest hypothetical  $Mg^{2+}$  binding sites within the IM30 tertiary and/or quaternary structure. In general, there are at least two possibilities: (i) one or more metal ions are coordinated inside the IM30 monomer or (ii) the binding is based on intermolecular coordination and, thus, several IM30 molecules bind one or more  $Mg^{2+}$  ions.

In the first scenario (i), it seems reasonable to assume electron donors from several helices to be involved in the binding of  $Mg^{2+}$ . However, typical features of  $Mg^{2+}$  binding proteins such as the unspecific primary structure motifs **-DXDD-** (Prisic *et al.* 2007), **-NADFDGD-**, **-YXDD-** or **-LXDD-** (Cowan 1998) as well as **-GK(T/S)T-** for binding via phosphate bridges (Mbah 2014; Khrustalev *et al.* 2016) cannot be found in the IM30 primary structure (*cf.* 5.1.1), although the similarity of the EDP(E) motif (E23-E26) to some of these binding motifs has been suggested recently (Hennig 2014). Furthermore, typical secondary structure combinations for  $Mg^{2+}$  binding such as  $\beta$ -strand-random coil- $\alpha$ -helix (Khrustalev *et al.* 2016), are lacking. However, it has been suggested that the C-terminal  $\alpha$ -helix is retracted from its location and forms a triple-helix with helices 4 and 5/6, stabilized by  $Mg^{2+}$  coordination (Junglas, p.c.) and the EDE motif (E207-E209), which is located in helix 6, has been suggested as a hypothetical  $Mg^{2+}$  binding site (Hennig 2014). This is supported by the increasing coiled-coil amount of IM30 in presence of  $Mg^{2+}$  (*cf.* 4.2.2). The C-terminal  $\alpha$ -helix, which is assumed to be located at the ring top site (Saur *et al.* 2017), could be moved inside the ring, resulting in the availability of hydrophobic surfaces for double-ring formation. Indeed, illustrating the amino acids of the neighboring linker region (A218-D249), the hydrophobic/neutral amino acids are outnumbering charged amino acids:

AGGALPGTSAATPQLEAAPVDSSVPANNASQD

where green, red and black letters represent hydrophobic, acidic and neutral amino acids, respectively. Calculating the hydrophobic and neutral character of this sequence revealed an amount of 50% and 40.63%, respectively (PEPTIDE2.0 2007). Thus,  $Mg^{2+}$ -bound IM30 could

hypothetically mimic the  $\Delta$ CT mutant (Junglas 2016), which is known to have increased double-ring formation and fusion activity (Hennig 2014). However, also the  $\Delta$ CT mutant needs  $\text{Mg}^{2+}$  for membrane fusion (Hennig 2014), indicating the necessity of additional structural alteration of the protein in presence of the ion or additional effects of  $\text{Mg}^{2+}$  on the IM30-membrane binding as temporal ring stabilization, which is discussed further in 4.3.4.

As a second possibility (ii),  $\text{Mg}^{2+}$  could be coordinated by four IM30 molecules inside a tetramer or by several ring subunits. Since the inner diameter of an IM30 ring is  $\sim 10$  nm (Fuhrmann *et al.* 2009a) and coordination distances of  $\text{Mg}^{2+}$  are usually in the Å range,  $\text{Mg}^{2+}$  ions cannot be coordinated in the center of an IM30 ring. However, as the tetramer forming mutant C7 does not bind  $\text{Mg}^{2+}$  (Hennig 2014) and the ring structure is most probably required for ion binding, as shown in the ANS experiments using the mutant A227C (*cf.* Fig. 3.14), an intermolecular coordination beyond the tetrameric ring subunits does not seem completely abstruse. In fact, delocalization of the IM30 C-terminus, a hypothetical coiled-coil formation with other helices, and the release of a hydrophobic area at the ring top is not excluded in this model, but might rather be a side effect of a structural reorganization of IM30. Considering the ring symmetry, it seems furthermore reasonable that several  $\text{Mg}^{2+}$  ions are coordinated by an IM30 ring. In the most extreme case, the ion could also be coordinated by two IM30 rings, which would also explain the increased formation of double-rings. Anyhow, it seems more likely that the enhanced double-ring generation originates from the structural alteration of an IM30 ring upon  $\text{Mg}^{2+}$  binding, *e.g.* due to an increased hydrophobic surface.

In both scenarios, the incorporation of the C-terminus inside the ring instead of outside seems more likely based on the decreased availability of the  $\alpha$ -helix for trypsin in the proteolysis assay (*cf.* Fig. 3.18), as described above.

A schematic overview for the discussed possibilities of  $\text{Mg}^{2+}$  coordination inside an IM30 ring is illustrated in Fig. 4.3.

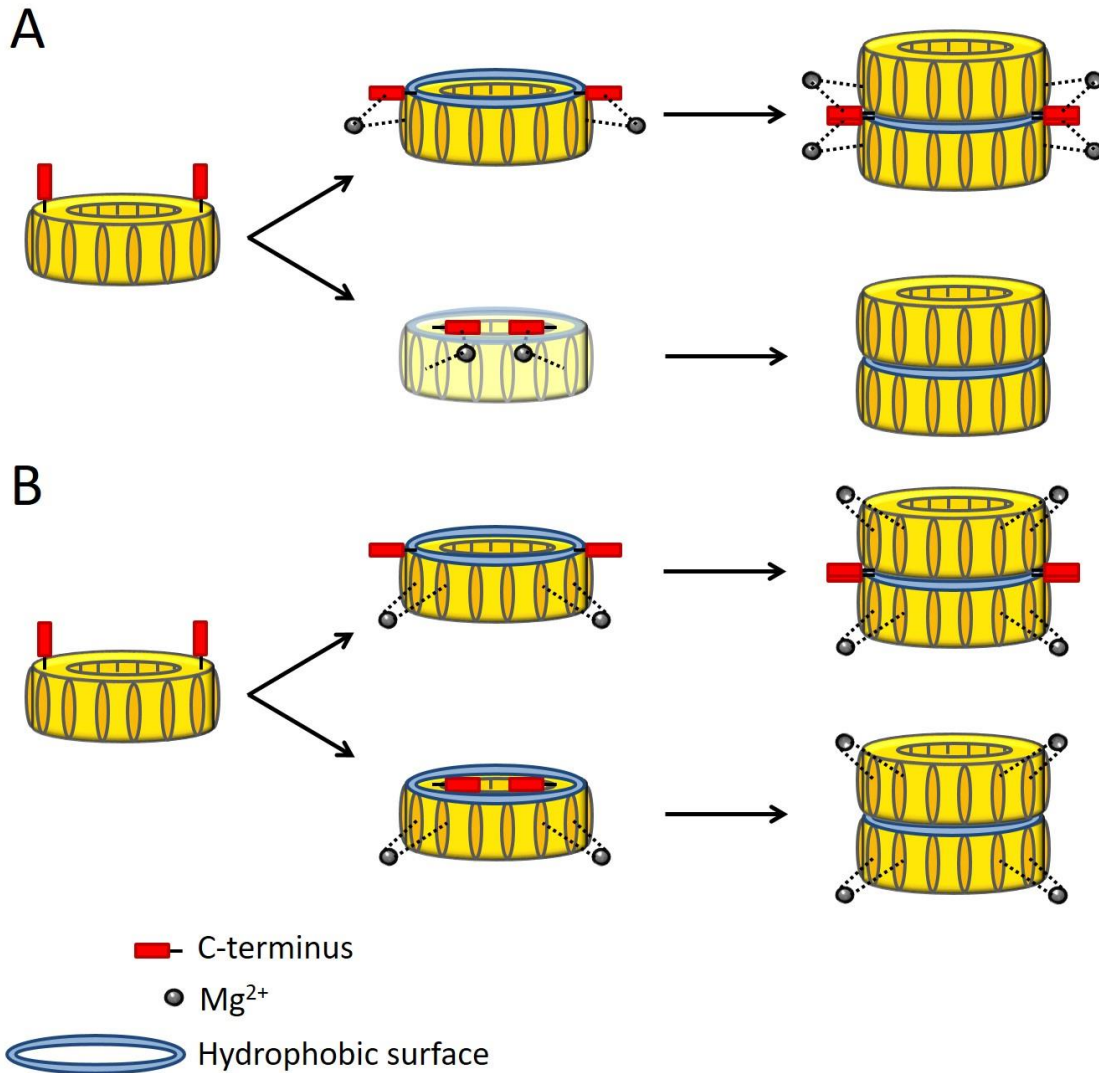


**Fig. 4.3: Possible binding of Mg<sup>2+</sup> by IM30 rings**

Different possibilities for Mg<sup>2+</sup> binding by IM30 are schematically illustrated. The ion could be coordinated protein-internally (A). In this case, the C-terminal  $\alpha$ -helix is dislocated due to Mg<sup>2+</sup> binding. The C-terminus could be located outside or inside the ring, possibly including coiled-coil formation. Upon Mg<sup>2+</sup> binding, hydrophobic areas at the ring top get exposed, resulting in double-ring formation. On the other hand, Mg<sup>2+</sup> might also be coordinated by two IM30 monomers from different ring subunits (B). The interaction eventually results in a structural rearrangement of the protein monomers inside the ring, also resulting in a hydrophobic surface and increased double-ring formation. Note that only two representative Mg<sup>2+</sup> ions and C-termini are shown per ring. The large distance between IM30 rings and Mg<sup>2+</sup> ions is not realistic and was chosen for a better overview. See text for further details and possibilities of the respective scenarios.

### 4.3 Interaction of IM30 with membranes

The ability of IM30 to interact with membranes has early been suggested (Li *et al.* 1994) and was recently confirmed via cryo-TEM (Hennig *et al.* 2015) and Laurdan experiments, showing that the protein binds to membranes containing the negatively charged lipids SQDG or PG (Suppes 2013; Hennig *et al.* 2015). Furthermore, the IM30-membrane interaction was supported by tryptic digestion, in which the digestion of IM30 was delayed when bound to 100% DOPG

liposomes (*cf. Fig. 3.26*). However, further information concerning this interaction are lacking. In the framework of this thesis, the forces driving the IM30-membrane interaction as well as the effect of the IM30 structure on the membrane binding were investigated. Furthermore, the effect of  $Mg^{2+}$  on the interaction of IM30 with negatively charged membrane models and the dissociation of IM30 rings on membranes were analyzed.

#### 4.3.1 Forces driving IM30 binding to membranes

Since IM30 binds to the negatively charged lipids PG and SQDG (Suppes 2013; Hennig *et al.* 2015), it seems reasonable to assume that the IM30-membrane interaction is driven by electrostatic forces. Thus, positively charged amino acids of the protein could play a crucial role during the binding process. Indeed, the basic amino acids arginine, lysine, and histidine can be found in all sections of IM30, especially in the PspA domain (*cf. 5.1.2*). Usually, peripheral membrane proteins associate to bilayers via electrostatic interactions followed by incorporation of hydrophobic groups or helices into the membrane (Khan *et al.* 2016). The electrostatic forces between protein and membranes normally have a long-range character, and each amino acid contributes  $\sim 1$  kcal/mol to the binding energy (Kim *et al.* 1991; Johnson & Cornell 1999).

In order to investigate a hypothetical electrostatic origin of the IM30-membrane interaction, a displacement assay was performed by titrating NaCl to 100% DOPG liposomes pre-incubated with IM30, where the  $Na^+$  ions were supposed to electrostatically shield the membrane surface resulting in a dissociation of IM30 (*cf. Fig. 3.27B*). The tryptophan fluorescence was monitored in this experiment since it depends on the environment of the amino acid. In the case of an altered environment for the only IM30 tryptophan residue W71 in presence and absence of negatively charged membranes, IM30 dissociation from the 100% DOPG liposomes into the buffer was expected to result in a shifted fluorescence upon dissociation. This was indeed observed upon increasing the NaCl concentration. When calculating the differences between the titration curve and the control curve from samples lacking liposomes, a dissociation curve for IM30-DOPG binding was revealed (*cf. Fig. 3.27C*), exhibiting a constant difference above  $\sim 100$  mM NaCl, which indicates a complete electrostatic shielding of the liposomes by  $Na^+$ . Thus, the results of this experiment strongly implied an electrostatic impetus of the IM30-membrane interaction.

It has previously been demonstrated that the lipid chain length is not crucial for IM30-membrane binding as the protein could interact with both 100% DOPG as well as 100% DMPG liposomes (Suppes 2013; Hennig *et al.* 2015; Heidrich *et al.* 2016). Whether the electrostatic interaction of IM30 with negatively charged membranes depends on the lipid head-groups and is, thus, specific for the negatively charged thylakoid lipids or not, was investigated further. The non-thylakoid lipid PS was therefore investigated by measuring relative Laurdan GP values for liposomes including 80% of the background lipid PC and 20% of the negatively charged lipids

thylakoid lipids PG, SQDG and PS, respectively (*cf. Fig. 3.28*). Indeed, the relative Laurdan GP values decreased for all tested negatively charged lipids in presence of IM30.

Obviously, IM30 binds specific to negatively charged membranes, independent from the lipid head-groups. This specificity further emphasizes the tendency of the protein to interact with membranes via electrostatic forces. Importantly, the experiments tackling the electrostatic membrane interaction of IM30, which were described in 3.5.2, do not exclude additional hydrophobic interactions of IM30 with negatively charged membranes. Indeed, the C-terminal  $\alpha$ -helix, which has been shown to have a conserved hydrophobic character (Vothknecht *et al.* 2012), was recently demonstrated to interact with membranes (Hennig *et al.* 2017). On the other hand, this was only confirmed for the isolated C-terminus and might only be valid for lower-ordered IM30 structures, which could occur upon IM30 ring dissociation on membranes (*cf. 4.3.4*).

When discussing the membrane binding site of IM30 rings, it has to be considered that the C-terminus, which is probably located at the top sites of the rings (Saur *et al.* 2017), seemed not to be specifically protected in the proteolysis assay, since the degradation band appeared contemporaneously in presence and absence of liposomes (*cf. Fig. 3.26*). Noteworthy, this experiment was not performed in excess of available lipid binding area compared to IM30, most probably excluding an excessive dissociation of IM30 on the membranes. Furthermore, the IM30 N-terminal PspA domain has repetitively been suggested to be involved in IM30-membrane interaction (Otters *et al.* 2013; McDonald *et al.* 2017). Thus, the IM30 ring binding via the bottom site, which might be occupied by the loop 2 region of IM30 (*cf. Fig. 1.5*) as suggested in (Saur *et al.* 2017), seems likely. When illustrating the amino acids in this area and additional amino acids from the surrounding helices (K69-S96), the charged amino acids are outnumbering hydrophobic/neutral amino acids:

KKWEDRAKLALTN~~GEEN~~LAREALARKKS

where green, red, blue and black letters represent hydrophobic, acidic, basic and neutral amino acids, respectively. Calculating the acidic and basic character of this sequence revealed an amount of 17.86% and 28.57%, respectively (PEPTIDE2.0 2007). Due to the presence of several basic amino acids in this region, in which R74, R88, R93, K94 and K95 are conserved in the PspA/IM30 family (*cf. 5.2*), it seems reasonable to assume that the IM30 ring bottom binds to anionic lipids via electrostatic forces, as already discussed above. Interestingly, the C4 mutant, which has a further decreased amount of hydrophobic amino acids in the loop 2 region but instead two additional polar serine residues, has an increased DOPG membrane binding affinity (*cf. Table 3.4*). Furthermore, the fluorescence of W71 of membrane-bound IM30 WT changed upon replacing IM30 from the membranes by Na<sup>+</sup> (*cf. 3.5.2*), indicating an initial influence of the membrane on W71. However, the presence of five acidic amino acids in the loop 2 region,

in which E84 and E89 are conserved in the PspA/IM30 family (*cf.* 5.2), could counteract the electrostatic attraction. Due to the lack of further data, it cannot be said if they might play a role in regulation of the membrane-interaction, IM30 ring dissociation or membrane fusion. Interestingly, cluster mutations including E84 and E89 resulted in fusion incompetent IM30 mutants (Hennig 2014; Saur *et al.* 2017). Noteworthy, conserved amino acids in the discussed region are also likely involved in coiled-coil formation (Osadnik *et al.* 2015).

#### 4.3.2 Effect of IM30 ring formation on membrane binding

Regardless of their potential physiological relevance, IM30 rings were shown *in vitro* via TEM to bind at negatively charged membranes (Hennig *et al.* 2015). However, whether also lower-ordered structures can interact with bilayers or not has not been demonstrated so far. This lack of information can be ascribed to the inability of TEM measurements to visualize smaller IM30 oligomers or monomers. However, since different oligomerization states of the protein could have an impact on IM30-mediated membrane fusion during a dissociation processes, the membrane binding affinity of IM30 proteins, which had different quaternary structures, was investigated further.

IM30 WT and the C7 mutant were used as representatives for rings and tetramers, respectively, based on former results from SEC (Heidrich *et al.* 2016), and the dissociation constants  $K_D$  were determined for the membrane interactions via recording of binding curves using Laurdan-labeled 100% DOPG liposomes (*cf.* Fig. 3.29). The results demonstrated that tetrameric IM30 could interact with DOPG membranes as well. Furthermore, calculation of the  $K_D$  values even indicated an increased binding affinity of the C7 mutant compared to IM30 WT (1.39 vs. 7.20  $\mu\text{M}$ ). Consequently, oligomerization into ring structures probably counteracts membrane binding of IM30. This discovery is important when discussing the dissociation of IM30 rings on membranes (*cf.* 4.3.2). Additionally, NanoSPR measurements showed a  $K_D$  of 0.4  $\mu\text{M}$  for the IM30-membrane interaction (Heidrich *et al.* 2016). This might be explainable by the assumption that the used Au nanoparticles, which were covered with a lipid bilayer, were too small to provide a binding surface for IM30 rings. Thus, the obtained  $K_D$  value was ascribed to the small fraction of IM30 lower-ordered structures in solution and therefore supported the  $K_D$  value gained for the C7 mutant.

The higher affinity of the IM30 tetramers (represented by the C7 mutant) might be explained by a different binding type. It seems unlikely for a single tetramer to bind in an upright position at the membrane, as it has been shown for IM30 subunits when part of the ring (Hennig *et al.* 2015). Instead, a parallel arrangement of the helices to the membrane surface appears reasonable. Thus, the possibility for amphipathic helices to incorporate into the membrane seems increased due to a potentially advantageous orientation. Furthermore, the C-terminus, which might have an increased membrane availability when the protein is arranged parallel to the bi-

layer surface, has been shown to interact with membranes (Hennig *et al.* 2017), as already discussed above.

### 4.3.3 Effect of $Mg^{2+}$ on IM30 membrane binding

Not only does  $Mg^{2+}$  influence the structural properties and thermodynamic stability of IM30, it also seems to affect the membrane binding affinity of the protein, as it has been indicated previously via SFG measurements (Hennig *et al.* 2015). In the past, the membrane binding affinity of several proteins has been demonstrated to be enhanced by divalent cations as for the neuronal calcium sensor recoverin, which binds to membranes in presence of  $Ca^{2+}$  due to structural alterations (Potvin-Fournier *et al.* 2017). To further investigate the effect of  $Mg^{2+}$  on IM30 membrane binding, SPR measurements were performed using the thiol-coupled fatty acid 16-MHDA. Importantly, the dissociation of IM30 rings on monolayers was excluded due to previously performed SFG measurements (Hennig *et al.* 2015). Addition of IM30 and IM30/ $Mg^{2+}$  was observed kinetically and in equilibrium via scan measurements (*cf.* Fig. 3.30A and B). In presence of  $Mg^{2+}$ , IM30 was able to bind twice as fast to the negatively charged surface as well as to a greater extent, since a thicker protein layer was calculated compared to the sample lacking  $Mg^{2+}$  (*cf.* Table 3.5). A faster binding of the protein/ $Mg^{2+}$  mixture to the 16-MHDA surface indicates an increased association rate constant  $k_{on}$ . On the other hand, the increased reflection  $I_{SPR}$  most probably revealed an enhanced binding affinity of the protein to the 16-MHDA surface in presence of  $Mg^{2+}$  and/or the hypothetical double-ring stabilization through  $Mg^{2+}$ . However, due to the non-reversibility of the binding reaction (*cf.* Fig. 5.29), the measurements were not performed on the same sensor chip. Since different sensor chips slightly vary in their surface coverage and thickness, the measurements were not compared with each other in a quantitative manner. Thus, two kinetic experiments including the addition of both components sequentially were performed on the identical sensor chip (*cf.* Fig. 3.30C and D). First, an IM30 sample was added to the negatively charged surface until a plateau for  $I_{SPR}$  was reached. Subsequently, IM30 pre-incubated with  $Mg^{2+}$  was added. Unsurprisingly, the latter addition had no further effect on  $I_{SPR}$  since the surface was most probably already completely covered. In a second approach, when adding IM30/ $Mg^{2+}$  prior to saturation, a second increase was recorded, which was significantly stronger than the first increase when IM30 alone was added. Thus, the enhancing effect of  $Mg^{2+}$  on association of IM30 at negatively charged surfaces was indicated in this experiment.

When transferring the results of the negatively charged 16-MHDA surface to membranes containing anionic lipids, an increased membrane binding affinity of IM30 in presence of  $Mg^{2+}$ , both kinetically and thermodynamically, is indicated. But how does the ion affect the protein-membrane interaction? There are at least two possibilities: (i)  $Mg^{2+}$  alters the structure of IM30 in a way that the proteins' interaction with the membrane is enhanced or (ii) the ion acts as a glue or bridge between IM30 and the membrane.

When discussing the first case (i), the conclusions described in 4.2 need to be considered. Most probably,  $\text{Mg}^{2+}$  induces the retraction of the C-terminus inside the ring, which results in an increase of hydrophobic surfaces at the ring top and an increased formation of double-rings. Furthermore, the higher-ordered oligomers probably exhibit an increased stability. Since the double-rings are likely connected in a top-to-top orientation, the ring bottom remains as a binding site for the membrane (*cf.* 4.3.1). Upon a structural rearrangement inside the IM30 ring during  $\text{Mg}^{2+}$  binding, a reorientation of basic amino acids in the IM30 loop 2 region, which is probably located at the ring bottom (Saur *et al.* 2017), could enhance the membrane binding affinity of the protein. However, since  $\text{Mg}^{2+}$  induces an increased formation of double-rings, the enhanced affinity of IM30 for negatively charged membrane, which was observed via the mass-weighing method SPR, might be rather apparent due to the assumption that simply more mass is bound to the same membrane area compared to IM30 in absence of  $\text{Mg}^{2+}$  (31% vs. 44% 16-MHDA surface coverage, when normalizing to ring structures, *cf.* Table 3.5). Interestingly, the IM30 mutant  $\Delta\text{CT}$  had a slightly smaller  $K_D$  value for the DOPG membrane interaction (*cf.* Table 3.4) compared to the wildtype. As already mentioned, upon  $\text{Mg}^{2+}$  binding, IM30 was suggested to mimic the  $\Delta\text{CT}$  mutant by relocating the C-terminus inside the ring (Junglas 2016). Indeed,  $\Delta\text{CT}$  has a pronounced tendency for double-ring formation (Hennig 2014). However, the  $K_D$  for the  $\Delta\text{CT}$  mutant was determined via Laurdan measurement, which provide information concerning the membrane polarity change rather than the bound mass. Thus, the informative value of this comparison needs to be taken with care.

Considering another possibility (ii),  $\text{Mg}^{2+}$  could, aside from binding to IM30, additionally connect the protein to negatively charged membranes by acting as a glue. In this case, the ion must interact with negatively charged lipid head groups as well as acidic amino acids of IM30, which can be found to some extent in the loop 2 region (*cf.* 4.3.1). Due to the observations that  $\text{Mg}^{2+}$  probably binds to IM30 rings (*cf.* 4.2.1), which (partly) dissociate upon membrane binding (*cf.* 4.3.4), an IM30- $\text{Mg}^{2+}$  complex formation prior to membrane fusion appears more likely. However, possibility (ii) cannot be excluded in the framework of this thesis. In fact, even the interplay of both cases (i) and (ii) might be possible.

#### **4.3.4 IM30 ring dissociation upon membrane binding in presence and absence of $\text{Mg}^{2+}$**

Recently, dissociation of IM30 rings upon membrane binding has been suggested to be crucial for the potential involvement of IM30 in membrane protection (Heidrich *et al.* 2017; Thurotte *et al.* 2017). This was supported by the observation that the tetramer forming IM30 mutant C7 exhibited a smaller dissociation constant  $K_D$  for the interaction with 100% DOPG membranes than the ring forming IM30 WT (*cf.* Table 3.4). However, no experiment explicitly tackling the IM30 deoligomerization on membranes has been conducted so far. Thus, the IM30 ring dissoci-

ation on liposomes containing different lipid compositions in presence and absence of  $Mg^{2+}$  was investigated as described in 3.8.

In a first experiment, IM30 was incubated with increasing concentrations of 100% DOPG or 60%/40% MGDG/DOPG liposomes, respectively, in presence and absence of  $Mg^{2+}$ . Upon ring dissociation on the respective membranes, monomers were not able to be crosslinked by glutaraldehyde. Loading the samples on an SDS gel revealed the extend of monomer appearance in each sample (*cf. Fig. 3.31 and Fig. 3.32*). Apparently, the IM30 monomer band intensity increased with increasing liposome concentrations for both lipid compositions. This correlation indicates dissociation of IM30 on membranes in absence of  $Mg^{2+}$ . Interestingly, the dissociation is not connected to an MGDG content inside the liposomes. However, the IM30 band intensities of the samples were in general very weak compared to a control sample lacking liposomes. This indicates an uncomplete binding of IM30 to the available liposomes and/or an uncomplete dissociation of bound IM30 rings. On the other hand, IM30 monomers might not be the only product of an IM30 ring dissociation. However, other lower-ordered IM30 oligomerization states were not resolved by using this method. When repeating the experiment in presence of  $Mg^{2+}$ , the monomer band of IM30 completely disappeared when incubated with 100% DOPG and 60%/40% MGDG/DOPG liposomes, respectively. This observation strongly supports a stabilization effect of the ion on IM30 (*cf. 4.2.2*). On the other hand, a ring dissociation into lower-ordered IM30 oligomers despite the presence of  $Mg^{2+}$  was not excluded.

Due to the limitation of the described experiment, another assay using IM30-CFP/Venus was performed next. The protein was incubated with increasing concentrations of 100% DOPG or 60%/40% MGDG/DOPG liposomes, respectively, in presence and absence of  $Mg^{2+}$  and the fluorescence was measured (*cf. Fig. 3.33*). In the case of IM30 ring dissociation, the FRET efficiency  $E_{rat}$  was expected to decrease since the monomers and/or subunits would be distributed on the membrane surface, resulting in less energy transfer. Indeed, in absence of  $Mg^{2+}$ ,  $E_{rat}$  decreased upon liposome addition for both, 100% DOPG and 60%/40% MGDG/DOPG liposomes. This indicated dissociation of the IM30 rings, independent from the lipid MGDG, in agreement with the results of the previous experiment. In presence of  $Mg^{2+}$ , the initial value for  $E_{rat}$  was generally increased ( $\sim 0.7$ ), which can be ascribed to an increased double-ring formation (*cf. Fig. 3.24*). In agreement with the results from the dissociation experiment using glutaraldehyde, the  $E_{rat}$  values did not decrease when 100% DOPG liposomes were added. In presence of 60%/40% MGDG/DOPG liposomes, on the other hand, a decrease of  $E_{rat}$  was observed indicating an MGDG-dependent dissociation of IM30 rings in presence of  $Mg^{2+}$ . Concerning the concentrations used, an excess of lipid binding areas and, thus, enough space for dissociation was assumed. However, in all approaches, the minimal  $E_{rat}$  value was found to remain rather high. This could be explained by a still uncomplete binding of the rings/double-rings and/or a dissoci-

ation into lower-ordered oligomers, apart from the formation of monomers. Additionally, it cannot be completely guaranteed that all membrane-bound IM30 rings are dissociated, which can also have steric reasons.

Overall, the results suggest a dissociation of IM30 rings on negatively charged membranes into monomers and smaller oligomers. This is in line with a recently suggested model of IM30 and PspA, in which the proteins form large scaffold-like structures on stressed membranes (Thurotte *et al.* 2017). Furthermore, GFP-labeled IM30 rings were found to dissociate in *Arabidopsis* upon hypotonic treatment via fluorescence live-imaging (Bryan *et al.* 2014; Zhang *et al.* 2016a). However, other experiments contradict this result. When extracted from membranes, IM30 was shown via SEC to exist in some higher-oligomerized forms, which were suggested to be rings (Fuhrmann *et al.* 2009a). On the other hand, these higher-ordered structures might as well be lower-ordered oligomers. Furthermore, in cryo-TEM experiments, IM30 rings were found attached to negatively charged liposomes (Hennig 2014). Otherwise, in the cryo-TEM measurements, the available lipid binding surface was not in excess compared to the protein (Hennig 2014), and lower-ordered IM30 oligomers resulting from ring dissociation might be present in the sample but were not visible.

Mg<sup>2+</sup> seems to prevent IM30 dissociation on pure DOPG membranes. This is in agreement with the stabilization of IM30 induced by Mg<sup>2+</sup>, which was discussed in 4.2.2. On the other hand, when using 60%/40% MGDG/DOPG liposomes and, thus, the identical conditions used in the membrane fusion assays, dissociation of IM30 rings and/or double-rings were observed to some extent. Most probably, lower-ordered IM30 oligomers were still present after dissociation since no monomers were found in the dissociation experiment using SDS-PAGE. This again supports the idea of Mg<sup>2+</sup> connecting several ring subunits (*cf.* 4.2.3). Furthermore, IM30 deoligomerization is most probably part of the fusion mechanism since the proteins' ring structure in presence of Mg<sup>2+</sup> only dissociates when the conditions used in the fusion assay are applied. The role of IM30 ring dissociation in the membrane fusion is further discussed in 4.4.3.

#### 4.3.5 A model for the IM30-membrane interaction

The following observations and assumptions allow the introduction of a model for the IM30-membrane interaction prior to membrane fusion:

- IM30 binds to negatively charged surfaces via electrostatic forces (*cf.* 3.5) (Suppes 2013; Hennig *et al.* 2015). Thus, it seems reasonable to assume that ring bottoms initially interact with membranes, which probably contain several conserved basic amino acids (*cf.* 4.3.1). The IM30 ring top-sites, at which the C-termini are located, were assumed to be involved in Mg<sup>2+</sup> coordination and double-ring formation (*cf.* 4.2.3).

- The necessity of the IM30 N-terminus (Otters *et al.* 2013; McDonald *et al.* 2017; Saur *et al.* 2017) and the hydrophobic IM30 C-terminus (Hennig *et al.* 2017) for membrane interaction has been suggested previously. Upon ring dissociation and parallel alignment of lower-ordered IM30 structures to the lipid bilayer, the membrane interaction with the IM30 C-termini and/or N-termini appears possible.
- In solution, the equilibrium between IM30 rings and lower-ordered subunits strongly favors the ring structure (Heidrich *et al.* 2016). However, IM30 tetramers have an increased binding affinity to negatively charged membranes (*cf.* 4.3.2), which could be ascribed to an interaction of the N-terminus and/or C-terminus with the bilayer.
- The membrane binding affinity for IM30 and all IM30 mutants is in the  $\mu\text{M}$  range (*cf.* 3.6) whereas the IM30- $\text{Mg}^{2+}$  interactions has a  $K_D$  value in the mM range (*cf.* 3.3.1). Thus, the protein- $\text{Mg}^{2+}$  binding prior to membrane interaction must be regulated via the  $\text{Mg}^{2+}$  concentration.
- Due to the increased membrane binding affinity of lower-ordered IM30 structures, IM30 rings probably dissociate on membranes into monomers and other lower oligomers (*cf.* 4.3.4). The dissociation seems to be prevented by  $\text{Mg}^{2+}$  until a second membrane is available for membrane fusion.
- In presence of  $\text{Mg}^{2+}$ , the membrane binding affinity of IM30 is apparently increased (*cf.* 4.3.3), which is probably based on a statistically advantageous ratio of IM30 mass to available lipid binding area due to ring/double-ring stabilization.

Due to the arguments summarized above, it seems reasonable to assume binding of different IM30 species as monomers, lower-ordered oligomers, rings and double-rings to negatively charged membranes. The equilibrium between the different IM30 oligomers in solution determines the type of binding. Due to the observation that the equilibrium between IM30 rings and lower-ordered IM30 subunits strongly favors the ring structure, it seems likely that mostly IM30 rings initially bind to membranes via the ring bottom site. However, the rings seem to dissociate on membranes, resulting in the distribution of monomers and other lower-ordered oligomers on the lipid bilayer. In presence of a certain threshold concentration of  $\text{Mg}^{2+}$ , on the other hand, double-ring formation of IM30 probably takes place prior membrane binding. Due to a stabilization effect of  $\text{Mg}^{2+}$ , the double rings do not dissociate when membrane-bound until another membrane is available for membrane fusion. Whether undissociated membrane-bound IM30 rings are also binding  $\text{Mg}^{2+}$  remains elusive at this point. The suggested series of events is illustrated in *Fig. 4.4*.

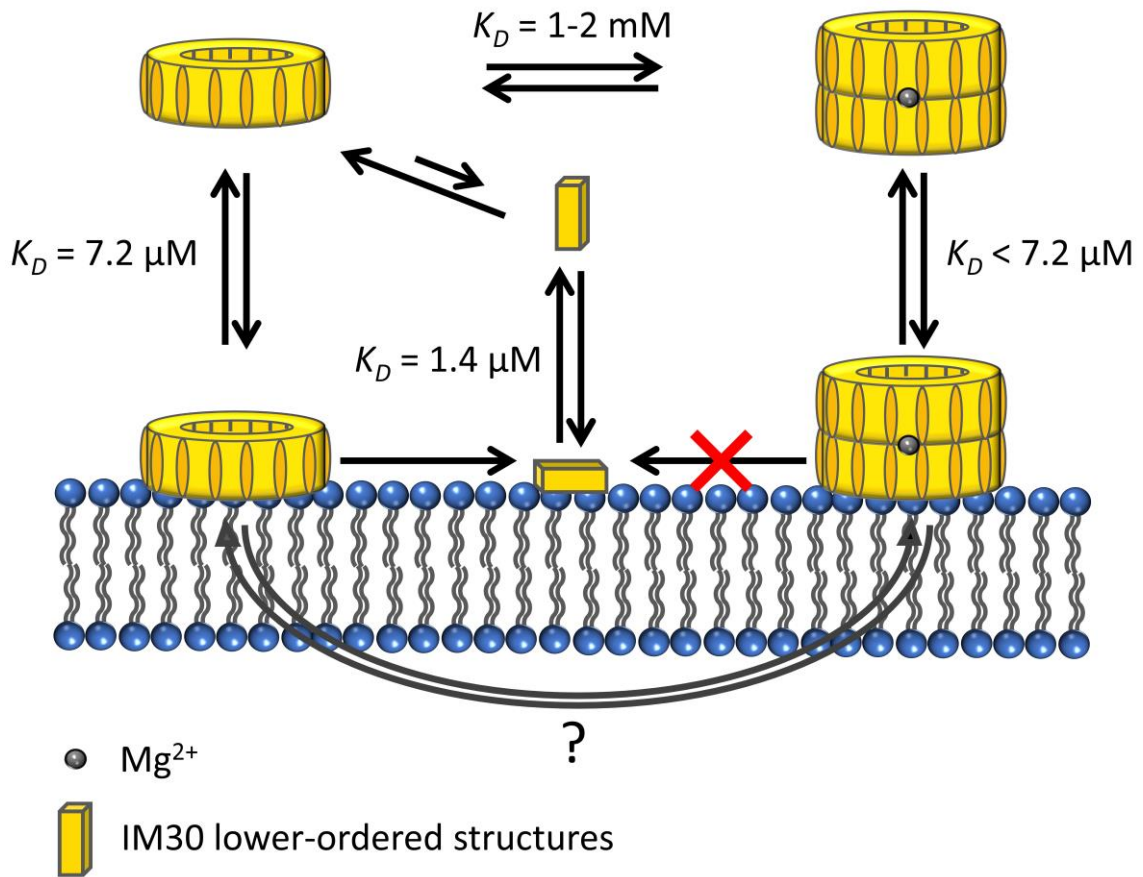


**Fig. 4.4:** Individual steps of the IM30-membrane interaction in presence and absence of  $\text{Mg}^{2+}$

Individual steps of the IM30-membrane interaction in presence and absence of  $\text{Mg}^{2+}$  are illustrated, including the respective equilibria between different IM30 oligomerization states (double-rings, rings and lower-ordered oligomers) in solution and on the membrane. Note that only one representative  $\text{Mg}^{2+}$  ion is shown per double-ring. See text for further details.

## 4.4 IM30-mediated membrane fusion

The *in vivo* function of IM30 is a widely discussed topic (*cf.* 1.4.5). Recently, it could be demonstrated that the protein mediates membrane fusion *in vitro* in dependence of the available  $\text{Mg}^{2+}$  concentration (Suppes 2013; Hennig *et al.* 2015). This was supported via SPT measurements (*cf.* 3.9.1). In the framework of this thesis, the required IM30 oligomerization and membrane composition, and the mechanism of the IM30-mediated membrane fusion were further investigated.

### 4.4.1 What is required for a functional IM30-mediated membrane fusion?

The observation that  $\text{Mg}^{2+}$  induces a stabilization of IM30 double-rings implies the necessity of this higher-ordered structure for IM30-mediated membrane fusion. Indeed, the C7 mutant, which is impaired of performing membrane fusion (Hennig 2014), forms mainly tetramers and cannot oligomerize into ring structures (Heidrich *et al.* 2016). Additionally, the C4 mutant, which is not able to fuse membranes either, only forms rings but no double-rings (Hennig

2014). Further requirements of the IM30-mediated membrane fusion were analyzed in this thesis concerning (i) the structural flexibility of IM30 rings and (ii) the liposome composition.

The dissociation of IM30 rings or, in other words, the structural flexibility of IM30 as a requirement in for a functional membrane fusion process was tested by performing a fusion assay with crosslinked IM30 (*cf. Fig. 3.36*). As expected, the fusion was almost completely prevented in the case of the crosslinked protein. Therefore, it seems likely that the flexibility of IM30 rings is a necessary requirement for a functional membrane fusion process. Anyhow, this result needs to be considered with reservation, since experiments including crosslinkers are usually critical when it comes to artefacts which might be induced by the crosslinker. In this case, protein sites involved in the fusion process might be blocked by glutaraldehyde. The ability of IM30-X to interact with membranes, on the other hand, has been observed this thesis (*cf. 3.6*). Furthermore, as discussed before (*cf. 4.2.1*), it is not clear whether IM30-X is able to bind  $Mg^{2+}$  or not. However, the IM30 deoligomerization experiments described in 3.8 indicated a stabilizing effect of  $Mg^{2+}$  on the IM30 ring structure on 100% DOPG membranes. When using 60%/40% MGDG/DOPG liposomes, on the other hand, this effect was missing and the higher-ordered oligomers dissolved in presence of  $Mg^{2+}$  (*cf. Fig. 3.33*). This result strikingly supported the assumption of a required structural flexibility of IM30 as part of the membrane fusion process. This was supported by the observation that another IM30 mutant, which did not dissociate in presence of  $Mg^{2+}$  and the 60%/40% MGDG/DOPG liposomes, is not able to mediate membrane fusion (Hennig *et al.* 2015).

The investigation of the membrane lipid composition based on observations described in 3.8, where IM30 ring dissociation on membranes in presence of  $Mg^{2+}$  was only possible when applying the same conditions as used in the fusion assays: the presence of the lipid MGDG. Indeed, a fusion assay indicated the enhancing effect of MGDG on IM30 mediated membrane fusion (*cf. Fig. 3.35*). Furthermore, fusion of liposomes containing <60% MGDG in sole presence of  $Mg^{2+}$  was observed. In fact,  $Mg^{2+}$  is known for enhancing the aggregation of liposomes (Leventis *et al.* 1986). However, the sample containing IM30/ $Mg^{2+}$  and 100% DOPG liposomes showed a slightly higher fusion activity compared to the identical sample lacking IM30. This small increase might not have originated from a typical IM30-mediated membrane fusion but rather from enhanced liposome aggregation leading to membrane fusion. This effect might have been supported by IM30 double-rings connecting two membranes via the bottom ring sites (*cf. 4.2.2*). Thus, it does not seem completely unlikely that IM30-mediated fusion of 100% DOPG liposomes is not possible in general and that a certain amount of MGDG needs to be present. Due to the observation that this lipid prefers the inverse-hexagonal lipid phase, it seems reasonable to assume an involvement of MGDG in lipid bilayer destabilization, which is further discussed below (*cf. 4.4.2*)

#### 4.4.2 The mechanism of the IM30-mediated membrane fusion

Membrane fusion processes usually involve the destabilization of lipid bilayers, so that the lipid hydrophobic carbon chains get into contact with the polar environment, which is disadvantageous from an energetic point of view (Arnold 1995; Xia *et al.* 2003; Chernomordik & Kozlov 2008; Marsden *et al.* 2011). Upon membrane aggregation and fusion, the lipid bilayers are restored (Janmey & Kinnunen 2006).

In order to investigate membrane disruption during IM30-mediated membrane fusion, a liposome destabilization assay was performed (*cf.* Fig. 3.37). Here, NBD-PE labeled 60%/40% MGDG/DOPG liposomes were exposed to the quencher sodium dithionite, which initially quenched the fluorophores located at the outer liposome leaflet. Subsequent addition of IM30/Mg<sup>2+</sup> resulted in further strong NBD quenching due to the availability of the inner liposome leaflet. This was possible in the case of membranes which increased permeability for dithionite. Importantly, this second decrease was not observable when only IM30 or Mg<sup>2+</sup> were added. This seems reasonable considering that in the fusion assay both protein and ion needed to be present for the membrane fusion (Suppes 2013). Overall, the results from the liposomes destabilization assay support the theory of membrane destabilization as part of the mechanism for the IM30-mediated membrane fusion. Anyhow, the experiment could not distinguish between a direct, controlled IM30-mediated membrane fusion, similar as in a SNARE mediated fusion (Marsden *et al.* 2011), and a random, uncontrolled fusion. Both cases are schematically illustrated for the *in vitro* situation in Fig. 4.5A and B.

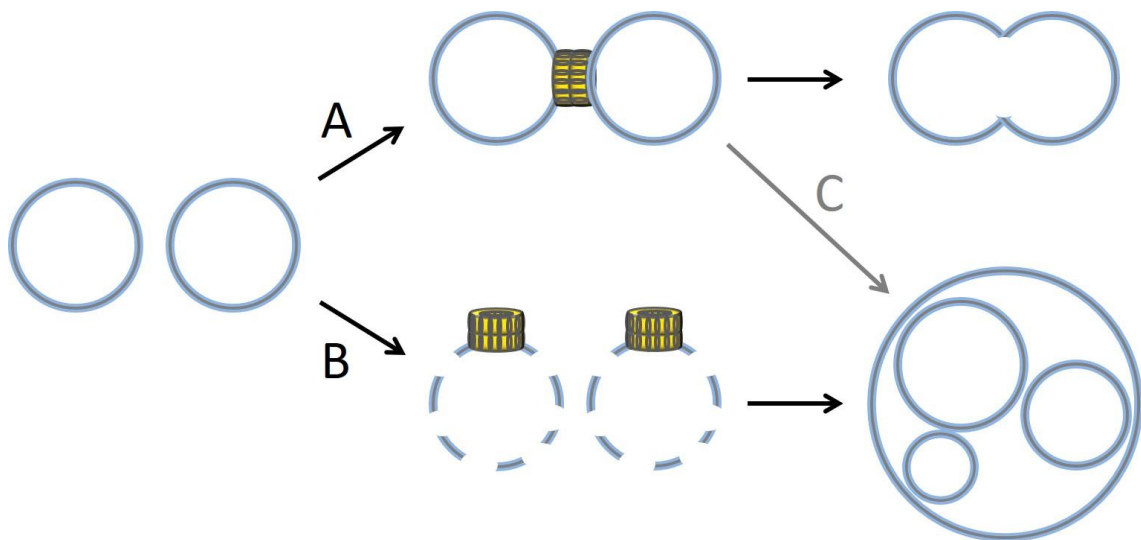


**Fig. 4.5: Model for controlled and uncontrolled *in vitro* IM30-mediated membrane fusion**

Controlled and uncontrolled IM30-mediated membrane fusion are illustrated. The fusion of two membranes could be happen through or adjacent to an Mg<sup>2+</sup>-stabilized IM30 double-ring, which would result in a larger, unilamellar liposome (A). On the other hand, IM30/Mg<sup>2+</sup> could as well destabilize liposomes in an uncontrolled manner, which would lead to oligovesicular and multilamellar liposomes (B). However, also a controlled fusion could result in the non-unilamellar vesicles (C). The latter case is further explained in Fig. 4.6.

In the first scenario, shown in *Fig. 4.5A*, the fusion of two membranes would probably take place through or adjacent to the  $Mg^{2+}$ -stabilized IM30 double-ring, ending up in one larger, still unilamellar liposome. This process does not exclude a temporary destabilization of the liposomes and an increased permeability for sodium dithionite, *e.g.* during IM30 double-ring dissociation. In the other case, illustrated in *Fig. 4.5B*, destabilization would be undirected and random, resulting in the formation of oligovesicular and multilamellar liposomes. Indeed, the latter were observed in TEM micrographs of 60%/40% MGDG/DOPG liposomes in presence of IM30/ $Mg^{2+}$  (Hennig *et al.* 2015). Thus, at first glance, it seems reasonable to assume an uncontrolled fusion mechanism. However, there is another possibility to explain the TEM observations in the context of direct, uncontrolled fusion, which is indicated in *Fig. 4.5C* and further illustrated in *Fig. 4.6*.

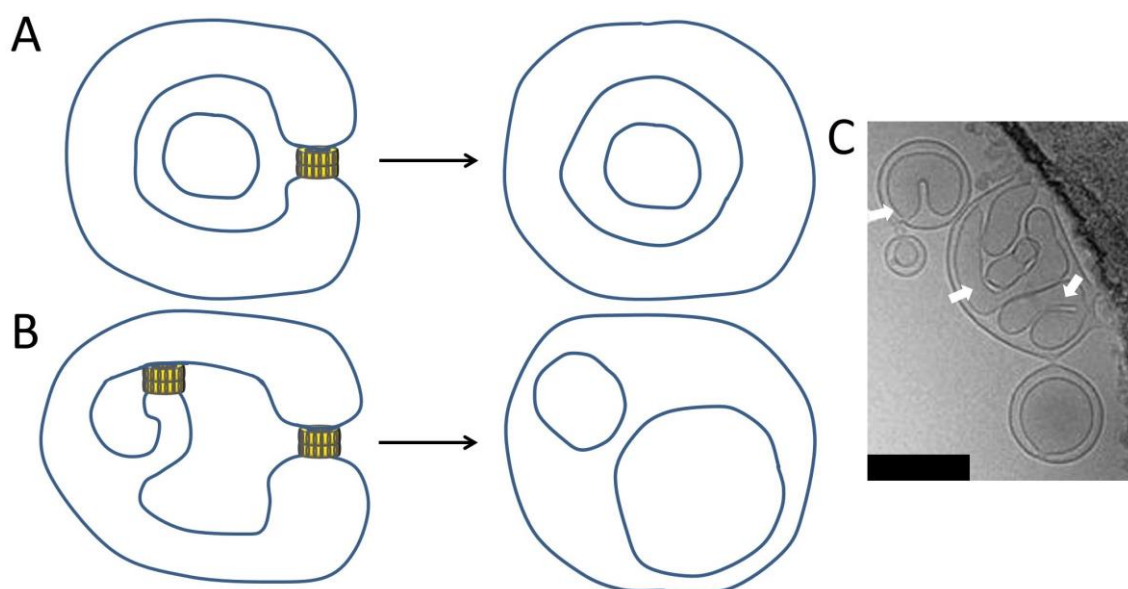


**Fig. 4.6: Formation of multilamellar and oligovesicular liposomes via direct, controlled IM30-mediated membrane fusion**

The formation of oligovesicular and multilamellar liposomes might be induced by a direct, controlled IM30-mediated membrane fusion. Liposome excrescences might fuse liposome-internally, mediated by IM30/ $Mg^{2+}$ . This could happen around a smaller liposome (A) or multiple times inside the same liposome (B), resulting in multilamellar or oligovesicular liposomes, respectively. This explanation was developed together with Adrien Thurotte. Curved liposomes can indeed be observed *in vitro* via TEM upon IM30/ $Mg^{2+}$  addition (C, indicated by arrows, scale bar represents 200 nm). The TEM picture (C) was reused and modified from (Hennig *et al.* 2015).

As demonstrated in *Fig. 4.6*, single liposomes might develop elongated excrescences, which are liposome-internally closed by a controlled IM30-mediated membrane fusion. This could take place around a smaller liposome, resulting in a multilamellar liposome (*Fig. 4.6A*) or multiple times inside the same liposome, which would end up in an oligovesicular liposome (*Fig. 4.6B*). Despite the energetic disadvantage, such curved liposomes can indeed be observed *in vitro* via TEM when applying fusion conditions (*Fig. 4.6C*) (Hennig 2014).

An important role of the lipid MGDG in the *in vivo* IM30-mediated membrane fusion was recently suggested (Bastien *et al.* 2016) and supported by an *in vitro* fusion assay in this thesis (*cf.*

3.9.2). The formation of local membrane areas of enriched MGDG content, which might result in a destabilization of the bilayer, could be a crucial step in the fusion process (Bastien *et al.* 2016; Heidrich *et al.* 2016) (*cf.* 4.4.3). This is further supported by the observation that IM30 binds to negatively charged lipids (Suppes 2013; Hennig *et al.* 2015) (*cf.* 3.5.1), which *in vivo* could result in a raft-like area formation of enriched SQDG/PG content, leaving a surrounding area with locally increased MGDG concentrations. Upon IM30 ring dissociation, the destabilized lipid area might come into closer contact and could be able to fuse. Indeed, the coexistence of lamellar and non-lamellar phases within the same membrane has been proposed in the past (Garab *et al.* 2000) and the presence of polymorphic phases, including the inverse-hexagonal phase in isolated spinach TM, has recently been observed (Garab *et al.* 2017). Furthermore, a strong cohesion force between membranes containing glycolipids based on water-headgroup interactions has been demonstrated for membrane stacks via atomistic molecular dynamics simulations (Kanduc *et al.* 2017). Thus, MGDG-enriched areas might additionally be attracted to each other.

On the protein secondary/tertiary structural level, the IM30-mediated fusion mechanism can only be discussed in a speculative manner. Known fusion proteins such as SNARE proteins and viral fusion proteins usually exhibit pronounced coiled-coil structures between two proteins, while the proteins incorporate into different membranes in order to connect them (White *et al.* 2008; Marsden *et al.* 2011). Whether IM30 also forms intermolecular coiled-coil structures when part of a ring, *e.g.* within a tetramer subunit, has not been investigated so far. However, upon  $Mg^{2+}$  addition, double-rings are formed and are probably connected via the ring top sites, leaving the bottom sites available for membrane interaction (*cf.* 4.2.2). Thus, it seems reasonable to assume a completely different mechanism for IM30 mediated membrane-fusion compared to eukaryotic and viral fusion proteins and rather a substitution of a single protein dimer by two IM30 rings, which bring two membranes in close proximity. The structural change in the coiled-coil area of SNARE proteins, which induces the encounter of the two membranes, is then hypothetically substituted by ring dissociation in the case of IM30.

#### 4.4.3 A model for the IM30-mediated membrane fusion

The observations, hints and ideas gained in this thesis and former work concerning the IM30/ $Mg^{2+}$ -mediated membrane fusion can be merged to a fusion model on the macromolecular level. Some of these arguments were already published in (Heidrich *et al.* 2017):

- Based on previous experiments, it can be assumed that the equilibria involved in the IM30-mediated membrane fusion include IM30- $Mg^{2+}$  complex formation (*cf.* 3.3.1), membrane binding of IM30 (Suppes 2013; Hennig *et al.* 2015) (*cf.* 3.5.1), and IM30 ring dissociation (*cf.* 3.8). The observations that the IM30 ring structure or other higher-ordered IM30 structures are most probably required for  $Mg^{2+}$  binding (*cf.* Fig.

3.14B) (Hennig 2014) and IM30 rings dissociate in absence of  $Mg^{2+}$  (4.3.4) indicate an IM30/ $Mg^{2+}$  binding prior to IM30 ring dissociation.

- $Mg^{2+}$  probably enhances IM30 double-rings formation with the C-termini facing each other via the ring top sites (*cf.* 4.2.2). Double-ring formation probably supports membrane binding of IM30 via the two bottom sites of the respective rings (*cf.* 4.2.3), which brings two membranes in close proximity to each other.
- Prior to membrane fusion, the IM30 double-ring structure likely does not dissolve due to stabilization by  $Mg^{2+}$  (*cf.* 4.3.4).
- MGDG is required for IM30-mediated membrane fusion (*cf.* 4.4.1). The inverse-hexagonal phase-forming lipid has been assumed to form destabilized MGDG-enriched areas (Bastien *et al.* 2016) and the existence of inverse-hexagonal phases in isolated spinach TM has recently been shown (Garab *et al.* 2017).
- IM30 binds to negatively charged lipids (*cf.* 4.3.1) (Suppes 2013; Hennig *et al.* 2015). Possibly, SQDG and PG accumulate at the ring bottom sites, which results in an MGDG/DGDG-enriched area in the ring center. Calculating the numbers of MGDG and DGDG molecules inside the inner IM30 ring resulted in ~70 and ~30 lipids, respectively (*cf.* 5.13.5).
- The concentration of the inverse-hexagonal phase-preferring lipid MGDG might result in membrane destabilization followed by fusion of two neighboring membranes through the IM30 ring center (*cf.* 4.4.2). Indeed, membranes bending toward the ring center have been observed (Hennig 2014).
- A dissociation of IM30 rings (*cf.* 4.3.4), likely upon release of  $Mg^{2+}$ , which probably does not interact with lower-ordered IM30 structures (*cf.* 4.2.1) might support membrane fusion by bringing the fusing membranes into closer contact.
- After membrane fusion is completed, IM30 needs to be detached from the membrane to be reused in another fusion process. The IM30 release most probably requires some external influence such as phosphorylation (*cf.* 3.1.3).

Due to the arguments summarized above, it can be assumed that an IM30 double-ring/ $Mg^{2+}$  complex binds to a membrane via one ring bottom site. The IM30 rings are stabilized by  $Mg^{2+}$  until another membrane binds to the other ring bottom site. Accumulation of MGDG in the ring centers might result in membrane destabilization and membrane fusion, which could be supported by contemporaneous IM30 ring dissociation. The detachment of IM30 from the membrane probably requires external influence. The suggested model for IM30-mediated membrane fusion is schematically illustrated in *Fig. 4.7*.

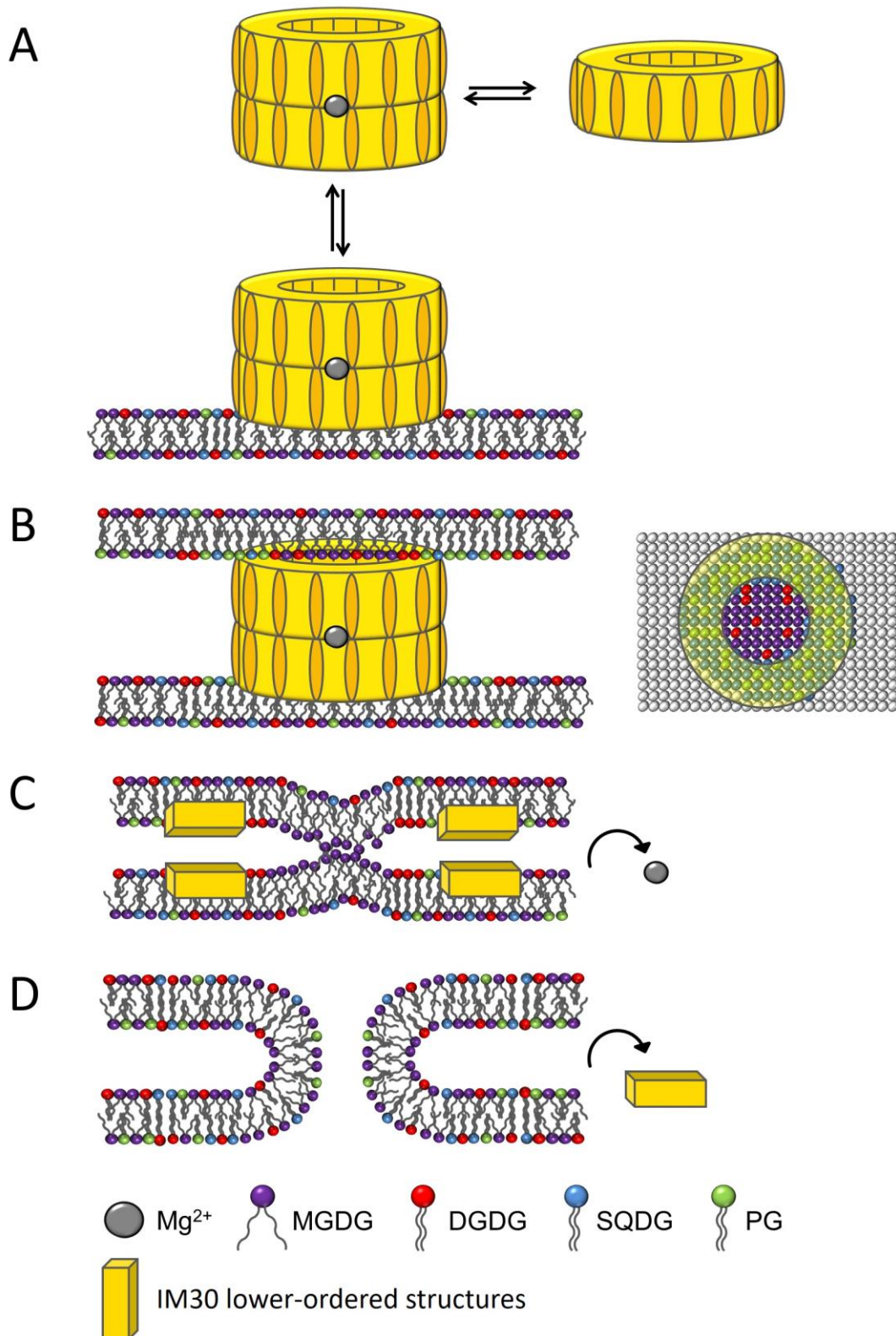


**Fig. 4.7: Model for IM30-mediated membrane fusion**

Shown are steps hypothetically involved in IM30-mediated membrane fusion:  $Mg^{2+}$  induces double-ring formation of IM30 via the ring top sites (A). The double-ring binds to two membranes via the ring bottom sites (A, B). The negatively charged lipids SDQG and PG are concentrated at the ring edges, whereas MGDG and DGDG are located at the ring center (B). Upon IM30 ring dissociation, the two membranes fuse through the IM30 ring center due to the destabilized bilayer and closer contact (C). After membrane fusion, IM30 lower-order oligomers are released from the membranes (D). Note that only one representative  $Mg^{2+}$  ion is shown per double-ring. Modified from (Heidrich *et al.* 2017), used with the permission from Elsevier (license number 4190941074655 via RightsLink).

## 4.5 The *in vivo* role of IM30

The role of IM30 in the TM biogenesis is a widely discussed topic, as already described in 1.4.5. Former findings found in (Suppes 2013; Hennig 2014; Hennig *et al.* 2015; Heidrich *et al.* 2016) and results described in this thesis lead to the assumption that the protein has a dual function in presence and absence of  $Mg^{2+}$ : membrane protection and membrane fusion.

Maintaining the membrane fluidity is a ubiquitous and necessary ability of cell membranes *in vivo* and is called homeoviscous adaptation (Ernst *et al.* 2016). However, there is also a limitation of the possible fluidity since the TM membrane integrity as well as an intact pH gradient between thylakoid lumen and cytoplasm/stroma are crucial for a functional photosynthesis. As already demonstrated in former work, IM30 binding to membranes decreases the membrane fluidity and makes it more rigid (Suppes 2013; Hennig *et al.* 2015; Heidrich *et al.* 2016) (*cf.* Fig. 3.28 and Fig. 3.29). Most probably, this feature can be ascribed to a membrane protection function since membranes get more fluid in several stress situations such as heat shock stress, oxidative stress and solvent stress, and this was counteracted by IM30 in *Arabidopsis* due to an overexpression of the protein (Zhang *et al.* 2012; Zhang *et al.* 2016a; Zhang *et al.* 2016b). By increasing the membrane rigidity, IM30 could reduce the proton and/or ion permeability and maintain the structure and integrity of TMs. Interestingly, IM30 is down-regulated under cold stress conditions in *Synechocystis* (Suzuki *et al.* 2001). In this case, a further decrease of the membrane polarity would be impedimental, as already mentioned in (Suppes 2013; Heidrich *et al.* 2016). Recently, the ability of IM30 to protect membranes was ascribed to the C-terminal  $\alpha$ -helix of IM30 (Zhang *et al.* 2016a). Strikingly, it was observed that the proteins' higher-ordered ring structures dissociate on 100% DOPG and 60%/40% MGDG/DOPG membranes in absence of  $Mg^{2+}$ , which hypothetically ends up in an interaction of the IM30 C-terminus with the respective membranes (*cf.* 4.3.4). Consequently, the dissociation of IM30 rings might result in formation of scaffold-like protective structures (Thurotte *et al.* 2017). Noteworthy, the membrane protection ability of IM30 is most probably a relic from a common ancestor with PspA, which has also been linked to membrane protection in the past (Kleerebezem *et al.* 1996; Kobayashi *et al.* 2007; Standar *et al.* 2008; Yamaguchi *et al.* 2013). Indeed, IM30 could replace PspA in *E. coli* (DeLisa *et al.* 2004; Zhang *et al.* 2012). However, PspA is still present in cyanobacteria and is probably involved in membrane protection. Thus, it seems likely to assume an additional function of IM30, *e.g.* membrane fusion. Indeed, PspA was not able to compensate an *im30* deletion in *Synechocystis* (Westphal *et al.* 2001a). Nevertheless, this does not exclude that IM30 has a dual function and is involved in membrane protection as well. Importantly, PspA is absent in plant chloroplasts. Thus, IM30 might play a role in membrane protection in eukaryotic cells.

The ability of IM30 to trigger membrane fusion seems to be the reason for the proteins' importance in TM biogenesis. All former *in vivo* observations in IM30 deletion strains are proba-

bly secondary effects due to an absence of membrane fusion. In this thesis, a model for the *in vitro* IM30-mediated membrane fusion has been suggested (*cf.* 4.4.3). However, the *in vivo* situation might be different and more complex. In fact, the TM differs from the *in vitro* model membrane used in that it is crowded with protein complexes. Indeed, no experiments tackling the IM30 fusion activity have been conducted for *in vivo* conditions so far. Thus, the following discussion must be seen as speculative.

As already described in 1.2.2, the protein and/or lipid transfer from the PM/IE to the constructive TM, which seems to be the centerpiece in TM biogenesis and maintenance, was suggested to be regulated via (i) soluble glycerolipid transfer proteins, (ii) direct connections of the PM/IE with the TM through thylakoid centers, T-zones and PM/IE invaginations or (iii) a vesicular pathway. In the past, IM30 has been connected to all three possibilities (*cf.* 1.4.5). However, the IM30 fusion model, which was established in this thesis (*cf.* 4.4.3), is only compatible with the latter two options (ii) and (iii), which involve the direct connection of different membranes.

Considering a direct connection between the PM/IE and the TM in cyanobacteria and chloroplasts, the TM structure strongly varies between different photo-autotrophic organisms as already summarized in 1.2.1. Consequently, multiple solutions for PM/IE-TM connection and transfer sites such as thylakoid centers, T-zones and PM/IE invaginations might have been developed independently from each other, and IM30 possibly can participate in all variants as a membrane fusion mediator. The thylakoid centers, which are found in *Synechocystis*, were repeatedly suggested to play a role in TM biogenesis (Nickelsen *et al.* 2011) and a structure containing a rotational symmetry similar to IM30 was found in the center of these biogenesis centers, based on EM studies (Kunkel 1982). In a recently suggested model for thylakoid centers, the TMs are hemi-fused with the PM via a circular structure called PratA-defined membrane (PDM) (Stengel *et al.* 2012). The hemi-fusion, which only involves the connection of one lipid layer, would solve a serious problem concerning the maintenance of the proton gradient in the thylakoid lumen and could be induced by IM30. In another model, the horizontal binding of IM30 rods to thylakoids was suggested as a scaffold for a tubular-like thylakoid center (Rutgers & Schroda 2013). Due to the observation that IM30 rings bind in a perpendicular manner via ring bottom and/or top sites to liposomes (Hennig *et al.* 2015), this model seems rather unlikely. The T-zones in *C. reinhardtii*, which are localized at the pyrenoid and contain an increased amount of mRNA and ribosomes, were found to be adjacent to thylakoid lobes and the IE (Schottkowski *et al.* 2012; Rast *et al.* 2015). This again might involve membrane fusion by IM30. Furthermore, the chloroplast translation membranes (CTMs), which are specialized TM and contain material for photosystem II translation, were found localized within the T-zones (Ossenbuhl *et al.* 2002; Bohne *et al.* 2013), emphasizing the analogy to thylakoid centers in cyanobacteria. In addition to thylakoid centers and T-zones, other hypothetical direct connec-

tions between the TM and the PM/IE were found in cyanobacteria and chloroplasts and discussed as exchange bridges (Shimoni *et al.* 2005; van de Meene *et al.* 2006; Charuvi *et al.* 2012; Engel *et al.* 2015). Additionally to TM-PM/IE connections, a material exchange between two TMs has been suggested to take place at membrane perforation sites in *Synechococcus* (Nevo *et al.* 2007), and the circular TMs in *Cyanothece* sp. ATCC51142 seem to be interconnected (Liberton *et al.* 2011b, a). Whether IM30 only fuses the PM/IE with constructive TMs or also several TM with each other or both cannot be said based on the available data. However, both cases seem possible.

IM30 might as well be involved in the fusion of PM/IE-originated vesicles with the TM, as it has been suggested for *Arabidopsis* due to experiments using cold stress conditions (Kroll *et al.* 2001). The protein was suggested to be involved in the induction of such vesicles, since they were lacking in absence of IM30 (Kroll *et al.* 2001). Thus, IM30 was temporally renamed to Vesicle-inducing protein in plastids 1 (Vipp1). This is contradictory considering the fusion function of IM30. If a vesicle transporting system exists in cyanobacteria and chloroplasts, IM30 would most probably be involved in the opposing event: the fusion of vesicles originating from the PM/IE with the TM. Furthermore, a vesicle exchange between several TMs might be thinkable. However, it has to be mentioned that further evidence for the existence of a vesicle transporting system in plant cells is lacking and no vesicles have been unambiguously detected in cyanobacteria so far (Rast *et al.* 2015). Interestingly, some proteins with homologies to components of the secretory pathway were found in *in silico* analysis to be present in chloroplasts and cyanobacteria (Andersson & Sandelius 2004; Khan *et al.* 2013).

#### 4.6 The *in vivo* regulation of IM30

A critical point to consider is the *in vivo* regulation of the IM30 activity. Accounting the hypothetical dual function of IM30, membrane protection and membrane fusion, the *in vivo* distinction between the two functions is not trivial. Considering the ability of IM30 to increase membrane rigidity in stress situations, the concentration of the protein (including the concentration of PspA) has to be carefully adjusted due to the observation that the membrane transition into the gel phase, which might occur upon an uncontrolled IM30/PspA membrane interaction, is counterproductive for a functional photosynthesis *in vivo* (Biswal *et al.* 1989; Murata 1989). Thus, the IM30 availability, which depends on IM30 expression and transportation, most probably has to underlie a strict control mechanism. Other proteins involved in such a control system have not been identified so far. Known transport systems are the Albino2.3 (Walter *et al.* 2015) and the Tat transport system (Lo & Theg 2012). However, the regulation gets more complicated when considering IM30-mediated membrane fusion. Based on former experiments, it can be assumed that there are different regulation levels of IM30 for a dynamic TM/PM and/or

TM/TM fusion: (i) the IM30 oligomerization into higher-ordered structures, (ii) the protein activation through  $Mg^{2+}$  and (iii) the dissociation of lower-ordered IM30 oligomers and monomers from membranes.

It has previously been suggested that the IM30 oligomerization (i) is controlled by chaperons, since rings and rods disassemble in presence of the heat shock protein 70B (Hsp70B) and the heat shock protein 40 (Hsp40) homologue chloroplast DnaJ-like protein (CDJ2) in *Chlamydomonas reinhardtii* (*C. reinhardtii*) (Liu *et al.* 2005; Liu *et al.* 2007). Other proteins, such as the heat shock protein 90C (Hsp90C), were also found to interact with IM30 (Gao *et al.* 2015). In cyanobacteria, IM30 might be regulated by the Hsp70/Hsp40 homologues DnaK and DnaJ (Liu *et al.* 2007; Bryan *et al.* 2014; Gao *et al.* 2015). *In vivo*, the retention of IM30 ring-structures via Hsp70B/CDJ2 (or homologues), might prevent an uncontrolled fusion. The deoligomerization might as well be useful in chloroplasts when it comes to the transport of IM30 into chloroplasts via the translocons at the inner and outer envelopes (TIC and TOC) (Li & Chiu 2010; Vothknecht *et al.* 2012).

The membrane binding affinity of IM30 is in the  $\mu M$  range (*cf.* 3.6), whereas the IM30- $Mg^{2+}$  interactions has a  $K_D$  value in the mM range (*cf.* 3.3.1) Thus, IM30 has a smaller binding affinity for the ion compared to membranes. This is problematic when it comes to activation of the IM30 fusion activity since the formation of an IM30 (ring)- $Mg^{2+}$  complex (ii) has been suggested to be the first step in the sequence of IM30-mediated membrane fusion (*cf.* 4.4.3) and IM30 dissociates on membranes in absence of  $Mg^{2+}$  (*cf.* 4.3.4). Thus, the ability of IM30 to fuse membranes must be regulated via drastic changes in the cytosolic/stromal  $Mg^{2+}$  concentration, which is given in cyanobacteria and chloroplasts upon light exposure and the release of  $Mg^{2+}$  from the thylakoid lumen (Shaul 2002). Interestingly, the light-induced increase of  $Mg^{2+}$  in chloroplasts was found to vary between 1 and 5 mM (Shaul 2002), which is in perfect agreement with threshold concentrations of 5-7.5 mM found in fusion assays (Suppes 2013; Hennig *et al.* 2015) and the urea denaturation experiment (*cf.* Fig. 3.17). This necessary threshold concentration might be crucial for *in vivo* regulation of IM30 functions in presence and absence of  $Mg^{2+}$ .

An additional regulation point might be dissociation of lower-ordered IM30 oligomers from membranes (iii). IM30 rings were observed to dissociate into unknown smaller oligomers upon applying fusion conditions (*cf.* 3.8). Due to the high affinity of lower-ordered IM30 oligomers (*cf.* 4.3.2) and the observation that the protein was not able to be completely washed off from 16-MHDA surfaces (*cf.* 3.7), the membrane detachment most probably requires some kind of external influence. This is supported by the observation that membrane fusion usually does not reach 100% fusion *in vitro* (*e.g.* as shown in Fig. 3.35) and further components supporting the membrane dissociation of IM30 are probably lacking in the samples. *In vivo*, a recycling of

already ‘used’ protein by membrane dissociation is most probably critical when it comes to a dynamic regulation of TM biogenesis. This recycling might be provided by a phosphorylation/dephosphorylation of IM30. Indeed, the phosphorylation of IM30 during heterologous expression in *E. coli* (cf. 3.1.3) as well as *in vivo* in *Synechocystis* cultures grown on nitrate (Spat *et al.* 2015) has been indicated. Phosphorylation of IM30 would require specific kinases which transfer phosphate residues from an ATP molecule onto the amino acid upon release of ADP. Indeed, several serine/threonine protein kinases (STPKs) in *Synechocystis* were connected to abiotic stress response in the past (Los *et al.* 2010; Zorina 2013; Zorina *et al.* 2014). In *Arabidopsis*, the STN7 kinase phosphorylates membrane proteins as the light-harvesting complex II (LHCII) in a light-dependent manner (Trotta *et al.* 2016). However, further experiments are required to identify a hypothetical IM30-specific kinase.

Another issue to consider is that due to a more determined localization of membranes in cyanobacteria and chloroplasts, the membrane fusion might be an *in vitro* “over-interpretation” and it could make more sense to consider simple temporal connections between membranes as mentioned above. However, this hemi-fusion has to be controlled by so far unknown factors. Indeed, unknown components involved in membrane remodeling were already suggested in the past (Kana & Govindjee 2016) and could be represented by protein complexes or the bilayer-forming galactolipid DGDG, which has been demonstrated to inhibit membrane fusion *in vitro* (Hennig & Schneider, p.c.).

Overall, the fusion function of IM30 seems to be in agreement with observations made in cyanobacteria and chloroplasts and does not contradict existing models for TM biogenesis and maintenance. Since all conclusions made in this thesis are based on *in vitro* experiments, it is difficult to speculate about the *in vivo* situation, which must be further investigated in the future. However, the results in this thesis might provide ideas for further experimental approaches dealing with the proteins’ structural properties, its interaction with  $Mg^{2+}$  and membranes, and its fusion function.

## 5 Appendix

### 5.1 Protein amino acid sequences

The following sequences were illustrated by ProtParam (Gasteiger *et al.* 2005). Mutated residues used in this study are indicated in green.

#### 5.1.1 *Synechocytis sll0617/IM30*

```

      10      20      30      40      50      60
MGLFDRLGRV VRANLNDLVS KAEDPEKVL E QAVIDMQEDL VQLRQAVART IAEEKRTEQR

      70      80      90     100     110     120
LNQDTQEAKK WEDRAKLALT NGEENLAREA LARKKSLTDT AAAYQTQLAQ QRTMSENLR

     130     140     150     160     170     180
NLAALEAKIS EAKTKKNMLQ ARAKAAKANA ELQOTLGGLG TSSATSAFER MENKVL DMEA

     190     200     210     220     230     240
TSQAAGELAG FGIENQFAQL EASSGVEDEL AALKASMAGG ALPGTSAATP QLEAAPVDSS

     250     260
VPANNASQDD AVIDQELDDL RRRLNLL

```

#### 5.1.2 His-tagged IM30 wild type

```

      10      20      30      40      50      60
MGHHHHHHHH HHSSGHIDDD DKHLGLFDRL GRVVRANLND LVSKAEDPEK VLEQAVIDMQ

      70      80      90     100     110     120
EDLVQLRQAV ARTIAEEKRT EQRLNQDTQE AKKWEDRAKL ALTNGEENLA REALARKKSL

     130     140     150     160     170     180
TDTAAAYQTQ LAQQRTMSEN LRRNLAALEA KISEAKTKKN MLQARAKAAK ANAELQOTLG

     190     200     210     220     230     240
GLGTSSATSÄ FERMENKVL D MEATSQAAGE LAGFGIENQF AQLEASSGVE DELAALKASM

     250     260     270     280     290
AGGALPGTSA ATPQLEAAPV DSSVPANNAS QDDAVIDQEL DDLRRRLNLL

```

**5.1.3 His-tagged IM30 ΔCT**

10            20            30            40            50            60  
 MGH<sup>10</sup>HHHHHHH<sup>19</sup> HHSSGHIDDD<sup>20</sup> DKHLGLFDRL<sup>30</sup> GRVVRANLND<sup>40</sup> LVSKAEDPEK<sup>50</sup> VLEQAVIDMQ<sup>60</sup>  
  
70            80            90            100            110            120  
 EDLVQLRQAV<sup>70</sup> ARTIAEEKRT<sup>80</sup> EQRLNQDTQE<sup>90</sup> AKKWEDRAKL<sup>100</sup> ALTNGEENLA<sup>110</sup> REALARKKSL<sup>120</sup>  
  
130            140            150            160            170            180  
 TDTAAAYQTQ<sup>130</sup> LAQORTMSEN<sup>140</sup> LRRNLAALEA<sup>150</sup> KISEAKTKKN<sup>160</sup> MLQARAKAAK<sup>170</sup> ANAELQQT<sup>180</sup>LG  
  
190            200            210            220            230  
 GLGTSSATS<sup>190</sup>A FERMENKVL<sup>200</sup>D MEATSQAAGE<sup>210</sup> LAGFGIENQF<sup>220</sup> AQLEASSGVE<sup>230</sup> DELAALKAS<sup>240</sup>

**5.1.4 His-tagged IM30 C4**

10            20            30            40            50            60  
 MGH<sup>10</sup>HHHHHHH<sup>19</sup> HHSSGHIDDD<sup>20</sup> DKHLGLFDRL<sup>30</sup> GRVVRANLND<sup>40</sup> LVSKAEDPEK<sup>50</sup> VLEQAVIDMQ<sup>60</sup>  
  
70            80            90            100            110            120  
 EDLVQLRQAV<sup>70</sup> ARTIAEEKRT<sup>80</sup> EQRLNQDTQE<sup>90</sup> AKKWEDR<sup>100</sup>SKL<sup>100</sup> SA<sup>110</sup>TNGEENLA<sup>110</sup> REALARKKSL<sup>120</sup>  
  
130            140            150            160            170            180  
 TDTAAAYQTQ<sup>130</sup> LAQORTMSEN<sup>140</sup> LRRNLAALEA<sup>150</sup> KISEAKTKKN<sup>160</sup> MLQARAKAAK<sup>170</sup> ANAELQQT<sup>180</sup>LG  
  
190            200            210            220            230            240  
 GLGTSSATS<sup>190</sup>A FERMENKVL<sup>200</sup>D MEATSQAAGE<sup>210</sup> LAGFGIENQF<sup>220</sup> AQLEASSGVE<sup>230</sup> DELAALKAS<sup>240</sup>M  
  
250            260            270            280            290  
 AGGALPGTSA<sup>250</sup> ATPQLEAAPV<sup>260</sup> DSSVPANNAS<sup>270</sup> QDDAVIDQEL<sup>280</sup> DDLRRRLNNL<sup>290</sup>

**5.1.5 His-tagged IM30 C7**

10            20            30            40            50            60  
 MGH<sup>10</sup>HHHHHHH<sup>19</sup> HHSSGHIDDD<sup>20</sup> DKHLGLFDRL<sup>30</sup> GRVVRANLND<sup>40</sup> LVSKAEDPEK<sup>50</sup> VLEQAVIDMQ<sup>60</sup>  
  
70            80            90            100            110            120  
 EDLVQLRQAV<sup>70</sup> ARTIAEEKRT<sup>80</sup> EQRLNQDTQE<sup>90</sup> AKKWEDRAKL<sup>100</sup> ALTNGEENLA<sup>110</sup> REALARKKSL<sup>120</sup>  
  
130            140            150            160            170            180  
 TDTAAAYQTQ<sup>130</sup> LAQORTMSEN<sup>140</sup> LRRNLAALEA<sup>150</sup> KISEAKTKKN<sup>160</sup> MLQARAKAAK<sup>170</sup> ANAELQQT<sup>180</sup>LG  
  
190            200            210            220            230            240  
 GLGTSSATS<sup>190</sup>A AAAA<sup>200</sup>ENKVL<sup>200</sup>D MEATSQAAGE<sup>210</sup> LAGFGIENQF<sup>220</sup> AQLEASSGVE<sup>230</sup> DKLAALKAS<sup>240</sup>M  
  
250            260            270            280            290  
 AGGALPGTSA<sup>250</sup> ATPQLEAAPV<sup>260</sup> DSSVPANNAS<sup>270</sup> QDDAVIDQEL<sup>280</sup> DDLRRRLNNL<sup>290</sup>

**5.1.6 His-tagged IM30 A227C**

10                    20                    30                    40                    50                    60  
 MGH~~HHHHHHH~~ HHSSGHIDDD DKHLGLFDRL GRVVRANLND LVSKAEDPEK VLEQAVIDMQ  
  
70                    80                    90                    100                    110                    120  
 EDLVQLRQAV ARTIAEEKRT EQRLNQDTQE AKKWEDRAKL ALTNGEENLA REALARKKSL  
  
130                    140                    150                    160                    170                    180  
 TD~~TAAAYQTQ~~ LAQ~~QRTMSEN~~ LRRNLA~~ALEA~~ KISEAKTKKN MLQARAKAAK ANAELQOTLG  
  
190                    200                    210                    220                    230                    240  
 GLGTSSATSÄ FER~~MENKVL~~D MEATSQAAGE LAGFGIENQF AQLEASSGVE DELAALKASM  
  
250                    260                    270                    280                    290  
 AGGALPGTSA ~~C~~ ATPQLEAAPV DSSVPANNAS QDDAVIDQEL DDLRRRLNNL

**5.1.7 His-tagged IM30-CFP**

10                    20                    30                    40                    50                    60  
 MGH~~HHHHHHH~~ HHSSGHIDDD DKHLGLFDRL GRVVRANLND LVSKAEDPEK VLEQAVIDMQ  
  
70                    80                    90                    100                    110                    120  
 EDLVQLRQAV ARTIAEEKRT EQRLNQDTQE AKKWEDRAKL ALTNGEENLA REALARKKSL  
  
130                    140                    150                    160                    170                    180  
 TD~~TAAAYQTQ~~ LAQ~~QRTMSEN~~ LRRNLA~~ALEA~~ KISEAKTKKN MLQARAKAAK ANAELQOTLG  
  
190                    200                    210                    220                    230                    240  
 GLGTSSATSÄ FER~~MENKVL~~D MEATSQAAGE LAGFGIENQF AQLEASSGVE DELAALKASM  
  
250                    260                    270                    280                    290                    300  
 AGGALPGTSA ATPQLEAAPV DSSVPANNAS QDDAVIDQEL DDLRRRLNNL GSVSKGEELF  
  
310                    320                    330                    340                    350                    360  
 TGVVPILVEL DGDVNGHRFS VSGEGEGDAT YGKLTLKFIC TTGKLPVPWP TLVTTTLTWGV  
  
370                    380                    390                    400                    410                    420  
 QCFSRYPDHM KQHDFFKSAM PEGYVQERTI FFKDDGNYKT RAEVKFEGDT LVNRIELKGI  
  
430                    440                    450                    460                    470                    480  
 DFKEDGNILG HKLE~~YNYISH~~ NVYITADKQK NGIKAHFKIR HNIEDG~~SVQL~~ ADHYQONTPI  
  
490                    500                    510                    520                    530  
 GDGPVLLPDN HYLSTQSKLS KDPNEKRDHM VLLEFVTAAG ITHGMDELYK GIQ

**5.1.8 His-tagged IM30-Venus**

10            20            30            40            50            60  
 MGHSHHHHHH HHSSGHIDDD DKHLGLFDRL GRVVRANLND LVSKAEDPEK VLEQAVIDMQ

70            80            90            100            110            120  
 EDLVQLRQAV ARTIAEEKRT EQRLNQDTQE AKKWEDRAKL ALTNGEENLA REALARKKSL

130            140            150            160            170            180  
 TDTAAAYQTQ LAQQRMSSEN LRRNLAALAE KISEAKTKKN MLQARAKAAK ANAELQQTIG

190            200            210            220            230            240  
 GLGTSSATSA FERMENKVL D MEATSQAAGE LAGFGIENQF AQLEASSGVE DELAALKASM

250            260            270            280            290            300  
 AGGALPGTSA ATPQLEAAPV DSSVPANNAS QDDAVIDQEL DDLRRRLNNL GSVSKGEEELF

310            320            330            340            350            360  
 TGVVPILVEL DGDVNGHKFS VSgegeG DAT YGKLTlKLiC TTGKLpVpWP TLVTTlGyGL

370            380            390            400            410            420  
 QCFARYPDHM KQHDFFKSAM PEGYVQERTI FFKDDGNYKT RAEVKFEGDT LVNRIELKGI

430            440            450            460            470            480  
 DFKEDGNILG HKLEYNYN SH NVYITADKQK NGIKANFKIR HNIEDGGVQL ADHYQQNTPI

490            500            510            520            530  
 GDGPVLLPDN HYLsyQSALS KDPNEKRDHM VLLEFVTAAG ITLGMDELYK

## 5.2 Sequence conservations within the PspA/IM30 family

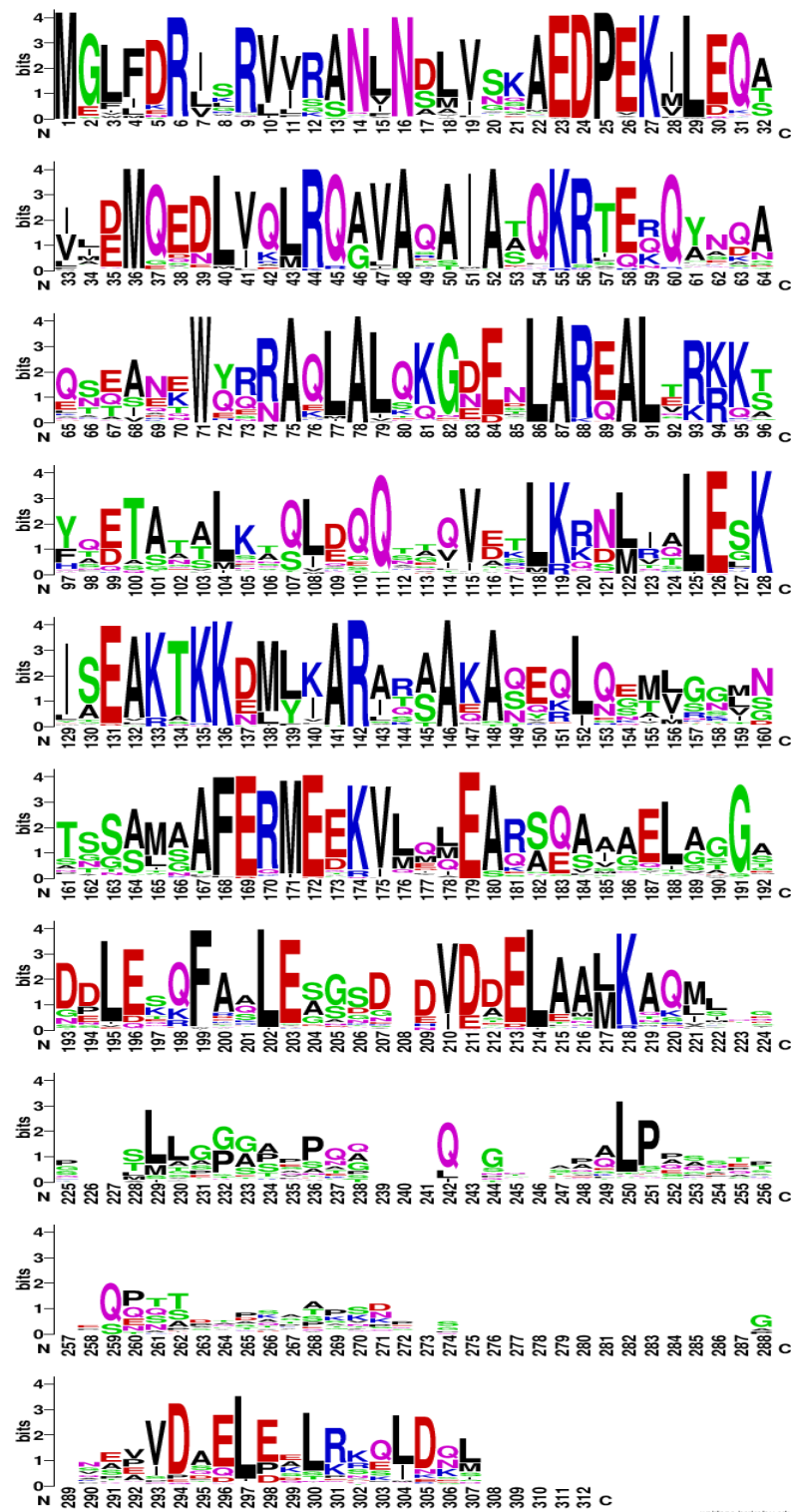


**Fig. 5.1:** Sequence conservations within the cyanobacterial PspA/IM30 family

A sequence alignment of the cyanobacterial PspA/IM30 family was performed by using sequence information from the Pfam database (Finn *et al.* 2014). In order to emphasize conserved amino acids, the web based application Web-Logo (Crooks *et al.* 2004) was used. Strongly differing sequences were removed manually. The degree of conservation is represented by the number of bits.

## 5.3 Fluorescence spectra of dyes used in the fusion assays

### 5.3.1 Green fusion assay

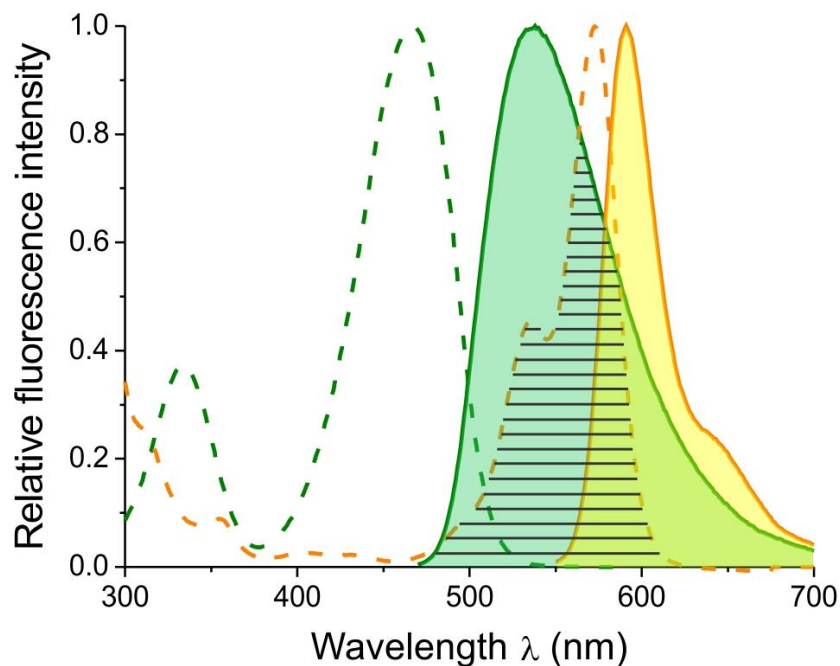


**Fig. 5.2:** Normalized fluorescence excitation and emission spectra of NBD-PE and LissRhod-PE

Typical fluorescence excitation (dashed line) and emission (continuous line) spectra of NBD-PE (green) and LissRhod-PE (yellow) are shown. The Spectral overlap  $J$  is indicated by shading. The data were obtained from Thermo Scientific (ThermoScientific™ 2017).

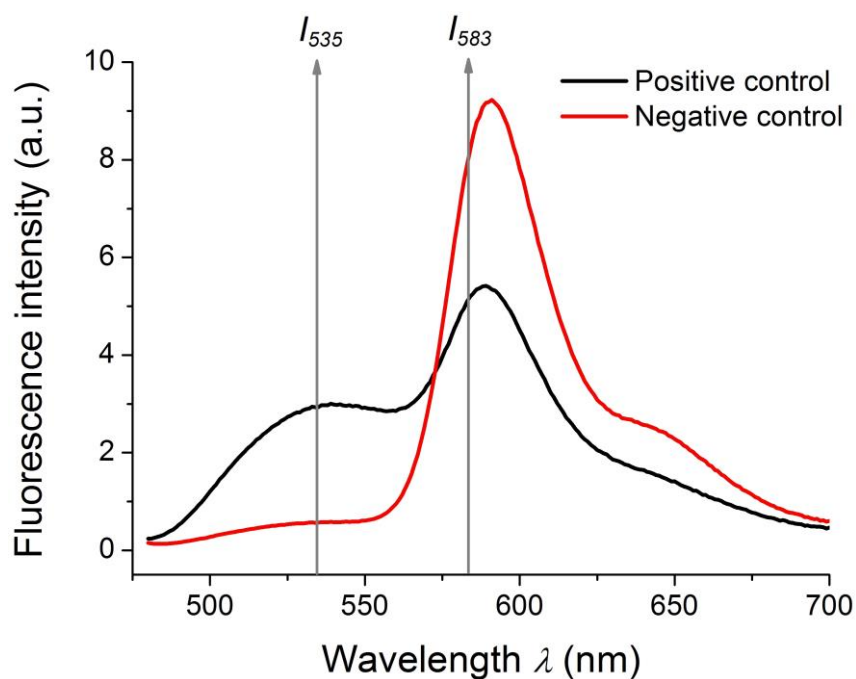


**Fig. 5.3:** Fluorescence spectra of the positive and negative controls of the green fusion assay

The fluorescence spectra of the positive and negative controls of the green fusion assay are shown. The donor emission peak at 535 and the acceptor emission peak at 583 nm are indicated.

### 5.3.2 Red fusion assay

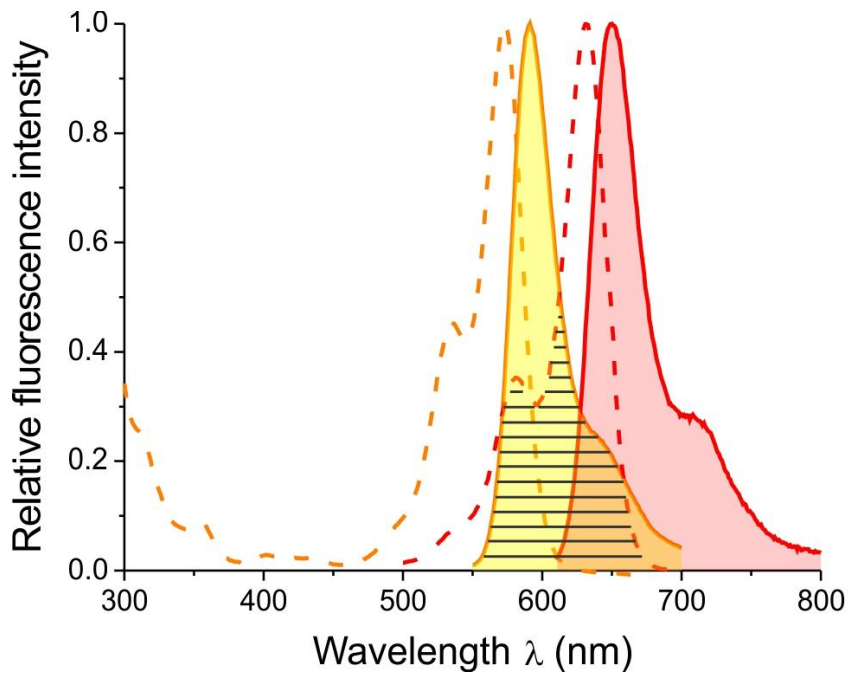


**Fig. 5.4: Normalized fluorescence excitation and emission spectra of LissRhod-PE and Atto633-PE**

Typical fluorescence excitation (dashed line) and emission (continuous line) spectra of LissRhod-PE (yellow) and Atto633-PE (red) are shown. The spectral overlap  $J$  is indicated by shading. The data were obtained from Thermo Scientific (ThermoScientific™ 2017).

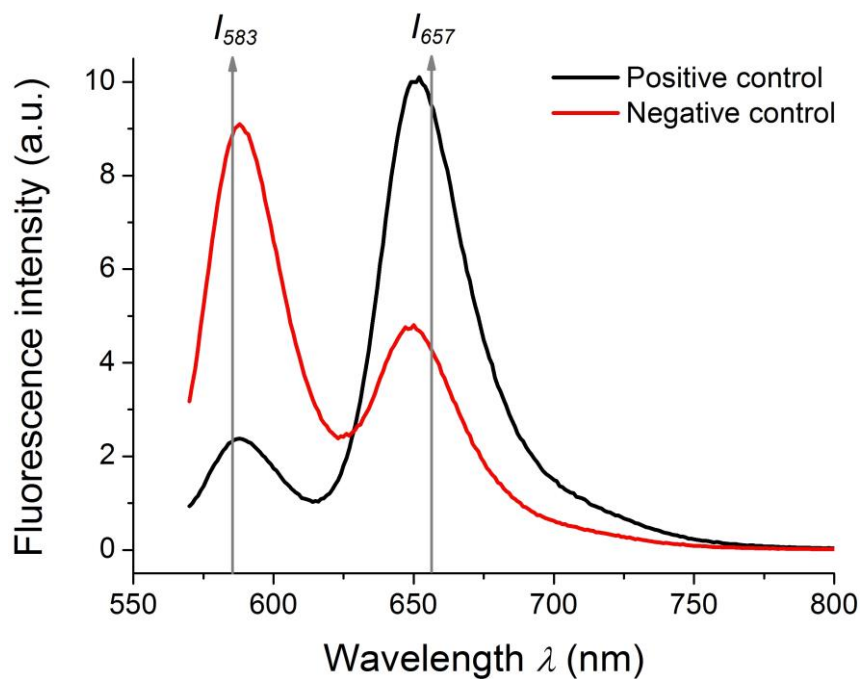


**Fig. 5.5: Fluorescence spectra of the positive and negative controls of the red fusion assay**

The fluorescence spectra of the positive and negative controls of the green fusion assay are shown. The donor emission peak at 583 and the acceptor emission peak at 657 nm are indicated.

#### 5.4 Fluorescence spectra of IM30-CFP and IM30-Venus

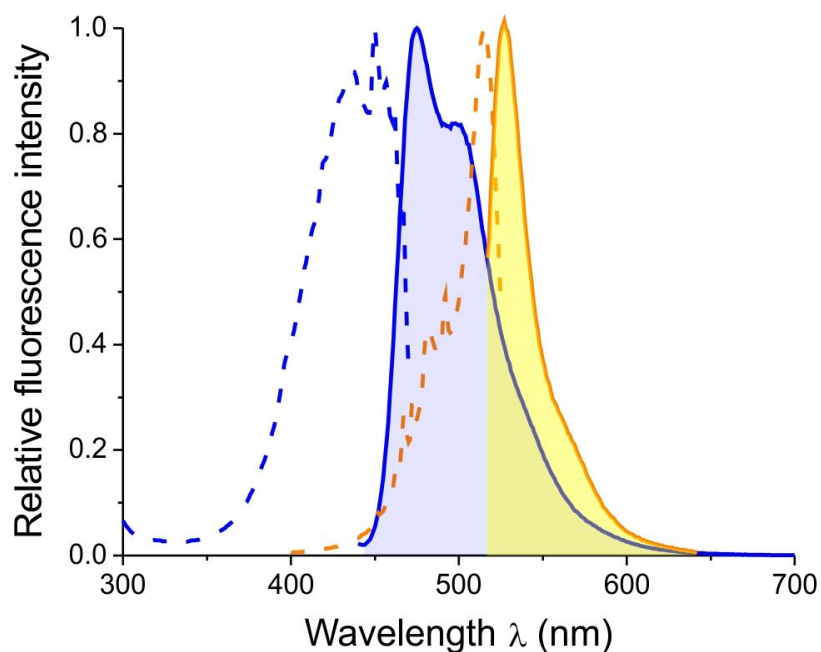


*Fig. 5.6: Normalized fluorescence excitation and emission spectra of IM30-CFP and IM30-Venus*

Typical fluorescence excitation (dashed line) and emission (continuous line) spectra of IM30-CFP (blue) and IM30-Venus (yellow) samples were recorded. For experimental reasons, the spectral overlap cannot be displayed.

#### 5.5 Fluorescence spectra (triplicate) of IM30-CFP/Venus (1/1)

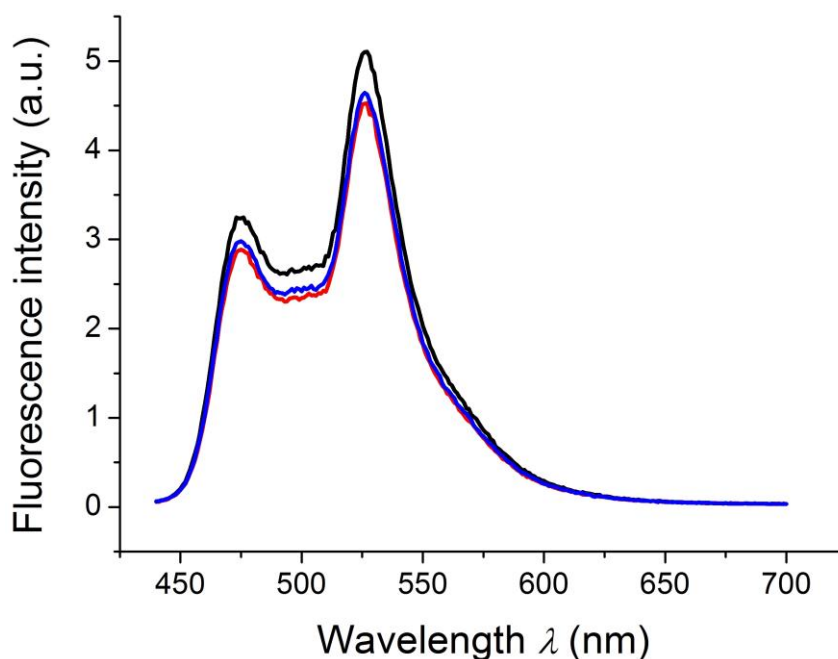


*Fig. 5.7: Fluorescence spectra (triplicate) of IM30-CFP/Venus 1/1 mixture*

Fluorescence spectra of IM30-CFP/Venus with a ratio of  $\sim 1/1$  were recorded in order to estimate a maximal  $E_{rat}$  for IM30-CFP/Venus mixtures. The results obtained from this figure are used in (Heidrich *et al.* 2018).

## 5.6 TEM micrographs of IM30-CFP, IM30-Venus and IM30-CFP/Venus

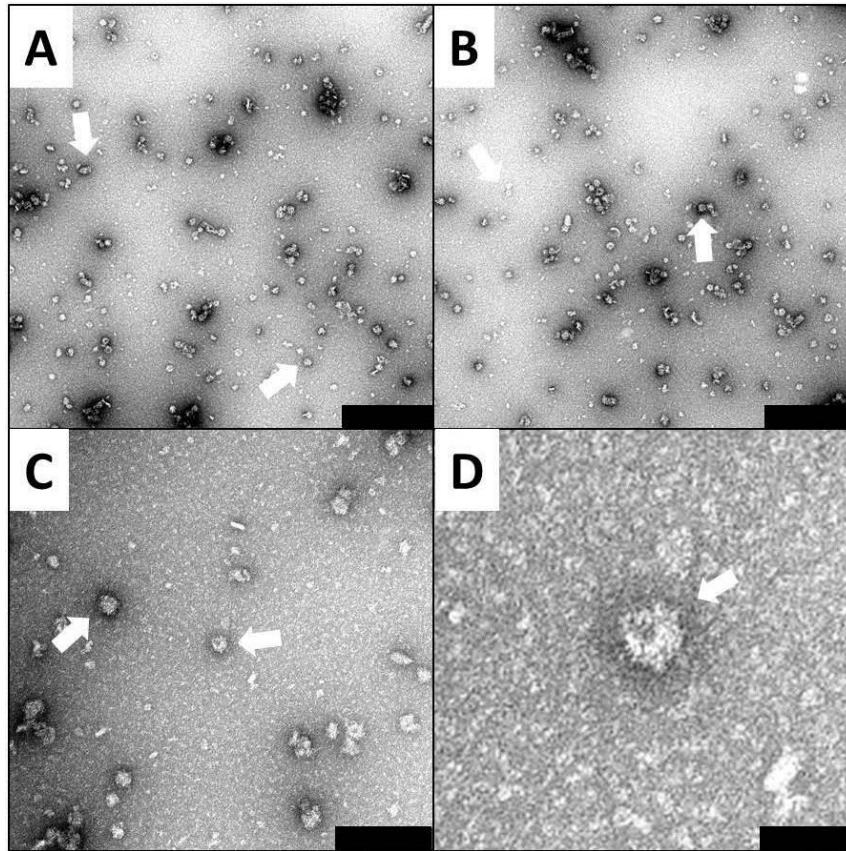


**Fig. 5.8: TEM micrographs of IM30-CFP**

Representative TEM micrographs of IM30-CFP samples are shown. Arrows indicate rings. Scale bars represent 500 nm (A, B), 200 nm (C) and 50 nm (D). In cooperation with Wolfgang Gebauer. Several results in this figure are published in (Heidrich *et al.* 2018).

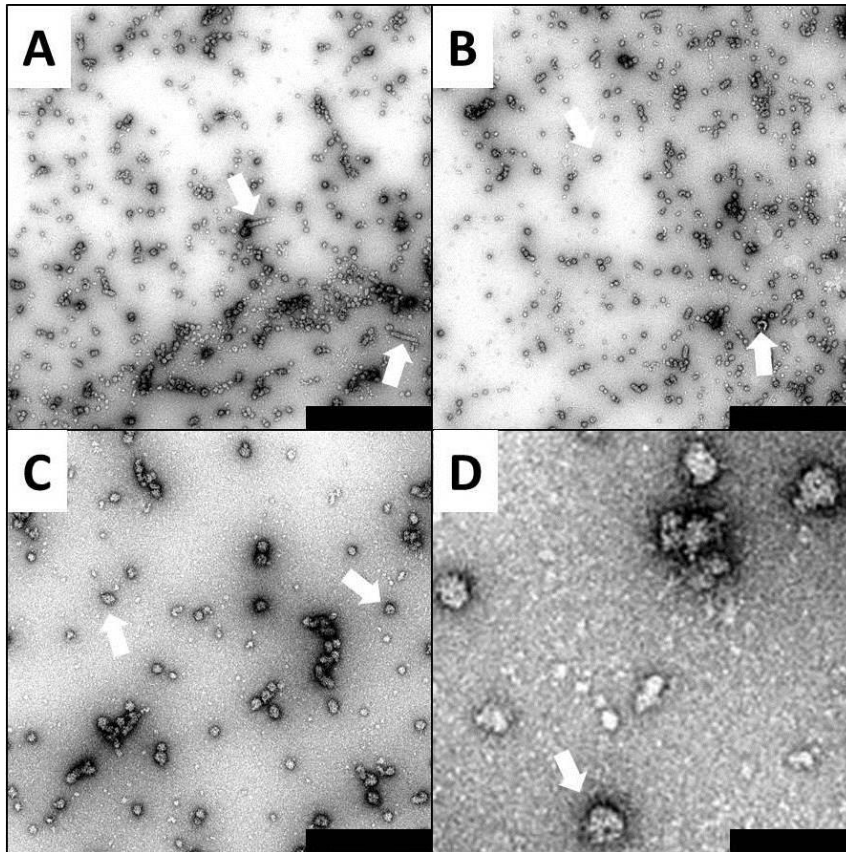


**Fig. 5.9: TEM micrographs of IM30-Venus**

Representative TEM micrographs of IM30-Venus samples are shown. Arrows indicate rods (A) and rings (B-D). Scale bars represent 1000 nm (A, B), 500 nm (C) and 200 nm (D). In cooperation with Wolfgang Gebauer.

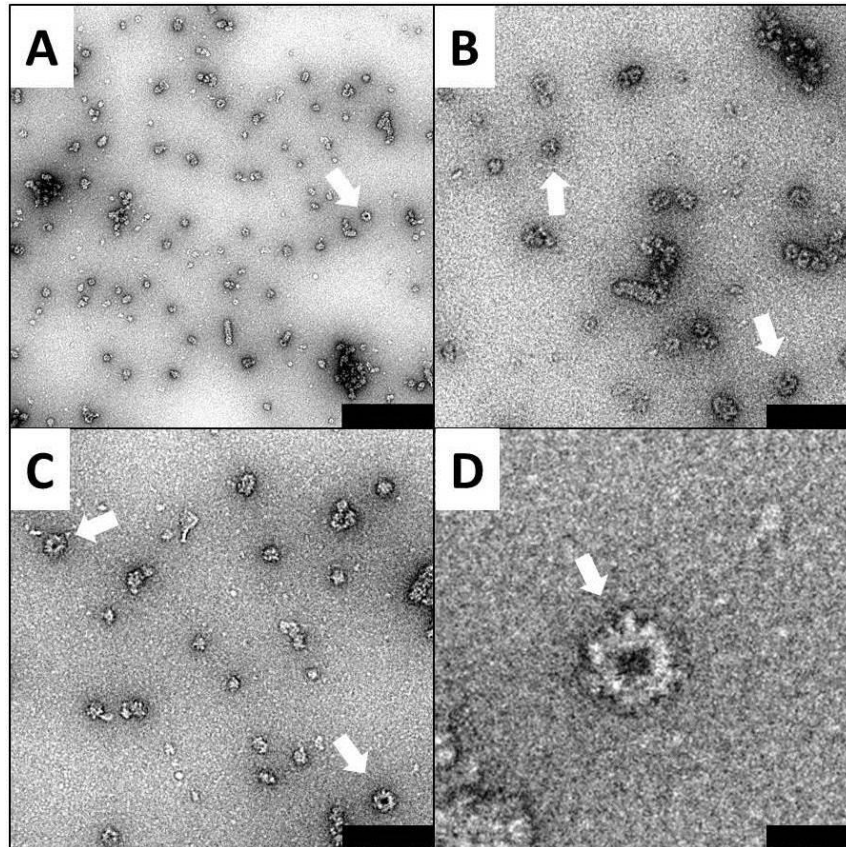


**Fig. 5.10: TEM micrographs of IM30-CFP/Venus**

Representative TEM micrographs of IM30-CFP/Venus samples (ratio: 52% CFP, 48% Venus (A, C, D) and 43% CFP, 57% Venus (B)) are shown. Arrows indicate rings. Scale bars represent 500 nm (A), 200 nm (B, C) and 50 nm (D). In cooperation with Wolfgang Gebauer.

## 5.7 Membrane fusion of IM30-CFP, IM30-Venus and IM30-CFP/Venus

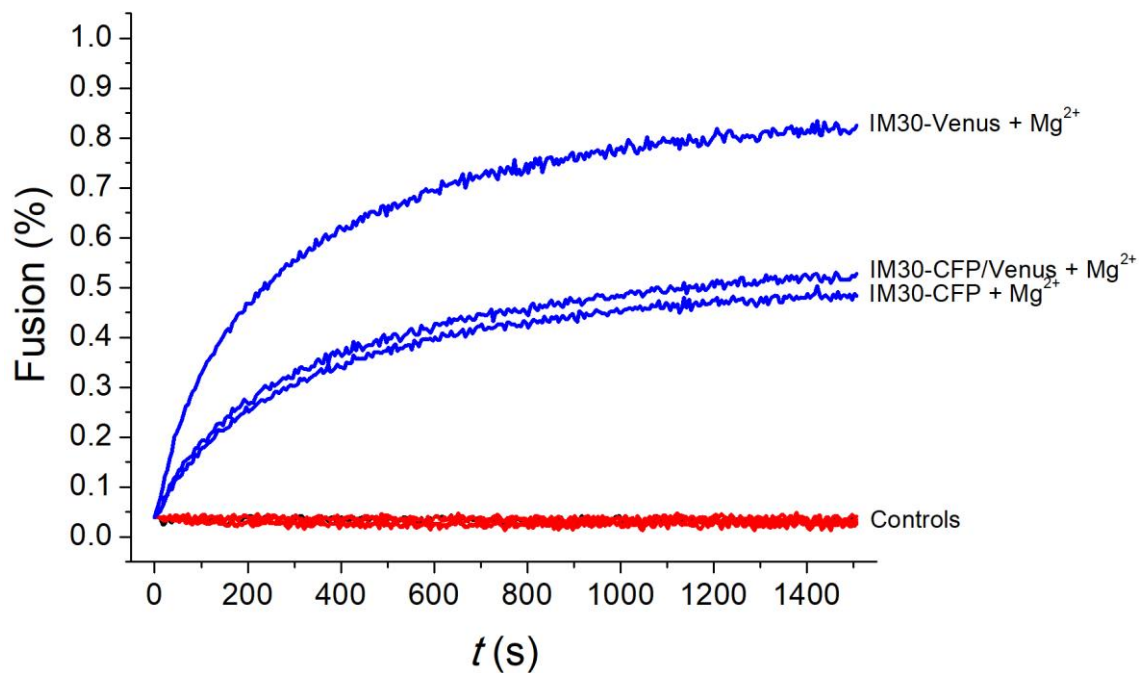


**Fig. 5.11:** Fusion assay of the labeled IM30 mutants IM30-CFP, IM30-Venus and IM30-CFP/Venus

A fusion assay was performed in order to confirm the membrane binding ability and fusion activity of the labeled IM30 mutants IM30-CFP, IM30-Venus and IM30-CFP/Venus (ratio: 52% CFP, 48% Venus). Control curves were recorded with samples containing only 1.5  $\mu$ M of the respective protein (red curves) or only 7.5 mM  $Mg^{2+}$  (black curve, not visible), respectively. Fusion was measured with samples containing 1.5  $\mu$ M of the respective protein and 7.5 mM  $Mg^{2+}$  (blue curves).  $\Delta$ Fusion =  $\pm$  4.3%,  $\Delta$  $t$  =  $\pm$  1 s. The experiment was repeated two times.

## 5.8 Correction factors of IM30-CFP and IM30-Venus

### 5.8.1 IM30-CFP and IM30-Venus fluorescence in presence of 100% DOPG liposomes

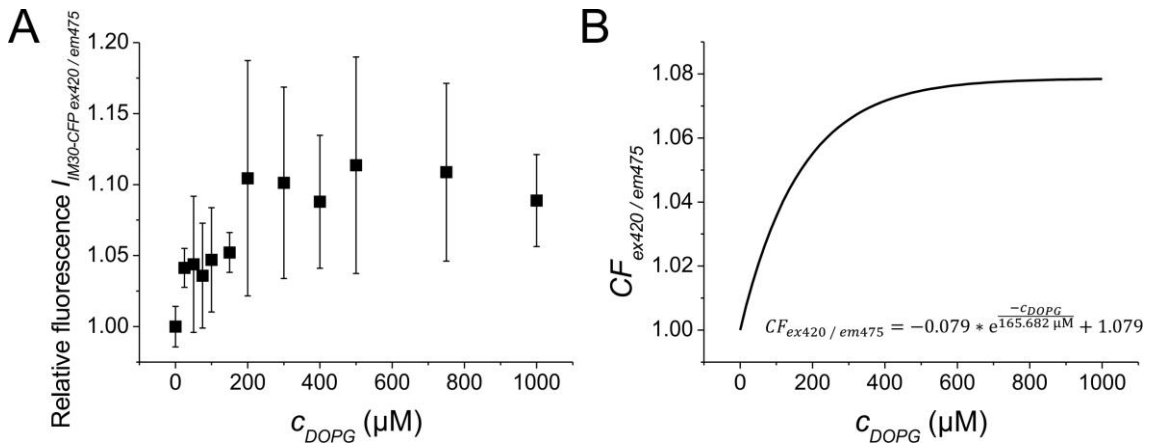


**Fig. 5.12: IM30-CFP fluorescence in presence of 100% DOPG liposomes (ex420/em475)**

In order to determine correction factors for the IM30-CFP/Venus fluorescence (ex420/em475) in presence of 100% DOPG liposomes, the IM30-CFP fluorescence was measured in presence of 100% DOPG liposomes (A). Error bars represent the standard deviation ( $n=3$ ). The obtained curve was fitted with an ExpDec1 fit, which was used to determine the correction factors in the main experiments (B).

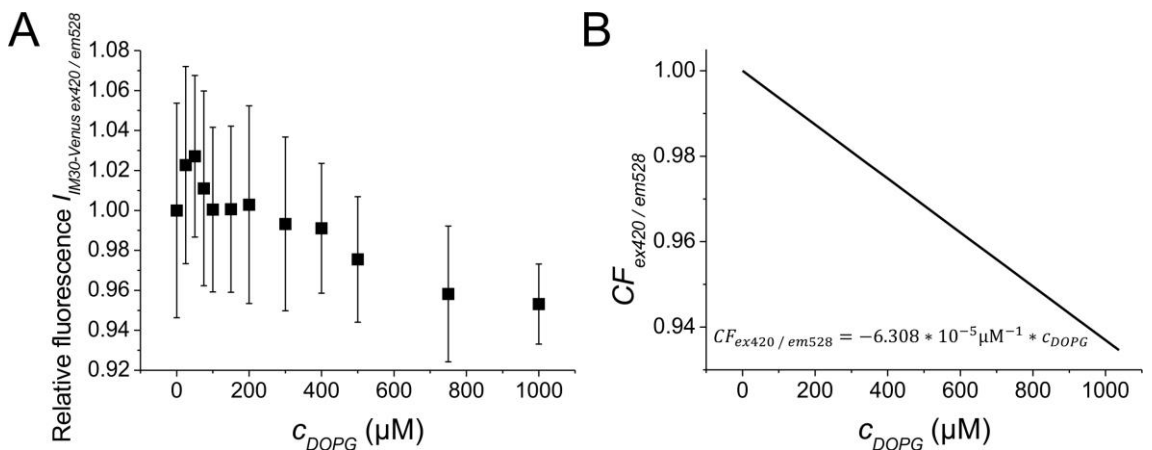


**Fig. 5.13: IM30-Venus fluorescence in presence of 100% DOPG liposomes (ex420/em528)**

In order to determine correction factors for the IM30-CFP/Venus fluorescence (ex420/em528) in presence of 100% DOPG liposomes, the IM30-Venus fluorescence was measured in presence of 100% DOPG liposomes (A). Error bars represent the standard deviation ( $n=3$ ). The obtained curve was fitted with a linear fit, which was used to determine the correction factors in the main experiments (B).

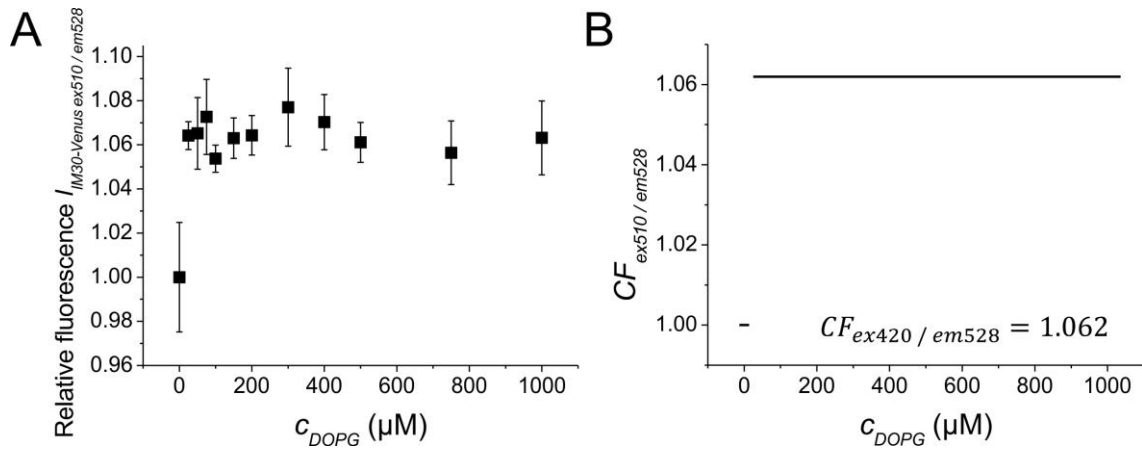


**Fig. 5.14: IM30-Venus fluorescence in presence of 100% DOPG liposomes (ex510/em528)**

In order to determine correction factors for the IM30-CFP/Venus fluorescence (ex420/em528) in presence of 100% DOPG liposomes, the IM30-Venus fluorescence was measured in presence of 100% DOPG liposomes (A). Error bars represent the standard deviation ( $n=3$ ). The obtained curve was fitted with a linear fit, which was used to determine the correction factors in the main experiments (B).

### 5.8.2 IM30-CFP and IM30-Venus fluorescence in presence of 60%/40% MGDG/DOPG liposomes

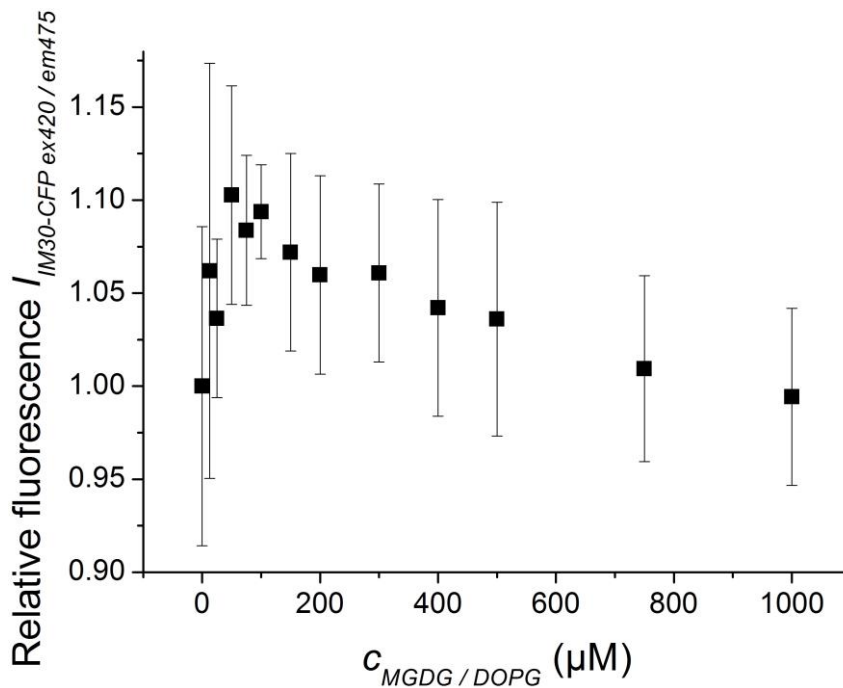


**Fig. 5.15: IM30-CFP fluorescence in presence of 60%/40% MGDG/DOPG liposomes (ex420/em475)**

In order to examine the necessity of correction factors for the IM30-CFP/Venus fluorescence (ex420/em475) in presence of 60%/40% MGDG/DOPG liposomes, the IM30-CFP fluorescence was measured in presence of 60%/40% MGDG/DOPG liposomes. In due consideration of the single measurements, which differ from each other concerning the trend, the data points were not fitted. Error bars represent the standard deviation ( $n=4$ ).

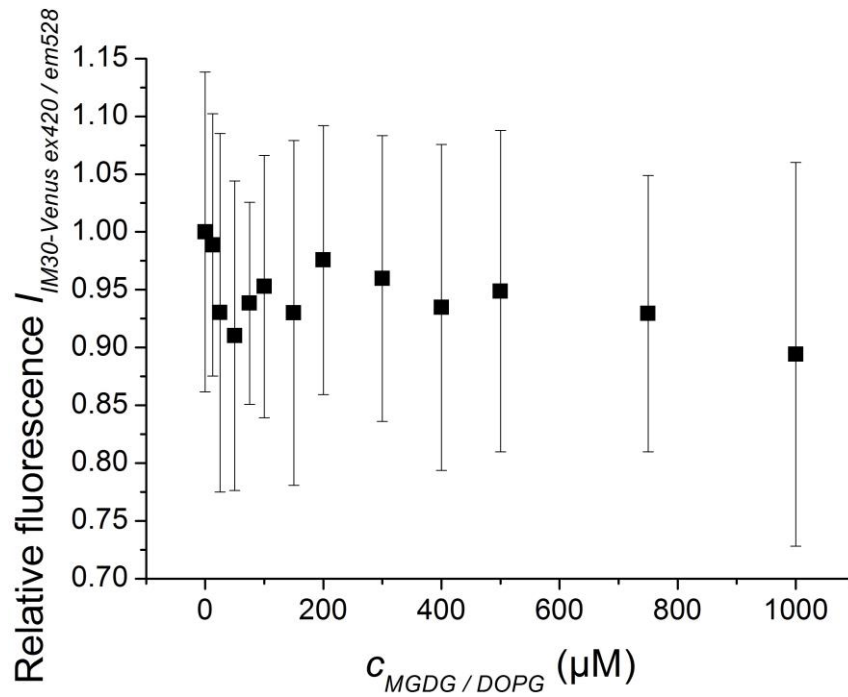


**Fig. 5.16: IM30-Venus fluorescence in presence of 60%/40% MGDG/DOPG liposomes (ex420/em528)**

In order to examine the necessity of correction factors for the IM30-CFP/Venus fluorescence (ex420/em528) in presence of 60%/40% MGDG/DOPG liposomes, the IM30-Venus fluorescence was measured in presence of 60%/40% MGDG/DOPG liposomes. In due consideration of the single measurements, which differ from each other concerning the trend, the data points were not fitted. Error bars represent the standard deviation (n=4).

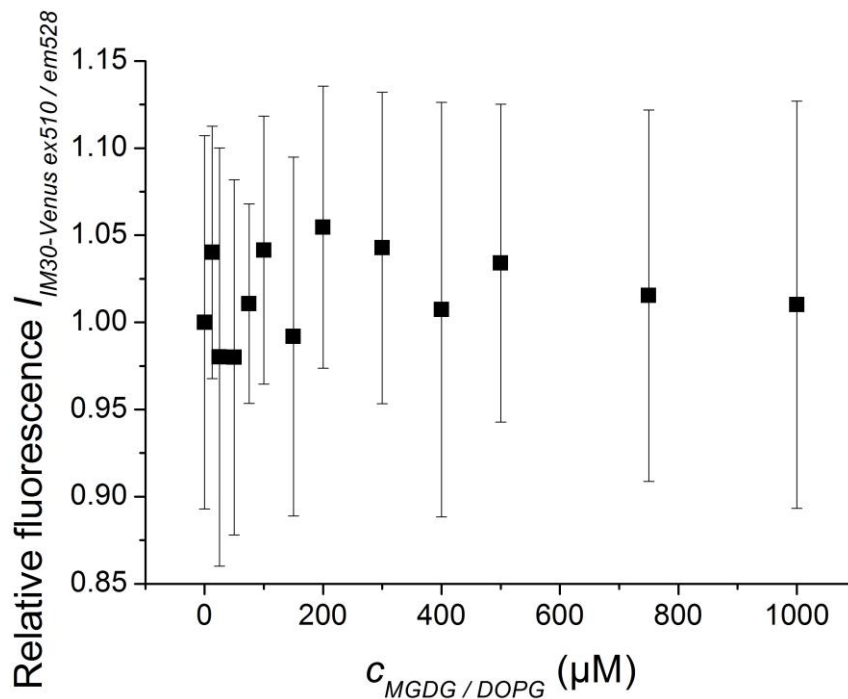


**Fig. 5.17: IM30-Venus fluorescence in presence of 60%/40% MGDG/DOPG liposomes (ex510/em528)**

In order to examine the necessity of correction factors for the IM30-CFP/Venus fluorescence (ex510/em528) in presence of 60%/40% MGDG/DOPG liposomes, the IM30-Venus fluorescence was measured in presence of 60%/40% MGDG/DOPG liposomes. In due consideration of the single measurements, which differ from each other concerning the trend, the data points were not fitted. Error bars represent the standard deviation (n=4).

### 5.8.3 IM30-CFP and IM30-Venus fluorescence in presence of $Mg^{2+}$

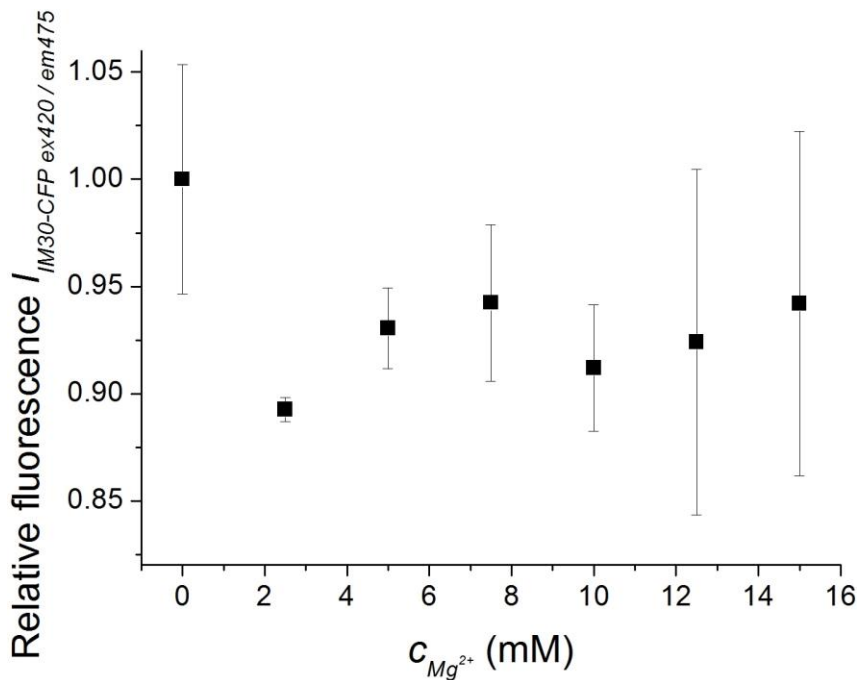


**Fig. 5.18: IM30-CFP fluorescence in presence of  $Mg^{2+}$  (ex420/em475)**

In order to examine the necessity of correction factors for the IM30-CFP/Venus fluorescence (ex420/em475) in presence of  $Mg^{2+}$ , the IM30-CFP fluorescence was measured in presence of  $Mg^{2+}$ . In due consideration of the single measurements, which differ from each other concerning the trend, the data points were not fitted. Error bars represent the standard deviation ( $n=3$ ).

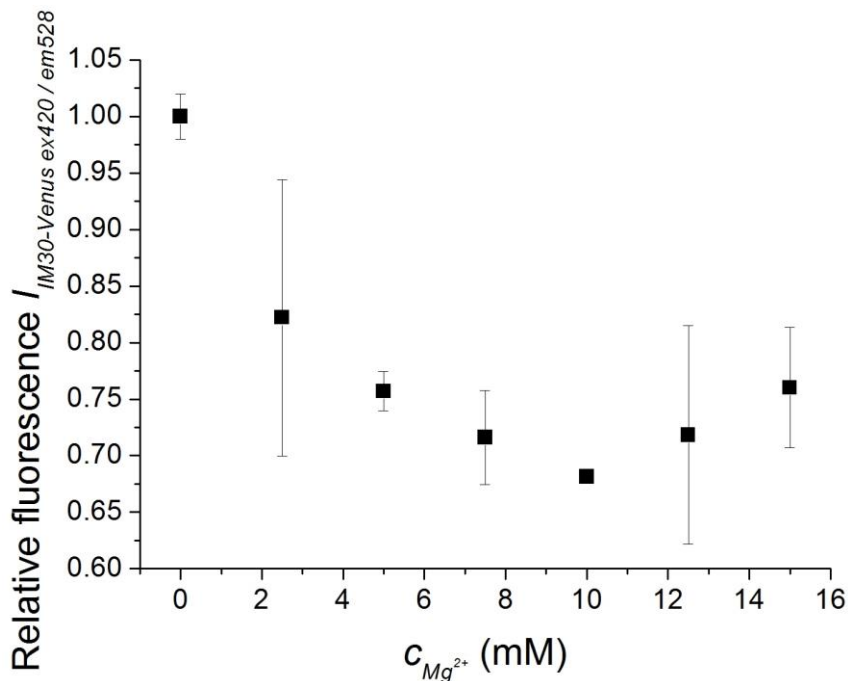


**Fig. 5.19: IM30-Venus fluorescence in presence of  $Mg^{2+}$  (ex420/em528)**

In order to examine the necessity of correction factors for the IM30-CFP/Venus fluorescence (ex420/em528) in presence of  $Mg^{2+}$ , the IM30-Venus fluorescence was measured in presence of  $Mg^{2+}$ . In due consideration of the single measurements, which differ from each other concerning the trend, the data points were not fitted. Error bars represent the standard deviation ( $n=3$ ).

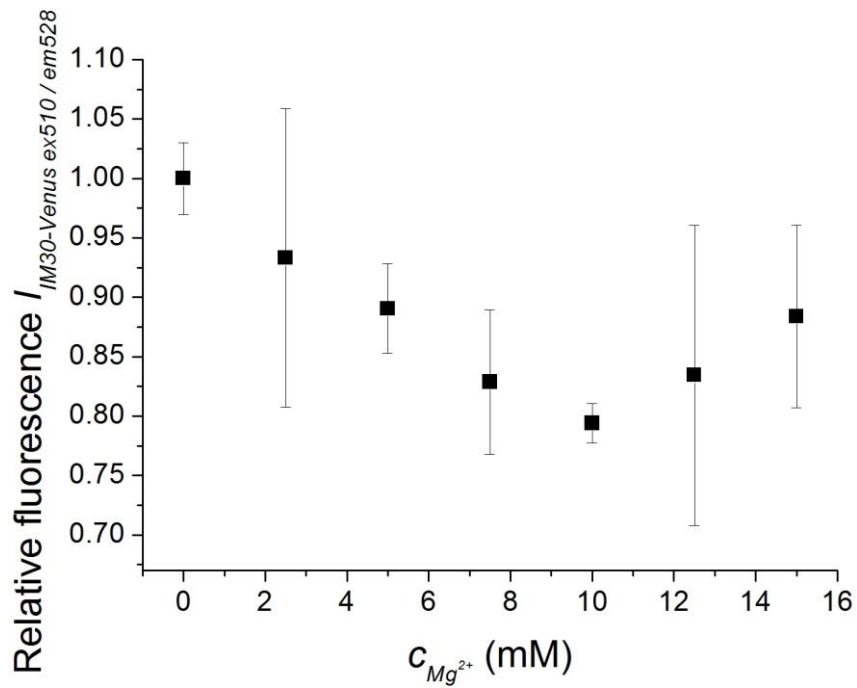


**Fig. 5.20: IM30-Venus fluorescence in presence of  $Mg^{2+}$  (ex510/em528)**

In order to examine the necessity of correction factors for the IM30-CFP/Venus fluorescence (ex510/em528) in presence of  $Mg^{2+}$ , the IM30-Venus fluorescence was measured in presence of  $Mg^{2+}$ . In due consideration of the single measurements, which differ from each other concerning the trend, the data points were not fitted. Error bars represent the standard deviation ( $n=3$ ).

## 5.9 Supplemental ITC data

### 5.9.1 ITC baselines

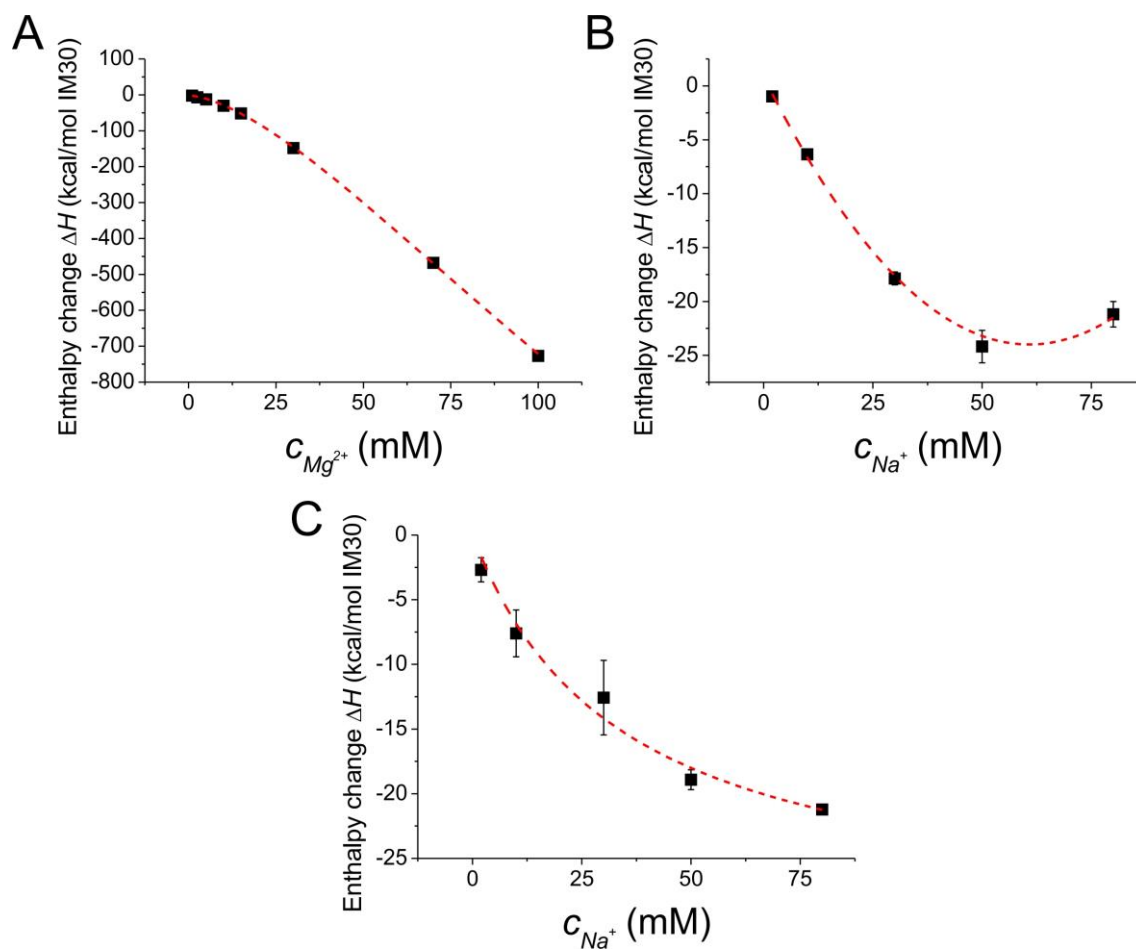


**Fig. 5.21: Background enthalpy changes of the reverse ITC measurements**

Shown are the enthalpy changes of  $Mg^{2+}$  (A) and  $Na^+$  (B) dilution in HEPES buffer and the effect of unspecific ionic interactions of IM30 with  $Na^+$  (C). The data were fitted using the following fit functions: Logistic fit,  $R^2=1.000$  (A), parable fit,  $R^2=1.000$  (B) and hyperbolic fit,  $R^2=0.979$  (C). Error bars represent the standard deviation ( $n=3$ ). In cooperation with Prof. Nadja Hellmann and Benedikt Junglas. The results in this figure are used in (Heidrich *et al.* 2018).

### 5.9.2 ITC raw data

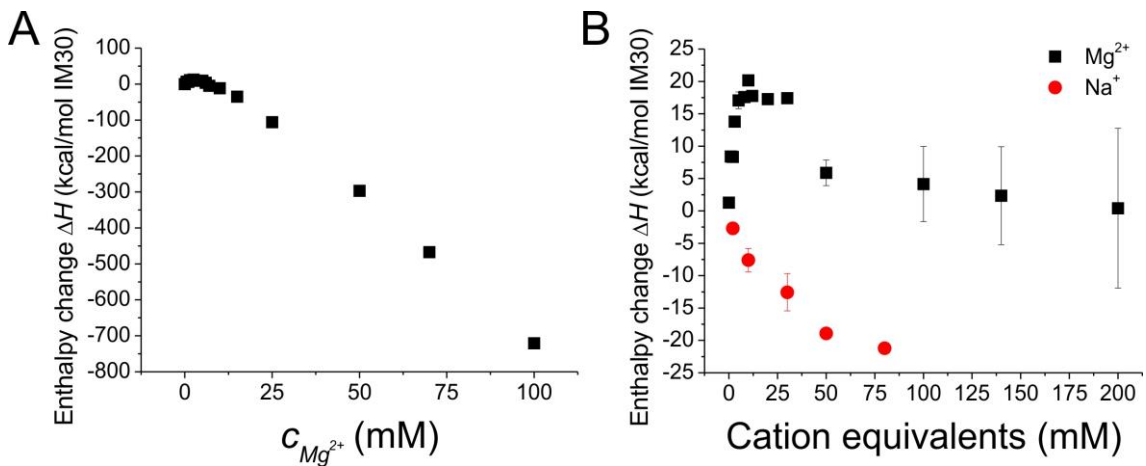


**Fig. 5.22: Raw data of the reverse ITC measurements**

Shown are the raw data of the reverse ITC measurement of IM30 in presence of different  $\text{Mg}^{2+}$  concentrations (A) and the baseline-corrected data of the reverse ITC measurements of IM30 in presence of different  $\text{Mg}^{2+}$  and  $\text{Na}^+$  concentrations (B), respectively. Error bars represent the standard deviation ( $n=3$ ). In cooperation with Prof. Nadja Hellmann and Benedikt Junglas. The results in this figure are used in (Heidrich *et al.* 2018).

### 5.10 Urea denaturation of IM30 in presence of $\text{Mg}^{2+}$

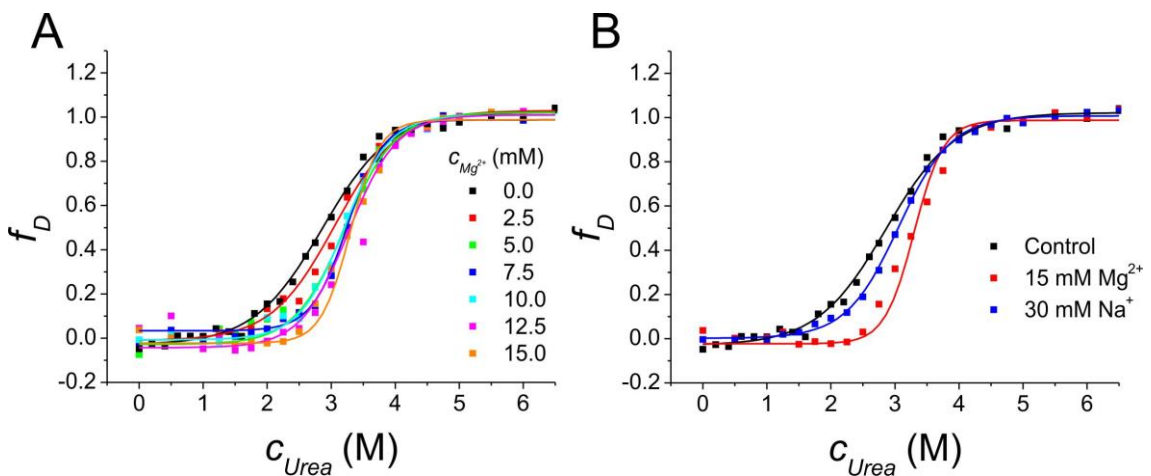


**Fig. 5.23: Urea denaturation of IM30 in presence of  $\text{Mg}^{2+}$**

Urea denaturation curves of IM30 were recorded at different  $\text{MgCl}_2$  concentrations and fitted with a Boltzmann fit (A).  $R^2=0.996$  (0.0 mM  $\text{Mg}^{2+}$ ),  $R^2=0.994$  (2.5 mM  $\text{Mg}^{2+}$ ),  $R^2=0.993$  (5.0 mM  $\text{Mg}^{2+}$ ),  $R^2=0.983$  (7.5 mM  $\text{Mg}^{2+}$ ),  $R^2=0.998$  (10.0 mM  $\text{Mg}^{2+}$ ),  $R^2=0.996$  (12.5 mM  $\text{Mg}^{2+}$ ),  $R^2=0.996$  (15.0 mM  $\text{Mg}^{2+}$ ). Furthermore, urea denaturation curves for IM30 at 0 mM  $\text{Mg}^{2+}$ , 15 mM  $\text{Mg}^{2+}$  and 30 mM  $\text{Na}^+$  are plotted separately (B).  $R^2=0.996$  (0 mM  $\text{Mg}^{2+}$ ),  $R^2=0.996$  (15 mM  $\text{Mg}^{2+}$ ),  $R^2=0.999$  (30 mM  $\text{Na}^+$ ). Shown are the mean values, error bars, which were calculated via Gaussian error distribution of three samples are not shown for a better overview. In cooperation with Benedikt Junglas. Several results in this figure are published in (Heidrich *et al.* 2018).

## 5.11 Binding curves of the DOPG interaction of IM30 mutants

### 5.11.1 Binding curve of the M30-X/DOPG interaction

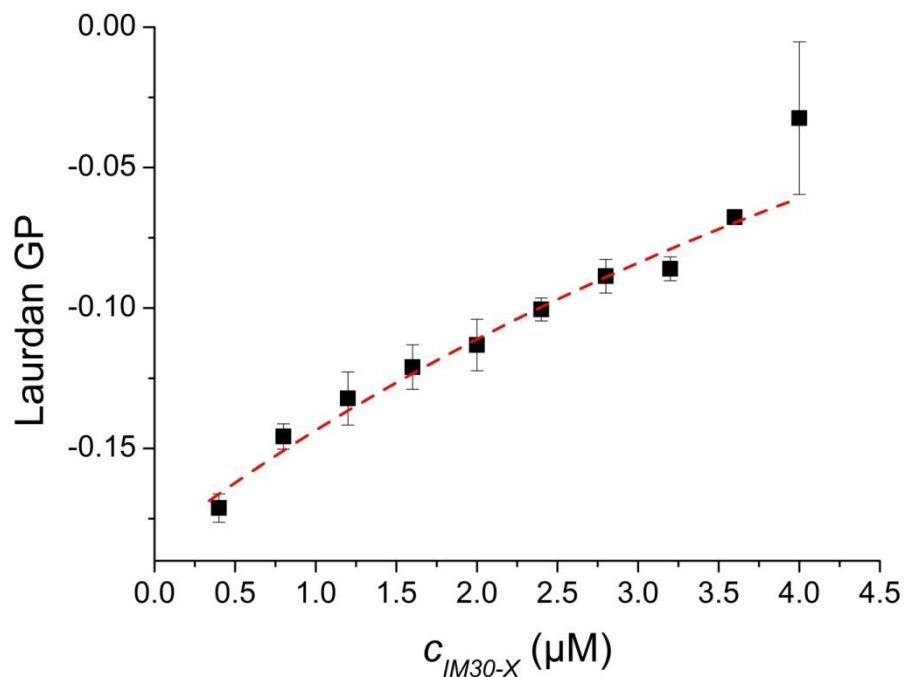


Fig. 5.24: Binding curve of the IM30-X/DOPG interaction

A binding curve for the IM30-X/DOPG interaction is shown. The data were fitted with a binding fit, from which the dissociation constant  $K_D$  could be calculated.  $R^2=0.986$ , error bars represent the standard deviation ( $n=3$ ).

### 5.11.2 Binding curve of the $\Delta CT$ /DOPG interaction

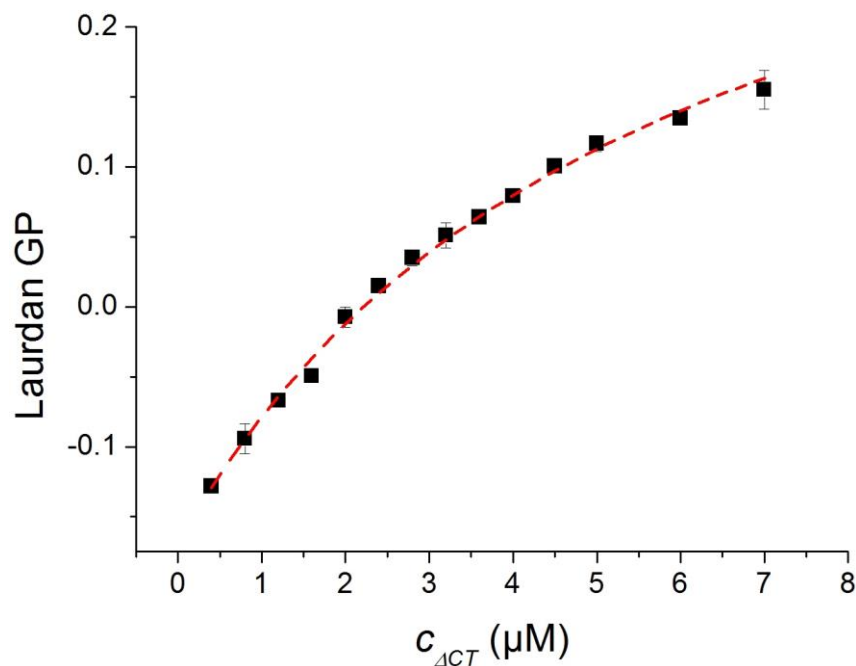
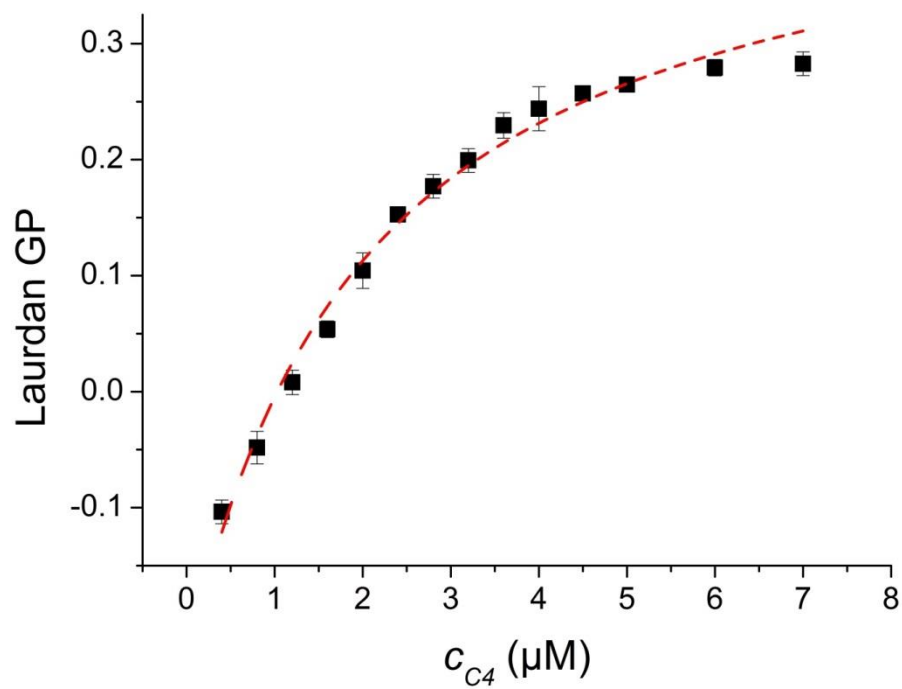


Fig. 5.25: Binding curve of the  $\Delta CT$ /DOPG interaction

A binding curve for the  $\Delta CT$ /DOPG interaction is shown. The data were fitted with a binding fit, from which the dissociation constant  $K_D$  could be calculated.  $R^2=0.998$ , error bars represent the standard deviation ( $n=3$ ).

### 5.11.3 Binding curve of the C4/DOPG interaction



**Fig. 5.26: Binding curve of the C4/DOPG interaction**

A binding curve for the C4/DOPG interaction is shown. The data were fitted with a binding fit, from which the dissociation constant  $K_D$  could be calculated.  $R^2=0.987$ , error bars represent the standard deviation ( $n=3$ ).

## 5.12 Supplemental SPR data

### 5.12.1 Raw data of the SPR kinetic experiments

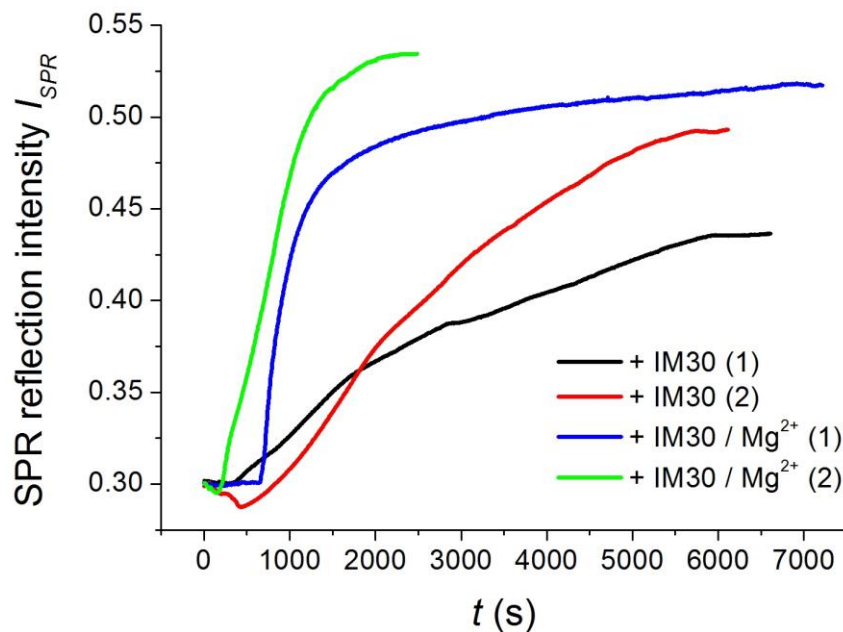


Fig. 5.27: Raw data of the SPR kinetic experiments

The raw data from the duplicate measurements of IM30 and IM30/Mg<sup>2+</sup> addition, respectively, to the negatively charged sensor chip surface is shown. Similar trends can be observed for each curve pair.

### 5.12.2 SPR control measurements

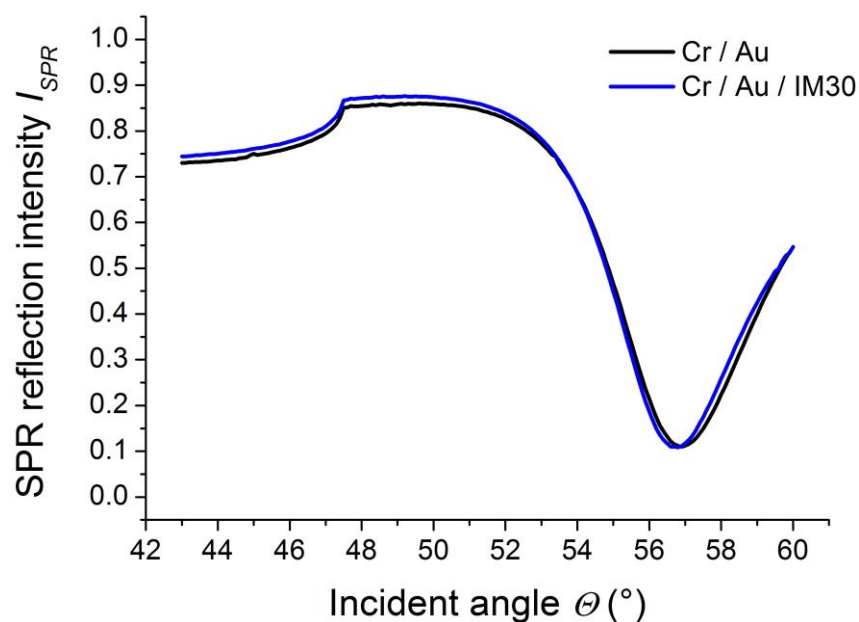


Fig. 5.28: SPR control measurements

As a control for the SPR measurements, IM30 was added to an empty Au surface and incubated for ~2 h. Scan measurements were conducted prior and after the addition and compared. No significant difference is observable. Thus, IM30 does not seem to bind to the Au surface.

### 5.12.3 IM30 dissociation from the 16-MHDA layer

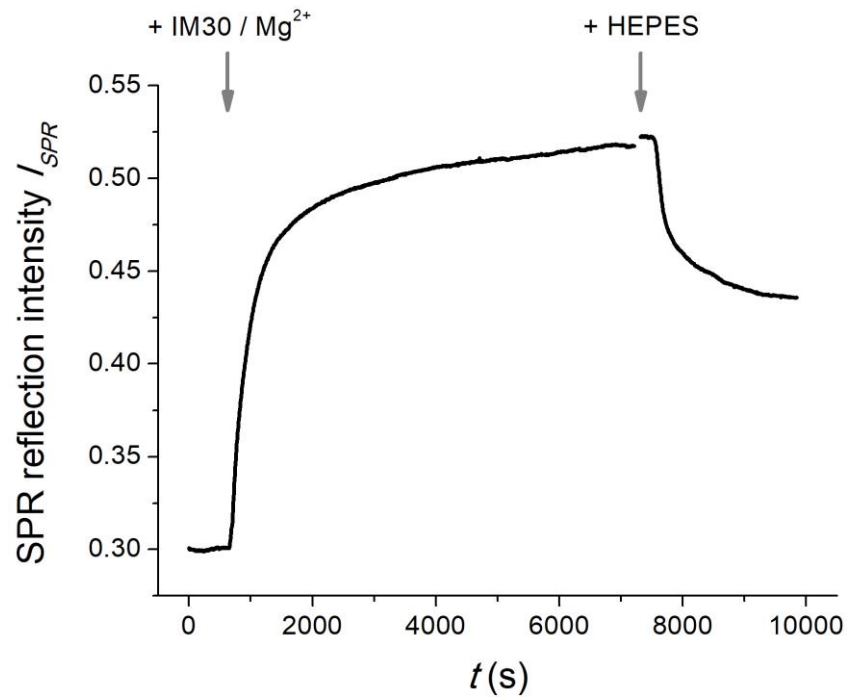


Fig. 5.29: IM30 dissociation from the 16-MHDA layers

After binding of IM30/Mg<sup>2+</sup> to the 16-MHDA surface, the protein cannot be completely washed off upon subsequent flushing with HEPES buffer.

## 5.13 Mathematical appendix

### 5.13.1 Fit functions

#### 5.13.1.1 Binding fit

$$y = F_{min} + \frac{\Delta F}{1 + \frac{K_D}{x}}$$

Variables:  $F_{min}$ ,  $\Delta F$ ,  $K_D$

#### 5.13.1.2 Boltzmann fit

$$y = \frac{A_1 - A_2}{1 + e^{-\frac{x - x_0}{dx}}} + A_2$$

Variables:  $A_1$ ,  $A_2$ ,  $x_0$ ,  $dx$

#### 5.13.1.3 ExpDec1 fit

$$y = A_1 \cdot e^{\frac{-x}{t_1}} + y_0$$

Variables:  $A_1$ ,  $t_1$ ,  $y_0$

$$k_{off} = \frac{1}{t_1}$$

**5.13.1.4 ExpDec2 fit**

$$y = A_1 \cdot e^{\frac{-x}{t_1}} + A_2 \cdot e^{\frac{-x}{t_2}} + y_0$$

Variables:  $A_1, A_2, t_1, t_2, y_0$ 

$$y(x = 0) = A_1 + A_2 + y_0$$

**5.13.1.5 Linear fit**

$$y = m \cdot x + b$$

Variables:  $m, b$ **5.13.1.6 Logistic fit**

$$y = \frac{A_1 - A_2}{1 + (\frac{x}{x_0})^p} + A_2$$

Variables:  $A_1, A_2, x_0, p$ **5.13.1.7 Hyperbolic fit**

$$y = \frac{P_1 \cdot x}{P_2 + x}$$

Variables:  $P_1, P_2$ **5.13.1.8 Parable fit**

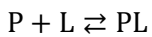
$$y = A + B \cdot x + C \cdot x^2$$

Variables:  $A, B, C$ **5.13.1.9 Scatter fit**

$$y = \log \frac{1}{1 - \frac{a}{x^4}} + b$$

Variables:  $a, b$ **5.13.2 Derivation of the binding fit**

Here shown for protein (P)-lipid area (L) interaction.



$K_D = \frac{P \cdot L}{PL} = \frac{(P_0 - PL)(L_0 - PL)}{PL}$  where  $P, L$  and  $PL$  are the equilibrium concentrations and  $P_0$  and  $L_0$  are the initial concentrations of P and L, respectively.

$$P_0 \gg L_0 \Rightarrow P_0 - PL = P_0$$

$$\Rightarrow K_D = \frac{P_0(L_0 - PL)}{PL}$$

$$\Leftrightarrow PL \cdot K_D = P_0 \cdot L_0 - P_0 \cdot PL$$

$$\Leftrightarrow PL(K_D + P_0) = P_0 \cdot L_0$$

$$\Leftrightarrow PL = \frac{P_0 \cdot L_0}{K_D + P_0} \quad \text{with } \alpha \stackrel{\text{def}}{=} \frac{PL}{L_0}$$

$$\Rightarrow \alpha = \frac{P_0 \cdot L_0}{L_0(K_D + P_0)} = \frac{P_0}{K_D + P_0} \stackrel{\text{def}}{=} \frac{F_0 - F}{F_0 - F_\infty}$$

$$\Leftrightarrow F_0 - F = (F_0 - F_\infty) \frac{P_0}{K_D + P_0}$$

$$\Leftrightarrow F = F_0 + \Delta F \frac{P_0}{K_D + P_0}$$

$$\Leftrightarrow F = F_0 + \frac{\Delta F}{\frac{K_D + P_0}{P_0}}$$

$$\Leftrightarrow F = F_0 + \frac{\Delta F}{\frac{K_D}{P_0} + 1} \blacksquare$$

### 5.13.3 Gaussian error distribution for $f_D$

$$\Delta f_D = \sqrt{\left(\left(\frac{-1}{y_N - y_D}\right) \Delta y\right)^2 + \left(\left(\frac{1}{y - y_D} - \frac{y_N - y}{(y_N - y_D)^2}\right) \Delta y_N\right)^2 + \left(\left(\frac{y_N - y}{(y_N - y_D)^2}\right) \Delta y_D\right)^2}$$

### 5.13.4 Estimation of the lipid binding areas for IM30/DOPG interaction

Table 5.1: Estimated binding areas of DOPG and IM30

Component	Exposed area $A$	Reference
DOPG	0.66 nm <sup>2</sup>	(Dahlberg 2007)
IM30 monomer	17.60 nm <sup>2</sup>	Calculated with PyMOL, simulation based on (Saur <i>et al.</i> 2017)
IM30 ring (symmetry of 15, 60 monomers)	804.25 nm <sup>2</sup>	Calculated, based on a cylindrical model and (Saur <i>et al.</i> 2017)

Number of DOPG molecules forming a binding area for IM30 monomer binding:

$$N_{DOPG}(\text{monomer}) = \frac{A_{IM30 \text{ monomer}}}{A_{DOPG}} = \frac{17.60 \text{ nm}^2}{0.66 \text{ nm}^2} \approx 27$$

Number of DOPG molecules forming a binding area for IM30 ring binding:

$$N_{DOPG}(\text{ring}) = \frac{A_{IM30 \text{ ring}}}{A_{DOPG}} = \frac{804.25 \text{ nm}^2}{0.66 \text{ nm}^2} \approx 1219$$

Thus, for a monomer as part of the ring:

$$N_{DOPG}(\text{monomer in ring}) = \frac{N_{DOPG}(\text{ring})}{60} = \frac{1219}{60} \approx 20$$

### 5.13.5 Estimation of the lipid molecules inside the inner IM30 ring diameter

Table 5.2: IM30 inner ring and lipid headgroup areas

Component	Area $A$	Reference
IM30 inner ring	80 nm <sup>2</sup>	Calculated, based on 10 nm diameter for the IM30 inner ring (Fuhrmann <i>et al.</i> 2009a)
MGDG	0.82 nm <sup>2</sup>	(Bottier <i>et al.</i> 2007)
DGDG	0.64 nm <sup>2</sup>	(Bottier <i>et al.</i> 2007)

Based on the *Synechocystis* TM lipid mass composition, the relative amount of MGDG and DGDG would be 75%/25% (Wada & Murata 1989).

Number of MGDG molecules inside the inner IM30 ring:

$$A_{MGDG,inner\ ring} = A_{IM30\ inner\ ring} \cdot 0.75 = 80\ \text{nm}^2 \cdot 0.75 = 60\ \text{nm}^2$$

$$N_{MGDG} = \frac{A_{MGDG,inner\ ring}}{A_{MGDG}} = \frac{60\ \text{nm}^2}{0.82\ \text{nm}^2} \approx 73$$

Number of DGDG molecules inside the inner IM30 ring:

$$A_{DGDG,inner\ ring} = A_{IM30\ inner\ ring} \cdot 0.25 = 80\ \text{nm}^2 \cdot 0.25 = 20\ \text{nm}^2$$

$$N_{DGDG} = \frac{A_{DGDG,inner\ ring}}{A_{DGDG}} = \frac{20\ \text{nm}^2}{0.64\ \text{nm}^2} \approx 31$$

## VI List of abbreviations

16-MHDA	16-Mercaptohexadecanoic acid
2YT	Yeast extract and tryptone
A	Acceptor
	Adenine
	Alanine
A	Absorption
	Area
Å	Angström, $10^{-10}$ m
A227C	IM30 A227C
abs.	absolute
ANS	8-Anilino-1-naphthalenesulfonic acid
APS	Ammonium persulfate
<i>Arabidopsis</i>	<i>Arabidopsis thaliana</i>
ATP	Adenosine triphosphate
Atto633-PE	1,2-Dioleoyl- <i>sn</i> -glycero-3-phosphoethanolamine labeled with Atto633
Au	Gold
a.u.	Arbitrary unit
BAEE	<i>N</i> <sub>α</sub> -Benzoyl- <i>L</i> -arginine ethylester
BSA	Bovine serum albumin
C	Cysteine
	Cytosine
°C	Degree Celsius
C-	Carboxy-
c	Speed of light
c	Concentration
C4	IM30 C4
C7	IM30 C7
Ca <sup>2+</sup>	Calcium ion
CD	Circular dichroism
CDJ2	Chloroplast DnaJ-like protein
CF	Correction factor
CFP	Cyan fluorescent protein
CIP	Alkaline phosphatase, calf intestinal
Coomassie	Coomassie Brilliant Blue G-250
Corr.	Corrected
Cr	Chromium
<i>C. reinhardtii</i>	<i>Chlamydomonas reinhardtii</i>
ΔCT	IM30 ΔCT
CURT1	Curvature thylakoid 1 protein
D	Aspartic acid or aspartate
	Denatured
	Denatured state
	Donor
<i>D</i> <sub>1/2</sub>	Inflection points of the denaturation curves
<i>d</i>	Diameter
	Cuvette pathlength
Δx	Difference of two variables x
	Error of a variable x
Da	Dalton

ddH <sub>2</sub> O	Double-distilled water
DGDG	Digalactosyldiacylglycerol
DMPG	Dimiristoylphosphatidylglycerol
DMSO	Dimethyl sulfoxide
DNA	Deoxyribonucleic acid
dNTP	Deoxynucleotidetriphosphate
DOPC	Dioleoylphosphatidylcholine
DOPG	Dioleoylphosphatidylglycerol
DOPS	Dioleoylphosphatidylserine
E	Glutamic acid or glutamate
<i>E</i>	FRET efficiency
<i>E<sub>rat</sub></i>	Ratiometric FRET efficiency
$\epsilon$	Dielectric constant
	Extinction coefficient
$\epsilon_m$	Dielectric constant of the metal
$\epsilon_p$	Dielectric constant of the prism
$\epsilon_s$	Dielectric constant of the surrounding media
ECL	Electrochemiluminescence
<i>E. coli</i>	<i>Escherichia coli</i>
EM	Electron microscopy
em	Emission
ex	Excitation
F	Fluorescence
	Fluorophore
	Phenylalanine
<i>f</i>	Dilution factor
<i>f<sub>D</sub></i>	Ratio of denaturated protein
FRET	Förster resonance energy transfer
FTIR	Fourier transform infrared spectroscopy
Fw	forward
G	Glycine
	Guanine
g	Gram
GP	Generalized polarization
<i>Gloeobacter</i>	<i>Gloeobacter violaceus</i>
H	Helix
	Histidine
<i>H</i>	Enthalpy
h	Gr.: <i>hora</i> , hour
HCl	Hydrochloric acid
He	Helium
HEPES	4-(2-Hydroxyethyl)-1-piperazineethanesulfonic acid
HF	High fidelity
H <sub>2</sub> O	Water
HRP	Horseradish peroxidase
HSAB	Hard and soft acids and bases
Hsp	Heat shock protein
I	Isoleucine
<i>I</i>	Intensity
<i>I<sub>A</sub></i>	Acceptor intensity
<i>I<sub>D</sub></i>	Donor intensity
<i>I<sub>SPR</sub></i>	SPR reflection intensity
<i>I<sub>t</sub></i>	Intensity at time <i>t</i>
<i>I<sub>x</sub></i>	Intensity at a wavelength of <i>x</i> nm
IE	Inner envelope
IM30	Inner membrane associated protein of 30 kDa

IM30-CFP	IM30 labeled with CFP
IM30-CFP/Venus	Mixture of IM30-CFP and IM30-Venus (co-purified)
IM30-Venus	IM30 labeled with Venus
IM30-X	Crosslinked IM30
img	Imaginary
IPTG	Isopropyl- $\beta$ -D-thiogalactopyranoside
$J$	Spectral overlap
K	Lysine
$K$	Equilibrium constant
$K_A$	Association constant
$K_D$	Dissociation constant
$k$	Velocity rate constant
	Wave vector
$k_0$	Wave vector of the incoming electric field
$k_{off}$	Dissociation rate constant
$k_{on}$	Association rate constant
$k_{sp}$	Wave vector of the surface plasmon
L	Leucine
	Lipid area
l	Liter
$\lambda$	Wavelength
$\lambda_{em}$	Emission wavelength
$\lambda_{ex}$	Excitation wavelength
$\lambda_{obs}$	Observed wavelength
LB	Luria-Bertani
LHCII	Light-harvesting complex II
LILBID-MS	Laser induced liquid bead ion desorption mass spectrometry
LissRhod-PE	1,2-Dioleoyl- <i>sn</i> -glycero-3-phosphoethanolamine- <i>N</i> -(lissaminerhodamine B sulfonyl)
M	Marker
	Methionine
	Molarity
$M$	Molar mass
m	Meter
$m$	Slope
$Mg^{2+}$	Magnesium ion
$MgCl_2$	Magnesium chloride
MGDG	Monogalactosyldiacylglycerol
min	Minute
MPGC	Max Planck Graduate Center
mRNA	Messenger RNA
MS	Mass spectrometry
MWCO	Molecular weight cut off in kDa
N	Asparagine
	Native
	Native state
$N$	Primer length
	Molar ratio
	Number
$n$	Molar amount
	Number of measurements
$Na^+$	Sodium ion
NaCl	Sodium chloride
$NaH_2PO_4 \cdot H_2O$	Monosodium phosphate monohydrate
$Na_2HPO_4 \cdot 2H_2O$	Disodium phosphate dihydrate
NaPh	Sodium phosphate

Na <sub>2</sub> S <sub>2</sub> O <sub>4</sub>	Sodium dithionite
NBD-PE	1,2-Dioleoyl- <i>sn</i> -glycero-3-phosphoethanolamine- <i>N</i> -(7-nitro-2-1,3-benzoxadiazol-4-yl)
Ne	Neon
Ni-NTA	Nickel nitrilotriacetic acid
<i>OD</i>	Optical density
<i>OD<sub>x</sub></i>	Optical density at a wavelength of x nm
OE	Outer envelope
OM	Outer membrane
P	Proline
	Protein
<i>P</i>	Heat rate
<i>p</i>	parallel
p.c.	Personal communication
PCR	Polymerase chain reaction
PDB	Protein data bank
PDM	PratA-defined membrane
PG	Phosphatidylglycerol
pH	Lat.: <i>potentia Hydrogenii</i>
PLB	Prolamellar bodies
PM	Cytoplasmic membrane
PMMA	Polymethylmethacrylate
PratA	Processing associated TPR protein
PS I	Photosystem I
PS II	Photosystem II
PspA	Phage shock protein A
Psp system	Phage shock proteins system
PVDF	Polyvinylidene fluoride
Q	Glutamine
Q.s.	Quantity sufficient
$\theta$	Incident angle
	Specific ellipticity
$\theta_c$	Incident angle of surface plasmon resonance
$\theta_{SPR}$	Incident angle of total internal reflection
$[\theta]_x$	Molar ellipticity at a wavelength of x nm
$R^2$	Coefficient of determination
R	Arginine
	Ideal gas constant
Rel.	Relative
Rev	Reverse
rpm	Rounds per minute
RT	Room temperature
RuBisCO	Ribulose-1,5-bisphosphate carboxylase/oxygenase
S	Serine
s	Second
$\sigma$	Standard deviation
SDS	Sodium dodecyl sulfate
SDS-PAGE	Sodium dodecyl sulfate polyacrylamide gel electrophoresis
SEC	Size exclusion chromatography
SFG	Sum frequency generation
SLS	Static light scattering
SNARE	Soluble <i>N</i> -ethylmaleimide-sensitive-factor attachment receptor
SPR	Surface plasmon resonance
SPT	Singe particle tracking
SQDG	Sulfoquinovosyldiacylglycerol
STPK	Serine/threonine protein kinases

---

<i>Synechococcus</i>	<i>Synechococcus elongatus</i> sp. PCC 7942
<i>Synechocystis</i>	<i>Synechocystis</i> sp. strain PCC 6803
T	Threonine
	Thymine
<i>T</i>	Temperature
<i>T<sub>m</sub></i>	Melting temperature
<i>t</i>	Time
$\Delta t$	Time between points
<i>t<sub>D</sub></i>	Death time
<i>t<sub>eq</sub></i>	Equilibration time
<i>t<sub>M</sub></i>	Total measuring time
Tat	Twin arginine transport
TBS	Tris-buffered saline
TBS-T	Tris-buffered saline with Tween20
TEM	Transmission electron microscopy
TEMED	<i>N,N,N',N'</i> -Tetramethylethylenediamine
TIC and TOC	Translocons at the inner and outer envelopes of chloroplasts
TLL	Lipase from <i>Thermomyces lanuginosus</i>
TM	Thylakoid membrane
Tris	Tris(hydroxymethyl)aminomethane
Tvp38	Tlg2-compartment vesicle protein of 38 kDa
T-zones	Translation zones
U	Enzyme unit
v/v	Volume/volume
V	Valine
	Volt
V	Volume
<i>V<sub>0</sub></i>	Start volume
<i>V<sub>added</sub></i>	Added volume
Vipp1	Vesicle-inducing protein in plastids 1
vol%	Volume percentage
W	Tryptophan
WT	IM30 wildtype
w/v	Weight/volume
w/w	Weight/weight
X	Random amino acid
Y	Tyrosine
<i>y</i>	Molar ellipticity at 222 nm
$\omega$	Frequency

## VII List of figures

<i>Fig. 1.1: Synechocystis</i> sp. PCC 6803 .....	14
<i>Fig. 1.2: Thylakoid lipids</i> .....	16
<i>Fig. 1.3: IM30/PspA secondary structure and hypothetical functions of predicted <math>\alpha</math>-helices</i> .....	20
<i>Fig. 1.4: Predicted tertiary structure of IM30</i> .....	20
<i>Fig. 1.5: Predicted IM30 monomer structure inside the ring</i> .....	21
<i>Fig. 1.6: In vitro oligomerization of IM30</i> .....	22
<i>Fig. 1.7: Postulated IM30 functions in chloroplasts and cyanobacteria</i> .....	24
<i>Fig. 1.8: IM30 interactions of interest</i> .....	27
<i>Fig. 2.1: Dissociation of IM30 rings</i> .....	47
<i>Fig. 2.2: Hydrolysis of BAEE via tryptic digestion</i> .....	49
<i>Fig. 2.3: Exemplary BAEE assay</i> .....	50
<i>Fig. 2.4: Typical CD spectra for <math>\alpha</math>-helices, <math>\beta</math>-sheets and <math>\beta</math>-turns</i> .....	53
<i>Fig. 2.5: Structure of ANS</i> .....	55
<i>Fig. 2.6: ANS fluorescence emission spectra blue shift upon IM30 and IM30/Mg<sup>2+</sup>-binding</i> ...	56
<i>Fig. 2.7: Evaluation of the final FRET spectra</i> .....	60
<i>Fig. 2.8: Structure of Laurdan</i> .....	63
<i>Fig. 2.9: Blue shift of the Laurdan fluorescence emission spectra upon IM30 membrane binding</i> .....	63
<i>Fig. 2.10: Liposome destabilization</i> .....	66
<i>Fig. 2.11: Liposome fusion assays</i> .....	67
<i>Fig. 2.12: Reverse ITC</i> .....	71
<i>Fig. 2.13: Exemplary ITC measurement</i> .....	72
<i>Fig. 2.14: Typical SPR scan measurement</i> .....	74
<i>Fig. 2.15: SPR</i> .....	75
<i>Fig. 3.1: Positions of cluster mutations in the IM30 secondary structure</i> .....	79
<i>Fig. 3.2: Purification of IM30, C4, C7 and <math>\Delta</math>CT</i> .....	79
<i>Fig. 3.3: TEM micrographs of IM30</i> .....	80
<i>Fig. 3.4: Dephosphorylation of IM30</i> .....	81
<i>Fig. 3.5: LILBID-MS of IM30</i> .....	82
<i>Fig. 3.6: ANS spectra of IM30 in presence and absence of Mg<sup>2+</sup></i> .....	84
<i>Fig. 3.7: Titration of IM30 with Mg<sup>2+</sup></i> .....	85
<i>Fig. 3.8: Reverse ITC of Mg<sup>2+</sup> titration with IM30</i> .....	86
<i>Fig. 3.9: Confirmation of successful IM30 crosslinking</i> .....	87

---

<i>Fig. 3.10:</i> TEM micrographs of IM30-X .....	88
<i>Fig. 3.11:</i> Position of the point mutation A227C in the IM30 secondary structure .....	89
<i>Fig. 3.12:</i> Purification and dimer formation of A227C in presence and absence of DTT .....	89
<i>Fig. 3.13:</i> TEM micrographs of A227C in presence and absence of DTT .....	90
<i>Fig. 3.14:</i> ANS spectra of IM30/IM30-X and A227C ( $\pm$ DTT) in presence and absence of $Mg^{2+}$ .....	91
<i>Fig. 3.15:</i> Urea denaturation and renaturation of IM30 in presence of $Mg^{2+}$ .....	93
<i>Fig. 3.16:</i> Urea denaturation of IM30 in presence and absence of 15 mM $Mg^{2+}$ and 30 mM $Na^+$ .....	94
<i>Fig. 3.17:</i> $D_{1/2}$ values of IM30 at different $Mg^{2+}$ concentrations .....	95
<i>Fig. 3.18:</i> Tryptic digestion of IM30 in presence and absence of 10 mM $Mg^{2+}$ .....	97
<i>Fig. 3.19:</i> ANS thermofluor experiment for the IM30/ $Mg^{2+}$ interaction .....	99
<i>Fig. 3.20:</i> Purification of IM30-CFP and IM30-Venus .....	100
<i>Fig. 3.21:</i> SEC of IM30 WT, IM30-CFP and IM30-Venus .....	101
<i>Fig. 3.22:</i> Fluorescence emission spectra of IM30-CFP, IM30-Venus and IM30-CFP/Venus .....	102
<i>Fig. 3.23:</i> IM30-CFP and IM30-Venus in presence and absence of different $Mg^{2+}$ concentrations .....	103
<i>Fig. 3.24:</i> IM30-CFP/Venus in presence and absence of different $Mg^{2+}$ concentrations.....	105
<i>Fig. 3.25:</i> TEM micrographs of IM30 in presence of $Mg^{2+}$ .....	106
<i>Fig. 3.26:</i> Tryptic digestion of IM30 in presence and absence of liposomes.....	108
<i>Fig. 3.27:</i> Electrostatic interaction of IM30 with DOPG membranes.....	110
<i>Fig. 3.28:</i> Negatively charged headgroup binding of IM30.....	111
<i>Fig. 3.29:</i> $K_D$ determinations of the interaction of IM30 and C7 with DOPG .....	113
<i>Fig. 3.30:</i> SPR measurements of IM30 interacting with 16-MHDA surfaces in presence and absence of $Mg^{2+}$ .....	117
<i>Fig. 3.31:</i> IM30 ring dissociation in presence of 100% DOPG liposomes .....	119
<i>Fig. 3.32:</i> IM30 ring dissociation in presence 60%/40% MGDG/DOPG liposomes.....	120
<i>Fig. 3.33:</i> IM30-CFP/Venus oligomer dissociation in presence of 100% DOPG and 60%/40% MGDG/DOPG liposomes .....	122
<i>Fig. 3.34:</i> Liposome size-distribution for IM30-mediated membrane fusion.....	124
<i>Fig. 3.35:</i> IM30-mediated fusion of differently composed liposome .....	125
<i>Fig. 3.36:</i> Fusion assay of IM30-X .....	126
<i>Fig. 3.37:</i> Liposome destabilization by IM30/ $Mg^{2+}$ .....	128
<i>Fig. 4.1:</i> <i>In vitro</i> oligomerization of IM30.....	130
<i>Fig. 4.2:</i> Suggested stabilizations of IM30 induced by $Mg^{2+}$ during thermal denaturation.....	134
<i>Fig. 4.3:</i> Possible binding of $Mg^{2+}$ by IM30 rings .....	138

<i>Fig. 4.4:</i> Individual steps of the IM30-membrane interaction in presence and absence of Mg <sup>2+</sup>	147
<i>Fig. 4.5:</i> Model for controlled and uncontrolled <i>in vitro</i> IM30-mediated membrane fusion ....	149
<i>Fig. 4.6:</i> Formation of multilamellar and oligovesicular liposomes via direct, controlled IM30-mediated membrane fusion .....	150
<i>Fig. 4.7:</i> Model for IM30-mediated membrane fusion.....	153
<i>Fig. 5.1:</i> Sequence conservations within the cyanobacterial PspA/IM30 family.....	163
<i>Fig. 5.2:</i> Normalized fluorescence excitation and emission spectra of NBD-PE and LissRhod-PE .....	164
<i>Fig. 5.3:</i> Fluorescence spectra of the positive and negative controls of the green fusion assay	164
<i>Fig. 5.4:</i> Normalized fluorescence excitation and emission spectra of LissRhod-PE and Atto633-PE.....	165
<i>Fig. 5.5:</i> Fluorescence spectra of the positive and negative controls of the red fusion assay ...	165
<i>Fig. 5.6:</i> Normalized fluorescence excitation and emission spectra of IM30-CFP and IM30-Venus.....	166
<i>Fig. 5.7:</i> Fluorescence spectra (triplicate) of IM30-CFP/Venus 1/1 mixture.....	166
<i>Fig. 5.8:</i> TEM micrographs of IM30-CFP .....	167
<i>Fig. 5.9:</i> TEM micrographs of IM30-Venus .....	168
<i>Fig. 5.10:</i> TEM micrographs of IM30-CFP/Venus.....	169
<i>Fig. 5.11:</i> Fusion assay of the labeled IM30 mutants IM30-CFP, IM30-Venus and IM30-CFP/Venus .....	170
<i>Fig. 5.12:</i> IM30-CFP fluorescence in presence of 100% DOPG liposomes (ex420/em475)....	171
<i>Fig. 5.13:</i> IM30-Venus fluorescence in presence of 100% DOPG liposomes (ex420/em528).	171
<i>Fig. 5.14:</i> IM30-Venus fluorescence in presence of 100% DOPG liposomes (ex510/em528).	172
<i>Fig. 5.15:</i> IM30-CFP fluorescence in presence of 60%/40% MGDG/DOPG liposomes (ex420/em475) .....	172
<i>Fig. 5.16:</i> IM30-Venus fluorescence in presence of 60%/40% MGDG/DOPG liposomes (ex420/em528) .....	173
<i>Fig. 5.17:</i> IM30-Venus fluorescence in presence of 60%/40% MGDG/DOPG liposomes (ex510/em528) .....	173
<i>Fig. 5.18:</i> IM30-CFP fluorescence in presence of Mg <sup>2+</sup> (ex420/em475).....	174
<i>Fig. 5.19:</i> IM30-Venus fluorescence in presence of Mg <sup>2+</sup> (ex420/em528).....	174
<i>Fig. 5.20:</i> IM30-Venus fluorescence in presence of Mg <sup>2+</sup> (ex510/em528).....	175
<i>Fig. 5.21:</i> Background enthalpy changes of the reverse ITC measurements .....	176
<i>Fig. 5.22:</i> Raw data of the reverse ITC measurements .....	177
<i>Fig. 5.23:</i> Urea denaturation of IM30 in presence of Mg <sup>2+</sup> .....	177
<i>Fig. 5.24:</i> Binding curve of the IM30-X/DOPG interaction .....	178

---

<i>Fig. 5.25: Binding curve of the <math>\Delta</math>CT/DOPG interaction .....</i>	<i>178</i>
<i>Fig. 5.26: Binding curve of the C4/DOPG interaction .....</i>	<i>179</i>
<i>Fig. 5.27: Raw data of the SPR kinetic experiments .....</i>	<i>180</i>
<i>Fig. 5.28: SPR control measurements.....</i>	<i>180</i>
<i>Fig. 5.29: IM30 dissociation from the 16-MHDA layers .....</i>	<i>181</i>

## VIII List of tables

<i>Table 2.1: Chemicals</i> .....	29
<i>Table 2.2: Buffers and solutions</i> .....	30
<i>Table 2.3: Oligonucleotides</i> .....	32
<i>Table 2.4: Plasmids</i> .....	32
<i>Table 2.5: Enzymes and buffers</i> .....	32
<i>Table 2.6: E. coli cells</i> .....	33
<i>Table 2.7: Cell culture media</i> .....	33
<i>Table 2.8: Kits</i> .....	34
<i>Table 2.9: DNA &amp; protein ladders</i> .....	34
<i>Table 2.10: Instruments</i> .....	34
<i>Table 2.11: Consumables</i> .....	35
<i>Table 2.12: Software</i> .....	36
<i>Table 2.13: Protocol for the PCR</i> .....	37
<i>Table 2.14: Protocol for the PCR running program</i> .....	37
<i>Table 2.15: Protocol for the site-directed mutagenesis</i> .....	37
<i>Table 2.16: Protocol for the site-directed mutagenesis running program</i> .....	38
<i>Table 2.17: Protocol for the pRSET IM30-CFP restriction</i> .....	39
<i>Table 2.18: Protocol for the pRSET IM30-CFP ligation</i> .....	39
<i>Table 2.19: Protocol for the pRSET IM30-Venus restriction</i> .....	40
<i>Table 2.20: Protocol for the pRSET IM30-Venus ligation</i> .....	40
<i>Table 2.21: Protocol for two loading and resolving gels</i> .....	44
<i>Table 2.22: Protocol for the Bradford assay</i> .....	45
<i>Table 2.23: Protocol for the BSA standard SDS-PAGE</i> .....	45
<i>Table 2.24: Protocol for the IM30 desphosphorylation</i> .....	48
<i>Table 2.25: Protocol for the IM30 lipolysis</i> .....	49
<i>Table 2.26: Parameters used for the urea denaturation curve CD measurements</i> .....	53
<i>Table 2.27: Parameters used for the ANS spectra recording</i> .....	56
<i>Table 2.28: Parameters used for the ANS titration curves</i> .....	57
<i>Table 2.29: Parameters used for the ANS thermofluor assays</i> .....	58
<i>Table 2.30: Parameters used for the dissociation experiments of co-purified IM30 on liposomes</i> .....	59
<i>Table 2.31: Parameters used for the Mg<sup>2+</sup> interaction experiments of separately purified labeled IM30 (equilibrium)</i> .....	61

---

<i>Table 2.32:</i> Parameters used for the Mg <sup>2+</sup> interaction experiments of separately purified labeled IM30 (kinetics).....	61
<i>Table 2.33:</i> Parameters used for the Mg <sup>2+</sup> interaction experiments of co-purified labeled IM3062	
<i>Table 2.34:</i> Parameters used for the Laurdan spectra recording .....	64
<i>Table 2.35:</i> Parameters used for the liposome destabilization assay .....	66
<i>Table 2.36:</i> Parameters used for the liposome fusion assay.....	68
<i>Table 2.37:</i> Parameters used for the replacement assay.....	69
<i>Table 2.38:</i> Parameters used for the ITC measurement .....	71
<i>Table 2.39:</i> Parameters used for the SPT measurements .....	73
<i>Table 2.40:</i> Parameters used for the SPR measurements .....	76
<i>Table 2.41:</i> Initial fitting parameters used for SPR scan measurements.....	76
<i>Table 3.1:</i> Calculated $K_D$ values from the ANS titration curves .....	85
<i>Table 3.2:</i> Ratio $[\Theta]_{222\text{ nm}}/[\Theta]_{208\text{ nm}}$ of IM30 in presence and absence of 15 mM Mg <sup>2+</sup> and 30 mM Na <sup>+</sup> .....	96
<i>Table 3.3:</i> Trypsin activity in presence of Mg <sup>2+</sup> .....	96
<i>Table 3.4:</i> $K_D$ determination for the DOPG interaction of IM30 and IM30 mutants .....	114
<i>Table 3.5:</i> Estimated layer thicknesses of the SPR experiments.....	116
<i>Table 5.1:</i> Estimated binding areas of DOPG and IM30 .....	183
<i>Table 5.2:</i> IM30 inner ring and lipid headgroup areas.....	183

## IX References

- Adam Z., Charuvi D., Tsabari O., Knopf R.R. & Reich Z. (2011) Biogenesis of thylakoid networks in angiosperms: knowns and unknowns. *Plant Mol Biol* **76**, 221-34
- Allwood A.C., Walter M.R., Kamber B.S., Marshall C.P. & Burch I.W. (2006) Stromatolite reef from the Early Archaean era of Australia. *Nature* **441**, 714-8
- Anderson J.M., Goodchild D.J. & Boardman N.K. (1973) Composition of the photosystems and chloroplast structure in extreme shade plants. *Biochim Biophys Acta* **325**, 573-85
- Andersson M.X. & Sandelius A.S. (2004) A chloroplast-localized vesicular transport system: a bio-informatics approach. *BMC Genomics* **5**, 40
- Andrews B.T., Capraro D.T., Sulkowska J.I., Onuchic J.N. & Jennings P.A. (2013) Hysteresis as a Marker for Complex, Overlapping Landscapes in Proteins. *J Phys Chem Lett* **4**, 180-8
- Aoki M., Sato N., Meguro A. & Tsuzuki M. (2004) Differing involvement of sulfoquinovosyl diacylglycerol in photosystem II in two species of unicellular cyanobacteria. *Eur J Biochem* **271**, 685-93
- Armbruster U., Labs M., Pribil M., Viola S., Xu W., Scharfenberg M., Hertle A.P., Rojahn U., Jensen P.E., Rappaport F., Joliot P., Dormann P., Wanner G. & Leister D. (2013) Arabidopsis CURVATURE THYLAKOID1 proteins modify thylakoid architecture by inducing membrane curvature. *Plant Cell* **25**, 2661-78
- Arnold K. (1995) Chapter 19 - Cation-Induced Vesicle Fusion Modulated by Polymers and Proteins. In: *Handbook of Biological Physics* (eds. by Lipowsky R & Sackmann E), pp. 903-57. North-Holland
- Aseeva E., Ossenbuhl F., Eichacker L.A., Wanner G., Soll J. & Vothknecht U.C. (2004) Complex formation of Vipp1 depends on its alpha-helical PspA-like domain. *J Biol Chem* **279**, 35535-41
- Ashton A.R. (1998) A simple procedure for purifying the major chloroplast fructose-1,6-bisphosphatase from spinach (*Spinacia oleracea*) and characterization of its stimulation by sub-femtomolar mercuric ions. *Arch Biochem Biophys* **357**, 207-24
- Auton M., Holthauzen L.M. & Bolen D.W. (2007) Anatomy of energetic changes accompanying urea-induced protein denaturation. *Proc Natl Acad Sci U S A* **104**, 15317-22
- Baker B.M. & Murphy K.P. (1996) Evaluation of linked protonation effects in protein binding reactions using isothermal titration calorimetry. *Biophys J* **71**, 2049-55

- Barthel S., Bernat G., Seidel T., Rupprecht E., Kahmann U. & Schneider D. (2013) Thylakoid membrane maturation and PSII activation are linked in greening *Synechocystis* sp. PCC 6803 cells. *Plant Physiol* **163**, 1037-46
- Bastien O., Botella C., Chevalier F., Block M.A., Jouhet J., Breton C., Girard-Egrot A. & Marechal E. (2016) New Insights on Thylakoid Biogenesis in Plant Cells. *Int Rev Cell Mol Biol* **323**, 1-30
- Bellsollell L., Prieto J., Serrano L. & Coll M. (1994) Magnesium binding to the bacterial chemotaxis protein CheY results in large conformational changes involving its functional surface. *J Mol Biol* **238**, 489-95
- Benning C., Beatty J.T., Prince R.C. & Somerville C.R. (1993) The sulfolipid sulfoquinovosyldiacylglycerol is not required for photosynthetic electron transport in *Rhodobacter sphaeroides* but enhances growth under phosphate limitation. *Proc Natl Acad Sci U S A* **90**, 1561-5
- Benning C., Xu C. & Awai K. (2006) Non-vesicular and vesicular lipid trafficking involving plastids. *Curr Opin Plant Biol* **9**, 241-7
- Bisicchia P., Botella E. & Devine K.M. (2010) Suite of novel vectors for ectopic insertion of GFP, CFP and IYFP transcriptional fusions in single copy at the amyE and bglS loci in *Bacillus subtilis*. *Plasmid* **64**, 143-9
- Biswal B., Raval M.K. & Biswal U.C. (1989) Changes in Chlorophyll Fluorescence during Aging of Cell Free Chloroplasts. *Biochemie und Physiologie der Pflanzen* **184**, 213-8
- Black C.B., Huang H.W. & Cowan J.A. (1994) Biological coordination chemistry of magnesium, sodium, and potassium ions. Protein and nucleotide binding sites. *Coordination Chemistry Reviews* **135-136**, 165-202
- Bohne A.V., Schwarz C., Schottkowski M., Lidschreiber M., Piotrowski M., Zerges W. & Nickelsen J. (2013) Reciprocal regulation of protein synthesis and carbon metabolism for thylakoid membrane biogenesis. *PLoS Biol* **11**, e1001482
- Bosak T., Liang B., Sim M.S. & Petroff A.P. (2009) Morphological record of oxygenic photosynthesis in conical stromatolites. *Proc Natl Acad Sci U S A* **106**, 10939-43
- Bottier C., Gean J., Artzner F., Desbat B., Pezolet M., Renault A., Marion D. & Vie V. (2007) Galactosyl headgroup interactions control the molecular packing of wheat lipids in Langmuir films and in hydrated liquid-crystalline mesophases. *Biochim Biophys Acta* **1768**, 1526-40
- Bradford M.M. (1976) A rapid and sensitive method for the quantitation of microgram quantities of protein utilizing the principle of protein-dye binding. *Anal Biochem* **72**, 248-54
- Brissette J.L., Russel M., Weiner L. & Model P. (1990) Phage shock protein, a stress protein of *Escherichia coli*. *Proc Natl Acad Sci U S A* **87**, 862-6

- Brissette J.L., Weiner L., Ripmaster T.L. & Model P. (1991) Characterization and sequence of the Escherichia coli stress-induced *psp* operon. *J Mol Biol* **220**, 35-48
- Broussard J.A., Rappaz B., Webb D.J. & Brown C.M. (2013) Fluorescence resonance energy transfer microscopy as demonstrated by measuring the activation of the serine/threonine kinase Akt. *Nat Protoc* **8**, 265-81
- Bryan S.J., Burroughs N.J., Shevela D., Yu J., Rupprecht E., Liu L.N., Mastroianni G., Xue Q., Llorente-Garcia I., Leake M.C., Eichacker L.A., Schneider D., Nixon P.J. & Mullineaux C.W. (2014) Localisation and interactions of the Vipp1 protein in cyanobacteria. *Mol Microbiol*
- Bultema J.B., Fuhrmann E., Boekema E.J. & Schneider D. (2010) Vipp1 and PspA: Related but not twins. *Commun Integr Biol* **3**, 162-5
- Cao Z.F., Luo W. & Zhou H.M. (1999) Effect of Mg<sup>2+</sup> on the thermal inactivation and unfolding of creatine kinase. *Int J Biochem Cell Biol* **31**, 1307-13
- Chapman D.J., De-Felice J. & Barber J. (1983) Growth temperature effects on thylakoid membrane lipid and protein content of pea chloroplasts. *Plant Physiol* **72**, 225-8
- Charuvi D., Kiss V., Nevo R., Shimoni E., Adam Z. & Reich Z. (2012) Gain and loss of photosynthetic membranes during plastid differentiation in the shoot apex of Arabidopsis. *Plant Cell* **24**, 1143-57
- Chernomordik L.V. & Kozlov M.M. (2008) Mechanics of membrane fusion. *Nat Struct Mol Biol* **15**, 675-83
- Chin-Sang I.D. & Spence A.M. (1996) Caenorhabditis elegans sex-determining protein FEM-2 is a protein phosphatase that promotes male development and interacts directly with FEM-3. *Genes Dev* **10**, 2314-25
- Correa F., Farah C.S. & Salinas R.K. (2009) Mg<sup>2+</sup> ions bind at the C-terminal region of skeletal muscle alpha-tropomyosin. *Biopolymers* **91**, 583-90
- Cowan J.A. (1998) Metal Activation of Enzymes in Nucleic Acid Biochemistry. *Chem Rev* **98**, 1067-88
- Crooks G.E., Hon G., Chandonia J.M. & Brenner S.E. (2004) WebLogo: a sequence logo generator. *Genome Res* **14**, 1188-90
- Dahlberg M. (2007) Polymorphic phase behavior of cardiolipin derivatives studied by coarse-grained molecular dynamics. *J Phys Chem B* **111**, 7194-200
- Darwin A.J. (2005) The phage-shock-protein response. *Mol Microbiol* **57**, 621-8
- Debus M. (2013) Examensarbeit: Einfluss des C-Terminus auf die Struktur und Funktion des Vipp1-Proteins aus Synechocystis sp. Stamm PCC 6803. In: *Institut für Pharmazie und Biochemie*. Johannes Gutenberg-Universität, Mainz
- DeLisa M.P., Lee P., Palmer T. & Georgiou G. (2004) Phage shock protein PspA of Escherichia coli relieves saturation of protein export via the Tat pathway. *J Bacteriol* **186**, 366-73

- Dorne A.J., Joyard J. & Douce R. (1990) Do thylakoids really contain phosphatidylcholine? *Proc Natl Acad Sci U S A* **87**, 71-4
- Douce R. (1974) Site of biosynthesis of galactolipids in spinach chloroplasts. *Science* **183**, 852-3
- Dudev M. & Lim C. (2007) Discovering structural motifs using a structural alphabet: application to magnesium-binding sites. *BMC Bioinformatics* **8**, 106
- Dudev T., Cowan J.A. & Lim C. (1999) Competitive Binding in Magnesium Coordination Chemistry: Water versus Ligands of Biological Interest. *J Am Chem Soc* **121**, 7665-73
- Elderkin S., Bordes P., Jones S., Rappas M. & Buck M. (2005) Molecular determinants for PspA-mediated repression of the AAA transcriptional activator PspF. *J Bacteriol* **187**, 3238-48
- EncapsulaNanoSciencesLLC (2012) Fluorescent Liposomes: Intermixing of lipids during liposome fusion (NBD/Rhodamine Assay). URL <http://www.liposomes.org/search/label/fusion%20assay>
- Engel B.D., Schaffer M., Kuhn Cuellar L., Villa E., Plitzko J.M. & Baumeister W. (2015) Native architecture of the Chlamydomonas chloroplast revealed by in situ cryo-electron tomography. *Elife* **4**
- Ernst R., Ejsing C.S. & Antonny B. (2016) Homeoviscous Adaptation and the Regulation of Membrane Lipids. *J Mol Biol* **428**, 4776-91
- Essigmann B., Guler S., Narang R.A., Linke D. & Benning C. (1998) Phosphate availability affects the thylakoid lipid composition and the expression of SQD1, a gene required for sulfolipid biosynthesis in Arabidopsis thaliana. *Proc Natl Acad Sci U S A* **95**, 1950-5
- Favre-Bonvin G., Bostancioglu K. & Wallach J.M. (1986) Ca<sup>2+</sup> and Mg<sup>2+</sup> protection against thermal denaturation of pancreatic elastase. *Biochem Int* **13**, 983-9
- Feng J., Fan P., Jiang P., Lv S., Chen X. & Li Y. (2014) Chloroplast-targeted Hsp90 plays essential roles in plastid development and embryogenesis in Arabidopsis possibly linking with VIPP1. *Physiol Plant* **150**, 292-307
- Finn R.D., Bateman A., Clements J., Coggill P., Eberhardt R.Y., Eddy S.R., Heger A., Hetherington K., Holm L., Mistry J., Sonnhammer E.L., Tate J. & Punta M. (2014) Pfam: the protein families database. *Nucleic Acids Res* **42**, D222-30
- Frain K.M., Gangl D., Jones A., Zedler J.A. & Robinson C. (2016) Protein translocation and thylakoid biogenesis in cyanobacteria. *Biochim Biophys Acta* **1857**, 266-73
- Fuhrmann E. (2010) Dissertation: Struktur und Funktion des vesicle-inducing protein in plastids 1 aus Synechocystis sp. PCC 6803. In: *Institut für Biochemie und Molekularbiologie*. Albert-Ludwigs-Universität Freiburg, Freiburg

- Fuhrmann E., Bultema J.B., Kahmann U., Rupprecht E., Boekema E.J. & Schneider D. (2009a) The vesicle-inducing protein 1 from *Synechocystis* sp. PCC 6803 organizes into diverse higher-ordered ring structures. *Mol Biol Cell* **20**, 4620-8
- Fuhrmann E., Gathmann S., Rupprecht E., Golecki J. & Schneider D. (2009b) Thylakoid membrane reduction affects the photosystem stoichiometry in the cyanobacterium *Synechocystis* sp. PCC 6803. *Plant Physiol* **149**, 735-44
- Gao F., Wang W., Zhang W. & Liu C. (2015) alpha-Helical Domains Affecting the Oligomerization of Vipp1 and Its Interaction with Hsp70/DnaK in *Chlamydomonas*. *Biochemistry* **54**, 4877-89
- Garab G., Lohner K., Laggnér P. & Farkas T. (2000) Self-regulation of the lipid content of membranes by non-bilayer lipids: a hypothesis. *Trends Plant Sci* **5**, 489-94
- Garab G., Ughy B., Waard P., Akhtar P., Javornik U., Kotakis C., Sket P., Karlicky V., Materova Z., Spunda V., Plavec J., van Amerongen H., Vigh L., As H.V. & Lambrev P.H. (2017) Lipid polymorphism in chloroplast thylakoid membranes - as revealed by <sup>31</sup>P-NMR and time-resolved merocyanine fluorescence spectroscopy. *Sci Rep* **7**, 13343
- Gasteiger E., Hoogland C., Gattiker A., Duvaud S.e., Wilkins M.R., Appel R.D. & Bairoch A. (2005) Protein Identification and Analysis Tools on the ExPASy Server. In: *The Proteomics Protocols Handbook* (ed. by Walker JM), pp. 571-607. Humana Press, Totowa, NJ
- Gohre V., Ossenbuhl F., Crevecoeur M., Eichacker L.A. & Rochaix J.D. (2006) One of two alb3 proteins is essential for the assembly of the photosystems and for cell survival in *Chlamydomonas*. *Plant Cell* **18**, 1454-66
- Gounaris K., Sundby C., Andersson B. & Barber J. (1983) Lateral heterogeneity of polar lipids in the thylakoid membranes of spinach chloroplasts. *FEBS Lett* **156**, 170-4
- Govindjee & Shevela D. (2011) Adventures with cyanobacteria: a personal perspective. *Front Plant Sci* **2**, 28
- Grossoehme N.E., Spuches A.M. & Wilcox D.E. (2010) Application of isothermal titration calorimetry in bioinorganic chemistry. *J Biol Inorg Chem* **15**, 1183-91
- Guler S., Seeliger A., Hartel H., Renger G. & Benning C. (1996) A null mutant of *Synechococcus* sp. PCC7942 deficient in the sulfolipid sulfoquinovosyl diacylglycerol. *J Biol Chem* **271**, 7501-7
- Hankamer B.D., Elderkin S.L., Buck M. & Nield J. (2004) Organization of the AAA(+) adaptor protein PspA is an oligomeric ring. *J Biol Chem* **279**, 8862-6
- Hazra S., Henderson J.N., Liles K., Hilton M.T. & Wachter R.M. (2015) Regulation of ribulose-1,5-bisphosphate carboxylase/oxygenase (rubisco) activase: product inhibition, cooperativity, and magnesium activation. *J Biol Chem* **290**, 24222-36

- Heide H., Nordhues A., Drepper F., Nick S., Schulz-Raffelt M., Haehnel W. & Schroda M. (2009) Application of quantitative immunoprecipitation combined with knockdown and cross-linking to *Chlamydomonas* reveals the presence of vesicle-inducing protein in plastids 1 in a common complex with chloroplast HSP90C. *Proteomics* **9**, 3079-89
- Heidrich J., Junglas B., Grytsyk N., Hellmann N., Rusitzka K., Gebauer W., Markl J., Hellwig P. & Schneider D. (2018) Mg<sup>2+</sup>-binding triggers rearrangement of the IM30 ring structure, resulting in augmented exposure of hydrophobic surfaces competent for membrane binding. *J Biol Chem*, in revision
- Heidrich J., Thurotte A. & Schneider D. (2017) Specific interaction of IM30/Vipp1 with cyanobacterial and chloroplast membranes results in membrane remodeling and eventually in membrane fusion. *Biochim Biophys Acta* **1859**, 537-49
- Heidrich J., Wulf V., Hennig R., Saur M., Markl J., Sonnichsen C. & Schneider D. (2016) Organization into Higher Ordered Ring Structures Counteracts Membrane Binding of IM30, a Protein Associated with Inner Membranes in Chloroplasts and Cyanobacteria. *J Biol Chem* **291**, 14954-62
- Heinz S., Rast A., Shao L., Gutu A., Gugel I.L., Heyno E., Labs M., Rengstl B., Viola S., Nowaczyk M.M., Leister D. & Nickelsen J. (2016) Thylakoid Membrane Architecture in *Synechocystis* Depends on CurT, a Homolog of the Granal CURVATURE THYLAKOID1 Proteins. *Plant Cell*
- Hennig R. (2014) PhD thesis: IM30, Vipp1 or PspA - Multiple names to describe a multi-functional protein? In: *Institut für Pharmazie und Biochemie*. Johannes Gutenberg-Universität Mainz, Mainz
- Hennig R., Heidrich J., Saur M., Schmuser L., Roeters S.J., Hellmann N., Woutersen S., Bonn M., Weidner T., Markl J. & Schneider D. (2015) IM30 triggers membrane fusion in cyanobacteria and chloroplasts. *Nat Commun* **6**, 7018
- Hennig R., West A., Debus M., Saur M., Markl J., Sachs J.N. & Schneider D. (2017) The IM30/Vipp1 C-terminus associates with the lipid bilayer and modulates membrane fusion. *Biochim Biophys Acta* **1858**, 126-36
- Hooper J.K., Boyd C.O. & Paavola L.G. (1991) Origin of Thylakoid Membranes in *Chlamydomonas reinhardtii* y-1 at 38 degrees C. *Plant Physiol* **96**, 1321-8
- Hope M.J., Bally M.B., Mayer L.D., Janoff A.S. & Cullis P.R. (1986) Generation of multilamellar and unilamellar phospholipid vesicles. *Chemistry and Physics of Lipids* **40**, 89-107
- Hope M.J., Bally M.B., Webb G. & Cullis P.R. (1985) Production of large unilamellar vesicles by a rapid extrusion procedure. Characterization of size distribution, trapped volume and ability to maintain a membrane potential. *Biochimica et Biophysica Acta (BBA) - Biomembranes* **812**, 55-65

- Ishijima S., Uchibori A., Takagi H., Maki R. & Ohnishi M. (2003) Light-induced increase in free Mg<sup>2+</sup> concentration in spinach chloroplasts: measurement of free Mg<sup>2+</sup> by using a fluorescent probe and necessity of stromal alkalization. *Arch Biochem Biophys* **412**, 126-32
- Janmey P.A. & Kinnunen P.K. (2006) Biophysical properties of lipids and dynamic membranes. *Trends Cell Biol* **16**, 538-46
- Johnson J.E. & Cornell R.B. (1999) Amphitropic proteins: regulation by reversible membrane interactions (review). *Mol Membr Biol* **16**, 217-35
- Joyard J. & Stumpf P.K. (1981) Synthesis of Long-Chain Acyl-CoA in Chloroplast Envelope Membranes. *Plant Physiol* **67**, 250-6
- Junglas B. (2016) Master thesis: Einfluss von Mg<sup>2+</sup> und anderen zweiwertigen Metallkationen auf die Struktur und Stabilität des IM30-Proteins aus *Synechocystis* sp. PCC 6803. In: *Institut für Pharmazie und Biochemie*. Johannes Gutenberg-Universität, Mainz
- Kana R. & Govindjee (2016) Role of Ions in the Regulation of Light-Harvesting. *Front Plant Sci* **7**, 1849
- Kanduc M., Schlaich A., de Vries A.H., Jouhet J., Marechal E., Deme B., Netz R.R. & Schneck E. (2017) Tight cohesion between glycolipid membranes results from balanced water-headgroup interactions. *Nat Commun* **8**, 14899
- Keller R. & Schneider D. (2013) Homologs of the yeast Tvp38 vesicle-associated protein are conserved in chloroplasts and cyanobacteria. *Front Plant Sci* **4**, 467
- Keren N., Liberton M. & Pakrasi H.B. (2005) Photochemical competence of assembled photosystem II core complex in cyanobacterial plasma membrane. *J Biol Chem* **280**, 6548-53
- Khan H.M., He T., Fuglebakk E., Grauffel C., Yang B., Roberts M.F., Gershenson A. & Reuter N. (2016) A Role for Weak Electrostatic Interactions in Peripheral Membrane Protein Binding. *Biophys J* **110**, 1367-78
- Khan N.Z., Lindquist E. & Aronsson H. (2013) New putative chloroplast vesicle transport components and cargo proteins revealed using a bioinformatics approach: an Arabidopsis model. *PLoS One* **8**, e59898
- Khrustalev V.V., Barkovsky E.V. & Khrustaleva T.A. (2016) Magnesium and manganese binding sites on proteins have the same predominant motif of secondary structure. *J Theor Biol* **395**, 174-85
- Kim J., Mosior M., Chung L.A., Wu H. & McLaughlin S. (1991) Binding of peptides with basic residues to membranes containing acidic phospholipids. *Biophys J* **60**, 135-48
- Kirsch R.D. & Joly E. (1998) An improved PCR-mutagenesis strategy for two-site mutagenesis or sequence swapping between related genes. *Nucleic Acids Res* **26**, 1848-50

- Kleerebezem M., Crielaard W. & Tommassen J. (1996) Involvement of stress protein PspA (phage shock protein A) of *Escherichia coli* in maintenance of the protonmotive force under stress conditions. *EMBO J* **15**, 162-71
- Kobayashi R., Suzuki T. & Yoshida M. (2007) *Escherichia coli* phage-shock protein A (PspA) binds to membrane phospholipids and repairs proton leakage of the damaged membranes. *Mol Microbiol* **66**, 100-9
- Krause G.H. (1977) Light-induced movement of magnesium ions in intact chloroplasts. Spectroscopic determination with Eriochrome Blue SE. *Biochim Biophys Acta* **460**, 500-10
- Kretschmann E. (1972) Decay of non radiative surface plasmons into light on rough silver films. Comparison of experimental and theoretical results. *Optics Communications* **6**, 185-7
- Kroll D., Meierhoff K., Bechtold N., Kinoshita M., Westphal S., Vothknecht U.C., Soll J. & Westhoff P. (2001) VIPP1, a nuclear gene of *Arabidopsis thaliana* essential for thylakoid membrane formation. *Proc Natl Acad Sci U S A* **98**, 4238-42
- Kunkel D.D. (1982) Thylakoid centers: Structures associated with the cyanobacterial photosynthetic membrane system. *Archives of Microbiology* **133**, 97-9
- Laemmli U.K. (1970) Cleavage of structural proteins during the assembly of the head of bacteriophage T4. *Nature* **227**, 680-5
- Lau S.Y., Taneja A.K. & Hodges R.S. (1984) Synthesis of a model protein of defined secondary and quaternary structure. Effect of chain length on the stabilization and formation of two-stranded alpha-helical coiled-coils. *J Biol Chem* **259**, 13253-61
- Lavinder J.J., Hari S.B., Sullivan B.J. & Magliery T.J. (2009) High-throughput thermal scanning: a general, rapid dye-binding thermal shift screen for protein engineering. *J Am Chem Soc* **131**, 3794-5
- Lester D.S., Doll L., Brumfeld V. & Miller I.R. (1990) Lipid dependence of surface conformations of protein kinase C. *Biochim Biophys Acta* **1039**, 33-41
- Leventis R., Gagne J., Fuller N., Rand R.P. & Silvius J.R. (1986) Divalent cation induced fusion and lipid lateral segregation in phosphatidylcholine-phosphatidic acid vesicles. *Biochemistry* **25**, 6978-87
- Li H.M. & Chiu C.C. (2010) Protein transport into chloroplasts. *Annu Rev Plant Biol* **61**, 157-80
- Li H.M., Kaneko Y. & Keegstra K. (1994) Molecular cloning of a chloroplastic protein associated with both the envelope and thylakoid membranes. *Plant Mol Biol* **25**, 619-32
- Liberton M., Austin J.R., 2nd, Berg R.H. & Pakrasi H.B. (2011a) Insights into the complex 3-D architecture of thylakoid membranes in unicellular cyanobacterium *Cyanothece* sp. ATCC 51142. *Plant Signal Behav* **6**, 566-9

- Liberton M., Austin J.R., 2nd, Berg R.H. & Pakrasi H.B. (2011b) Unique thylakoid membrane architecture of a unicellular N<sub>2</sub>-fixing cyanobacterium revealed by electron tomography. *Plant Physiol* **155**, 1656-66
- Liberton M., Howard Berg R., Heuser J., Roth R. & Pakrasi H.B. (2006) Ultrastructure of the membrane systems in the unicellular cyanobacterium *Synechocystis* sp. strain PCC 6803. *Protoplasma* **227**, 129-38
- Lim W.K., Rosgen J. & Englander S.W. (2009) Urea, but not guanidinium, destabilizes proteins by forming hydrogen bonds to the peptide group. *Proc Natl Acad Sci U S A* **106**, 2595-600
- Lin D.C. & Novel P.S. (1971) Control of photosynthesis by Mg<sup>2+</sup>. *Arch Biochem Biophys* **145**, 622-32
- Lindquist E., Solymosi K. & Aronsson H. (2016) Vesicles Are Persistent Features of Different Plastids. *Traffic* **17**, 1125-38
- Liu C., Willmund F., Golecki J.R., Cacace S., Hess B., Markert C. & Schroda M. (2007) The chloroplast HSP70B-CDJ2-CGE1 chaperones catalyse assembly and disassembly of VIPP1 oligomers in *Chlamydomonas*. *Plant J* **50**, 265-77
- Liu C., Willmund F., Whitelegge J.P., Hawat S., Knapp B., Lodha M. & Schroda M. (2005) J-domain protein CDJ2 and HSP70B are a plastidic chaperone pair that interacts with vesicle-inducing protein in plastids 1. *Mol Biol Cell* **16**, 1165-77
- Liu J., Chen L., Wang J., Qiao J. & Zhang W. (2012) Proteomic analysis reveals resistance mechanism against biofuel hexane in *Synechocystis* sp. PCC 6803. *Biotechnology for Biofuels* **5**, 68
- Lo S.M. & Theg S.M. (2012) Role of vesicle-inducing protein in plastids 1 in cpTat transport at the thylakoid. *Plant J* **71**, 656-68
- Los D.A., Zorina A., Sinetova M., Kryazhov S., Mironov K. & Zinchenko V.V. (2010) Stress sensors and signal transducers in cyanobacteria. *Sensors (Basel)* **10**, 2386-415
- Majeran W., Cai Y., Sun Q. & van Wijk K.J. (2005) Functional differentiation of bundle sheath and mesophyll maize chloroplasts determined by comparative proteomics. *Plant Cell* **17**, 3111-40
- Marsden H.R., Tomatsu I. & Kros A. (2011) Model systems for membrane fusion. *Chem Soc Rev* **40**, 1572-85
- Martin W. & Kowallik K. (1999) Annotated English translation of Mereschkowsky's 1905 paper 'Über Natur und Ursprung der Chromatophoren im Pflanzenreiche'. *European Journal of Phycology* **34**, 287-95
- Matsuzaki K., Murase O., Sugishita K., Yoneyama S., Akada K., Ueha M., Nakamura A. & Kobayashi S. (2000) Optical characterization of liposomes by right angle light scattering and turbidity measurement. *Biochim Biophys Acta* **1467**, 219-26

- Matulis D., Baumann C.G., Bloomfield V.A. & Lovrien R.E. (1999) 1-anilino-8-naphthalene sulfonate as a protein conformational tightening agent. *Biopolymers* **49**, 451-8
- Mbah A.N. (2014) Application of Hybrid Functional Groups to Predict ATP Binding Proteins. *ISRN Computational Biology* **2014**, 11
- McDonald C., Jovanovic G., Ces O. & Buck M. (2015) Membrane Stored Curvature Elastic Stress Modulates Recruitment of Maintenance Proteins PspA and Vipp1. *MBio* **6**, e01188-15
- McDonald C., Jovanovic G., Wallace B.A., Ces O. & Buck M. (2017) Structure and function of PspA and Vipp1 N-terminal peptides: Insights into the membrane stress sensing and mitigation. *Biochim Biophys Acta* **1859**, 28-39
- McIntyre J.C. & Sleight R.G. (1991) Fluorescence assay for phospholipid membrane asymmetry. *Biochemistry* **30**, 11819-27
- Migneault I., Dartiguenave C., Bertrand M.J. & Waldron K.C. (2004) Glutaraldehyde: behavior in aqueous solution, reaction with proteins, and application to enzyme crosslinking. *Biotechniques* **37**, 790-6, 8-802
- Morgner N., Barth H.-D. & Brutschy B. (2006) A New Way To Detect Noncovalently Bonded Complexes of Biomolecules from Liquid Micro-Droplets by Laser Mass Spectrometry. *Australian Journal of Chemistry* **59**, 109-14
- Morgner N. & Robinson C.V. (2012) Massign: an assignment strategy for maximizing information from the mass spectra of heterogeneous protein assemblies. *Anal Chem* **84**, 2939-48
- Morre D.J., Sellden G., Sundqvist C. & Sandelius A.S. (1991) Stromal low temperature compartment derived from the inner membrane of the chloroplast envelope. *Plant Physiol* **97**, 1558-64
- Mullis K.B. & Faloona F.A. (1987) Specific synthesis of DNA in vitro via a polymerase-catalyzed chain reaction. *Methods Enzymol* **155**, 335-50
- Murata N. (1989) Low-temperature effects on cyanobacterial membranes. *J Bioenerg Biomembr* **21**, 61-75
- Nagai T., Ibata K., Park E.S., Kubota M., Mikoshiba K. & Miyawaki A. (2002) A variant of yellow fluorescent protein with fast and efficient maturation for cell-biological applications. *Nat Biotechnol* **20**, 87-90
- Nakamura Y., Kaneko T., Sato S., Mimuro M., Miyashita H., Tsuchiya T., Sasamoto S., Watanabe A., Kawashima K., Kishida Y., Kiyokawa C., Kohara M., Matsumoto M., Matsuno A., Nakazaki N., Shimpo S., Takeuchi C., Yamada M. & Tabata S. (2003) Complete genome structure of *Gloeobacter violaceus* PCC 7421, a cyanobacterium that lacks thylakoids. *DNA Res* **10**, 137-45

- Nevo R., Charuvi D., Shimoni E., Schwarz R., Kaplan A., Ohad I. & Reich Z. (2007) Thylakoid membrane perforations and connectivity enable intracellular traffic in cyanobacteria. *EMBO J* **26**, 1467-73
- Nevo R., Charuvi D., Tsabari O. & Reich Z. (2012) Composition, architecture and dynamics of the photosynthetic apparatus in higher plants. *Plant J* **70**, 157-76
- Nickelsen J., Rengstl B., Stengel A., Schottkowski M., Soll J. & Ankele E. (2011) Biogenesis of the cyanobacterial thylakoid membrane system--an update. *FEMS Microbiol Lett* **315**, 1-5
- Nimura K., Yoshikawa H. & Takahashi H. (1996) DnaK3, one of the three DnaK proteins of cyanobacterium *Synechococcus* sp. PCC7942, is quantitatively detected in the thylakoid membrane. *Biochem Biophys Res Commun* **229**, 334-40
- Ohki S., Ikura M. & Zhang M. (1997) Identification of Mg<sup>2+</sup>-binding sites and the role of Mg<sup>2+</sup> on target recognition by calmodulin. *Biochemistry* **36**, 4309-16
- Okuda K., Urabe I., Yamada Y. & Okada H. (1991) Reaction of glutaraldehyde with amino and thiol compounds. *Journal of Fermentation and Bioengineering* **71**, 100-5
- Olsen J.V., Ong S.E. & Mann M. (2004) Trypsin cleaves exclusively C-terminal to arginine and lysine residues. *Mol Cell Proteomics* **3**, 608-14
- Osadnik H., Schopf M., Heidrich E., Mehner D., Lilie H., Parthier C., Risselada H.J., Grubmuller H., Stubbs M.T. & Bruser T. (2015) PspF-binding domain PspA1-144 and the PspA.F complex: New insights into the coiled-coil-dependent regulation of AAA+ proteins. *Mol Microbiol* **98**, 743-59
- Ossenbuhl F., Hartmann K. & Nickelsen J. (2002) A chloroplast RNA binding protein from stromal thylakoid membranes specifically binds to the 5' untranslated region of the psbA mRNA. *Eur J Biochem* **269**, 3912-9
- Otters S. (2011) Dissertation: Strukturelle Analyse zur Oligomerisierung und Membranassoziation von Vipp1 aus *A. Thaliana*. In: *Fakultät für Biologie*. Ludwig-Maximilians-Universität München
- Otters S., Braun P., Hubner J., Wanner G., Vothknecht U.C. & Chigri F. (2013) The first alpha-helical domain of the vesicle-inducing protein in plastids 1 promotes oligomerization and lipid binding. *Planta* **237**, 529-40
- Pace C.N. (1986) Determination and analysis of urea and guanidine hydrochloride denaturation curves. *Methods Enzymol* **131**, 266-80
- Pannwitt S. (2015) Diplomarbeit: Bestimmung des optimalen effektiven Partikelradius zur Detektion von Proteinmonolagen an plasmonischen Nanopartikeln mittels optischer Dunkelfeldspektroskopie. In: *Institut für Physikalische Chemie*. Johannes Gutenberg-Universität, Mainz

- Patterson G.H., Piston D.W. & Barisas B.G. (2000) Forster distances between green fluorescent protein pairs. *Anal Biochem* **284**, 438-40
- PEPTIDE2.0 (2007) Peptide Hydrophobicity/Hydrophilicity Analysis. URL [https://www.peptide2.com/N\\_peptide\\_hydrophobicity\\_hydrophilicity.php](https://www.peptide2.com/N_peptide_hydrophobicity_hydrophilicity.php)
- Piovesan D., Profiti G., Martelli P.L. & Casadio R. (2012) The human "magnesome": detecting magnesium binding sites on human proteins. *BMC Bioinformatics* **13 Suppl 14**, S10
- Pitt-Rivers R. & Impiombato F.S. (1968) The binding of sodium dodecyl sulphate to various proteins. *Biochem J* **109**, 825-30
- Portis A.R. (1981) Evidence of a Low Stromal Mg(2+) Concentration in Intact Chloroplasts in the Dark: I. STUDIES WITH THE IONOPHORE A23187. *Plant Physiol* **67**, 985-9
- Portis A.R. (1992) Regulation of Ribulose 1,5-Bisphosphate Carboxylase/Oxygenase Activity. *Annual Review of Plant Physiology and Plant Molecular Biology* **43**, 415-37
- Portis A.R., Jr., Chon C.J., Mosbach A. & Heldt H.W. (1977) Fructose-and sedoheptulosebisphosphatase. The sites of a possible control of CO<sub>2</sub> fixation by lightdependent changes of the stromal Mg<sup>2+</sup> concentration. *Biochim Biophys Acta* **461**, 313-25
- Portis A.R., Jr. & Heldt H.W. (1976) Light-dependent changes of the Mg<sup>2+</sup> concentration in the stroma in relation to the Mg<sup>2+</sup> dependency of CO<sub>2</sub> fixation in intact chloroplasts. *Biochim Biophys Acta* **449**, 434-6
- Potvin-Fournier K., Valois-Paillard G., Lefèvre T., Cantin L., Salesse C. & Auger M. (2017) Membrane fluidity is a driving force for recoverin myristoyl immobilization in zwitterionic lipids. *Biochem Biophys Res Commun* **490**, 1268-73
- Prisic S., Xu J., Coates R.M. & Peters R.J. (2007) Probing the role of the DXDD motif in Class II diterpene cyclases. *Chembiochem* **8**, 869-74
- Rasmussen B., Fletcher I.R., Brocks J.J. & Kilburn M.R. (2008) Reassessing the first appearance of eukaryotes and cyanobacteria. *Nature* **455**, 1101
- Rast A., Heinz S. & Nickelsen J. (2015) Biogenesis of thylakoid membranes. *Biochim Biophys Acta* **1847**, 821-30
- Rexroth S., Mullineaux C.W., Ellinger D., Sendtko E., Rogner M. & Koenig F. (2011) The plasma membrane of the cyanobacterium *Gloeobacter violaceus* contains segregated bioenergetic domains. *Plant Cell* **23**, 2379-90
- Rippka R., Waterbury J. & Cohen-Bazire G. (1974) A cyanobacterium which lacks thylakoids. *Archives of Microbiology* **100**, 419-36
- Rupprecht E., Duppre E. & Schneider D. (2010) Similarities and singularities of three DnaK proteins from the cyanobacterium *Synechocystis* sp. PCC 6803. *Plant and Cell Physiology* **51**, 1210-8

- Rutgers M. & Schroda M. (2013) A role of VIPP1 as a dynamic structure within thylakoid centers as sites of photosystem biogenesis? *Plant Signal Behav* **8**, e27037
- Sanchez S.A., Triccerri M.A. & Gratton E. (2012) Laurdan generalized polarization fluctuations measures membrane packing micro-heterogeneity in vivo. *Proc Natl Acad Sci U S A* **109**, 7314-9
- Sato N., Tsuzuki M., Matsuda Y., Ehara T., Osafune T. & Kawaguchi A. (1995) Isolation and characterization of mutants affected in lipid metabolism of *Chlamydomonas reinhardtii*. *Eur J Biochem* **230**, 987-93
- Saur M., Hennig R., Young P., Rusitzka K., Hellmann N., Heidrich J., Morgner N., Markl J. & Schneider D. (2017) A Janus-Faced IM30 Ring Involved in Thylakoid Membrane Fusion Is Assembled from IM30 Tetramers. *Structure* **25**, 1380-90 e5
- Schneider D., Fuhrmann E., Scholz I., Hess W.R. & Graumann P.L. (2007) Fluorescence staining of live cyanobacterial cells suggest non-stringent chromosome segregation and absence of a connection between cytoplasmic and thylakoid membranes. *BMC Cell Biol* **8**, 39
- Schottkowski M., Peters M., Zhan Y., Rifai O., Zhang Y. & Zerges W. (2012) Biogenic membranes of the chloroplast in *Chlamydomonas reinhardtii*. *Proc Natl Acad Sci U S A* **109**, 19286-91
- Selao T.T., Zhang L., Knoppova J., Komenda J. & Norling B. (2016) Photosystem II Assembly Steps Take Place in the Thylakoid Membrane of the Cyanobacterium *Synechocystis* sp. PCC6803. *Plant and Cell Physiology* **57**, 95-104
- Shaul O. (2002) Magnesium transport and function in plants: the tip of the iceberg. *Biometals* **15**, 309-23
- Shimoni E., Rav-Hon O., Ohad I., Brumfeld V. & Reich Z. (2005) Three-dimensional organization of higher-plant chloroplast thylakoid membranes revealed by electron tomography. *Plant Cell* **17**, 2580-6
- Simidjiev I., Stoylova S., Amenitsch H., Javorfi T., Mustardy L., Laggner P., Holzenburg A. & Garab G. (2000) Self-assembly of large, ordered lamellae from non-bilayer lipids and integral membrane proteins in vitro. *Proc Natl Acad Sci U S A* **97**, 1473-6
- Sissi C. & Palumbo M. (2009) Effects of magnesium and related divalent metal ions in topoisomerase structure and function. *Nucleic Acids Res* **37**, 702-11
- Slavik J. (1982) Anilinonaphthalene sulfonate as a probe of membrane composition and function. *Biochim Biophys Acta* **694**, 1-25
- Spat P., Macek B. & Forchhammer K. (2015) Phosphoproteome of the cyanobacterium *Synechocystis* sp. PCC 6803 and its dynamics during nitrogen starvation. *Front Microbiol* **6**, 248

- Standar K., Mehner D., Osadnik H., Berthelmann F., Hause G., Lunsdorf H. & Bruser T. (2008) PspA can form large scaffolds in Escherichia coli. *FEBS Lett* **582**, 3585-9
- Stengel A., Gugel I.L., Hilger D., Rengstl B., Jung H. & Nickelsen J. (2012) Initial steps of photosystem II de novo assembly and preloading with manganese take place in biogenesis centers in Synechocystis. *Plant Cell* **24**, 660-75
- Struck D.K., Hoekstra D. & Pagano R.E. (1981) Use of resonance energy transfer to monitor membrane fusion. *Biochemistry* **20**, 4093-9
- Suppes J. (2013) Diplomarbeit: Lipidinteraktion und Funktion des Vipp1 Proteins aus *Synechocystis* sp. Stamm PCC 6803. In: *Institut für Pharmazie und Biochemie*. Johannes Gutenberg-Universität, Mainz
- Suzuki I., Kanesaki Y., Mikami K., Kanehisa M. & Murata N. (2001) Cold-regulated genes under control of the cold sensor Hik33 in Synechocystis. *Mol Microbiol* **40**, 235-44
- ThermoScientific™ (2017) Fluorescence SpectraViewer. URL <https://www.thermofisher.com/de/de/home/life-science/cell-analysis/labeling-chemistry/fluorescence-spectraviewer.html>
- Thurotte A., Brüser T., Mascher T. & Schneider D. (2017) Membrane chaperoning by members of the PspA/IM30 protein family. *Communicative & Integrative Biology* **10**, e1264546
- Trotta A., Suorsa M., Rantala M., Lundin B. & Aro E.M. (2016) Serine and threonine residues of plant STN7 kinase are differentially phosphorylated upon changing light conditions and specifically influence the activity and stability of the kinase. *Plant J* **87**, 484-94
- van de Meene A.M., Hohmann-Marriott M.F., Vermaas W.F. & Roberson R.W. (2006) The three-dimensional structure of the cyanobacterium Synechocystis sp. PCC 6803. *Arch Microbiol* **184**, 259-70
- Vothknecht U.C., Otters S., Hennig R. & Schneider D. (2012) Vipp1: a very important protein in plastids?! *J Exp Bot* **63**, 1699-712
- Wada H. & Murata N. (1989) Synechocystis PCC6803 Mutants Defective in Desaturation of Fatty Acids. *Plant and Cell Physiology* **30**, 971-8
- Walter B., Hristou A., Nowaczyk M.M. & Schunemann D. (2015) In vitro reconstitution of co-translational D1 insertion reveals a role of the cpSec-Alb3 translocase and Vipp1 in photosystem II biogenesis. *Biochem J* **468**, 315-24
- Wang J., Bello O., Auclair S.M., Wang J., Coleman J., Pincet F., Krishnakumar S.S., Sindelar C.V. & Rothman J.E. (2014a) Calcium sensitive ring-like oligomers formed by synaptotagmin. *Proc Natl Acad Sci U S A* **111**, 13966-71
- Wang W., Piao H., Choi D. & Son Y. (2014b) Nanodielectric properties of 16-MHDA self-assembled monolayers. *RSC Advances* **4**, 43387-91

- Westphal S., Heins L., Soll J. & Vothknecht U.C. (2001a) Vipp1 deletion mutant of *Synechocystis*: a connection between bacterial phage shock and thylakoid biogenesis? *Proc Natl Acad Sci U S A* **98**, 4243-8
- Westphal S., Soll J. & Vothknecht U.C. (2001b) A vesicle transport system inside chloroplasts. *FEBS Lett* **506**, 257-61
- White J.M., Delos S.E., Brecher M. & Schornberg K. (2008) Structures and mechanisms of viral membrane fusion proteins: multiple variations on a common theme. *Crit Rev Biochem Mol Biol* **43**, 189-219
- Winter R. & Noll F. (1998) *Methoden der Biophysikalischen Chemie*. Vieweg+Teubner Verlag.
- Xia X.F., Zhang F., Shaw P.C. & Sui S.F. (2003) Trichosanthin induces leakage and membrane fusion of liposome. *IUBMB Life* **55**, 681-7
- Yamaguchi S., Reid D.A., Rothenberg E. & Darwin A.J. (2013) Changes in Psp protein binding partners, localization and behaviour upon activation of the *Yersinia enterocolitica* phage shock protein response. *Mol Microbiol* **87**, 656-71
- Yamashita M.M., Wesson L., Eisenman G. & Eisenberg D. (1990) Where metal ions bind in proteins. *Proc Natl Acad Sci U S A* **87**, 5648-52
- Yu B., Xu C. & Benning C. (2002) Arabidopsis disrupted in SQD2 encoding sulfolipid synthase is impaired in phosphate-limited growth. *Proc Natl Acad Sci U S A* **99**, 5732-7
- Zak E., Norling B., Maitra R., Huang F., Andersson B. & Pakrasi H.B. (2001) The initial steps of biogenesis of cyanobacterial photosystems occur in plasma membranes. *Proc Natl Acad Sci U S A* **98**, 13443-8
- Zhang L., Kato Y., Otters S., Vothknecht U.C. & Sakamoto W. (2012) Essential role of VIPP1 in chloroplast envelope maintenance in Arabidopsis. *Plant Cell* **24**, 3695-707
- Zhang L., Kondo H., Kamikubo H., Kataoka M. & Sakamoto W. (2016a) VIPP1 Has a Disordered C-Terminal Tail Necessary for Protecting Photosynthetic Membranes against Stress. *Plant Physiol* **171**, 1983-95
- Zhang L., Kusaba M., Tanaka A. & Sakamoto W. (2016b) Protection of Chloroplast Membranes by VIPP1 Rescues Aberrant Seedling Development in Arabidopsis nyc1 Mutant. *Front Plant Sci* **7**, 533
- Zhou N.E., Kay C.M. & Hodges R.S. (1992) Synthetic model proteins. Positional effects of interchain hydrophobic interactions on stability of two-stranded alpha-helical coiled-coils. *J Biol Chem* **267**, 2664-70
- Zorina A.A. (2013) Eukaryotic protein kinases in cyanobacteria. *Russian Journal of Plant Physiology* **60**, 589-96

- 
- Zorina A.A., Bedbenov V.S., Novikova G.V., Panichkin V.B. & Los' D.A. (2014) Involvement of serine/threonine protein kinases in the cold stress response in the cyanobacterium *Synechocystis* sp. PCC 6803: Functional characterization of SpkE protein kinase. *Molecular Biology* **48**, 390-8

## **X Danksagung**



## **XI Curriculum vitae**





## **XII Declaration**

I hereby declare that I wrote the dissertation submitted without any unauthorized external assistance and used only sources acknowledged in the work. All textual passages which are appropriated verbatim or paraphrased from published and unpublished texts as well as all information obtained from oral sources are duly indicated and listed in accordance with bibliographical rules. In carrying out this research, I complied with the rules of standard scientific practice as formulated in the statutes of Johannes Gutenberg University Mainz to insure standard scientific practice.

---

Jennifer Heidrich

Mainz, den 28.02.2018